



**Metal-organic Framework (MOFs) Derived Nanocomposites:
Synthesis and Applications in Photocatalysis**

Submitted by

Mian Zahid Hussain

**to the University of Exeter as a thesis for the degree of Doctor of
Philosophy (PhD) in Physics/Engineering, November 2020.**

This thesis is available for Library use on the understanding that it is copyright material and that no quotation from the thesis may be published without proper acknowledgement.

I certify that all material in this thesis which is not my own work has been identified and that no material has previously been submitted and approved for the award of a degree by this or any other University.

Signature:

Mian Zahid Hussain

Abstract

Metal-organic frameworks (MOFs) are exceptionally porous coordination polymers forming highly crystalline reticular networks via the coordination bonds between organic ligands and inorganic metal clusters. In the past 10 years, MOFs have been proved to be excellent rationally designed precursors and sacrificial templates to derive metal compounds, metal compounds/carbon composites, porous carbons and related nanostructures. The inherited morphologies, adjustable structural and textural properties, in-situ modifiable physicochemical and semiconducting properties make MOFs derived composites excellent nanomaterials for a wide variety of applications in chemistry, physics, electronics and medical sciences. This thesis demonstrates the synthesis of selected Zn-MOFs and Ti-MOFs and their derived functionalised nanocomposites for applications in environment and energy. Briefly, this thesis systematically presents the following research findings:

The role of pyrolysis temperature and gaseous atmosphere in Zn-MOF derived composites was studied. Homogeneously dispersed crystalline ZnO nanoparticles embedded in a porous carbon matrix were synthesised via simple one-step carbonisation of MOF-5 at 800 °C and 1000 °C in air, argon and water vapour atmospheres. The resulting carbon doped ZnO, ZnO/C or porous carbon, decorated with hydrophilic functional groups retains the inherited cubic morphology of the precursor MOF-5. Built on the finding of the optimal synthesis conditions for best performing ZnO/C composites, a comparative study of 3 different Zn-MOFs including MOF-5, MOF-74 and ZIF-8 derived ZnO/C nanocomposites was carried out to further understand the structure-property-application relationships. The photocatalytic performance of these derived composites was also evaluated for photodegradation of organic dye pollutants and photocatalytic H₂ evolution reaction.

Moreover, an in-depth in-situ study was carried out to understand the pyrolytic conversion mechanism of Ti-MOF precursors into the desired TiO₂/C nanocomposites. The in-situ TGA-MS and in-situ STEM/EDX combined with other characterisation techniques were employed to investigate the evolution of the structural, physicochemical, textural and morphological properties of the NH₂-MIL-125(Ti) derived nanocomposites. Based on the understanding of the thermal

decomposition mechanism of $\text{NH}_2\text{-MIL-125(Ti)}$, Cu species were loaded into $\text{NH}_2\text{-MIL-125(Ti)}$ via the post-synthetic method to obtain bimetallic $\text{NH}_2\text{-MIL-125(Ti/Cu)}$. The effect of pyrolysis temperature on the thermal decomposition of $\text{NH}_2\text{-MIL-125(Ti/Cu)}$ under water vapour atmosphere and the subsequent in-situ formation of the p-n heterojunction between TiO_2 and Cu_xO nanoparticles were investigated, and their performance in photocatalytic H_2 evolution from water splitting was evaluated.

Contents

Abstract	3
Acknowledgements	9
Publications and presentations	11
List of abbreviations	15
List of figures and tables	18
Chapter 1 Introduction	27
Chapter 2 Literature review	34
2.1 Introduction.....	35
2.2 Basic principles of the synthesis of MOF derived nanocomposites	37
2.3 Photocatalysis mechanism of nanocomposites	39
2.4 MOF derived nanocomposites for photocatalytic applications.....	42
2.5 MOF derived nanocomposites for photocatalytic hydrogen (H ₂) evolution.....	44
2.5.1 0D nanocomposites	45
2.5.1.1 Polyhedra	45
2.5.1.2 Hollow nanocomposites.....	47
2.5.2 1D nanocomposites	49
2.5.2.1 Nanoshuttles.....	49
2.5.2.2 Nanorods	51
2.5.3 2D nanocomposites	52
2.5.3.1 Single metal nanosheets	53
2.5.3.2 Multi-metallic nanosheets	56
2.5.4 3D nanocomposites	60
2.5.4.1 Nanocubes	60
2.5.4.2 Nanodiscs.....	61

2.5.5	Summary of MOF derived nanocomposites for photocatalytic H ₂ evolution.....	62
2.6	MOF derived nanocomposites for photodegradation of pollutants.....	62
2.6.1	0D nanocomposites	63
2.6.1.1	Polyhedra	63
2.6.1.2	Self-templated core-shell nanostructures	66
2.6.1.3	External-templated core-shell nanostructures	68
2.6.2	1D nanocomposites	68
2.6.2.1	Nanorods	68
2.6.2.2	Nanotubes	69
2.6.2.3	Nanoshuttles.....	70
2.6.3	2D nanocomposites	72
2.6.3.1	Nanoplatelets.....	72
2.6.3.2	External-templated nanosheets	72
2.6.4	3D nanocomposites	75
2.6.4.1	Nanocubes	75
2.6.4.2	Nanodiscs.....	75
2.6.4.3	External-templated 3D nanocages and nanosponges	75
2.6.5	Summary of MOF derived nanocomposites for photodegradation of pollutants.....	79
Chapter 3 Experimental methodologies		81
3.1	Introduction.....	81
3.2	Synthesis of MOF precursors	81
3.2.1	Synthesis of MOF-5	81
3.2.2	Synthesis of MOF-74	81
3.2.3	Synthesis of ZIF-8.....	82
3.2.4	Synthesis of NH ₂ -MIL-125(Ti)	82
3.2.5	Synthesis of NH ₂ -MIL-125(Ti/Cu).....	82

3.3	Synthesis of MOF derived nanocomposites	83
3.3.1	Preparation of MOF derived ZnO/C nanocomposites	83
3.3.2	Synthesis of MOF derived TiO ₂ /C nanocomposites	84
3.3.3	Synthesis of MOF derived TiO ₂ /Cu _x O/C nanocomposites.....	84
3.4	Characterisation techniques	85
3.4.1	Powder X-ray Diffraction (PXRD).....	85
3.4.2	Thermogravimetric Analysis-Mass Spectrometer (TGA-MS)	86
3.4.3	N ₂ Physisorption Measurements.....	87
3.4.4	Fourier-Transform Infrared Spectroscopy (FTIR).....	87
3.4.5	Raman Spectroscopy.....	88
3.4.6	X-Ray Photoelectron Spectroscopy (XPS).....	89
3.4.7	Scanning Electron Microscopy (SEM).....	89
3.4.8	Transmission Electron Microscopy (TEM) and Energy Dispersive X-ray Spectroscopy (EDX).....	90
3.4.9	UV-Visible Spectrophotometer.....	91
3.4.10	Electrochemical Impedance Spectroscopy (EIS)	92
3.5	Photocatalytic applications	92
3.5.1	Photodegradation of Methylene Blue	92
3.5.2	Photocatalytic water splitting for H ₂ evolution	93
Chapter 4 MOF-5 derived porous ZnO/C nanocomposites for efficient dye photodegradation		95
4.1	Introduction.....	95
4.2	Results and discussion.....	97
4.2.1	Characterisations of MOF-5 derived ZnO, ZnO/C and porous carbon.....	97
4.2.2	Optical properties and photodegradation performance	108
4.3	Summary	114
Chapter 5 A comparative study of three Zn-MOFs derived ZnO/C nanocomposites for photocatalytic applications		115

5.1	Introduction.....	115
5.2	Results and discussion.....	117
5.2.1	Characterisations of MOFs and derived ZnO/C composites	117
5.2.2	Photocatalytic performances of the ZnO/C composites	134
5.2.2.1	Photodegradation of methylene blue	136
5.2.2.2	Photocatalytic H ₂ evolution	141
5.3	Summary	143
Chapter 6 An in-situ investigation of the thermal decomposition of metal-organic framework NH₂-MIL-125(Ti)		145
6.1	Introduction.....	145
6.2	Results and discussion.....	147
6.2.1	Composition and structural properties	147
6.2.2	Textural properties	155
6.2.3	Morphology	157
6.3	Summary	162
Chapter 7 Bimetal-organic framework (bi-MOFs) derived TiO₂/Cu_xO/C multi-heterostructured nanocomposites for highly efficient photocatalytic H₂ evolution		163
7.1	Introduction.....	163
7.2	Results and discussion.....	165
7.2.1	Characterisations of NH ₂ -MIL-125(Ti/Cu) and derived TiO ₂ /Cu _x O/C.....	165
7.2.2	Photocatalytic H ₂ evolution	180
7.3	Summary	190
Chapter 8 Conclusions and further work		191
8.1	Conclusions.....	191
8.2	Further work	194
References		196

Acknowledgements

I believe that life is a journey from nowhere to nowhere. The pleasure of living is in the process itself, and destinations only milestones leading us to the next journey. On this path, we meet all kinds of people. While some settle down on the way, others continue to live nomadic academic lives. As a foreign student, I identify myself with migratory birds, who leave behind many relationships, friendships, cultural and sensory experiences of material and non-material things, seeking better learning and living conditions. In the quest of knowledge and professional opportunities, the continuous struggle to assimilate into a new environment provides us with great learning opportunities, which broaden our mental horizons and deepen the understanding of life indeed.

The last 4 years of my life at the University of Exeter have been full of happenings, professionally and personally. Many interactions turned into enduring friendships for which I am thankful. First of all, I would like to express my deepest gratitude to my supervisor Dr Yongde Xia for his continuous support, mentorship and professional guidance during my PhD project. I can say that his trust in me to take decisions freely about the research project made me confident and mature. I would also like to thank Prof. Yanqiu Zhu as my second supervisor for providing an excellent working environment in Functional Materials Laboratory (Lab 08) which helped me to grow as an independent researcher. Equally, I would like to thank my colleagues and friends in the research group, including Dr Zhuxian Yang, Zheng Huang and other lab fellows, for their help, support and joyful time. I would like to especially thank Dr Hong Chang for her support and upbeat attitude to help with the characterisation of materials in the Imaging Suite. Special thanks to Dr Asif Tahir and Dr Govinder Pawar at Penryn campus for their help and fruitful collaboration. Outside the lab, I would like to thank my friends Emanuele Gemo and Caterina Palange for good conversations and jolly evenings. Moreover, I would like to extend my thanks to the Centre for Doctoral Training in Metamaterials (CDT XM²) and the Engineering and Physical Sciences Research Council (EPSRC), for funding this project. I also owe Prof. Alastair Hibbins and Dr Anja Roeding for their efforts and support.

I consider it a great fortune to collaborate with Prof. Roland A. Fischer at the Technical University of Munich (TUM). His guidance, support and trust in me have a great impact on my growth and development as a researcher. During my

short stay at TUM, I met many wonderful people. I would like to thank Dr Andreas Schneemann, Katia Rodewald, Tim Kratky, Andrea Abram, Dr Wei-Jin Li and Prof. Tom Nilges and other colleagues at AMC chair for their help in the characterisation of materials. Beyond that, with Werner Heinz and Stefano Dissegna, I made real friends.

I would also like to thank Prof. Freek Kapteijn with whom a brief interaction at the British Zeolite Association (BZA) meeting turned into a very useful and productive collaboration. Thanks go to Bart van der Linden also at the Technical University, Delft, the Netherlands, who was an excellent host during my brief visit to his lab, and he spent a significant amount of time to test my materials for the application. I am also thankful to Prof. Ovidiu Ersen at the University of Strasbourg, France, for the characterisation of my materials.

Above all, I owe a lot to my parents, Amin and Zahida, and my brothers, Waqar and Saqib for their unconditional love, enormous trust and unflagging support. They always gave me space, strength, resources and opportunities to become what I am today and helped me to live my dreams. Thank you for being there for me through thick and thin.

Along with the PhD, the last 4 years have been the most important time of my life. I married my partner Anna-Maria and became a parent of our lovely daughter Selma, as if a sailboat navigating without a compass saw the shore and anchored. Countless moments of joy, peace and contentment, as well as many sleepless nights of childcare, frustrating days, lockdown months of Covid-19 and moving back and forth from Exeter to Munich, all make this life substantial. Your love and support as a partner provide me with inimitable stability and strength. With you, I got a loving family and a big circle of friends where I felt at home right away.

Anna-Maria and Selma, this PhD thesis is dedicated to you.

Mian Zahid Hussain

October 2020

Publications and presentations

Peer-reviewed publications from this thesis:

- **M. Z. Hussain**, M. Bahri, W. R. Heinz, O. Ersen, T. Kratky, R. A. Fischer, Y. Zhu, Y. Xia, An in-situ investigation of the thermal decomposition of metal-organic framework NH₂-MIL-125(Ti), *Microporous and Mesoporous Materials*, **316**, 2021, 110957.
- **M. Z. Hussain**, B. van der Linden, Z. Yang, Q. Jia, H. Chang, R. A. Fischer, F. Kapteijn, Y. Zhu, Y. Xia, Bimetal-organic framework derived multi-heterostructured TiO₂/Cu_xO/C nanocomposites with superior photocatalytic H₂ generation performance, *Journal of Materials Chemistry A*, **9**, 2021, 4103-4116.
- **M. Z. Hussain**, Z. Yang, B. van der Linden, Z. Huang, Q. Jia, E. Cerrato, R. A. Fischer, F. Kapteijn, Y. Zhu, Y. Xia, Surface functionalised N-C-TiO₂/C nanocomposites derived from metal-organic framework in water vapour for enhanced photocatalytic H₂ generation, *Journal of Energy Chemistry*, **57**, 2021, 485-495.
- **M. Z. Hussain**, G.S. Pawar, Z. Huang, A. A. Tahir, R. A. Fischer, Y. Zhu, Y. Xia, Porous ZnO/Carbon nanocomposites derived from metal-organic frameworks for highly efficient photocatalytic applications: A correlational study, *Carbon*, **146**, 2019, 348-363.
- **M. Z. Hussain**, A. Schneemann, R. A. Fischer, Y. Zhu, Y. Xia, MOF derived porous ZnO/C nanocomposites for efficient dye photodegradation, *ACS Applied Energy Materials*, **1**, 2018, 4695-4707. (Selected for the front cover of the journal issue)

Peer-reviewed publications outside the scope of this thesis:

- Y. Chen; O. Ola, G. Liu, L. Han, **M. Z. Hussain**, K. Thummavichai, J. Wen, L. Zhang, N. Wang, Y. Xia and Y. Zhu, Multifunctional porous SiC

nanowire scaffolds, *Journal of the European Ceramic Society*, 2021. (In press), doi.org/10.1016/j.jeurceramsoc.2021.02.021

- K. Thummavichai, L. A. Thi, S-Y. Pung, O. Ola, **M. Z. Hussain**, Y. Chen, F. Xu, W. Chen, N. Wang, and Yanqiu Zhu, Sodium tungsten oxide bronze nanowires bundles in adsorption of methylene blue dye under UV and visible light exposure, *Energies*, 2021. (Accepted)
- Z. Huang, Z. Yang, **M. Z. Hussain**, Q. Jia, Y. Zhu, Y. Xia, Bimetallic Fe-Mo sulphide/carbon nanocomposites derived from phosphomolybdic acid encapsulated in MOF for efficient hydrogen generation, *Journal of Materials Science and Technology*, **84**, 2021, 76-85.
- Z. Huang, Z. Yang, **M. Z. Hussain**, B. Chen, Q. Jia, Y. Zhu, Y. Xia, Polyoxometallates@zeolitic-imidazolate-framework derived bimetallic tungsten-cobalt sulphide/porous carbon nanocomposites as efficient bifunctional electrocatalysts for hydrogen and oxygen evolution, *Electrochimica Acta*, **330**, 2020, 135335.
- N. Bibi, **M. Z. Hussain**, S. Hussain, S. Ahmed, I. Ahmad, S. Zhang, A. Iqbal, Excellent electrochemical performance of SrZrO₃ nanorods as supercapacitor electrode in aqueous electrolytes, *Applied Surface Science*, **495**, 2019, 143587.
- S. U. Awan, S. K. Hasanain, J. Rashid, S. Hussain, S. A. Shah, **M. Z. Hussain**, M. Rafique, M. Aftab, R. Khan, Structural, optical, electronic and magnetic properties of multiphase ZnO/Zn(OH)₂/ZnO₂ nanocomposites and hexagonal prism shaped ZnO nanoparticles synthesised by pulse laser ablation in Heptanes, *Materials Chemistry and Physics*, **211**, 2018, 510-521.
- **M. Z. Hussain**, R. Khan, R. Ali, Y. Khan, Optical properties of laser ablated ZnO nanoparticles prepared with Tween-80, *Materials Letters*, **122**, 2014, 147-150.

Manuscripts submitted to the peer-reviewed journals:

- **M. Z. Hussain**, Z. Yang, A. M. E. Khalil, S. Hussain, S. U. Awan, Y. Zhu, and Y. Xia, Metal-organic framework derived multi-functionalized and co-doped TiO₂/C nanocomposites for excellent visible-light photocatalysis, *Chemical Engineering Journal*, 2021.
- **M. Z. Hussain**, Z. Yang, Z. Huang, Q. Jia, Y. Zhu and Y. Xia, Metal-organic frameworks derived nanocomposites for photocatalytic applications in energy and environment, *Advanced Science*, 2021.

Manuscripts in preparation:

- **M. Z. Hussain**, B. van der Linden, M. Bahri, O. Ersen, F. Kapteijn, Y. Zhu and Y. Xia, Deciphering the role of metal oxides and porous carbon in MOF derived TiO₂/Cu_xO/C composites for photocatalytic H₂ evolution, 2021.
- **M. Z. Hussain**, C. Yao, Y. Xia, Metal-organic frameworks (MOFs) and Derivatives for applications in dye-sensitized solar cells, 2021.

Selected conference presentations

Oral presentations

- **M. Z. Hussain**, Y. Xia, Bi-MOF derived nanocomposites_applications in photocatalysis, *GWPore: Conference on Porous Materials for Energy, Environment and Healthcare Applications*, U.K. February 2021. (2nd best presentation award)
- **M. Z. Hussain**, Y. Zhu, Y. Xia, MOF derived photocatalysts for high efficient solar-light-driven H₂ evolution. *MCEC 2019, Conference on Materials for Clean Energy*, NPL, London, U.K. April 2019.
- **M. Z. Hussain**, R. A. Fischer, Y. Zhu, Y. Xia, MOF derived bimetal oxide/carbon composites: Synthesis and photocatalytic applications, *6th International Conference on Multifunctional, Hybrid and Nanomaterials*, Sitges, Spain, March 2019.

- **M. Z. Hussain**, Y. Zhu, Y. Xia, MOF derivatives for visible-light-driven photocatalytic applications, *41st Annual Meeting of the British Zeolite Association (BZA)*, Cumbria, Ambleside, U.K. July 2018.

Poster presentations

- **M. Z. Hussain**, R. A. Fischer, Y. Zhu, Y. Xia, Making heterostructures with water: Role of temperature and water steam in MOF derived TiO₂/CuO_x/Cu/C nanocomposites, *Euromof-2019, 3rd International Conference on MOFs and Porous Polymers*, Paris, France. October 2019.
- **M. Z. Hussain**, R. A. Fischer, Y. Zhu, Y. Xia, MOF derived TiO₂/C nanocomposites for photocatalysis, *ICS Winter School on Catalysis, Innovative Catalysis and Sustainability Scientific and Socio-Economic Aspects*, Turin, Italy. January 2019.
- **M. Z. Hussain**, Y. Zhu, Y. Xia, Black porous ZnO@C nanocomposites derived from MOF-5 for highly efficient photocatalytic application, *RAMS-Recent Appointees in Materials Science*, University of Exeter, U.K. September 2017.
- **M. Z. Hussain**, Y. Zhu, Y. Xia, MOF-5 derived ZnO/C nanocomposites for adsorption and photodegradation of organic pollutants, *NIM Conference on Nanostructured Functional Materials for Sustainable Energy Provision*, Munich, Germany. July 2017.

List of abbreviations

AC	Alternating current
AE	Auger electrons
AQY	Apparent quantum yield
BET	Brunauer-Emmett-Teller
BF-STEM	Bright field scanning transmission electron microscope
BSE	Backscattered electrons
CB	Conduction band
DMF	Dimethylformamide
DP	Depth profiling
DRS	Diffuse reflectance spectroscopy
DSC	Differential scanning calorimetry
e ⁻	Electrons
EBG	Energy Band Gap
EDX	Energy dispersive X-ray spectroscopy
EIS	Electrochemical impedance spectroscopy
EM	Elemental mapping
EPR	Electron paramagnetic resonance
EY	Eosin Y
FESEM	Field emission scanning electron microscopy
FTIR	Fourier transform infrared spectroscopy
FWHM	Full width half maximum
GC	Gas chromatography
GO	Graphene oxide
h ⁺	Holes
H ₂ BDC	Terephthalic acid
H ₄ DOBDC	2,5-dihydroxyterephthalic acid
HAADF-STEM	High-angle annular dark field scanning transmission electron microscope
HER	Hydrogen evolution reaction
HOMO	Highest occupied molecular orbital
HRTEM	High-resolution transmission electron microscopy
ICP	Inductively coupled plasma

IR	Infrared
LED	Light emitting diode
LUMO	Lowest unoccupied molecular orbital
MB	Methylene blue
MEMS	Micro-electrical-mechanical systems
MO	Methylene orange
MOF	Metal-organic framework
MOM	Metal-organic materials
MS	Mass spectroscopy
NHE	Normal hydrogen electrode
NLDFT	Non-local density functional theory
NP	Nanoparticles
PC	Porous carbon
PCN	Porous coordination networks
PCP	Porous coordination polymers
PSD	Pore size distribution
PVP	Polyvinyl pyrrolidone
PXRD	Powder X-ray diffraction
QDs	Quantum dots
rGO	Reduced graphene oxide
RhB	Rhodamine-B
SAED	Selected area electron diffraction
SBU	Secondary building unit
SE	Secondary electrons
SEM	Scanning electron microscope
SSA	Specific surface area
STEM	Scanning transmission electron microscopy
TAA	Thioacetamide
TEM	Transmission electron microscope
TEOA	Triethanolamine
TGA	Thermogravimetric analysis
UV	Ultraviolet
UV-Vis spectroscopy	Ultraviolet-Visible spectroscopy
VB	Valence band

VBE	Valence band edge
XPS	X-ray photoelectron spectroscopy
ZIF	Zeolitic imidazolate frameworks

List of figures and tables

Figures

- 1.1 Cartoons of the (a) formation of MOFs with different topologies (b) MOF single crystal with functionalised organic linkers and (c) carbonised MOF derivative representing the preserved morphology.....29
- 1.2 Crystalline structures of some representative Zn-MOF and Ti-MOF.....31
- 2.1 A schematic summary of the dimension and morphology of the MOF derived nanocomposites for photocatalytic applications.....44
- 2.2 (a) Schematic representation of hollow Cu–TiO₂/C nanospheres derived from the external-templated core-shell SiO₂@SURMOF nanospheres (b, c) TEM images of SiO₂@Cu–TiO₂/C (d) Photocatalytic H₂ evolution of MOF derived nanocomposites (e) the recyclability of best performing hollow Cu–TiO₂/C nanospheres under solar irradiation (f) H₂ evolution rates in mmol g_{cat}⁻¹ h⁻¹ and (g) photocurrent measurements of nanospheres under simulated solar irradiation.....48
- 2.3 (a) STEM-EDX image and the elemental mapping of C-N/FeNi_{7.47}P/g-C₃N₄ composite for Fe, Ni, P, C, N (b) Proposed mechanism of photocatalytic H₂ evolution over the EY-sensitised C-N/FeNiP/g-C₃N₄ composite in the presence of sacrificial agent TEOA under irradiation of visible light (c) Transient photocurrent responses under visible light and (d) EIS curves of external-templated MOF derived optimised CN/FeNi_{7.47}P/g-C₃N₄ composites.....51
- 2.4 (a) Schematic diagram shows the synthesis strategy of Fe-MOF/g-C₃N₄ derived g-C₃N₄/α-Fe₂O₃ nanocomposite (b) Photocatalytic H₂ evolution by g-C₃N₄/α-Fe₂O₃ nanocomposite (c) EPR spectra measured in MeOH for DMPO-•O₂⁻ (d) EPR spectra measured in aqueous solution for DMPO-•OH and (e) Photocatalytic H₂ evolution mechanism of the g-C₃N₄/α-Fe₂O₃ nanocomposite under visible light (300 W Xe lamp and λ > 420 nm) (f) Schematic representation of 2D Ni-MOF/g-C₃N₄ derived Ni/g-C₃N₄.....55
- 2.5 (a) Schematic diagram of the g-C₃N₄/MOF derived g-C₃N₄-NiCoP₂-PC nanocomposite (b) Proposed mechanism of photoinduced separation of

	charge carriers in the g-C ₃ N ₄ -NiCoP ₂ -PC composite and the reduction process for H ₂ evolution under UV-Vis light (c) PL emission spectra (d) EIS spectra (e) transient photocurrent responses under irradiation of UV-Vis light and (f) Mott-Schottky plots of g-C ₃ N ₄ /NiCoP ₂ -PC.....	58
2.6	(a) Schematic drawing of the synthesis process of the CdS/MPC nanocomposites (b) SEM images of ZIF-8 precursor (c) SEM of ZIF-8 derived 20 wt.% CdS/MPC nanocomposite and (d) Schematic illustration of the photocatalytic mechanism over the CdS/MPC nanocomposite.....	66
2.7	(a-e) TEM images of the thermal transformation of Zn/Co-ZIF into ZnO@C-N-Co nanocomposites at different carbonisation times and (f) Schematic representation of the formation of the core-shell ZnO@C-N-Co.....	67
2.8	(a) Schematic diagram of the carbonisation process of hollow TiO ₂ @C/FeTiO ₃ nanotubes (b) FESEM image of Fe-MOF precursor (c) TCF-25 % nanotubes and (d) TEM images of TCF 20 %.....	71
2.9	(a) Schematic diagram of the formation of the rGO@ZnCo ₂ O ₄ . SEM images of (b) rGO-ZnCo-ZIF precursor (c) nanocomposite GZC-300 and (d) GZC-500. TEM images of (e) rGO-ZnCo-ZIF precursor (f) GZC-300 and (g) GZC-500. (h) Cartoon of the photocatalytic mechanism of NO oxidation by GZC-300 under the visible-light.....	74
2.10	(a) Schematic diagram of the formation process of ZnO _{ZIF-8} /rGO/Carbon sponge (b) Photodegradation of RhB under UV-Visible light irradiation (c) Change in intensity of absorption peak of RhB with the progression of time during photocatalysis (inset shows the change in colour of RhB dye before and after complete photodegradation)	77
3.1	Schematics of the experimental setup for the preparation of MOF derived composites.....	85
4.1	Structures of SBU Zn ₄ O, organic linker and crystalline MOF-5.....	96
4.2	PXRD patterns of nanocomposites obtained in different carbonisation atmospheres at (a) 800 °C and (b) 1000 °C. ZnO-Air, ZnO/C-Ar+W(L), ZnO/C-Ar+W(S) and ZnO/C-Ar are represented in black, light blue, dark blue and red, respectively. Numbers in brackets mark the miller indices of	

	the lattice plane reflections of the wurtzite modification of ZnO. Inset to (a) is the amplified PXRD pattern of peak (101)	98
4.3	TGA profiles of MOF-5 derived composites ZnO-Air (black), ZnO/C-Ar+W(L) (blue), ZnO/C-Ar+W(S) (dark blue) and ZnO/C-Ar (red) obtained under different gaseous atmospheres at (a) 800 °C and (b) 1000 °C.....	99
4.4	Representative SEM micrographs of (a, b) MOF-5, (c) ZnO/C-Ar+W(S) ₈₀₀ and (d) ZnO/C-Ar+W(S) ₁₀₀₀	100
4.5	TEM and HRTEM images of (a, b, c) ZnO/C-Ar+W(S) ₈₀₀ and (d, e, f) ZnO/C-Ar+W(S) ₁₀₀₀ at different magnifications.....	101
4.6	The EDX elemental maps of (a) ZnO/C-Ar+W(S) ₈₀₀ and (b) ZnO/C-Ar+W(S) ₁₀₀₀ . The coloured images show the distribution of elements throughout the composite. The C, Zn, and O are represented in yellow, red and blue respectively.....	102
4.7	Raman Spectra of ZnO-Air (black), ZnO/C-Ar (red), ZnO/C-Ar+W(S) (dark blue) and ZnO/C-Ar+W(L) (light blue) prepared at (a) 800 °C and (b) 1000 °C. FTIR spectra of ZnO/C-Ar+W(S) derived at (c) 800 °C and (d) 1000 °C after heat treatment of the materials at RT (black), 100 °C (red), 200 °C (blue), 300 °C (pink) and 400 °C (green), respectively.....	104
4.8	XPS spectra of (a) elemental survey (b) Zn 2p (c) O 1s (d) C 1s for ZnO-Air ₈₀₀ (black) and ZnO/C-Ar ₈₀₀ (red) and ZnO/C-Ar+W(S) ₈₀₀ (dark blue)	106
4.9	N ₂ sorption isotherms measured at 77 K for ZnO/C-Ar and C-Ar (red squares), ZnO/C-Ar+W(S) (dark blue circles) and ZnO/C-Ar+W(L) (light blue triangles) derived at (a) 800 °C and (b) 1000 °C respectively. NLDFIT PSD of samples derived at (c) 800 °C and (d) 1000 °C respectively. Filled and empty symbols represent adsorption and desorption. The lines are a guide to the eye only.....	108
4.10	(a) Reflectance spectra of selected samples ZnO-Air ₁₀₀₀ (black, insets), ZnO/C-Ar+W(S) ₈₀₀ (red) and ZnO/C-Ar+W(S) ₁₀₀₀ (dark blue) and (b) EBGs of these composites calculated by the Kubelka-Munk function (Tauc plots)	109

4.11	The adsorption and photodegradation of MB by ZnO-Air (black circles), ZnO/C-Ar (red triangles), ZnO/C-Ar+W(L) (light blue diamonds) and ZnO/C-Ar+W(S) (dark blue triangles) derived at (a, c) 800 °C and 1000 °C in dark and (b, d) under visible light irradiation respectively. Green squares represent blind test without any catalysts.....	111
4.12	Proposed mechanism of dye photodegradation by MOF-5 derived ZnO/C composites under visible light irradiation.....	112
4.13	(a) Recyclability test of the composite ZnO/C-Ar+W(S) ₁₀₀₀ for the adsorption and photodegradation of MB in water under visible-light irradiation for 180 min (b) UV-Vis absorption spectra of adsorption and photodegradation of ZnO/C-Ar+W(S) ₁₀₀₀ with time t.....	113
5.1	Chemical structures of metal clusters (Zn ₄ O(CO ₂) ₆ for MOF-5 and Zn ₃ [O ₃ (CO ₂) ₃] for MOF-74), organic linkers (C ₈ H ₆ O ₄ for MOF-5, C ₈ H ₆ O ₆ for MOF-74 and C ₄ H ₆ N ₂ for ZIF-8) and the respective MOF-5, MOF-74 and ZIF-8.....	116
5.2	PXRD patterns of (a) as-synthesised MOF-5, MOF-74 and ZIF-8 and the (b) derived nanocomposites ZnO/C obtained at 800 °C under water vapour atmosphere. MOF-5 and ZnO/C _{MOF-5} are represented in black, MOF-74 and ZnO/C _{MOF-74} in red while ZIF-8 and ZnO/C _{ZIF-8} in blue respectively. Miller indices of the lattice plane reflections of the wurtzite ZnO are presented in brackets. The inset in (b) is the amplified PXRD pattern of ZnO peak (101)	118
5.3	TGA profiles of (a) MOFs and (b) derived composites obtained at 800 °C under water vapour atmosphere. MOF-5 and ZnO/C _{MOF-5} are represented in black, MOF-74 and ZnO/C _{MOF-74} in red while ZIF-8 and ZnO/C _{ZIF-8} in blue respectively.....	119
5.4	The SBUs of Zn ions and organic linkers in crystal structures of (a) MOF-5 (b) MOF-74 and (c) ZIF-8 and the proposed decomposition mechanisms 1 , 2 and 3	120
5.5	XPS spectra of (a) elemental survey (b) Zn 2p (c) O 1s (d) C 1s (e) N 1s for ZnO/C _{MOF-5} (black) and ZnO/C _{MOF-74} (red) and ZnO/C _{ZIF-8} (blue).....	124

5.6	SEM micrographs of (a) MOF-5 (b) MOF-74 (c) ZIF-8 (d) ZnO/C _{MOF-5} (e) ZnO/C _{MOF-74} and (f) ZnO/C _{ZIF-8} respectively.....	125
5.7	HRTEM micrographs of (a, b) ZnO/C _{MOF-5} (c, d) ZnO/C _{MOF-74} and (e, f) ZnO/C _{ZIF-8} respectively.....	126
5.8	Low magnification TEM micrographs and their respective EDX elemental mappings of (a) ZnO/C _{MOF-5} (b) ZnO/C _{MOF-74} and (c) ZnO/C _{ZIF-8} . The coloured images show the distribution of elements throughout the composite. Here, C, Zn, O and N are represented in yellow, red, blue/grey and cyan colours respectively. There is no N present in samples ZnO/C _{MOF-5} and ZnO/C _{MOF-74}	127
5.9	(a) Raman spectra of ZnO/C _{MOF-5} (black) ZnO/C _{MOF-74} (red) and ZnO/C _{ZIF-8} (blue). Insets show the highlighted main $E_2(\text{high})$ and $E_2(\text{M})$ modes of ZnO, additional modes (B_1) as well as D and G bands of amorphous carbon (b) FTIR spectra of fresh ZnO/C _{MOF-5} (black), ZnO/C _{MOF-74} (red) and ZnO/C _{ZIF-8} (blue) (c) FTIR spectra of MB (navy blue), ZnO/C _{MOF-5} (black), ZnO/C _{MOF-74} (red) and ZnO/C _{ZIF-8} (blue) after dye degradation. These FTIR spectra confirm that all three MOFs derived composites are chemically stable, and no peaks of MB are found after the photocatalytic reactions completed.....	130
5.10	(a) The UV-Vis absorption spectra of ZnO/C _{MOF-5} (black), ZnO/C _{MOF-74} (red) and ZnO/C _{ZIF-8} (blue) (b) direct EBGs (Tauc plots) of the composites.....	131
5.11	(a) N ₂ sorption isotherms (at 77 K) and (b) PSD of nanocomposites ZnO/C _{MOF-5} (black circles), ZnO/C _{MOF-74} (red triangles) and ZnO/C _{ZIF-8} (blue squares)	132
5.12	Proposed mechanism of photocatalytic HER and the photodegradation of organic pollutant dye MB by ZnO/C _{MOF-5} , ZnO/C _{MOF-74} and ZnO/C _{ZIF-8} under visible light. The photocatalytic oxidation (degradation of MB) reaction takes place through the photogenerated holes (h^+_{VB} and OH \cdot radicals) in valence band (half-reaction is shown here) whereas the reduction reaction (H ₂ evolution) takes place by photogenerated electrons (e^-_{CB}) in the conduction band (half-reaction is shown here)	136

5.13	(a) The adsorption of MB by ZnO/C _{MOF-5} (black circles), ZnO/C _{MOF-74} (red triangles), ZnO/C _{ZIF-8} (blue squares) respectively in the dark (b) the adsorption and photodegradation of MB by ZnO/C _{MOF-5} (black circles), ZnO/C _{MOF-74} (red triangles) and ZnO/C _{ZIF-8} (blue squares) under visible light irradiation respectively. Olive hexagons represent photodegradation by ZnO _{MOF-5} prepared at 800 °C under air atmosphere. Violet triangles represent the blind test of MB without any catalyst (c) H ₂ evolution (HER) reaction by ZnO/C _{MOF-5} , ZnO/C _{MOF-74} and ZnO/C _{ZIF-8} nanocomposites under visible light irradiation.....	138
5.14	SEM micrographs of (a) ZnO/C _{MOF-5} (b) ZnO/C _{MOF-74} and (c) ZnO/C _{ZIF-8} after photodegradation of MB under visible light.....	139
5.15	PXRD patterns of (a) ZnO/C _{MOF-5} (b) ZnO _{MOF-74} and (c) ZnO _{ZIF-8} before and after photodegradation of MB under visible light irradiation respectively. The dark colours represent the PXRD patterns of fresh samples whereas the lighter colours show the PXRD patterns of used ZnO/C _{MOF-5} (grey), ZnO/C _{MOF-74} (light red) and ZnO/C _{ZIF-8} (light blue) samples. The crystallinity of the photocatalysts remains unaffected after being used for photocatalytic dye degradation of MB under visible light.....	140
6.1	Chemical structures of metal clusters, organic linkers and the crystalline NH ₂ -MIL-125(Ti).....	146
6.2	TGA of NH ₂ -MIL-125(Ti) (a) under synthetic air and (b) under argon atmosphere. The MS of NH ₂ -MIL-125(Ti) (c) under synthetic air and (d) under argon atmosphere.....	148
6.3	A proposed scheme of thermal decomposition and putative reaction products of NH ₂ -MIL-125(Ti) under synthetic air and argon atmosphere based on TGA-MS results.....	149
6.4	(a) PXRD patterns of NH ₂ -MIL-125(Ti) heat treated from RT to 900 °C. The NH ₂ -MIL-125(Ti) structure is stable up to 300 °C. The MOF structure disintegrates at above 350 °C followed by the recrystallisation of TiO ₂ nanoparticles at above 550 °C. (b) Highlighted rutile TiO ₂ peaks show the shift in peak positions due to modified crystalline structure.....	150

6.5	(a) FTIR spectra of heat treated NH ₂ -MIL-125(Ti) from RT to 900 °C (b) Raman spectra of selected samples at 200 °C (orange) 500 °C (black) and 800 °C (blue).....	153
6.6	XPS spectra of (a) Ti 2p (b) O 1s (c) C 1s and (d) N 1s of selected heat treated NH ₂ -MIL-125(Ti) at 200 °C (orange) 500 °C (black) and 800 °C (blue).....	155
6.7	(a) BET and (b) PSD of as-prepared NH ₂ -MIL-125(Ti) (red) and heat treated at 200 °C (orange) 500 °C (black) and 800 °C (blue).....	157
6.8	(a-l) In-situ STEM images recorded during the heat treatment of NH ₂ -MIL-125(Ti) under argon atmosphere displaying the porosity formation and shrinkage of the crystals at higher temperature with the preservation of the general morphology.....	159
6.9	SEM images of selected samples obtained by heat treatment of NH ₂ -MIL-125(Ti) at (a) 200 °C (b) 500 °C and (c) 800 °C.....	160
6.10	HRTEM images of selected samples obtained by heat treatment of NH ₂ -MIL-125(Ti) at (a, b) 200 °C (c, d) 500 °C and (e, f) 800 °C.....	160
6.11	In-situ EDX elemental maps of samples (a) NH ₂ -MIL-125(Ti) and heat treated at (b) 800 °C.....	161
7.1	(a) PXRD patterns of simulated (dark grey), as-synthesised NH ₂ -MIL-125(Ti) (orange) and NH ₂ -MIL-125(Ti/Cu) (olive) (b) Deconvoluted N 1s XPS spectra of as-prepared NH ₂ -MIL-125(Ti/Cu) (c) schematics diagram of the charge transfer to coordinated Cu ²⁺	165
7.2	(a) PXRD (b) TGA profiles of as-prepared NH ₂ -MIL-125(Ti) and NH ₂ -MIL-125(Ti/Cu) in air and (c) TGA profiles of derived composites in air. Inset in (a) shows deconvoluted peaks separating rutile TiO ₂ and Cu ₂ O.....	168
7.3	(a) SEM images and (b) representative schematic diagrams of bi-MOF NH ₂ -MIL-125(Ti/Cu) derived nanocomposites named TiCuC550, TiCuC700 and TiCuC800 obtained at temperatures 550, 700 and 800 °C respectively. TEM images of (c) TiCuC550 (d) TiCuC700 and (e) TiCuC800.....	169

7.4	N ₂ sorption isotherms of (a) NH ₂ -MIL-125(Ti) and NH ₂ -MIL-125(Ti/Cu) and (b) derived nanocomposites. Insets in (a) and (b) correspond to their respective PSDs.....	170
7.5	(a) Raman spectra and (b) FTIR spectra of TiCuC550 (black), TiCuC700 (red) and TiCuC800 (blue) (c) UV-Vis absorption spectra of NH ₂ -MIL-125(Ti) and NH ₂ -MIL-125(Ti/Cu). (d) Tauc plots (UV-Vis absorption spectra in inset) and (e) XPS valence band positions of TiCuC550, TiCuC700 and TiCuC800.....	174
7.6	Representative HRTEM images of (a, d) TiCuC550 (b, e) TiCuC700 and (c, f) TiCuC800 (SAED in inset)	175
7.7	EDX elemental mappings of Ti, O, C, N and Cu for sample (a) NH ₂ -MIL-125(Ti/Cu) (b) TiCuC550 (c) TiCuC700 and (d) TiCuC800.....	176
7.8	XPS spectra for (a) Elemental survey (b) Ti 2p (c) O 1s (d) Cu 2p (e) C 1s (f) N 1s of samples TiCuC550 (black), TiCuC700 (red) and TiCuC800 (blue).....	180
7.9	The XPS depth profiles of the selected sample TiCuC700.....	181
7.10	Photocatalytic setup with HER reaction cell with temperature controller and magnetic stirrer. The HER reaction cell is connected to GC. On the left side, there is a 500 W Xe/Hg lamp with a 285 nm cut-off filter.....	182
7.11	(a) Photocatalytic H ₂ evolution performance of samples with reaction time (b) comparison of the photocatalytic H ₂ evolution in $\mu\text{mol g}_{\text{cat}}^{-1} \text{h}^{-1}$ of TiCuC550 (black), TiCuC700 (red) and TiCuC800 (blue) (c) the recyclability test of the selected TiCuC700 nanocomposite and (d) EIS Nyquist plots of TiCuC550, TiCuC700 and TiCuC800 under the same potential in 0.5 M H ₂ SO ₄	186
7.12	The schematic illustration of the proposed mechanism of photocatalytic H ₂ evolution over NH ₂ -MIL-125(Ti/Cu) derived multi-heterojunction TiCuC700 under UV-Vis light.....	189

Tables

2.1	Comparison of selected MOF derived nanocomposites for photocatalytic H ₂ evolution.....	59
2.2	Comparison of selected MOF derived nanocomposites for photodegradation of organic pollutants.....	77
4.1	Summary of the BET surface areas, EBGs and photocatalytic performance of the MOF-5 derived composites.....	113
5.1	A comparison of photodegradation of MB by undoped and doped ZnO nanoparticles synthesised by different methods.....	140
5.2	A comparison of photocatalytic H ₂ evolution under visible light by selected doped ZnO composites with different morphologies.....	143
5.3	Summary of the surface areas, pore sizes, EBGs and functionalisation of the MOF-5, MOF-74 and ZIF-8 derived composites.....	143
6.1	Summary of the textural properties of as-prepared and selected heat treated NH ₂ -MIL-125(Ti).....	157
6.2	Summary of XPS data of samples treated at 200, 500 and 800 °C respectively.....	161
7.1	Textural properties, estimated EBGs from Tauc plots, H ₂ evolution activities and the calculated AQY (%) at 435 nm of the bi-MOF derived composites.....	185
7.2	A comparison of photocatalytic HER performances of the selected materials reported in the literature.....	188

Chapter 1

Introduction

A highly industrialised global economy requires plenty of cost-effective energy resources. Solar energy has become a key renewable and sustainable energy resource, and the efficient photocatalytic materials with optimal properties are essential for solar energy-driven applications for clean energy production and mitigation of environmental pollution. For that purpose, an ideal material should possess high porosity with appropriate pore sizes, functionalised surfaces and appropriate semiconducting properties to be photoactive under the visible light. However, it is still very challenging to form such symbiosis of physical and chemical properties in one material for high performing photocatalysis.¹⁻⁴ Conventional semiconducting metal oxides face serious limitations due to their wide energy band gaps (EBGs), low surface areas and agglomerations of particles, and therefore, inadequate accessible active sites. Expensive cocatalysts such as Pt, Pd and Au are loaded to increase the catalytic active sites which seems, not a feasible method for the large-scale industrialisation of photocatalysts.

To deal with the issues of lower photocatalytic performance and loading of expensive cocatalysts, many efforts have been made to modify the conventional metal oxide photocatalysts by tuning their EBGs through metal and/or non-metal doping, forming the defects in crystal structure or constructing the heterostructures for maximum photoexcitation of electrons and holes with minimum electron-hole recombination.^{2, 5-11} On the other hand, to overcome the challenges of poor surface area and inaccessibility of active sites due to the surface agglomeration, many efforts have been made to synthesise metal-oxide/carbon composites, hoping that these composites may show synergistic effects for highly efficient photocatalysis due to the combined actions of modified metal oxides and conductive carbon.^{9, 12-22} However, the physical and mechanical mixing approaches do not produce a homogeneous distribution of metal oxides in a carbon matrix. Also, poor interfacial contacts between metal-oxide and carbon result in an insignificant improvement in the photocatalytic performance of those composites. Therefore, new approaches are required to synthesise novel materials to solve these extensively discussed scientific problems.

Metal-organic frameworks (MOFs), porous inorganic-organic hybrid crystalline materials, are built from the self-assembling metal ions (or oxo-clusters) linked by the organic linkers.²³ They can be defined as a class of crystalline materials that comprise coordination bonds (reticular synthesis) between multidentate organic linkers and transition-metal cations which act as secondary building units (SBUs). The organic linkers can be ditopic or polytopic organic carboxylates. The MOF structures are open isorecticular frameworks with well-defined pores, flexible geometry, tunable crystal sizes and functionalities.²⁴ ²⁵ The Brunauer-Emmett-Teller (BET) surface area of MOFs typically range between 1000 and 10,000 m² g⁻¹ with the porosity of larger than 50% of MOF crystal volume. These aspects make MOFs different from conventional porous materials such as carbon and zeolites.²⁶ Historically, the term “coordination polymer” was coined in 1916 for the compounds synthesised by linking of metal ions to either inorganic or organic ligands by coordinate bonds. Using the transition metals such as Cu, Zn, Ag and Cd, these coordination polymers could be formed in 0D, 1D, 2D or 3D (D stands for dimensional) frameworks. Figure 1.1 shows the cartoons of the linking of metal ions and organic linkers to form MOFs with different topologies.

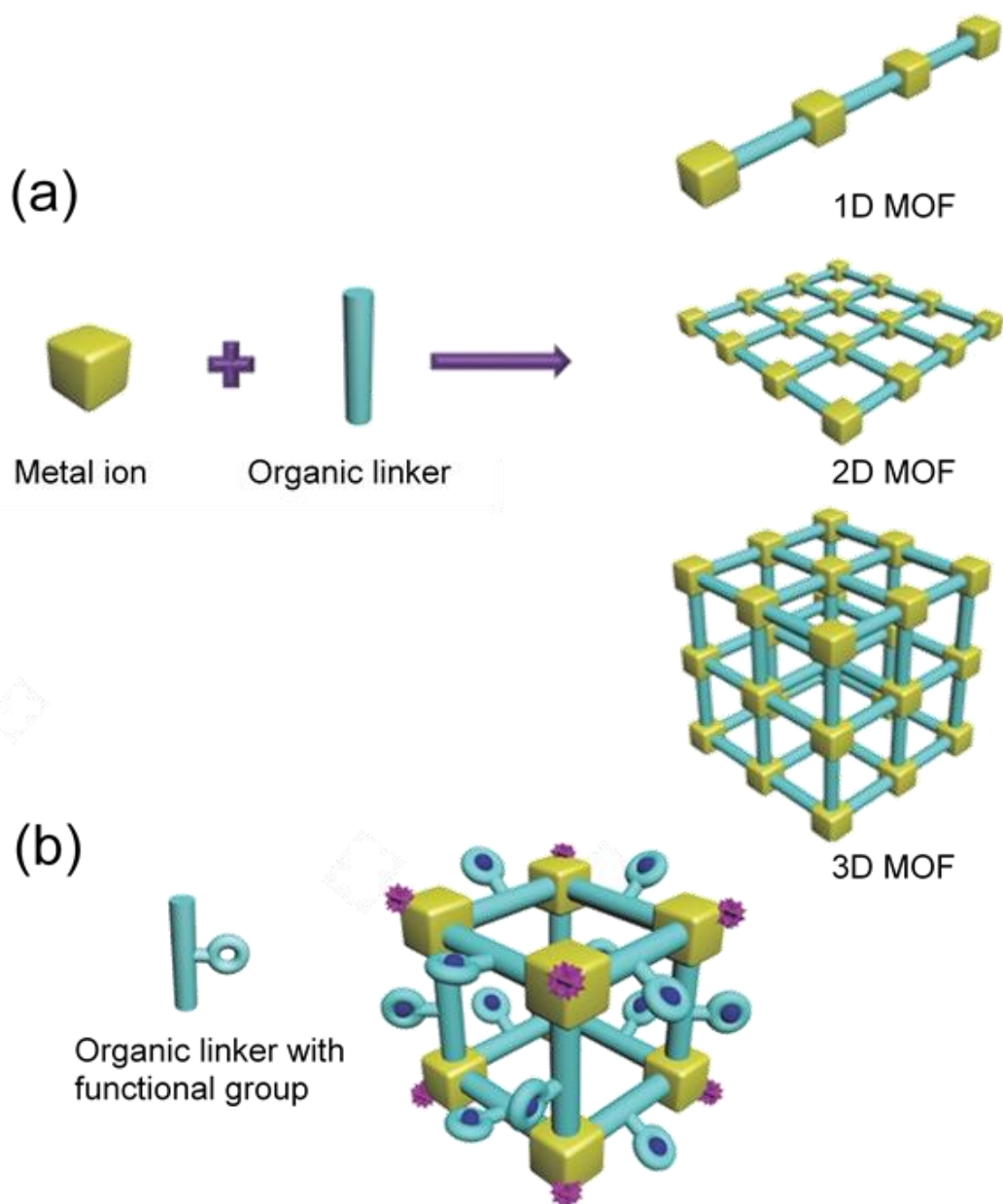


Figure 1.1 Cartoons of the (a) formation of MOFs with different topologies and (b) MOF single crystal with functionalised organic linkers.²⁷

The advent of single-crystal X-ray diffraction (SCXRD) made it possible to determine and verify coordination polymer structures. The discovery of the Prussian blue in 1936 made it evident that 3D coordination frameworks can be formed. Currently, the terms porous coordination polymers (PCP) and MOF are used synonymously in a broader sense. However, there has been a debate among scientists about the terminology of these materials. For instance, G. Férey claimed that MOFs should be called “coordination polymers” whereas Omar Yaghi and O’Keeffe define MOFs as a different class of materials that are built by

polyatomic cluster linked through the strong covalent bonds.²⁸ The coordination polymers generally have weaker bonds and thus show lower stability. The PCPs do not necessarily have to be crystalline materials. Other terms are also used for this class of compounds such as metal-organic materials (MOMs) by Perry, porous coordination networks (PCNs) by Ma and PCP by Kitagawa.^{29, 30} Robson argued that it is unnecessary to distinguish MOFs and PCPs since there is a huge similarity between these two types of compounds.³⁰⁻³² After Yaghi *et al.*, the term MOF has become archetypal. It is used for the solid compounds that comprise tight bonding, linking organic and inorganic units of a well-defined and highly crystalline geometric composition which can also be modified by post-treatment. The structural chemistry of these compounds is determined by several key factors including coordination framework, organic-inorganic hybrid materials, and high porosity. As shown in Figure 1.2, a unit cell of crystalline MOF involves a ditopic or polytopic organic linker and the SBU, a finite polyatomic inorganic cluster with two or more metal atoms acting as a metal cation. The shapes of SBUs could be polyhedron, polygon, or infinite rods which are defined by their point of extension. The organic linkers usually have a multidentate custom shape. These organic and inorganic components are primarily linked by coordination bonds as well as some weak interactions such as van der Waals forces and H-bonds. These additional weak interactions provide more flexibility to the porous crystalline materials which make them useful to attach different functional groups.^{23, 24}

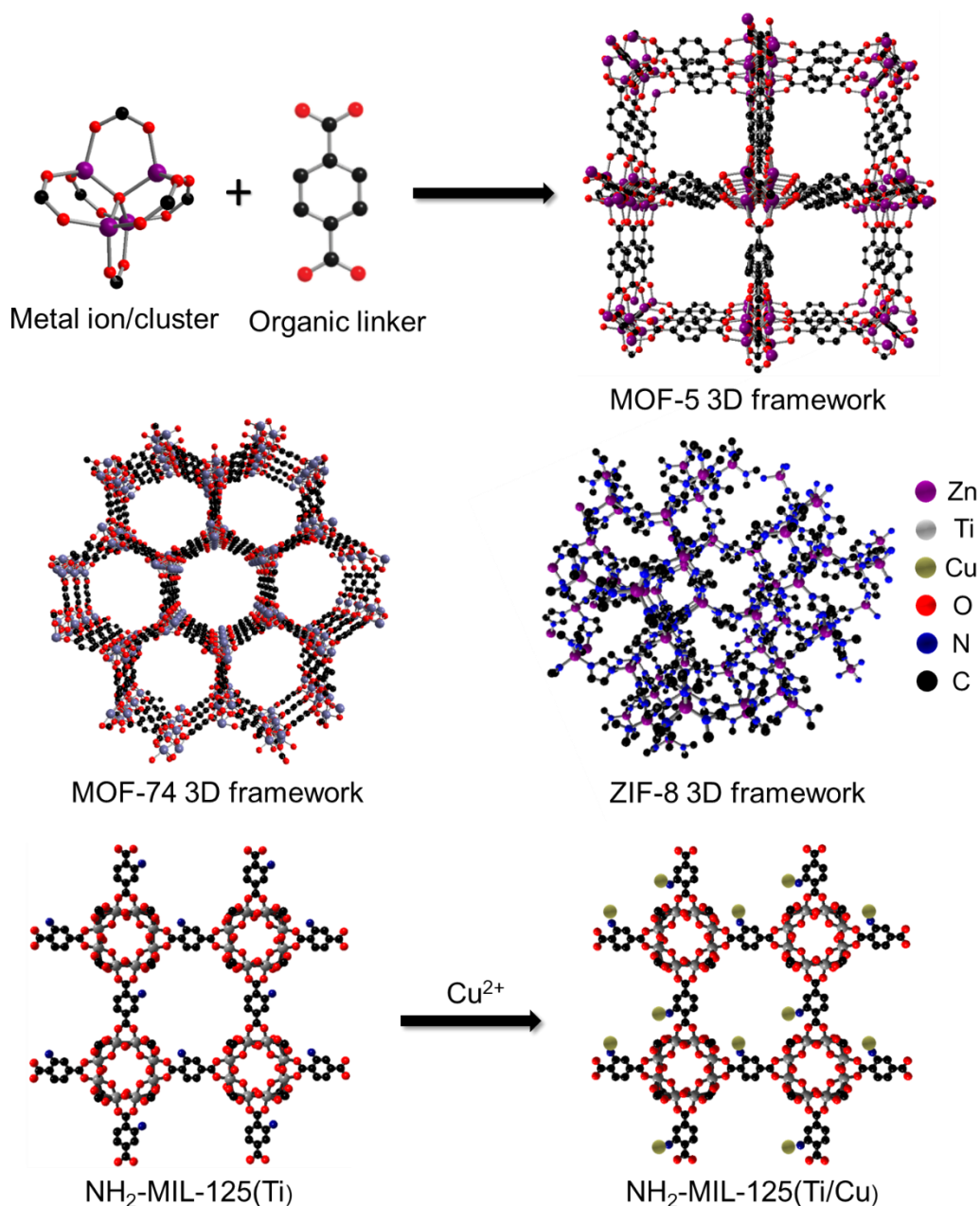


Figure 1.2 Crystalline structures of some representative Zn-MOFs, Ti-MOF and bi-MOF.³³

Despite the large surface areas, ultrahigh porosity, structural flexibility, a large variety of functionalisation and tunable optical band gaps, MOFs face several limitations and challenges to be employed as photocatalysts.³⁴⁻⁴⁰ The moderate strength of coordination bonds between the metal ions (oxo-cluster) and organic linkers, the wide EBGs and poor semiconducting properties (with limited electric charge generation and charge transfer) make the pristine MOFs less favourable candidates to be directly used for photocatalytic applications.^{34, 39, 41-43} However, their distinct features such as rationally designed structures,

high crystallinity, engineered morphologies, high specific surface area (SSA) (also called BET surface area) and modifiable porosities make them exceptional platform materials as precursors or sacrificial templates to generate a variety of nanocomposites comprising pure metals, multi-metals, alloys, oxides, carbides, chalcogenides or phosphides embedded in the porous carbon matrix.⁴⁴⁻⁵⁵ These MOF derived nanocomposites offer exceptional symbiosis of properties such as high crystallinities, inherited morphologies with choice of dimensions (0D, 1D, 2D or 3D), high SSA and tunable porosities. In particular, the adjustable energy band positions achieved by in-situ tailored self/external doping of non-metal or metal heteroatoms into the derived metal compounds and the controllable surface functionalities of these nanocomposites make them promising photocatalysts for H₂ evolution by water splitting, photodegradation of environmental pollutants and CO₂ reduction or conversion into value-added hydrocarbons. Though some excellent works have demonstrated the potential of MOFs derived nanocomposites for photocatalytic applications, many fundamental questions remain to be addressed and an in-depth understanding of the relationships among the structures, properties and photocatalytic application of these nanocomposites needs to be built.

The motivation behind this PhD project was to understand the relationships among the structure, morphology, textural properties, surface functionalities, chemical compositions, semiconducting properties and the optimal photocatalytic performance of MOF derived metal oxide/carbon nanocomposites. In particular, the recent findings of hydrogenated “black” TiO₂ that can expand photocatalytic activity from ultraviolet to the visible light region have inspired worldwide interest in developing “black” semiconductive TiO₂ or ZnO materials for photocatalytic applications in energy and environment. For instance, one of the most feasible and simple ways to produce “black” ZnO or TiO₂ is doping with non-metals like carbon. It can significantly enhance the visible-light activity of C doped ZnO and TiO₂ due to the overlapping of energy orbitals between the O 2p and C 2p states. However, the key issue is how to effectively control the dopant concentrations and their spatial distribution in the modified semiconductors, particularly how to realise homogeneously distributed dopants in the semiconductor matrix at the atomic level, therefore, to achieve the remarkable visible light photocatalytic activities. Other key challenges are to control the homogeneous distribution of

metal oxides in hydrophilic and conductive porous carbon to enhance their overall photocatalytic activity. This PhD project aims at:

1. using MOFs as precursors and sacrificial templates to produce in-situ heteroatom doped (such as C and N) “black” metal oxide nanostructures uniformly dispersed in a functionalised porous carbon matrix.
2. systemically investigating the effects of variable morphologies and textural properties of precursor Zn-MOFs and Ti-MOFs on the crystallinity, morphology, chemical and semiconducting properties of resulting MOFs derived black ZnO/C and TiO₂/C composites.
3. understanding the role of structure, porosity, graphiticity and physicochemical properties of the Zn-MOFs and Ti-MOFs derived porous carbons on overall photocatalytic performances of these composites.

Specifically, the objectives of this project can be described as follows:

1. To synthesise Zn-MOFs and Ti-MOFs derived non-metal doped and surface functionalised black ZnO/C and TiO₂/C nanocomposites.
2. To explore the simple synthesis methods, to rationally design MOFs derived bi-metal oxide/carbon (TiO₂/Cu_xO/C) composites and study the in-situ formation of heterojunctions.
3. To systematically investigate the role of experimental conditions to homogeneously distribute doped metal oxides in a porous carbon matrix at the atomic scale.
4. To examine and in-depth analysis of the structural, morphological, textural, functional, physicochemical, optical and semiconducting properties of selected Zn-MOFs and Ti-MOFs derived metal oxides and porous carbons.
5. To evaluate these Zn-MOFs, Ti-MOFs and Bi-metal MOFs derived black nanocomposites for applications in the environment and energy including photodegradation of organic pollutants and photocatalytic water splitting for H₂ evolution.

This PhD thesis has been organised into 8 chapters. Chapter 1 provides a very brief introduction of the research project followed by the motivation, aims and objectives. Chapter 2 presents the detailed literature survey and critical review of the MOFs derived nanocomposites for photocatalytic applications in

energy and environment including photodegradation of organic pollutants and water splitting for H₂ evolution. Chapter 3 briefly describes the synthesis methodologies of Zn-MOFs, Ti-MOFs, Bi-metal MOFs (bi-MOFs) precursors and their derivatives. Also, this chapter provides a very brief description of the analytical techniques employed to characterise the synthesised materials and the experimental setups for the application tests. In Chapter 4, the effect of temperature and the gaseous atmosphere on the compositions, the morphologies and physicochemical properties of the MOF derived ZnO, ZnO/C nanocomposites and the porous carbon are systematically investigated. Moreover, this work provides a novel insight to understand the role of ZnO and carbon species in MOF-5 derived nanocomposites for the adsorption and photodegradation of methylene blue (MB). Chapter 5 explores the correlation between Zn-MOFs precursors and their derived ZnO/C composites to understand how the transformation from Zn-MOFs to ZnO/C nanocomposites takes place upon high-temperature pyrolysis in a certain gaseous atmosphere. This chapter discusses some primary parameters such as crystallinity of derived composites, composition, structural and textural properties, N and/or C doping, functionalities attached on the surface of the porous carbon matrix and their chemical properties and investigate their role in the photocatalytic performance. Chapter 6 presents an in-situ investigation of thermal decomposition of Ti-MOF, NH₂-MIL-125(Ti) under an inert atmosphere. The in-situ STEM and other analytical techniques reveal the mechanism of thermal decomposition of the Ti-MOF precursor and the subsequent formation of TiO₂/C composite. This chapter discusses the changes that occur in the structure, crystallinity, morphology, textural and physicochemical properties during high temperature pyrolysis of derived composites. Based on these findings, chapter 7 presents that Cu²⁺ coordinated bi-MOF, NH₂-MIL-125(Ti/Cu) can be employed as an appropriate sacrificial template to form TiO₂/Cu_xO/C multi-heterojunction at optimal synthesis conditions. This chapter discusses the role of temperature and gaseous atmosphere in the in-situ formation of multi-heterostructures (simultaneous phase junctions between anatase/rutile TiO₂ and Cu₂O/CuO as well as p-n heterojunction between TiO₂ and Cu_xO) by simple one-step pyrolysis of bi-MOF. Finally, chapter 8 summarises the conclusions as well as some suggestions for future work on these MOF derived composites and their applications in the related research areas.

Chapter 2

Literature review

2.1 Introduction

The forthcoming depletion of fossil fuel-based energy resources such as oils, gases and coal make it compelling to develop alternative clean and cost-effective energy resources to fulfil the ever-growing worldwide energy demand. Concurrently, the release of toxic organic pollutants such as textile dyes, pharmaceutical contaminants and antibiotics into the water system as well as the emission of greenhouse gases (such as carbon dioxide and methane) into the atmosphere from industries pose great challenges to the environment, which has caused water pollution, incurable global warming and climate change. On the other hand, due to the abundant availability of sunlight, solar energy has become a key renewable and sustainable energy resource and photocatalysis has emerged as one of the most attractive approaches to practically solve environmental and energy problems. A variety of nanomaterials including metal nanoparticles, metal oxides, alloys, carbons and their composites have been explored as photocatalysts for hydrogen (H₂) generation by water splitting, photodegradation of organic pollutants in the wastewater as well as CO₂ reduction into value-added hydrocarbons. However, it remains a great challenge to find the appropriate photocatalytic materials with optimal properties and excellent performance to meet the practical applications. MOFs based materials offer a viable solution to tackle above-mentioned energies and environmental problems.

MOFs are a class of crystalline porous solids which consist of metal ions and organic linkers (ligands) bound together by the coordination bonds between metal ions/clusters and organic ligands (called secondary building units, SBUs).^{23, 24} When MOFs were first synthesised in the 1990s, they were initially studied mainly for gas separation and storage.^{24, 25} Later, MOFs were widely investigated for other applications such as sensing, energy storage and conversion, drug delivery, optoelectronics, batteries, supercapacitors, fuel cells and catalysis.^{26, 40, 49, 50, 53, 56-67} Since the past few years, MOFs have further been used in solar energy-driven applications especially as photocatalysts for H₂ evolution, dye degradation and CO₂ reduction.^{36, 38, 59, 61, 68-74} The moderate strength of coordination bonds between the metal nodes and organic ligands, the wide

EBGs, the poor semiconducting properties (with limited electric charge generation and charge transfer) of pristine MOFs make them less favourable to be directly employed in photocatalytic applications.^{34, 39, 41-43} However, their distinct features such as rationally designed structures, high crystallinity, engineered morphologies, high SSA and tunable porosities make them exceptional platform materials as precursors or sacrificial templates to generate porous carbon-based nanocomposites for various applications.^{44-46, 49-55}

Many excellent critical reviews on the synthesis and applications of MOF derived metals, metal oxides and porous carbons have been published in the past several years.^{34, 36, 42, 47, 48, 50, 51, 60, 61, 65, 66, 72, 75-79} However, so far no dedicated reports are available providing critical analysis and overview of MOF derived nanocomposites for photocatalytic applications, which is pivotal for further design and development of advanced photocatalytic nanocomposites for highly efficient solar energy-driven utilisations. In this chapter, I aim to review the generation of MOF derived composite materials focusing on their applications in one of the most important renewable energy technologies-photocatalysis. Not only the state-of-the-art progress on MOF derived nanocomposite materials for solar energy-driven applications is summarised, but also highlights on their structure-property-performance relationship are provided. In particular, a detailed review on the synthesis methods of MOF derived nanocomposites and the optimisation strategies which can enable better control over particle sizes, chemical compositions, morphologies, textural properties, in-situ EBG engineering, crystalline phase compositions and surface-functionalisation for improved photocatalytic performance is presented. In this review chapter, first, the basic principles of the synthesis of MOF derived nanocomposites are briefly summarised, followed by the discussion on the photocatalysis mechanisms of nanomaterials in typical applications including photocatalytic H₂ evolution from water splitting, photodegradation of organic pollutants and photocatalytic carbon dioxide reduction. Then, the recent progress on the optimisation of physicochemical properties and the applications of these MOF derived nanocomposite materials are reviewed in detail based on their structures, dimensions (0D, 1D, 2D, 3D) and morphology. Finally, the aims, challenges and opportunities to the further development of the structure-property-application relationship of MOF derived nanocomposites are also discussed, offering some

concluding remarks for the future design of high-performance photocatalytic nanocomposite materials for renewable energy applications.

2.2 Basic principles of the synthesis of MOF derived nanocomposites

MOFs can be directly pyrolysed to derive metal oxides, metal oxide/carbon composites and highly porous carbons under suitable conditions.^{46, 47, 52, 64, 80} The morphologies of the derived materials depend upon the morphologies of the initial MOFs used as precursors or sacrificial templates. The MOF precursors can be divided into two categories as self-templated MOFs and external-templated MOFs.⁴² The self-templated MOFs include pristine MOF structures constructed by the self-assembly of metal ions/clusters and organic linkers. They consist of a single metal or multi-metal, encapsulated metals and heteroatom (N, C, S and P) doped metal(s) either directly loaded or modified through post-synthesis treatment, impregnation or ion/linker exchange. The morphology of these self-templated MOFs stems solely from the reticular structure formed by the coordination bonds between metal clusters and organic linkers which do not change after introducing the guest species.^{56, 81, 82} These self-templated MOFs can readily replicate their morphologies into the MOF derived nanocomposites. As for the external-templated MOFs, they primarily consist of composite MOFs combined with other materials. They can be prepared by mechanical mixing or in-situ growth of MOFs on a supporting external-template such as spherical SiO₂, layered-like g-C₃N₄, graphene oxide or reduced graphene oxide. In this case, the morphology of the MOF derived nanocomposites mainly depends upon the morphology of the supporting external-template.^{42, 71} Generally, MOFs and their derived nanocomposites can be classified as 0D, 1D, 2D and 3D (D stands for dimension). While those nanocomposites which possess more or less spherical shapes such as polyhedra, core/shell and hollow structures are regarded as 0D materials; those composites with structural shapes like nanorods, nanoshuttles, nanotubes or nanowires are considered as 1D materials; nanocomposites such as nanoplatelets and nanosheets with a thickness in the nanometer range are categorised as 2D materials, and those possessing the shapes/morphologies like nanodiscs, nanocubes, nanocages and nanosponges are regarded as 3D materials.^{42, 53, 77, 83}

Early reports suggested that MOFs decompose at high temperature and lose their morphologies to form featureless bulk materials.⁸⁴ However, recent studies reveal that if rationally designed MOF precursors are selected, under controlled pyrolysis conditions, MOF derived nanomaterials tend to retain the morphologies of the MOF precursors.^{49, 85} By carefully choosing the suitable MOF precursors, a variety of 0D, 1D, 2D and 3D nanomaterials that possess robust structural and chemical stabilities, desired morphologies, adjustable textural properties and various surface functionalities can be derived.^{36, 56, 75, 77, 86, 87} In addition, the crystallite sizes, chemical compositions, atomic and weight percentages and optimised crystalline phases of the resultant nanocomposites can be readily controlled by tuning the pyrolysis conditions including temperature, dwell time, heating rate and gaseous atmosphere.^{46, 52, 88} Compared with the conventional approaches to prepare photocatalysts, the carbonisation of MOF precursor method not only offers a simple way to control the derivatives but also shows a great advantage of in-situ modification of the textural, electronic and semiconducting properties of the resulting materials, which are crucial to obtain high performance photocatalysts.⁸⁹⁻⁹² For instance, by using the heteroatom-containing pristine MOFs or MOFs introduced with metal/non-metal guest species as precursors, the resulting nanocomposites can be in-situ doped with metals and/or heteroatoms such as N, C, S and P to modify the energy band positions, electronic structures and semiconducting properties to enable broader sunlight absorption and improved charge separation.⁹³⁻⁹⁶ Interestingly, in MOF derived nanocomposites, the crystalline phases and atomic ratios of metal oxides (TiO_x, FeO_x, CuO_x etc) embedded in the carbon matrix can be in-situ adjusted by controlling the pyrolysis temperature and gas atmosphere to optimise for high efficient photocatalysis.⁹⁷⁻¹⁰⁰ Moreover, the porous carbons derived from MOFs can also be in-situ functionalised with hydrophilic and/or hydrophobic functional groups via altering the pyrolysis gas atmospheres.^{76, 101}

Normally, at pyrolysis temperature higher than 350 °C, the well-ordered MOF crystalline structures tend to collapse and the metal ions or clusters will transform into metals or metal compounds while the organic linkers will convert to amorphous or partially graphitic porous carbon matrices.^{47, 102} To obtain the MOF derived nanocomposites with desired morphologies, chemical compositions and structural properties, the following two basic parameters should be

considered: (i) the reduction potential of metal ions in MOFs; Das *et al.* reported that the metal ions in MOFs with reduction potential of -0.27 V or higher (such as Co^{2+} , Cu^{2+} , Ni^{2+} etc.) formed pure metal nanoparticles upon pyrolysis in an inert atmosphere whereas those having a reduction potential lower than -0.27 V (such as Zn^{2+} , Ti^{4+} , Fe^{3+} , Al^{3+} etc.) formed metal oxides by reacting with the oxygen present in organic linker under an inert atmosphere;¹⁰³ (ii) the Tamman temperature of the metal species; it controls the homogeneous distribution and particle sizes of nanoparticles in MOF derived nanocomposites. The Tamman temperature, which is approximately equal to half of the melting point of the metal itself, is the point at which the atoms and molecules attain adequate energies for their bulk diffusion and can easily agglomerate and sinter.⁴¹ When MOF structures decompose at a higher temperature, the metal species begin to collide and form the respective nanoparticles such as pure metals, metal oxides, metal sulphides, metal carbides, metal phosphides and/or their multimetallic combinations. Meanwhile, the organic linkers transform into carbon functioning as a barrier to keep the metal species localised and prevent their bulk agglomerations, which results in a homogeneous distribution of nanoparticles throughout the porous carbon matrix. Usually, as the pyrolysis temperature increases above 600 °C, relatively more carbon species in the MOF precursors evaporate in the form of CO or CO_2 and concurrently larger metal or metal compound nanoparticles are formed due to the high temperature sintering process.⁴¹ Therefore, MOF precursors (depending on the type of metals), the pyrolysis temperature together with the gas atmosphere are the crucial parameters to control the particle sizes, the chemical composition and morphologies of MOF derived nanocomposites.

2.3 Photocatalysis mechanism of nanocomposites

The fundamental reaction mechanisms of photocatalytic processes for semiconducting nanomaterials have already been covered in reviews and book chapters.^{22, 104-107} Therefore, this section briefly discusses the reaction mechanisms and steps of photocatalysis for MOF derived nanocomposites in photodegradation of environmental pollutants, photocatalytic water splitting for H_2 evolution and photocatalytic reduction of CO_2 . Photocatalysis, a term that originated from the combination of photochemistry and catalysis, suggests that a photo-sensitive redox reaction can be accelerated by the presence of a

photoactive semiconductor catalyst. In general, heterogeneous photocatalysis can be realised via the following three basic steps:

(a) *Absorption of photons from the sunlight and generation of electron and hole pairs (e^- / h^+).* If the energy of photons of the incident light is greater than the EBG between valence bands (VB) and conduction bands (CB) of the semiconductor material, the electrons (e^-) jump from the valence band to the conduction band generating holes (h^+) in the valence bands. The absorption of light and the generation of electron/hole pairs (e^-/h^+) depend upon multiple factors including EBGs, absorption coefficient, densities of states, reflectance/scattering and the absorption depths of nanocomposites. It is well understood that semiconducting metal compounds encapsulated in porous carbon matrix are better light absorbers compared to the pristine semiconducting nanoparticles.¹⁰⁸⁻

110

(b) *Charge separation and diffusion to the surface of the catalyst.* The successful charge diffusion/migration depends upon the charge/carrier mobility, diffusion coefficient, carrier lifetime, diffusion length, carrier concentration and the charge recombination kinetics.¹¹¹ In this critical step, the photoexcited charge carriers (e^- and h^+) can recombine either on the surface of the catalyst or within the catalyst (bulk or volume recombination) very quickly (within nanoseconds) to dissipate their energies in the form of heat. The surface and bulk charge recombination are influenced by the crystallinity, particle sizes, surface/bulk defects and crystal structures (phase types and ratios) of the photocatalyst. Usually, the lower the number of defects in the catalyst, the higher crystallinity of the material. The presence of cocatalysts and the formation of heterojunctions inhibit the recombination of the photoexcited charge carriers by spatially separating and prolonging the lifetime of photoexcited charge carriers.^{1, 90, 104, 112,}

113

(c) *Reduction and oxidation (redox) of the chemical species by the photoexcited electrons and holes.* The morphology of the photocatalysts, the surface area, the surface-active sites, metal cocatalysts and the surface functionalities play a critical role in this step. Therefore, it is of vital importance to optimise the morphologies, compositions and interfacial contacts of metal compounds and carbon matrix in MOF derived nanocomposites to enhance photocatalytic performance.^{62, 109, 114, 115}

In photodegradation of pollutants, the photogenerated holes (h^+) in the valence band and the formed oxidant species such as hydroxyl ($\cdot\text{OH}$) and superoxide ($\cdot\text{O}_2^-$) radicals transform the organic pollutants into benign mineral acids, H_2O and CO_2 . It is important to scavenge the photogenerated electrons to avoid the surface/bulk recombination of e^- and h^+ pairs. It is observed that in most photodegradation reactions, superoxide radicals ($\cdot\text{O}_2^-$) also produce hydroperoxyl radicals ($\text{HOO}\cdot$) by further protonation which acts as electron scavengers.^{80, 107} The thermodynamic and kinetic studies via applying various models have been carried out to understand the adsorption and photocatalytic decomposition mechanisms of the organic pollutants. Factors such as the wavelength (UV, UV-Vis or full spectrum) and the flux of incident light, temperature, pH value of the media in the reactor, concentration of photocatalyst and organic pollutant, reaction time and charge carrier dynamics are key parameters determining the photodegradation performance.^{116, 117} The concentration of an organic pollutant can be monitored by measuring the intensity of the absorption peak, and the photodegradation efficiency of a photocatalyst can be determined by the following equation (1):

$$\text{Photodegradation efficiency (\%)} = \frac{C_o - C}{C_o} * 100 \quad (1)$$

where C_o and C are the initial (before irradiation at $t = 0$) and final (after irradiation for some time) concentrations of the organic pollutant in solution respectively.¹⁰⁷

The photocatalytic water splitting to generate H_2 is a typical uphill (endothermic) reaction that requires the Gibbs free energy ($\Delta G = 238 \text{ kJ mol}^{-1}$) to overcome the energy barrier, which means that the energy of the incident photons should be higher than 1.23 eV ($\lambda < 1000 \text{ nm}$) to realise the reaction. Regarding the photocatalyst for H_2 evolution from water splitting, two key requirements should be fulfilled: (i) the EBG between the valence and conduction bands should be above 1.23 eV and below 3.26 eV and (ii) the valence band position (VB maxima) should be more positive than the oxidation potential of $\text{O}_2/\text{H}_2\text{O}$ (1.23 eV vs NHE at pH = 0) whereas the conduction band position (CB minima) should be more negative than the reduction potential of H^+/H_2 (0 eV vs NHE at pH = 0). The doping of heteroatoms such as metallic or non-metallic species, the formation of the heterojunctions and the interfacial contacts between the semiconductors and the carbon matrix can cause the narrowing of EBGs, which dominantly result in

enhanced light absorption and better charge separation.^{22, 49, 105, 118} An ideal photocatalyst for H₂ evolution from water splitting would be the one which absorbs the maximum amount of photons in the UV-Vis and IR range because the visible light region accounts for a larger proportion of the electromagnetic spectrum. The apparent quantum yield (AQY %) at a certain wavelength of light can be calculated by the following equation (2):¹¹⁸

$$AQY_{\lambda} = \frac{2 \times \text{number of evolved H}_2 \text{ molecules}}{\text{Total number of incident photons}} \times 100 \% \quad (2)$$

The photocatalytic CO₂ reduction and conversion into CO or other hydrocarbons are rather complicated multistep reactions. CO₂ is a chemically stable molecule with no dipole moment and possesses a linear geometry and closed-shell configuration.¹¹⁹ However, the carbon atom in the CO₂ molecule can gain electrons which causes a repulsive force among the lone pair of electrons in oxygen atoms. It lowers the bond angle of O-C-O and activates the CO₂ molecule to form carbonate-like anion radical (CO₂^{•-}) species. The one electron-based photo-reduction is quite unlikely due to the very strong electrochemical potential (E^o_{redox} = - 1.90 V vs NHE) and practically no semiconducting nanomaterial offers such negative electrochemical potential. In the presence of multiple electrons and H₂O (at pH = 7) as a proton donor, the CO₂ molecules can be reduced to different hydrocarbon species by a different number of electrons and corresponding protons, such as formic acid (2e⁻), carbon monoxide (2e⁻), formaldehyde (4e⁻), methanol (6e⁻) and methane (8e⁻) respectively.^{104, 119} Similar to the photocatalytic H₂ evolution from water splitting, the photocatalytic CO₂ reduction also depends on many factors such as wavelength and intensity of the irradiated light, absorption efficiency, types of heterojunctions, energy band positions of the semiconductors, crystallinities, morphologies, SSA and other textural properties of the photocatalysts.^{65, 109, 119-121} The photocatalytic CO₂ reduction is beyond the scope of this PhD thesis. Therefore, no detailed discussion is presented in the review chapter.

2.4 MOF derived nanocomposites for photocatalytic applications

A variety of strategically selected MOFs with desired morphologies and tunable pore sizes can be transformed into nanocomposites by controlled thermal treatments.^{41, 51} The pyrolysis of thermally stable MOF precursors under inert gas

atmosphere generates metals, metal oxides, metal sulphides and metal phosphides embedded in porous carbon matrix with micro/mesoporous structures.⁴⁰ Depending upon the pyrolysis conditions such as temperature, time, heating rate and gas atmosphere, these resulting nanocomposites can preserve the inherited morphologies of MOF precursors. The rational design of MOF precursors allows the derived nanocomposites in 0D, 1D, 2D and 3D nanostructures with morphologies including polyhedral, core-shell structures, nanorods, nanotubes, nanocubes, nanodiscs and nanospheres.¹²²⁻¹²⁴ Moreover, the external-templated MOF precursors can be transformed into hybrid composites such as carbon nanosheets (graphene, graphene oxide or carbon nitride) decorated with oxides, sulphides or phosphides in customisable dimensions.^{42, 125} In the past decade, MOF derived nanocomposites have shown great promise as highly efficient photocatalysts in some typical solar energy-driven applications, outperforming the commercially available counterparts. This part of the review chapter summarises the reported strategies on morphology control and the physicochemical property tuning of the MOF derived nanocomposites, which optimise the performance in photocatalytic applications including photocatalytic water splitting for H₂ evolution and photodegradation of organic pollutants.

The reported dimensions and morphologies of the MOF derived nanocomposites for various photocatalytic applications are summarised in Figure 2.1. It is important to highlight that in this review 0D nanocomposites are not classified by the size and dimension of the nanoparticles because in MOF derived composites, each crystallite can consist of a large number of small nanoparticles. Therefore, the dimension and morphology of the MOFs crystallites and derived composites are classified in generic terms.^{42, 77}

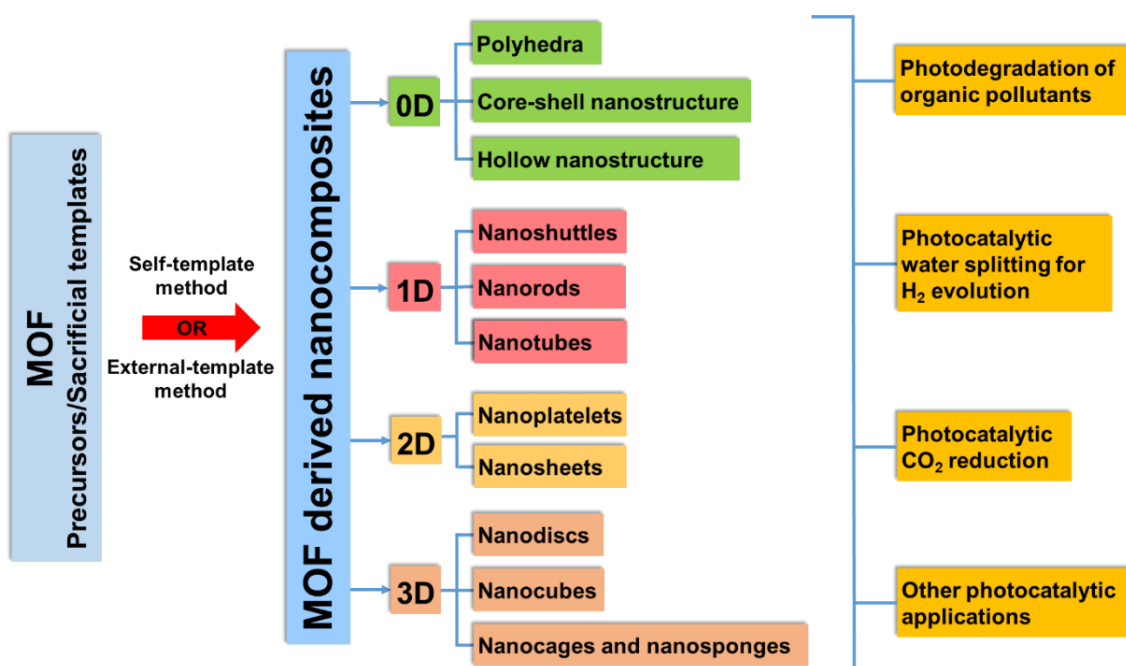


Figure 2.1 A schematic summary of the dimension and morphology of the MOF derived nanocomposites for photocatalytic applications.

2.5 MOF derived nanocomposites for photocatalytic hydrogen (H₂) evolution

The depletion of fossil fuels, environmental pollution and growing energy demand have made the H₂ generated by photocatalytic water splitting to be one of the clean and cost-effective alternative energy sources. Since Fujishima and Honda discovered the possibility of mimicking photosynthesis to generate H₂ using sunlight and water in 1972, tremendous efforts have been devoted to synthesising highly efficient and stable heterogeneous catalysts for photocatalytic H₂ evolution.¹²⁶ It has been established that the photocatalytic H₂ evolution strongly depends on the photo-absorption capability of the semiconducting catalysts, the accessibility of active sites, the EBG positions and the charge separation/transfer efficiencies. The conventional semiconducting photocatalysts generally suffer from the low surface area, limited visible light absorption, inaccessible active sites and large EBGs.⁵² Physicists and chemists have been trying to enhance the surface area by producing carbon-based composite materials and optimise the EBGs by introducing metal and/or non-metal dopants and/or forming heterojunctions.^{22, 105-107} However, the maximisation of visible light absorption for photocatalytic reactions is still a challenge. Transition metal based

photocatalysts (other than TiO₂ and ZnO) such as oxides, sulphides and carbides have been demonstrated to obtain narrow EBGs by introducing anionic and cationic dopants.^{22, 105, 127-129} MOF derived nanocomposites have exhibited a great potential to be used as photocatalysts for H₂ evolution from water splitting since they offer symbiotic effects of tunable morphologies and chemical properties to enhance the photocatalytic performance.^{36, 41, 130} In the following section, MOF derived nanocomposites with different dimensions (0D, 1D, 2D or 3D) for photocatalytic H₂ production from water splitting are summarised. Moreover, the structure-property-application relationship as well as physicochemical properties of the MOF derived nanocomposites are analysed and reviewed.

2.5.1 0D nanocomposites

2.5.1.1 Polyhedra

Among the self-templated MOF derived 0D nanocomposites, the polyhedral morphologies are the earliest reported and the most common nanostructures with relatively high surface area and hierarchical pores.^{93, 95, 131} Transition metal-based MOFs (such as Cu and Fe) can be employed to derive respective CuO_x and Fe_xO_y nanoparticles due to their narrow EBGs. For instance, Fe-MOF derived octahedral Fe₂O₃/C nanocomposites show a reasonably good HER performance under visible light. Xu *et al.* have reported that structurally and chemically stable composites obtained from self-templated MOF precursor via a mild in-situ carbonisation process are highly efficient for H₂ evolution under the white LED light. MIL-101 (Fe) with ~500 nm octahedral morphology transforms into magnetic metal oxide/carbon/oxyhydroxide (FeO_{3.3}C_{0.2}H_{1.0}) nanocomposite that possesses the partial characteristics of γ -Fe₂O₃, α -FeOOH and amorphous carbon. This octahedral shaped nanocomposite offers well-exposed active sites with a BET surface area of 93.7 m² g⁻¹ and wide pore diameter distribution in the range of 2-140 nm. In the presence of Eosin Y, triethylamine in acetonitrile/water solution, this self-templated MOF derived magnetic nanocomposite shows highly efficient H₂ evolution activity of 4.2 mmol g_{cat}⁻¹ h⁻¹ under the white LED light (400-700 nm) due to the synergistic effect of ferric oxide and O-containing functional groups (such as -OH, -COOH) tethered on the surface of amorphous carbon. However, further investigations are required to understand the decomposition and

transformation mechanism of the MOF precursors into the in-situ formed products.¹⁰⁰

Several studies have revealed that the charge transfer problems in MOF derived nanocomposites can be solved by the incorporation of conductive graphene or carbon-based materials in semiconducting photocatalysts to form heterojunctions.^{110, 132} The hybrid nanocomposites fabricated by the combination of various counterparts (such as MOF derived metal oxides) and functionalised semiconducting carbon-based materials with a narrow EBG can further improve the charge separation and transfer due to the formation of heterojunction. For instance, Cu₂O/C₃N nanocomposites with octahedral morphology can be obtained by carbonising self-templated Cu-MOF, HKUST-1 loaded with urea (H₂N)₂CO as an additional nitrogen precursor at moderate temperature (above 450 °C) under nitrogen atmosphere. The p-type Cu₂O nanoparticles and nitrogen-rich n-type graphitic carbon form a p-n heterojunction resulting in an overall EBG of 1.97 eV for the Cu₂O/C₃N composite. The p-n heterojunction facilitates the spatial separation and efficient transfer of photoinduced electrons from the Cu₂O to the nitrogen-rich carbon due to the interfacial contact, minimising the charge recombination. This MOF derived Cu₂O/C₃N nanocomposite shows relatively higher H₂ evolution activity under visible light compared to the pristine Cu₂O and/or g-C₃N₄, although its photocatalytic performance is poor compared to other reported MOF derived nanomaterials.¹³³

Single metal oxides derived from MOFs, in general, show relatively poor light absorption capacities and quick charge recombination, which result in limited photocatalytic performance. Efforts have been devoted to engineering the EBGs of multi-metallic MOF derived nanocomposites to enhance the visible light absorption for improved H₂ evolution due to the synergistic effects.^{88, 90, 96} Self-templated bimetallic MOF/TiO₂ precursors can be carbonised to obtain the nanocomposites that exhibit the symbiotic of properties. For example, TiO₂-NiCoMOF-S_{powder}, a mixture containing amorphous TiO₂ nanoparticles encapsulated in Ni-Co-ZIF-67 mixed with sulphur powder, can produce crystalline TiO₂ nanoparticles well-dispersed onto the porous carbon (PC) shell decorated with Co/NiS nanoparticles (TiO₂@CoNiS-PC) by pyrolysing at 600 °C in an argon atmosphere. This TiO₂@NiCoS-PC nanocomposite inherits the polyhedral morphologies of the precursor and exhibits a moderate BET surface area of 93.5

$\text{m}^2 \text{g}^{-1}$. Under UV-Vis light irradiation, the photoexcited electrons in TiO_2 nanoparticles transfer to NiCoS/PC shell due to their lower overpotential and the holes are consumed by the sacrificial agent (MeOH). The spatial separation of photogenerated electrons and holes in well-dispersed TiO_2 inhibits the surface charge recombination because the conductive porous carbon (PC) matrix facilitates the fast charge transfer. The NiCoS nanoparticles decorated on the PC matrix act as cocatalyst to offer additional active sites which further improve the charge separation and the utilisation efficiency of UV-Vis light.¹³⁰ Following this MOF-templated approach, a variety of high performing multi-metal oxides uniformly embedded in a conductive porous carbon matrix can be synthesised with desired morphologies and favourable physicochemical properties.

2.5.1.2 Hollow nanocomposites

Nanocomposites with 0D hollow spherical morphologies exhibit short path lengths and higher charge transfer efficiency which could boost the photocatalytic H_2 evolution. To date, no self-templated MOF derived hollow nanostructures for photocatalytic H_2 evolution have been reported, only a few external-templated MOFs have been investigated to derive the hollow metal oxide/carbon composites by direct pyrolysis at high temperatures. For example, using the SiO_2 sphere as an external template, a uniform thin shell of HKUST-1 can be coated and grown on the surface of SiO_2 spheres by a liquid phase epitaxial layer by layer immersion method. Then a Ti-containing precursor can be introduced to the SiO_2 @HKUST-1 spheres, followed by a two-step heat treatment at 400°C and 800°C under N_2 atmosphere to generate the SiO_2 @Cu- TiO_2 /C composite. Finally, SiO_2 in the composite can be etched in 1 M KOH aqueous solution at 80°C for 12 hours to obtain hollow Cu- TiO_2 /C nanospheres. The Cu_2O and TiO_2 nanoparticles homogeneously disperse in the porous carbon nanospheres and form p-n heterojunction at the interface that exhibits a bulk EBG of 2.89 eV. As shown in Figure 2.2, the Cu- TiO_2 /C nanocomposite with hollow spherical morphologies demonstrates a significant improvement of photocatalytic H_2 evolution compared to the Cu- TiO_2 /C nanocomposite derived from HKUST-1-Ti prepared without using SiO_2 as an external template. This two-fold increase in photocatalytic H_2 evolution performance under simulated sunlight is due to the improved light absorption, better separation and migration of photoexcited electrons/holes as well as the enhanced H_2 diffusion.¹¹⁴ This external-templated

MOF as precursors for the preparation of nanocomposite possessing the morphology of the external template method can be extended to prepare other metal oxides/carbon nanospheres with single and/or multilayered complex morphologies for various photocatalytic and energy applications.

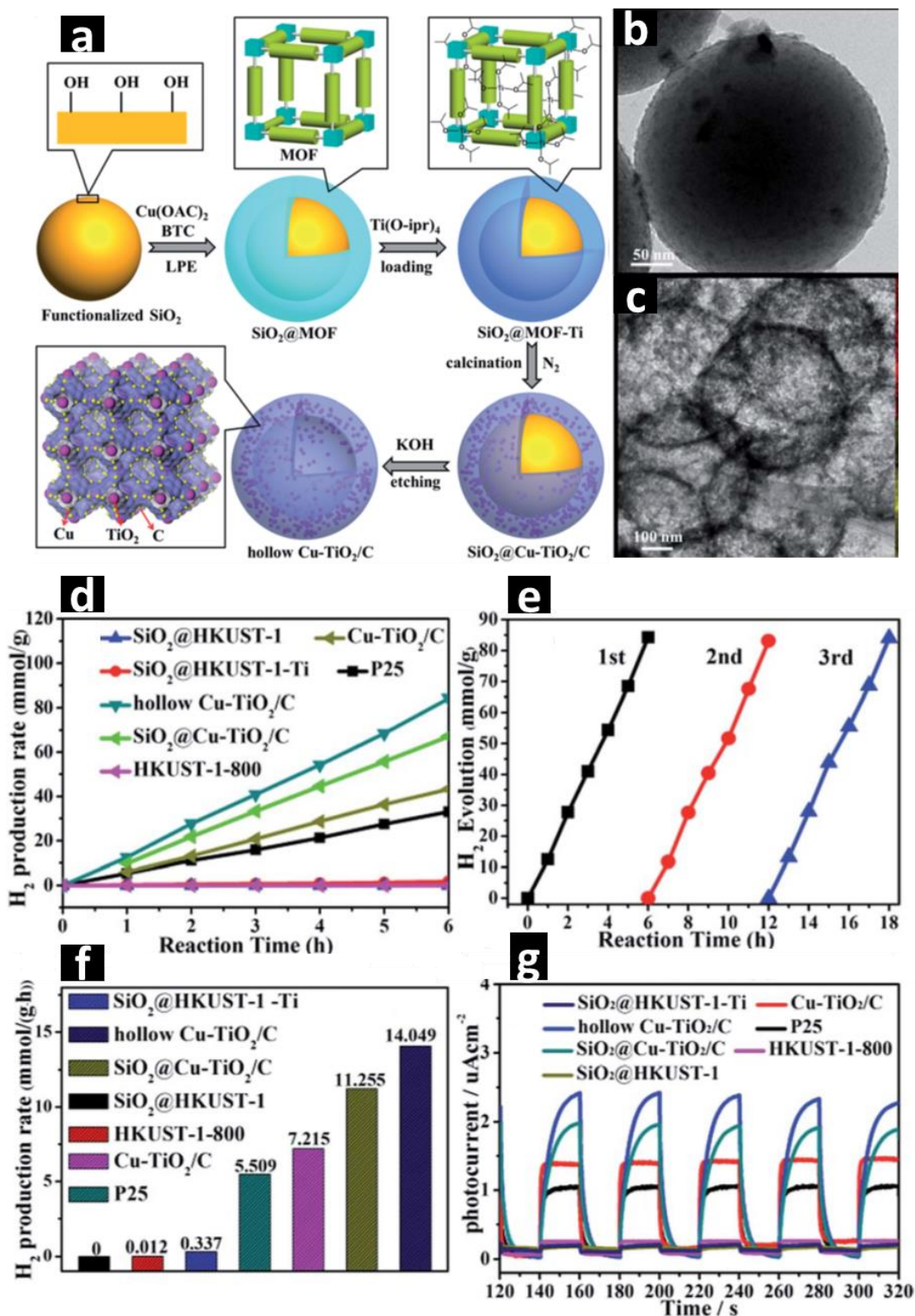


Figure 2.2 (a) Schematic representation of hollow Cu-TiO₂/C nanospheres derived from the external-templated core-shell SiO₂@SURMOF nanospheres (b, c) TEM images of SiO₂@Cu-TiO₂/C (d) Photocatalytic H₂ evolution of MOF

derived nanocomposites (e) the recyclability of best performing hollow Cu–TiO₂/C nanospheres under solar irradiation (f) H₂ evolution rates in mmol g_{cat}⁻¹ h⁻¹ and (g) photocurrent measurements of nanospheres under simulated solar irradiation.¹¹⁴

2.5.2 1D nanocomposites

Although recent reports have demonstrated that transition metals (e.g., Cd, Co, Ni) based MOF precursors pristine or composite, can be used as sacrificial templates to obtain metal/multi-metal oxides, sulphides, phosphides or carbides embedded in a 1D carbon matrix, MOF-templated 1D nanocomposites are commonly derived from Fe-MOFs. 1D MOF precursors with different morphologies such as nanorods, nanotubes and nanoshuttles can be synthesised by using specifically designed SBUs (metal ions/clusters), organic linkers, suitable solvents and controlling the ratios of chemical reactants.^{77, 134, 135} MOF derived 1D nanocomposites can be advantageous over bulk counterparts due to their enhanced surface with easily accessible active sites and controllable charge flow in a specific direction which consequently shorten the charge migration/transfer distances in photocatalytic reactions. Though several studies are available on the synthesis and applications of 1D MOFs composites, only a few are dealing with photocatalytic water splitting for H₂ evolution.^{57, 136, 137}

2.5.2.1 Nanoshuttles

NH₂-MIL-101(Fe), a MOF consisting of Fe oxo-clusters and amino-terephthalate, can be phosphidised to prepare FeP polyhedra with high SSA and exposed active sites. Moreover, if MOFs are anchored/grown on g-C₃N₄, the FeP/g-C₃N₄ composites with strong interfacial contact can be prepared for highly efficient photogenerated charge transfer. Taking advantage of these possibilities, Xu *et al.* used NH₂-MIL-101(Fe) as a precursor to anchor the Ni(OH)₂ nanoparticles.⁹⁴ In the second step, g-C₃N₄ nanosheets prepared by thermal treatment of melamine were deposited on the surface of as-prepared NH₂-MIL-101(Fe)/Ni(OH)₂ composite under constant stirring at 60 °C overnight. The as-prepared MIL-101(Fe)/Ni(OH)₂/g-C₃N₄ sacrificial template with shuttle-like morphology was then phosphidised in the presence of NaH₂PO₂ (with optimum mass ratios of 1:5) by heat treatment at 350 °C under N₂ atmosphere, which

resulted in C/N co-doped FeNiP/g-C₃N₄ nanocomposite. Figure 2.3 shows that the obtained 1D nanocomposite retains the inherited hexagonal micro-spindle (shuttle-like) morphologies with all the elements homogeneously distributed throughout the sample. Under visible light irradiation, the optimised CN/FeNiP/g-C₃N₄ nanocomposite with 1.0 mmol L⁻¹ Eosin Y (EY) photosensitiser, exhibits exceptionally high H₂ evolution activity of 13.81 mmol g_{cat}⁻¹ h⁻¹ in 10 % triethanolamine (TEOA) solution. The presence of EY sensitiser prolongs the lifetime of the photogenerated charge carriers compared to pure g-C₃N₄. Furthermore, decorating the nanocomposite with Ni₂P as a cocatalyst dramatically enhances the photocurrent response with the most efficient charge transfer. Without Ni₂P, the plain CN/Fe₂P/g-C₃N₄ shows H₂ evolution rate of 2.73 mmol g_{cat}⁻¹ h⁻¹ under identical conditions whereas without adding EY photosensitiser, the CN/FeNiP/g-C₃N₄ hexagonal nanoshuttles only exhibit H₂ evolution rate of 0.196 mmol g_{cat}⁻¹ h⁻¹. The optimised amount of EY photosensitiser and Ni₂P play crucial roles in this 1D CN/FeNiP/g-C₃N₄ nanocomposite.⁹⁴ The same strategy can be applied to fabricate a variety of complex multi-functionalised bimetal oxide/carbon composites via this method. However, it is worth noting that the involvement of multiple steps and a lack of simplicity make the nanocomposites obtained in this way less promising for practical applications. Simple one-step methods are desirable to obtain scalable, highly efficient and stable photocatalysts for H₂ evolution.

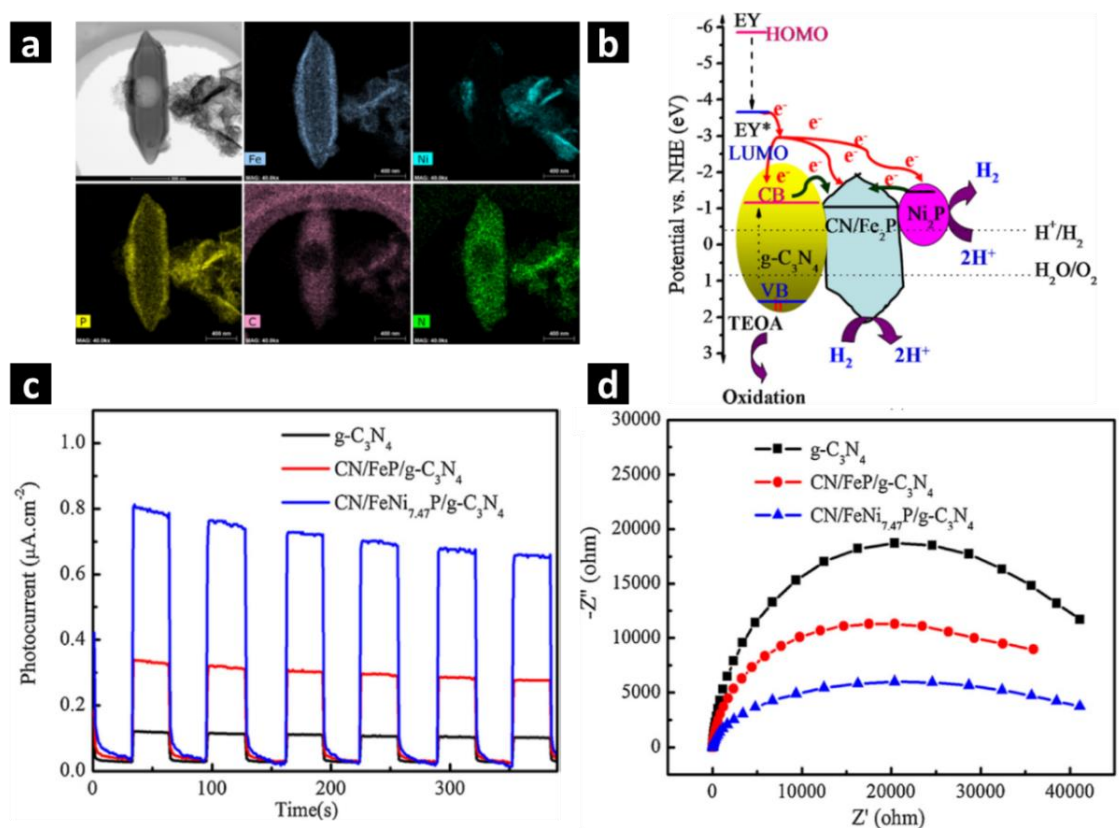


Figure 2.3 (a) STEM-EDX image and the elemental mapping of C-N/FeNi_{7.47}P/g-C₃N₄ composite for Fe, Ni, P, C, N (b) Proposed mechanism of photocatalytic H₂ evolution over the EY-sensitised C-N/FeNiP/g-C₃N₄ composite in the presence of sacrificial agent TEOA under irradiation of visible light (c) Transient photocurrent responses under visible light and (d) EIS curves of external-templated MOF derived optimised CN/FeNi_{7.47}P/g-C₃N₄ composites.⁹⁴

2.5.2.2 Nanorods

Theoretically, all MOFs can be pyrolysed to derive composite nanomaterials. However, Fe-MOF precursors have mostly been employed to yield 1D nanocomposites due to their 1D self-assembly, water-based synthesis and low toxicity.¹²⁴ For example, self-templated MOF, NH₂-MIL-88B(Fe) can be directly carbonised at 600 °C in an inert atmosphere to fabricate magnetic 1D Fe₂C nanorods without compromising the inherited morphology. The reduction potential of metal ions that constitute the MOF precursors plays a key role in determining the nature of metal species in the derived products. The in-situ formed carbon (from the thermal decomposition of organic ligands in the MOF templates during the thermolysis process) is a strong reducing agent and the metal ions can be readily reduced to metal nanoparticles or form metal carbides

at higher carbonisation temperature in an inert atmosphere. The reduction potential and Gibbs free energies (ΔG) of the reactant species in MOF templates are vital in determining whether metals or metal carbide species can be formed.^{89, 103} Upon pyrolysis under argon atmosphere, nanorod shaped $\text{NH}_2\text{-MIL-88B(Fe)}$ precursor with the rod length of ~ 300 nm and width of ~ 50 nm decomposes and transforms into crystalline Fe_2C nanorods with shrunk sizes and coarse surfaces. These magnetic Fe_2C nanorod shaped particles show relatively good performance in photocatalytic activity under visible light due to the well-exposed active sites and easy charge transfer. The magnetic property makes these composites easy to collect after the reaction for recycling.¹³⁸ Such a simple method can be optimised to fabricate desirable morphologies for other transition metal based MOFs. Furthermore, the formation mechanisms of porosities and the charge generation/charge transfer of the 1D MOF derivatives need in-depth investigation by employing in-situ imaging and operando spectroscopy techniques.

2.5.3 2D nanocomposites

It is of particular importance to synthesise 2D MOF sacrificial templates because of their promising physicochemical and optoelectrical properties. The 2D MOFs with desirable properties can be achieved by optimising the compositions, growth of crystal phases, the formation of the surface/bulk defects and the textural properties for a variety of catalytic and energy applications.^{77, 139} Generally, self-templated ultrathin 2D MOF precursors can be synthesised by various methods such as surfactant-assisted bulk solutions (structure-directing agent to direct the orientation of crystal growth), interfacial growth at air/liquid, liquid/liquid or liquid/solid interface, sonication/mechanical exfoliation and chemical intercalation.^{77, 139-142} For external-templated 2D MOF precursors, 2D carbon structures such as carbon nanosheets, graphene or graphene nitride are used, which have the benefit of combining the characteristics of MOFs and the external templates.¹⁴³⁻¹⁴⁵ However, developing direct synthesis methods to produce metal/multi-metal 2D-MOF precursors can be a convenient approach to overcome the complications of exfoliation or multi-step external-templating method.⁷⁷ The controlled pyrolysis of 2D MOFs precursors can produce 2D nanosheets, nanofilms and nanoflakes of porous carbon materials uniformly

decorated with metal oxides, sulphides or phosphides which can be excellent nanocomposites for photocatalytic H₂ evolution applications.^{146, 147}

2.5.3.1 Single metal nanosheets

Direct pyrolysis of hybrid MOF precursors (MOFs grown on 2D external templates) is a relatively simple method to fabricate MOF derived 2D metal oxide/C nanocomposites. Combining two semiconducting nanomaterials with finely tunable energy band positions can form heterojunctions that are desirable to enhance the photoexcited charge separation/transfer efficiencies. For example, Fe-MOF derived α -Fe₂O₃ nanoparticles with modified EBGs coupled with carbon nitride (g-C₃N₄) can form Z-scheme heterojunctions through a rationally designed MOF-template method.^{1, 145, 148} Melamine derived g-C₃N₄ nanosheets can be used as external-template to grow MIL-100(Fe) on it, followed by the calcination at 400 °C to obtain g-C₃N₄/ α -Fe₂O₃ hybrid nanocomposite with 2D nanosheet morphology. As shown in Figure 2.4a and b, MOF derived α -Fe₂O₃ polyhedral nanoparticles uniformly dispersed on g-C₃N₄ nanosheets with optimised composition and morphology exhibit a promising H₂ evolution rate of 2.07 mmol g_{cat}⁻¹ h⁻¹ under visible light in the presence of Pt cocatalyst. The charge generation/transfer mechanisms in the direct Z-scheme heterojunctions can be investigated by electron paramagnetic resonance spectroscopy (EPR), transient photocurrent density measurement and electrochemical impedance spectroscopy (EIS) shown in Figure 2.4c, d and e. In traditional heterojunctions, photogenerated electrons and holes jump to the conduction band of g-C₃N₄ and valence band of α -Fe₂O₃ respectively. However, such charge mobility has not been observed in Z-scheme heterojunction. Instead, the photogenerated electrons and holes in Z-scheme g-C₃N₄/ α -Fe₂O₃ nanocomposites stay spatially separated because the valence band position of g-C₃N₄ (1.58 V vs. NHE) is more negative than the standard redox potential of OH⁻/[•]OH (2.34 V vs. NHE) and H₂O/[•]OH (1.99 V vs. NHE), while the conduction band position of α -Fe₂O₃ (0.33 V vs. NHE) is lower than that of the O₂/[•]O₂⁻ (-0.33 V vs. NHE). Therefore, like traditional heterojunction, the optimised Z-scheme heterojunctions such as g-C₃N₄/ α -Fe₂O₃ can also enhance the visible light absorption, consequently accelerate the photogenerated charge separation and migration.¹⁴⁸

Similarly, other transition metals can also be loaded on g-C₃N₄ nanosheets. For example, surface modified Ni/g-C₃N₄ nanosheets have been derived from

external-templated-MOF composites.¹⁴⁹ A 2D Ni-MOF precursor was prepared by the ultrasonication method while g-C₃N₄ nanosheets were derived by thermal polymerisation of urea at 550 °C in the air (Figure 2.4f). Both as-prepared precursors (2D Ni-MOF and g-C₃N₄) was mechanically mixed. The resulting mixture was pyrolysed under argon atmosphere above 500 °C to obtain Ni/g-C₃N₄ nanosheets, in which the 2D-Ni-MOF transforms into Ni and/or NiO forming mixed Ni/NiO nanoparticles. The interfacial contacts between the Ni/NiO nanoparticles and the g-C₃N₄ nanosheets offer enhanced light absorption as well as improved charge separation and transfer. Under visible light irradiation, the photogenerated electrons and holes carry out the redox reactions at the respective energy bands. The presence of Ni particles as a cocatalyst may contribute to the significant suppressing of the charge recombination. Adding EY as a photosensitiser, the optimised Ni/g-C₃N₄ nanosheets exhibited high photocatalytic H₂ evolution activity of 2.99 mmol g_{cat}⁻¹ h⁻¹, attributed to the high conductivity of g-C₃N₄ and efficient charge separation/transfer.¹⁴⁹ A variety of transition metals such as Fe, Ni, Cu, Co-based-MOF derived metal/metal oxides can be studied as cocatalysts decorated on surface-modified 2D nanosheets as an alternative to noble metals for effective H₂ evolution from photocatalytic water splitting.

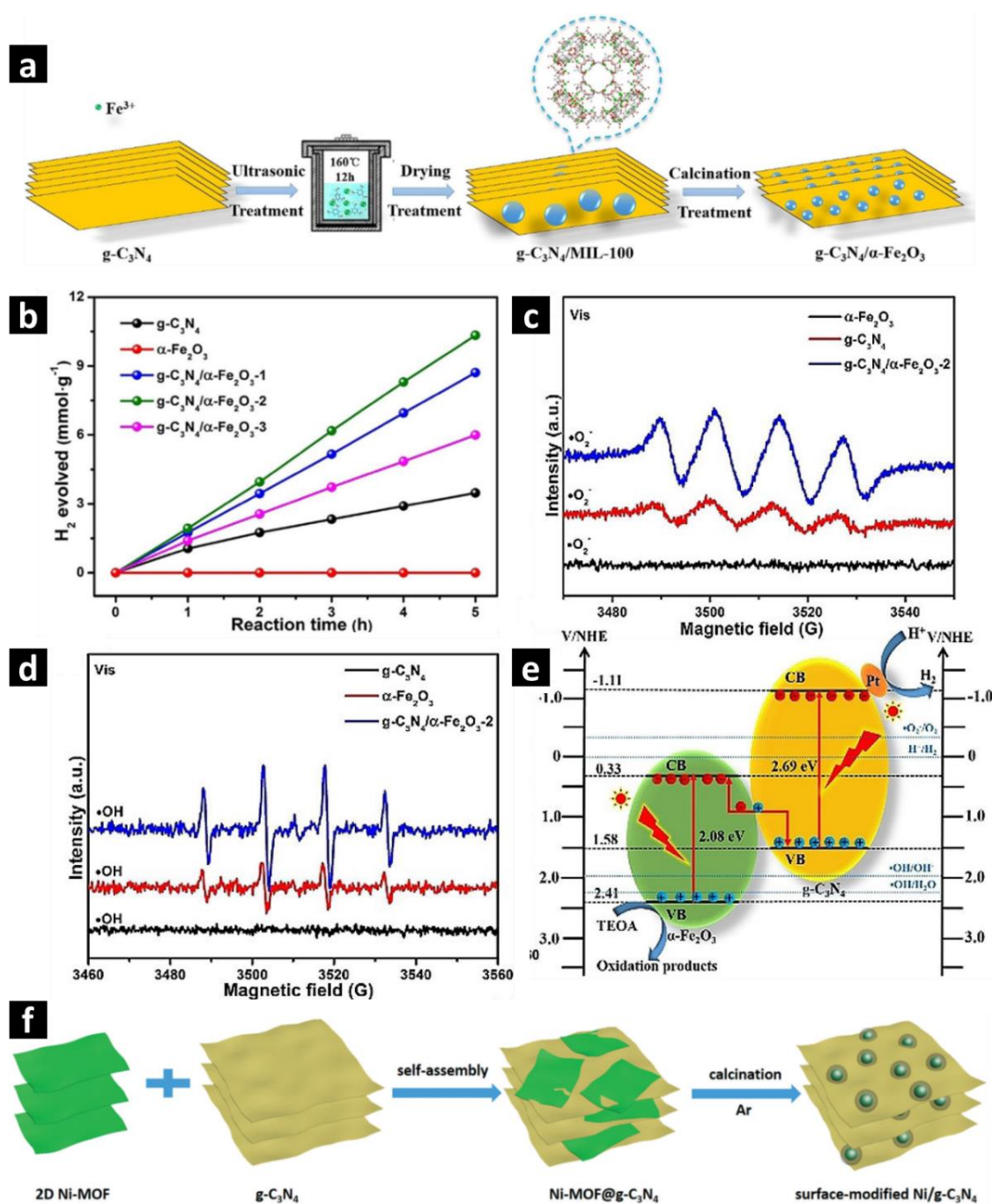


Figure 2.4 (a) Schematic diagram shows the synthesis strategy of Fe-MOF/ $g\text{-C}_3\text{N}_4$ derived $g\text{-C}_3\text{N}_4/\alpha\text{-Fe}_2\text{O}_3$ nanocomposite (b) Photocatalytic H_2 evolution by $g\text{-C}_3\text{N}_4/\alpha\text{-Fe}_2\text{O}_3$ nanocomposite (c) EPR spectra measured in MeOH for DMPO- $\bullet\text{O}_2^-$ (d) EPR spectra measured in aqueous solution for DMPO- $\bullet\text{OH}$ and (e) Photocatalytic H_2 evolution mechanism of the $g\text{-C}_3\text{N}_4/\alpha\text{-Fe}_2\text{O}_3$ nanocomposite under visible light (300 W Xe lamp, $\lambda > 420 \text{ nm}$)¹⁴⁸ (f) Schematic representation of 2D Ni-MOF/ $g\text{-C}_3\text{N}_4$ derived Ni/ $g\text{-C}_3\text{N}_4$.¹⁴⁹

2.5.3.2 Multi-metallic nanosheets

Different from single metal or metal oxide based MOF derived composites, 2D nanocomposites with multi-metallic sulphide and phosphide based heterojunction can be excellent nanomaterials for photocatalytic applications due to their promising optoelectronic and photochemical properties.^{150, 151} Metal sulphides such as CdS and ZnS with morphologies of nanosheets, nanoflowers and core/shell nanostructures have been extensively studied for photocatalytic applications. However, the low surface area, the environmental unfriendliness of CdS and the wide EBG of ZnS together with their poor photostability limit their practical applications.^{58, 152} The challenges of poor photostability and the low surface area can be tackled by employing rationally designed bimetallic MOFs combined with external templates such as rGO or g-C₃N₄ 2D nanosheets to fabricate stable metal and/or bimetal sulphide nanoparticles uniformly distributed in porous carbon matrix for enhanced photocatalytic H₂ evolution. For example, ZnS/rGO/CuS nanocomposites can be derived from a mixture of ZIF-8, thioacetamide (TAA) and rGO, which is obtained by simple solvothermal and ion-exchange methods.¹⁴⁶ The resulting ZnS/CuS nanoparticles retain the polyhedral morphology of ZIF-8 precursor with a particle size of ~150 nm. These ZnS/CuS nanoparticles form heterojunctions and uniformly distribute in rGO 2D nanosheets, which enhances the photostability of ZnS/CuS nanoparticles and inhibit the agglomeration of the nanoparticles. The interfacial contacts between the ZnS/CuS nanoparticles and the conductive rGO nanosheets can facilitate the charge transfer of photoexcited electrons and holes, and consequently improve the spatial charge separation and transport efficiency. The external-templated MOF derived porous ZnS/rGO/CuS 2D nanosheets with optimised 7 wt.% Cu and 0.5 wt.% rGO exhibit higher H₂ evolution activity of 2.61 mmol g_{cat}⁻¹ h⁻¹ under visible light compared to the counterpart bimetallic sulphide heterojunction derived from conventional inorganic precursors.¹⁴⁶ This method may provide a viable route to synthesise noble metal-free high efficient multi-metallic sulphides/carbon nanocomposites for environment and energy applications.

The issues of band gap and photostability of CdS nanoparticles can be addressed by adopting the external-templated MOF method. Recently, Malgorzata *et al.* reported 2D nanosheets of Cd(OH)₂/CdS/g-C₃N₄/NPC nanocomposite derived from external-templated MOF for H₂ evolution under the

solar simulator.¹⁵³ Specifically, nanoporous carbon (NPC) matrix was obtained from the direct carbonisation of Al-MOF at 750 °C under an inert atmosphere followed by washing with 17 % HCl to remove the Al species. The g-C₃N₄ nanosheets were derived from calcination of urea in a muffle furnace at 550 °C for 4 hours under air. Finally, CdSO₄ mixed with thiourea and NH₃.H₂O were added into g-C₃N₄ and NPC under constant stirring followed by filtering and drying to collect Cd(OH)₂/CdS/g-C₃N₄/NPC nanocomposite. The resulting nanocomposite exhibited a BET surface area of 92.7 m² g⁻¹ and pore volume of 0.044 cm³ g⁻¹. With the EBG of 2.32 eV, 40 wt.% of Cd(OH)₂/CdS nanoparticles embedded in g-C₃N₄/NPC matrix showed moderate H₂ evolution activity of 148.13 μmol g_{cat}⁻¹ h⁻¹ under the solar simulator. It is claimed that the formation of heterojunction between g-C₃N₄ and Cd(OH)₂/CdS nanoparticles can provide insights into the photoexcited charge generation and migration pathways. The photogenerated electrons in g-C₃N₄ may migrate to Cd(OH)₂/CdS compound due to its less negative conduction band maxima (CBM) compared to g-C₃N₄. Then both the migrated electrons from g-C₃N₄ and the electrons photogenerated in Cd(OH)₂/CdS, may partially migrate to the NPC. A large number of catalytic active sites participate in water reduction due to the synergistic effects.¹⁵³ Nonetheless, detailed in-situ microscopic and photoelectrochemical characterisations are required to further understand the mechanism of heterojunction formation and charge transfer in this type of complex nanocomposites.

Similarly, bimetallic phosphide particles encapsulated in porous carbon hybrids and uniformly dispersed on 2D g-C₃N₄ nanosheets have been derived by heat treatment of external-templated bimetallic-MOF precursors and the resulting composites are promising materials for photocatalytic applications. For example, as-prepared bimetallic Ni-Co-C₆H₃(COOH)₃, NaH₂PO₂ and g-C₃N₄ were ground together in appropriate ratios, followed by phosphorisation under an argon atmosphere at 350 °C for 2 hours to obtain ternary g-C₃N₄-Ni_xCo_{1-x}P₂-PC nanocomposite. The optimal ternary g-C₃N₄-NiCoP₂-PC nanocomposite (Figure 2.5) with a BET surface area of 56.32 m² g⁻¹ showed a maximum H₂ evolution activity of 2.1 mmol g_{cat}⁻¹ h⁻¹ under UV-Vis light in 20 % TEOA/H₂O solution, which was attributed to the low HER overpotential and the flat-band potential of NiCoP₂, as well as the high electrical conductivity of the MOF-templated porous carbon/g-

C_3N_4 .¹⁴⁷ A library of MOF derived 2D multi-metallic oxide, phosphide and sulphide-based nanocomposites with a variety of morphologies such as nanoplatelets, nanosheets and nanoribbons, can be designed and produced from selected bimetallic MOF precursors via self-templated and external-templated approaches. These new types of nanocomposites can effectively improve the photoexcited charge carrier separation and transport which consequently enhance their photocatalytic H_2 evolution performance. In Table 2.1, a summary of the selected MOF derived nanocomposites for photocatalytic H_2 evolution from water splitting is presented.

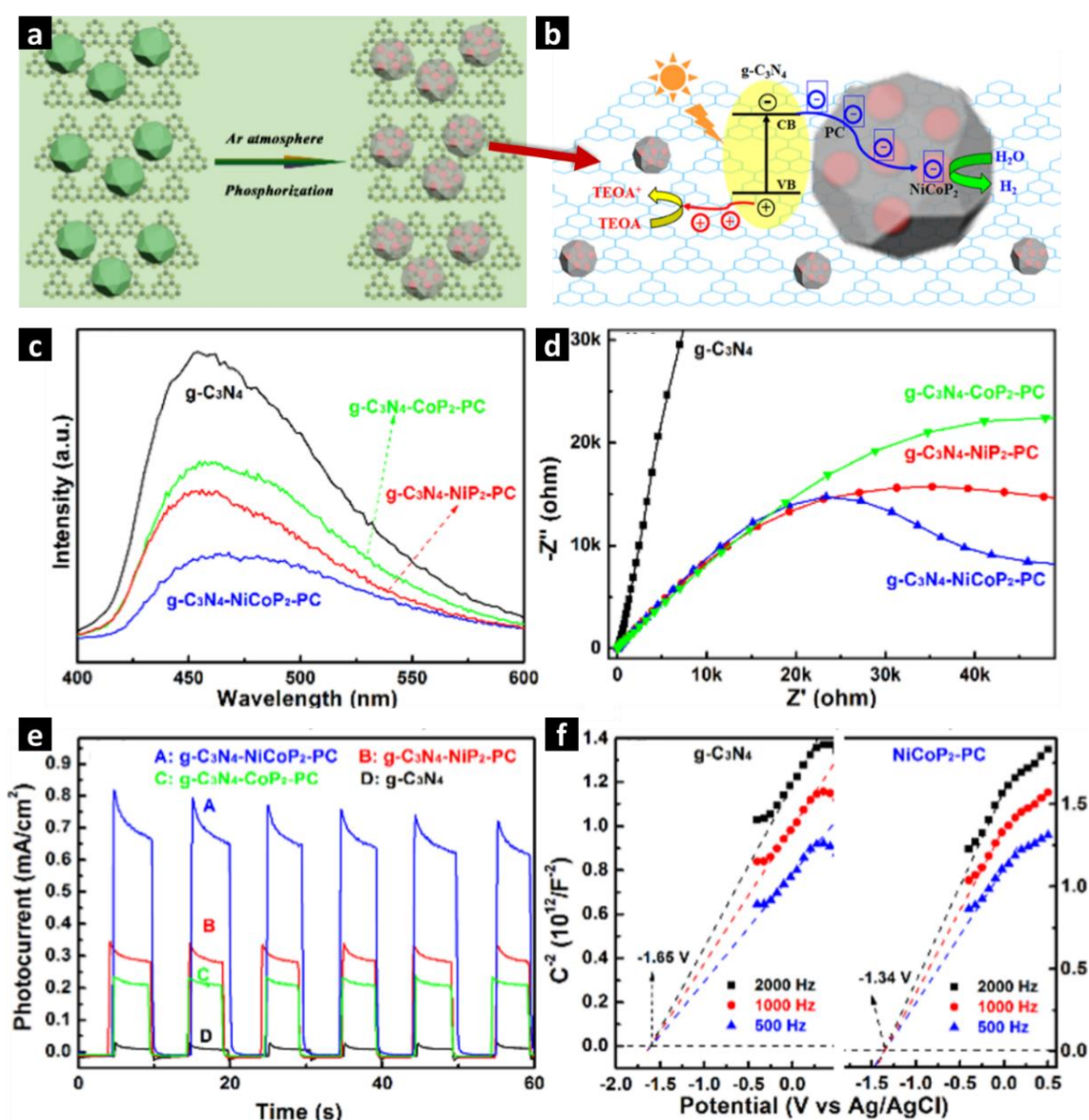


Figure 2.5 (a) Schematic diagram of the $g-C_3N_4$ /MOF derived $g-C_3N_4$ -NiCoP₂-PC nanocomposite (b) Proposed mechanism of photoinduced separation of charge carriers in the $g-C_3N_4$ -NiCoP₂-PC composite and the reduction process for H_2 evolution under UV-Vis light (c) PL emission spectra (d)

EIS spectra (e) transient photocurrent responses under irradiation of UV-Vis light and (f) Mott–Schottky plots of *g*-C₃N₄/NiCoP₂-PC.¹⁴⁷

Table 2.1 Comparison of selected MOF derived nanocomposites for photocatalytic H₂ evolution.

MOF precursor	Catalyst	Morphology	Experimental conditions		H ₂ evolution (mmol g _{cat} ⁻¹ h ⁻¹)	Ref.
			Cocatalyst	Light source		
HKUST-1@Urea	Cu ₂ O@C ₃ N	Octahedron	-	> 420 nm 500 W Xe lamp	0.026	133
MIL-101 (Fe)	Fe ₂ O ₃ /FeOOH/C	Octahedron	EY	> 400 nm White LED	4.167	100
TiO ₂ -NiCo-ZIF	TiO ₂ -NiCoS-PC	Core/shell	NiCoS-PC	UV-Vis 300 W Xe lamp	1.29	130
SiO ₂ @HKUST-1-Ti	Cu-TiO ₂ /C	Hollow nanospheres	Pt	Simulated sunlight 300 W Xe lamp	14.05	114
UiO-66-NH ₂ /g-C ₃ N ₄	C-ZrO ₂ /g-C ₃ N ₄ /Ni ₂ P	Nanosheet	EY and Ni ₂ P	> 420 nm 300 W Xe lamp	10.04	115
MIL-100(Fe)/ g-C ₃ N ₄	g-C ₃ N ₄ /α-Fe ₂ O ₃	Nanosheet	Pt	> 420 nm 300 W Xe lamp	2.07	148
NiCo-MOF@g-C ₃ N ₄	g-C ₃ N ₄ -NiCoP ₂ -PC	Nanosheet	-	UV-Vis 300 W Xe lamp	2.1	147
g-C ₃ N ₄ /Al-MOF	Cd(OH) ₂ /CdS/g-C ₃ N ₄ /NPC	Nanosheet	-	Simulated sunlight 150 W Xe lamp	0.15	153
rGO/ZIF-8	ZnS/rGO/CuS	Nanosheet	-	> 420 nm 300 W Xe lamp	2.61	146
Ni-MOF@g-C ₃ N ₄	Ni@ g-C ₃ N ₄	Nanosheet	EY	> 420 nm 300 W Xe lamp	2.99	149

Fe/MIL-125	Fe/TiO ₂ @C	Nanodisc	-	UV-Vis 500 W Xe/Hg lamp	215	154
NH ₂ -MIL-101(Fe)/Ni(OH) ₂ /g-C ₃ N ₄	C-N/Fe ₂ P/Ni ₂ P/g-C ₃ N ₄	Nanoshuttle	EY and Ni ₂ P	> 420 nm 300 W Xe lamp	13.81	94

2.5.4 3D nanocomposites

Compared to the low-dimensional (0D, 1D and 2D) MOF templates, it is relatively easy to synthesise 3D MOFs precursors. The 3D MOF precursors offer great flexibility of choices for template materials, chemical compositions and morphologies which possess much higher surface area, tailorable pore sizes and easy hydrophilic/hydrophobic surface functionalisation.⁶⁰ In particular, 3D MOF precursors can host a variety of guest species to derive unlimited nanocomposites that combine the conductive porous carbons and metallic/multi-metallic oxides, sulphides, phosphides, carbides and alloy nanoparticles with engineered EBGs, which can potentially absorb a major part of sunlight in the UV-Vis-IR range for efficient heterostructured photocatalytic applications.^{36, 52, 56, 62, 89, 155} The MOF derived nanocomposites with desirable morphologies and chemical properties can be readily replicated from the rationally designed MOF precursors. A variety of morphologies such as cubes, discs, spheres and sponges can be easily obtained by the direct pyrolysis of the 3D MOFs precursors.

2.5.4.1 Nanocubes

The morphologies and crystallite sizes of the MOF precursors can be adjusted via a wet-chemical approach by adjusting the pH values and the concentrations of the solvents and reactants. The 3D cubic MOF precursors such as ZIF-67, ZIF-8 and UiO-66 can easily be synthesised via the modified solvothermal method.^{45, 156} Nanocubic composites derived from these cubic MOF precursors exhibit higher SSA and exposed active sites, which can improve photocatalytic performance. However, as discussed in previous sections, MOF derived single metal oxide/carbon composites only show moderate catalytic activities due to the limitations of light absorption and the poor charge generation/transport.¹⁵⁷ Therefore, it is important to synthesise multi-metallic MOFs derived nanocomposites coupled with noble metal-free cocatalysts to form heterojunctions for improved H₂ evolution under visible light irradiation. For

example, NH₂-UiO-66 (Zr) was mixed with melamine derived g-C₃N₄ by self-assembly mechanism under ultrasonication, followed by heat treatment at 600 °C first in an inert atmosphere and then in the air to obtain 3D cubic C/N co-doped ZrO₂/g-C₃N₄ nanocomposites. Finally, different wt.% of Ni₂P as a cocatalyst was deposited to obtain C/N co-doped ZrO₂/g-C₃N₄/Ni₂P nanocomposite.¹¹⁵ This external-templated MOF derived cubic C, N-ZrO₂/g-C₃N₄/Ni₂P nanocomposite showed an exceptionally high photocatalytic H₂ evolution rate of 10.04 mmol g_{cat}⁻¹ h⁻¹ under visible light and an AQY (%) of 35.5 % at 420 nm. The dramatically improved H₂ evolution activity was attributed to the enhanced light absorption and spatial separation of photogenerated charge carriers due to the formation of staggered band heterojunction resulting from the narrow EBG of C/N co-doped ZrO₂ with the semiconducting g-C₃N₄ (type II heterostructure). Furthermore, the highly conductive g-C₃N₄ and the uniformly anchored Ni₂P cocatalyst accelerated the charge transfer and the surface photocatalytic reactions respectively.¹¹⁵

2.5.4.2 Nanodiscs

One of the most stable Ti-MOF, self-templated MIL-125 can be pyrolysed under the inert gas atmosphere to derive TiO_x/C nanocomposites with disc-like 3D morphologies. Benefited from the structural stability of Ti-MOF, various transition metal guest species, such as Fe, Ni, Co, Cu, Zn, Ag, Au, can be loaded onto the as-prepared MIL-125 precursor by impregnation method.^{81, 82} Bimetallic compound/carbon composites can be easily formed via pyrolysis of the transition metal loaded Ti-MOF at high temperature. For example, Valero-Romero *et al.* demonstrated that the carbonisation of Fe impregnated MIL-125(Ti) above 500 °C in inert atmosphere produced Fe doped TiO₂ nanoparticles embedded in amorphous carbon matrix with inherited 3D disc-like morphology. Furthermore, by controlling the pyrolysis conditions of MIL-125, the phase ratios of polymorph TiO₂ with tunable crystalline phases (anatase, rutile, and brookite) in the derived nanocomposites could be in-situ optimised to achieve higher photocatalytic performance. The porous carbon matrix kept the TiO₂ nanoparticles from agglomerations, which resulted in uniform dispersion of polymorph TiO₂ for enhanced light absorption and better exposed active sites. The Fe doped mixed-phase (anatase/rutile) TiO₂/C nanocomposite obtained by pyrolysis of 0.15 wt.% Fe loaded MIL-125 at 700 °C showed photocatalytic H₂ activity of 215 μmol g_{cat}⁻¹ h⁻¹ under UV-Vis light.¹⁵⁴ This simple method can be extended to prepare other

metal/metal oxide/carbon 3D nanocomposites with high SSA, controllable crystal sizes and tunable chemical phases and compositions for enhanced photocatalytic H₂ evolution. Particularly, studies to explore rationally designed 3D MOF derived nanocomposites with diverse morphologies such as nanocages, nanospheres, nanoarrays, honeycomb structures and nanofibers for visible light photocatalysis are highly desirable.⁴²

2.5.5 Summary of MOF derived nanocomposites for photocatalytic H₂ evolution

The photocatalytic H₂ evolution performance of semiconductor materials mainly depends upon the appropriate energy band position for light absorption, the charge generation/migration and the accessible active sites. Moreover, the high SSA of the MOF derived metal compound/carbon composites with various dimensions and morphologies also play important role in better light absorption and improved catalytic activity by preventing catalyst particle agglomeration and providing well exposed active sites. Also, it is worth mentioning that the energy band positions of metal compounds (oxides, sulphides or phosphides) in MOF derived composites can be in-situ tuned by doping heteroatoms, creating phase/heterojunctions between metal-metal or metal-carbon compounds to enhance charge migration and suppress charge recombination. Loading non-noble co-catalysts in MOF derived composites can decorate the porous carbon matrix providing additional active sites for highly efficient photocatalytic performance. In MOF derived nanostructures, photogenerated charge flow can be regulated in a specific direction in 1D and 2D nanocomposites for improved photocatalytic performance. However, only a few 2D external-templated MOFs with g-C₃N₄ and rGO derived nanocomposites are reported due to the difficulty in morphology control. More efforts need to be dedicated to the synthesis and in-depth investigation of MOF derived composites with optimal semiconducting and catalytic properties to achieve viable highly efficient photocatalysts for H₂ evolution.

2.6 MOF derived nanocomposites for photodegradation of pollutants

The presence of alarmingly high amounts of toxic industrial organic pollutants is one of the greatest challenges to our environment and society. MOF derived

composites have widely been explored for the photodegradation of organic pollutants such as textile dyes, pharmaceutical contaminants, phenols and antibiotics.^{101, 122, 158, 159} The MOF derived composites with surface-functionalised porous carbons offer a high SSA and pore volume with appropriate pore size for the adsorption of pollutant molecules. The adsorbed pollutant molecules are simultaneously photodegraded into H₂O and CO₂ by the metal oxides, sulphides or phosphides with optimised EBGs embedded in the MOF derived porous carbon matrix.⁵¹ In 2010 Yang *et al.* reported that 3D cubic ZnO@C composite, which was derived from MOF-5 under N₂ atmosphere at 600 °C, exhibited BET surface area of > 500 m² g⁻¹ and demonstrated higher adsorption and photocatalytic degradation of Rhodamine-B (RhB) under UV irradiation.⁸⁰ Since then, efforts have been made to produce MOF derived nanocomposites with a variety of morphologies for photodegradation of industrial and organic pollutants. These nanocomposites can be decorated with hydrophilic/hydrophobic functional groups and doped with heteroatoms (metals and/or non-metals) to achieve the desired properties. Moreover, complicated nanocomposites including multi-metallic oxides, sulphides and phosphides embedded in in-situ formed porous carbon matrix can be generated from selected MOFs or MOF-based composites.^{93, 101, 144} In the following section, the relationship of morphologies between MOF precursors and the derived nanocomposites for photodegradation of organic pollutants are presented. Moreover, the effects of the physicochemical properties of these derived nanocomposites on their photocatalytic applications are also analysed and summarised.

2.6.1 0D nanocomposites

2.6.1.1 Polyhedra

It is highly desirable to find materials that can not only show high adsorption capacities but also simultaneously photodegrade the adsorbed species into neutral products with high efficiency. Zhang *et al.* reported that MIL-53(Fe) derived γ -Fe₂O₃/C nanoparticles with polyhedral morphologies possessing a surface area of 397 m² g⁻¹ were more efficient for dye adsorption and photodegradation (863 mg g⁻¹) in the presence of a scavenger H₂O₂.¹⁶⁰ Other magnetic nanocomposites such as Co/CoO nanoparticles embedded in the nanoporous carbon (NPC) matrix with rhombic dodecahedral morphology can be derived from one-step direct carbonisation of ZIF-67 under N₂ at 800 °C.¹²² The

highly crystalline Co/CoO nanoparticles are spatially distributed in the NPC matrix with a high BET surface area of $345 \text{ m}^2 \text{ g}^{-1}$ and open network of micro/mesopores which facilitate the fast diffusion of organic pollutant methylene blue (MB) molecules. However, despite the strong magnetic response and high adsorption capabilities (500 mg g^{-1}) of MB molecules due to the π - π interaction between the MB molecules and the graphitic carbon, the photodegradation performance of this materials tends to be poor.¹²² Though FeO_x and CoO_x nanoparticles are easy to collect after the completion of photocatalytic reactions due to their magnetic properties, their photo-response is generally poor compared to the ZnO and TiO_2 semiconducting nanoparticles.

The direct carbonisation of MOFs with polyhedral morphologies (such as MOF-5, ZIF-8, and ZIF-67) in the inert gas atmosphere above $500 \text{ }^\circ\text{C}$ results in metal or metal oxide/carbon composites. The morphologies and particle sizes of the MOF precursors can be tuned by the selection of synthesis method and the reaction conditions such as molar ratio and concentration of the reactants, type of solvents, synthesis temperatures and duration of the reaction.^{44, 53} These multi-edge and multi-facet composites offer numerous accessible catalytic active sites and interconnected open pores with tunable pore diameters. Zhang *et al.* reported octahedral porous ZnO@C nanocomposites (with the EBG of 2.92 eV) derived from MOF-5 at different carbonisation temperatures for photocatalytic degradation of RhB under visible light.¹⁶¹ However, pure ZnO and TiO_2 semiconducting nanoparticles show limited photocatalytic performance due to their relatively large EBGs ($> 3.2 \text{ eV}$). To overcome this limitation, the presence of heteroatoms such as C, N, S and P (either self-doped or introduced as a guest species) in the MOF derived nanocomposites can narrow the EBGs and enhance the visible light absorption capability. Liang *et al.* have reported the fabrication of C/N co-doped ZnO nanoparticles with a narrowed EBG of 2.98 eV embedded in porous carbon matrix by a two-step thermal conversion of ZIF-8 (N-rich and Zn-containing) at $600 \text{ }^\circ\text{C}$.⁹³ These polyhedral ZnO/porous carbon composite show superior MB adsorption and photodegradation capacity under the simulated sunlight due to the higher number of active sites, N/C dopants and oxygen vacancies. Also, the presence of hydrophilic functional groups attached to the surface of the carbon matrix can further enhance the adsorption of MB on the carbon matrix. Further, the carboxylate functional groups ($-\text{COOH}/-\text{OH}$) can be

easily introduced by carbonising MOFs in a controlled water vapour atmosphere at higher temperatures. For instance, the carbonisation of ZIF-8 at 800 °C under water vapour as mild oxidising agent results in the atomically homogeneous distribution of N doped ZnO nanoparticles embedded in -COOH functionalised porous carbon matrix with roughly rhombic dodecahedron morphology. The resulting ZnO/C nanocomposite with high BET surface area (up to 995 m² g⁻¹), large pore volume (up to 0.58 cm³ g⁻¹) and excessive oxygen-containing hydrophilic functional groups exhibit stronger interaction between the porous carbon and the MB molecules and facilitates the simultaneous adsorption and photodegradation of MB under visible light.¹⁰¹

A variety of doped metal oxides embedded in polyhedral carbon matrix can be derived from MOFs. For example, octahedral P doped Cu₂O/C composite can be prepared by pyrolysis of the modified HKUST-1 at a moderate temperature of 300 °C. This nanocomposite shows the relatively narrow EBG (2.04 eV) and exposed active sites present in the porous carbon matrix and exhibits superior photodegradation of phenol under visible light irradiation due to the better sunlight absorption capability.¹⁵⁹ Among the other semiconductors with a narrow EBG, CdS is a prominent photocatalyst with a bandgap of 2.4 eV. However, the easy agglomeration and fast charge recombination of CdS nanoparticles restrict their photocatalytic activity. This issue can be tackled by using MOF as a sacrificial template to produce CdS/Carbon composites with uniformly dispersed CdS nanoparticles by the high-temperature carbonisation. As shown in Figure 2.6, first, polyhedral ZIF-8 precursor was employed to derive N-rich mesoporous carbon (MPC) with a large surface area of 933 m² g⁻¹ and pore volume of 0.64 cm³ g⁻¹. Then optimised CdS/MPC composites were obtained by loading different wt.% of CdS for photodegradation of antibiotics and other pharmaceutical contaminants.¹⁵⁸ Compared to the composite obtained by the conventional physically mixed method, this MOF derived composite offers the better distribution of semiconducting nanomaterials in carbon matrix preventing

agglomerations, reduced charge recombination and enhanced adsorption and photodegradation capability.

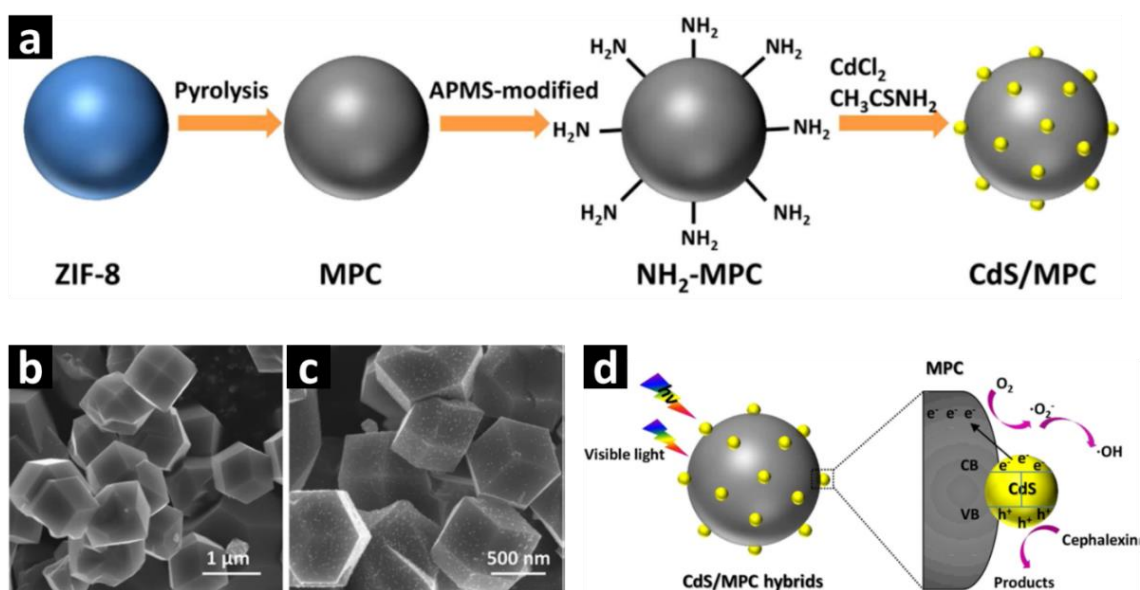


Figure 2.6 (a) Schematic drawing of the synthesis process of the CdS/MPC nanocomposites (b) SEM images of ZIF-8 precursor (c) SEM of ZIF-8 derived 20 wt.% CdS/MPC nanocomposite and (d) Schematic illustration of the photocatalytic mechanism over the CdS/MPC nanocomposite.¹⁵⁸

2.6.1.2 Self-templated core-shell nanostructures

The core-shell nanocomposites offer synergistic effects between the core and the shell components of the nanocomposites with enhanced structural stability, tunable functionalities and good dispersibility, consequently improved photodegradation performance. The core-shell nanostructures can be usually derived from the pre-designed bimetallic self-templated MOF precursors. For example, one-step direct carbonisation of the as-synthesised Fe₃O₄@HKUST-1 in N₂ at 500 °C can readily transform the bimetallic MOF precursor into Fe₃O₄ core encapsulated in the carbon shell (~50 nm thick) decorated with Cu nanoparticles. The thickness and porosity of the carbon shell around the metal oxide core can be easily tuned by controlling the pyrolysis conditions. This MOF derived Fe₃O₄@C/Cu core-shell nanostructure shows good absorption of visible light due to the narrow EBG of 1.97 eV. Moreover, the magnetic response of the Fe₃O₄ core makes these core-shell nanocomposites easy to collect after the photocatalytic reaction. Though this Fe₃O₄@C/Cu core-shell nanocomposite outperforms the commercial TiO₂ and g-C₃N₄ in photodegradation of MB, H₂O₂

needs to be added to enhance the production of active oxygen species for the photodegradation of MB.¹⁰⁸ To overcome the limitations of low photocatalytic performance of Fe₃O₄@C/Cu core-shell nanostructure, Ti or Zn based MOF precursor can be employed to form metal oxide core. Using self-templated precursor, bimetallic Zn/Co-MOF composite with Zn-ZIF-8 as the shell and Co-ZIF-67 as the core, ZnO@C-N-Co core-shell nanocomposite was synthesised by the direct pyrolysis of the as-prepared Zn/Co-ZIF at 600 °C for 2 hours under argon atmosphere. The time-dependent pyrolysis observed by TEM shown in Figure 2.7 reveals that Zn²⁺ in the ZIF-8 shell is converted into ZnO nanoparticles (NPs) which are uniformly distributed in the amorphous carbon shell within the first 10 minutes of the pyrolysis. With the progression of pyrolysis, ZnO NPs left the mesoporous carbon shell, migrated to the hollow interior cavity and aggregated to produce larger ZnO particles, whereas Co ions were in-situ reduced to Co NPs by the formed carbon and migrated inversely from the hollow interior to the ligand-derived N doped graphitised carbon shell. The highly synergistic effect between the robust ZnO core and the C-N-Co shell in the derived ZnO@C-N-Co core-shell nanocomposite demonstrates remarkable photocatalytic degradation of methylene orange. Moreover, the uniform distribution of Co NPs on the mesoporous C shell facilitates easy separation of photocatalysts by using an external magnet.¹²³ Based on this work, various core-shell multi-metal oxide/carbon composites can be expected to be produced via the pyrolysis of rationally designed self-templated hollow MOF precursors.

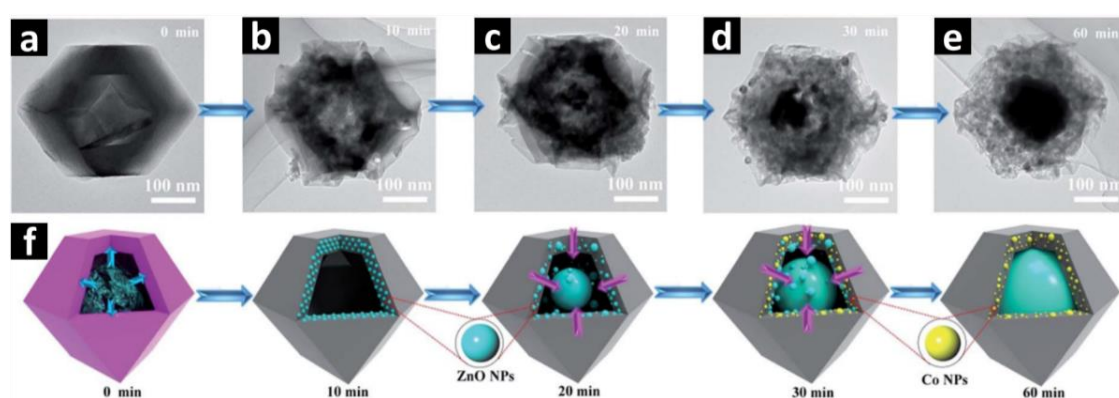


Figure 2.7 (a-e) TEM images of the thermal transformation of Zn/Co-ZIF into ZnO@C-N-Co nanocomposites at different carbonisation times and (f) Schematic representation of the formation of the core-shell ZnO@C-N-Co.¹²³

2.6.1.3 External-templated core-shell nanostructures

It is a persisting challenge to achieve scalable production of MOF derived core-shell nanocomposites with morphological uniformity and high efficiency. Preparation of core-shell nanostructures obtained by one-step direct pyrolysis of self-templated MOF works only for a few MOF precursors. Most importantly, it remains a great challenge to precisely control the thickness and reproducible porosities of the MOF derived carbon shells. An alternative approach such as external-templated MOF derived nanocomposites may offer the solutions to this problem. For example, ZIF-8 was first grown on the surface of reduced graphene oxides (rGO), followed by the calcination of the as-synthesised ZIF-8/rGO in the air at 500 °C. The ZIF-8 precursor decomposed at above 400 °C in the air to release C and N species in the form of CO₂ and NO₂ and left behind the ZnO nanoparticles encapsulated in the rGO shell of less than 10 nm thickness. The thickness of the rGO shell and wt.% of ZnO/rGO was optimised by tuning the ratios of ZIF-8 and rGO precursors. These external-templated-MOF derived composites showed good photocatalytic activity for the degradation of contaminant Orange II under simulated sunlight irradiation. The rGO shell traps the photogenerated electrons and enhances the conductivity of the composite, resulting in reduced charge recombination and consequently improved photodegradation activity.¹²⁵ Compared to the self-templated MOF derived core-shell structures, in general, these external-templated metal oxide/rGO core-shell structures offer a lower SSA that limits their adsorption capacities. So far, there are only a few studies published on MOF derived core-shell nanostructures for photocatalytic applications.^{108, 123, 125} More investigations need to find new combinations of MOF derived core-shell nanostructures with a high surface area that contains not only metal oxides but also other metal compounds such as metal sulphides and metal phosphides.

2.6.2 1D nanocomposites

2.6.2.1 Nanorods

The 1D nanocomposite with nanorod morphology can be synthesised by employing self-templated Fe-MOF precursor. For example, MIL-88A can be carbonised at 600 °C under N₂ atmosphere to derive Fe₂O₃ nanoparticles uniformly distributed in a rod-like porous carbon matrix, making it magnetic porous adsorbent for decolourisation of RhB dye from wastewater. Though Fe₂O₃

nanoparticles make this composite easily collectable due to the magnetic property, their photo-response is not as good as semiconducting ZnO or TiO₂ nanoparticles. It is necessary to add additional oxidants such as peroxides and/or persulfates with the magnetic Fe₂O₃/C photocatalyst to generate a combined catalytic effect for photodegradation of the RhB under UV light.¹²⁴ Despite the limitation, this nanocomposite shows structural stability and good recyclability to remove RhB from wastewater.

Apart from metal oxide/C composites, it is important to explore new efficient visible-light photocatalysts. In this respect, cadmium sulphide (CdS) can be a suitable photocatalyst owing to its narrow EBG (2.4 eV) that guarantees photoactivity under visible light irradiation. However, CdS based semiconductors are prone to photocorrosion in the aqueous medium, which leads to the potential release of toxic Cd²⁺ ions. This issue can be tackled by combining the CdS semiconductor particles with carbon materials which function not only as stable support to effectively distribute the CdS particles but also offering higher surface area for the adsorption of the contaminants. Self-templated Cd-MOF can be an excellent precursor for the in-situ derivation of N doped carbon-supported CdS nanocomposites with nanorod morphologies for visible-light-driven photodegradation of antibiotics. Recently, Cao *et al.* reported CdS/NC nanorods derived from direct carbonisation of Cd-MOF at different temperatures (400-700 °C) under an inert atmosphere. They demonstrated that CdS/NC derived at 500 °C showed the highest photodegradation (83 %) of Tetracycline (TC) antibiotic in 1 hour under visible light. The improved performance of photodegradation of TC was ascribed to the efficient transportation of photogenerated charge (e⁻/h⁺) carriers due to the enhanced interfacial interactions of CdS nanoparticles uniformly distributed in the N doped carbon matrix.¹⁶²

2.6.2.2 Nanotubes

A very few studies are available on self-templated MOF precursor derived 1D hollow nanocomposites with well-defined morphologies for photocatalytic applications. One of the main challenges in MOF derived composites is to strictly produce tailored porosities and atomic ratios of metals, metal oxides and functionalised porous carbon components.⁴² If the distribution of metal or metal oxide nanoparticles in porous carbon matrix is optimised, the obtained nanocomposites can exhibit exceptionally high photocatalytic performance due

to the improved photoinduced electric charge generation and the efficient photoelectrochemical reactions. For example, TiO₂ coated MIL-88(Fe) precursor with nanorod morphology has been directly carbonised at 600 °C under N₂ atmosphere for a few hours to obtain respective hollow ternary TiO₂@C/FeTiO₃ nanocomposites with different Ti/Fe molar ratios. These one-step MOF derived novel bimetallic nanocomposites possess hollow nanotube morphology, in which the TiO₂ layer was deposited onto the surface of FeTiO₃, embedded in an inner porous carbon layer. Such bimetal oxide/carbon hollow nanostructures can maximise the sunlight absorption for efficient photoelectrochemical degradation of phenol. Wang *et al.* demonstrated in Figure 2.8 that the wall thickness of the TiO₂ layer (20 to 25 nm) can be tuned by adjusting the molar ratio of Fe and Ti species between 15 to 25 %. This self-templated multi-metallic MOF precursor strategy offers the flexibility to regulate the structural, textural and morphological features related to their photocatalytic properties. The photoelectrochemical efficiency is improved due to the synergistic effects between the middle conductive layer, suitable EBGs, full-spectrum light absorption and electro-oxidation assisted photocatalysis.¹⁶³

2.6.2.3 Nanoshuttles

Photocatalytically active 1D metal oxide/C nanocomposites can be prepared by physical and chemical mixing of metal oxides with carbonaceous matrix (e.g. carbon nanotubes, rGO, or graphene nanosheets).^{164, 165} Self-templated MOF precursors can offer the flexibility of a “two-for-one” approach to directly carbonise the as-synthesised MOFs to yield 1D metal oxide/carbon nanocomposites with high surface area and accessible chemically reactive sites. Recently, Pang *et al.* reported the successful synthesis of α -Fe₂O₃/C nanoshuttles via direct pyrolysis of the self-templated Fe-MIL-88B precursor at 550 °C for 2 hours in argon. Upon carbonisation, the hexagonal prism (with a truncated hexagonal cone at each end) shaped Fe-MIL-88B crystals with an average size of 1.8 μ m were transformed into shuttle-like α -Fe₂O₃/C nanocomposite with mesoporosity and uniform elemental distribution. These α -Fe₂O₃/C nanoshuttles demonstrated superior photocatalytic activity towards the photodegradation of MB under simulated sunlight, due to the effective separation and fast migration of

photogenerated charges on α -Fe₂O₃ as well as the relatively large number of exposed chemical reaction active sites on the mesoporous carbon matrix.¹⁶⁶

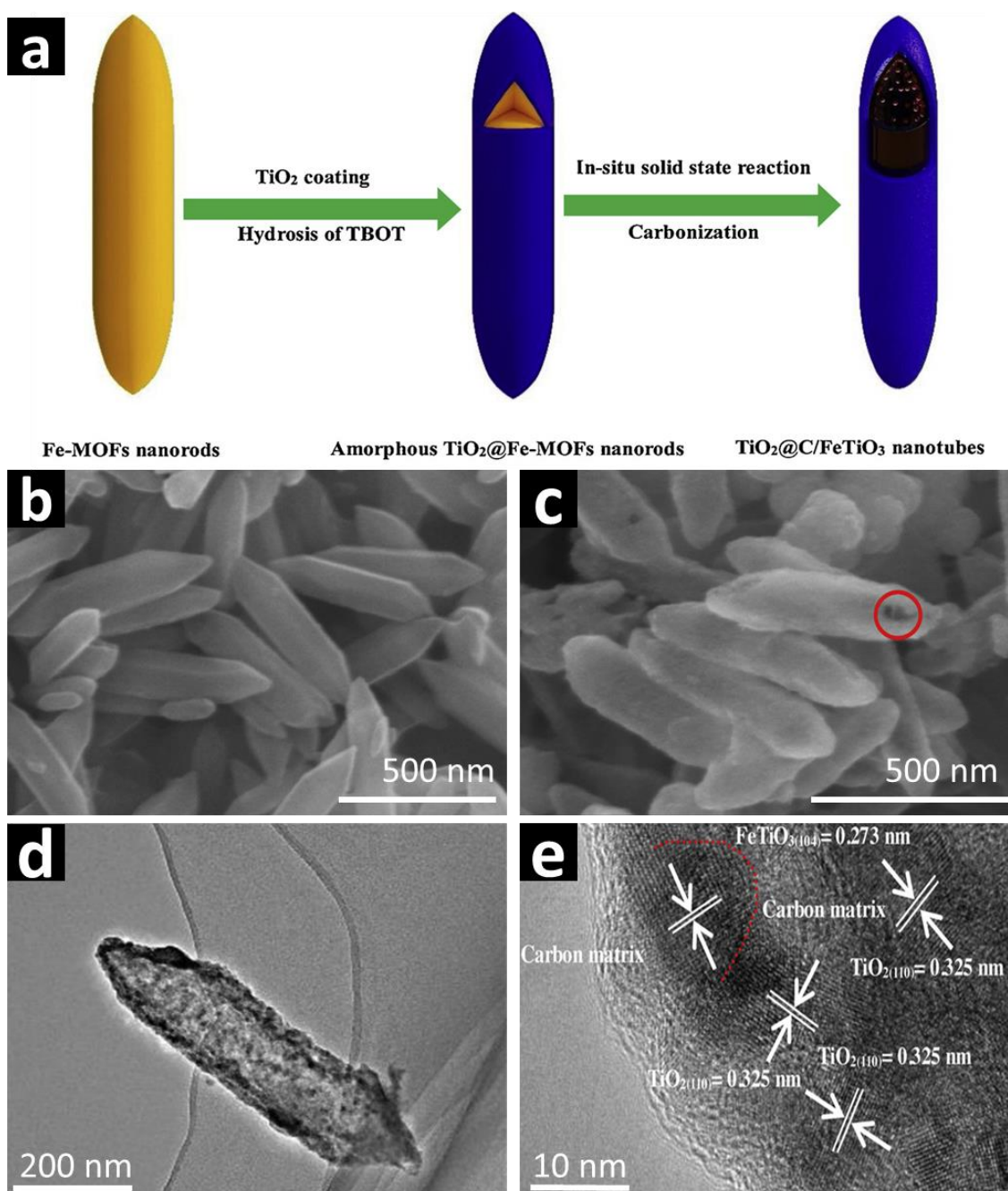


Figure 2.8 (a) Schematic diagram of the carbonisation process of hollow TiO₂@C/FeTiO₃ nanotubes (b) FESEM image of Fe-MOF precursor (c) TCF-25% nanotubes and (d) TEM images of TCF 20%.¹⁶³

Currently, self-templated MOF derived nanocomposites are dominantly reported in the literature for photodegradation applications. Using external-templated methods, rationally designed new 1D MOF structures with well-

controlled morphologies could be synthesised to derive 1D nanocomposites for highly efficient and stable photocatalysts for photodegradation of organic and industrial pollutants.

2.6.3 2D nanocomposites

2.6.3.1 Nanoplatelets

Recently, Lin *et al.* reported that a square-shaped 2D Cu-MOF precursor with lateral dimensions of 4-6 μm and average thickness of 80 nm was prepared through a classic solvothermal treatment of metal node $\text{Cu}(\text{NO}_3)_2$, organic ligand 4,4'-bipyridine and surfactant polyvinyl pyrrolidone (PVP) in ethanol under 100 $^\circ\text{C}$. The PVP acted as an "inhibitor" preventing the layer stacking growth and directing the coordination of Cu metal nodes with the linear ligand 4,4'-bipyridine.¹⁶⁷ Controlling the pyrolysis conditions such as temperature and gas atmosphere is critical to deriving the $\text{Cu}_2\text{O}/\text{C}$ composite with the 2D morphology and high SSA. When the Cu-MOF precursor decomposed at higher temperatures (above 500 $^\circ\text{C}$) under argon, Cu species transformed into Cu^0 and diffused to the surface of the carbon matrix. At relatively lower temperature (below 300 $^\circ\text{C}$) under argon, the 2D morphologies of the MOF precursor can be retained. The BET surface area of the 2D MOF precursor and the derived $\text{Cu}_2\text{O}/\text{C}$ square nanoplatelets is 7.4 and 109.5 $\text{m}^2 \text{g}^{-1}$ respectively. The interesting 15-fold increase in BET surface area with preserved square-like nanoplatelet morphology was attributed to the flexibility of the carbon matrix with slit-like pores. These 2D $\text{Cu}_2\text{O}/\text{C}$ square nanoplatelets showed superior photodegradation rate (2.5 $\text{mg min}^{-1} \text{g}_{\text{cat}}^{-1}$) of methylene orange (MO) under visible light compared to other $\text{Cu}_2\text{O}/\text{C}$ based photocatalysts.¹⁶⁷ So far, only a few self-templated 2D MOF derived metal oxide/carbon composites have been reported due to the challenges of controlling the morphologies of the self-assembled MOF precursors. To overcome this challenge, 2D external templates such as carbon structures can be used to direct the growth of MOF precursors.

2.6.3.2 External-templated nanosheets

In an early attempt, MOF derived metal oxides (ZnO) were combined with rGO by the microwave-assisted method to generate the synergic effect between the ZnO nanoparticle with semiconducting property and the rGO with high light absorption property for photodegradation of MB.¹⁴³ Though this ZnO/rGO nanosheet showed improved photodegradation performance compared to

pristine ZnO, it is challenging to obtain homogeneous loading of ZnO on rGO nanosheets. The 2D nanostructures such as graphene, graphene oxide (GO) or reduced graphene oxide (rGO) can be employed as an external template to grow MOFs, and the resulting MOF/2D carbon nanostructures possess combined properties of the porous MOF and the conductive external template. For example, Zn-Co-ZIF can be directly grown on GO assisted by PVP as a capping agent. As shown in Figure 2.9, rhombic dodecahedron shaped Zn-Co-ZIF crystals (~150 nm) are uniformly dispersed on exfoliated rGO wrinkled nanosheets. Heat treatment of this bimetallic rGO/ZnCo-ZIF precursor at 300 °C in air for 3 hours transforms it into rGO@ZnCo₂O₄ (GZC-300) 2D nanosheets with the inherited morphology. This well-preserved N doped bimetal oxide 2D nanocomposite with BET surface area of 892 m² g⁻¹ and high electrical conductivity proves to be excellent photocatalyst for NO oxidation with the conversion of 92.6 % under sunlight.¹⁴⁴

Semiconducting heterojunctions exhibit higher photocatalytic activities because the spatial distribution of photogenerated holes and electrons reduces the charge recombination, which results in improved charge separation and transfer, consequently enhanced photocatalytic performances. For example, 2D g-C₃N₄/TiO₂ nanosheets prepared by in-situ calcination of the mixture of as-prepared Ti-MOF, MIL-125 (Ti) ground with melamine powder at 500 °C under air atmosphere. The 2D g-C₃N₄/TiO₂ nanosheets with TiO₂ nanoparticles embedded in 8 wt.% g-C₃N₄ exhibit BET surface area of 177.3 m² g⁻¹ and enhanced photodegradation of MB under visible light. The valence and conduction band edges of the TiO₂ nanoparticles and the g-C₃N₄ nanosheets are positioned at such energies that they form direct Z-scheme heterojunctions which spatially separate the oxidation sites on TiO₂ and the reduction sites on g-C₃N₄, suppressing the charge recombination.¹⁴⁵ From the above mentioned few examples, it can be seen that it is challenging to prepare MOF derived 2D nanocomposites due to the difficulties to achieve the uniform growth of MOF with a controllable thickness on the 2D external templates. The rationally designed transition metal nodes and organic linkers can form a variety of simple 2D MOF precursors with a high density of uniformly distributed exposed catalytic active sites. Moreover, a variety of MOFs can be grown on other than carbon 2D

external templates to further explore the structures-application relationships of the resulting 2D composites.

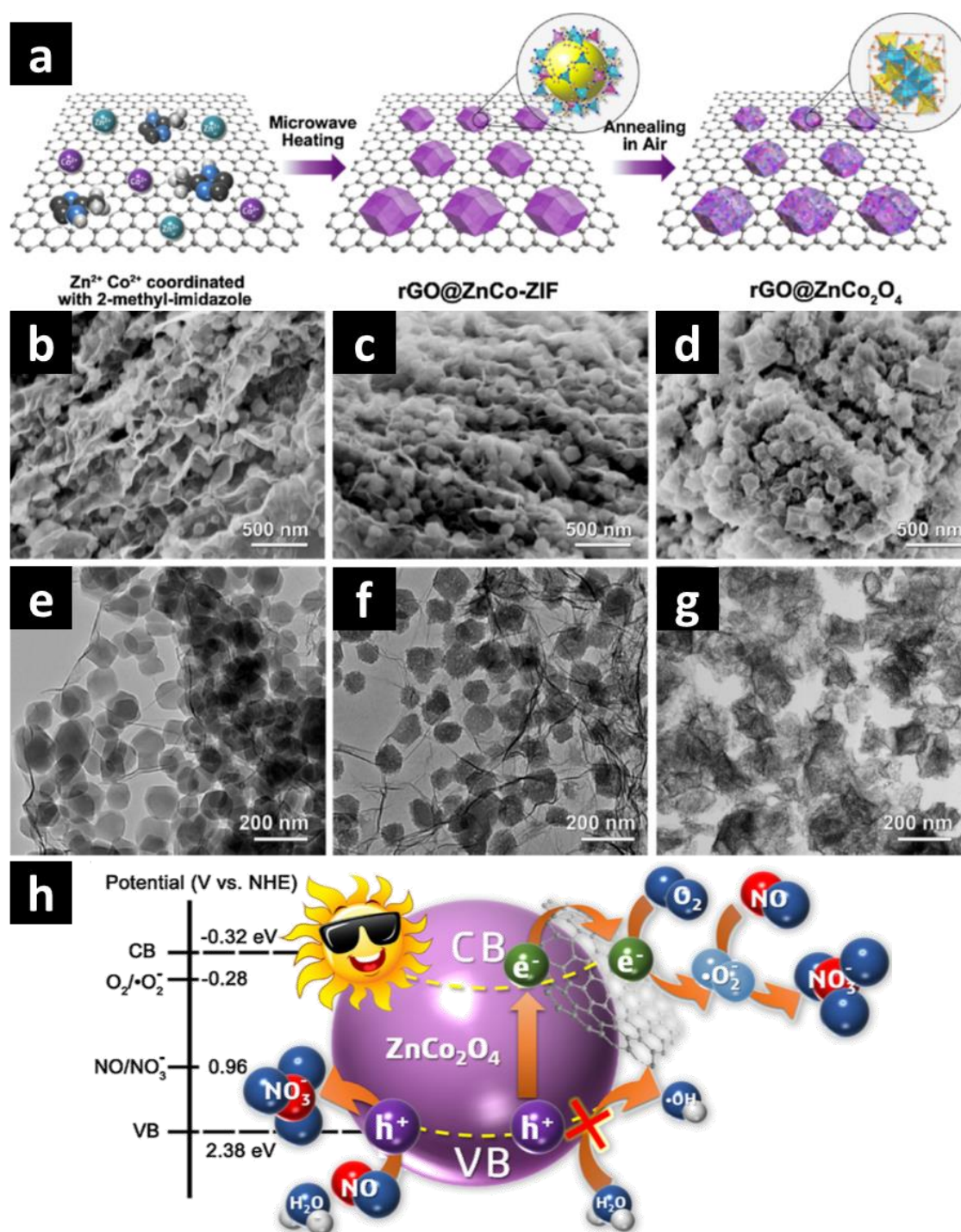


Figure 2.9 (a) Schematic diagram of the formation of the $rGO@ZnCo_2O_4$. SEM images of (b) $rGO-ZnCo-ZIF$ precursor (c) nanocomposite GZC-300 and (d) GZC-500. TEM images of (e) $rGO-ZnCo-ZIF$ precursor (f) GZC-300 and (g) GZC-500. (h) Cartoon of the photocatalytic mechanism of NO oxidation by GZC-300 under the visible-light.¹⁴⁴

2.6.4 3D nanocomposites

2.6.4.1 Nanocubes

Almost a decade ago, in one of the early efforts, direct carbonisation of as-prepared cubic MOF-5 precursor in an inert atmosphere at 600 °C resulted in a well-defined cubic ZnO/C nanocomposite with BET surface area of 576 m² g⁻¹. This self-templated MOF derived ZnO/C nanocomposite showed exceptionally high adsorption and photodegradation of RhB due to the π-π interactions between the MOF derived graphitic carbon layer with sp² bonding and the aromatic rings of the organic dye molecules.⁸⁰ Such an attempt to pyrolyse MOFs offered the opportunities to understand these porous coordination polymers as sacrificial templates for the formation of 3D porous nanocomposites.⁸⁰ A variety of cubic MOFs precursors can be synthesised by rationally designed synthesis experiments and optimising the experimental parameters.

2.6.4.2 Nanodiscs

Simple one-step pyrolysis of self-templated MOF, MIL-125 precursor at high temperature in an inert atmosphere can result in the formation of highly stable 3D disc-like TiO_x/C composites.¹⁶⁸ By controlling the pyrolysis temperature, the crystallinity and polymorphic phase ratios (anatase/rutile/brookite) of MOF derived TiO₂ nanoparticles can be tailored. In MIL-125 derived composite, TiO₂ of anatase phase forms at pyrolysis temperatures below 600 °C, whereas rutile phase emerges at pyrolysis temperature above 600 °C. However, at 1000 °C, Ti₃O₅ forms, which is embedded in a porous carbon matrix with a BET surface area of 329 m² g⁻¹. The high surface area and conductive carbon matrix make this nanocomposite an excellent photocatalyst for dye degradation.¹⁶⁸ Although TiO₂ is one of the most promising semiconducting materials, the large EBG limits its potential to be directly used as a photocatalyst in the visible light range. Further investigations are necessary to optimise the pyrolysis conditions to tailor the textural properties, polymorph structures and elemental doping with N, C of TiO_x/C nanocomposites through the rationally selected functional MOF precursors.

2.6.4.3 External-templated 3D nanocages and nanosponges

The generation of 3D nanocomposites is not limited to self-templated MOF precursor approach. The external-templated MOF hybrid precursor method opens a door of opportunities to fabricate a large variety of 3D nanocomposites

such as nanofoams, nanocages, nanosponges and graphitised carbon cloths.^{40, 42, 90, 169} Rationally designed external-templated MOF hybrid precursors offer relatively easy ways to engineer the physicochemical properties of the derived nanocomposites. For example, ZIF-8 can be grown on a porous three-dimensional graphene network (3DGN) in a methanolic solution at room temperature. Heat treatment of this external-templated ZIF-8/3DGN in argon followed by annealing in air below 400 °C can produce ZnO coated 3DGN composite (ZnO/3DGN).¹⁷⁰ Benefitting from the 3D porous graphene network as a backbone, this nanocomposite show good structural stability. The photocatalytic performance is improved due to the better charge conductivity of 3DGN as well as the high surface area of the ZnO/3DGN composites. The effective interfacial contact between the MOF derived ZnO nanoparticles and the 3DGN can minimise the recombination of the photoinduced holes and electrons during the photocatalytic process.

Usually, the MOF derived composites are in the form of powder, which in some cases do not conform to the practical requirements due to their poor dispersibility in certain solutions. The external-templated MOF precursors approach can be advantageous to fabricate MOF derived nanocomposites with porous metal oxides uniformly loaded on the surfaces of reduced graphene oxide (rGO) which is coated on the carbon sponge frameworks. Such monolithic microreactor-like 3D nanostructures offer higher structural stability and good opportunities in morphological control. For example, ZnO nanocages decorated on rGO coated 3D carbon sponge (ZnO/rGO/Carbon sponge) has been obtained from direct calcination of dip-coated ZIF-8 on graphene oxide coated melamine foam at 350 °C. Figure 2.10 shows the schematic diagram of the fabrication process of ZnO_{ZIF-8}/rGO/Carbon sponge. This external-templated N/C co-doped ZnO decorated 3D nanosponge microreactor proved to be effective for both photodegradation of organic pollutants and photocatalytic hydrogen evolution under simulated sunlight. Such 3D nanocomposite can offer high structural stability as well as multiple functionalities as absorbent and photocatalyst.¹⁶⁹ Some self-templated and external-templated MOF derived nanocomposites as photocatalysts for photodegradation of organic pollutants or dyes are summarised and presented in Table 2.2.

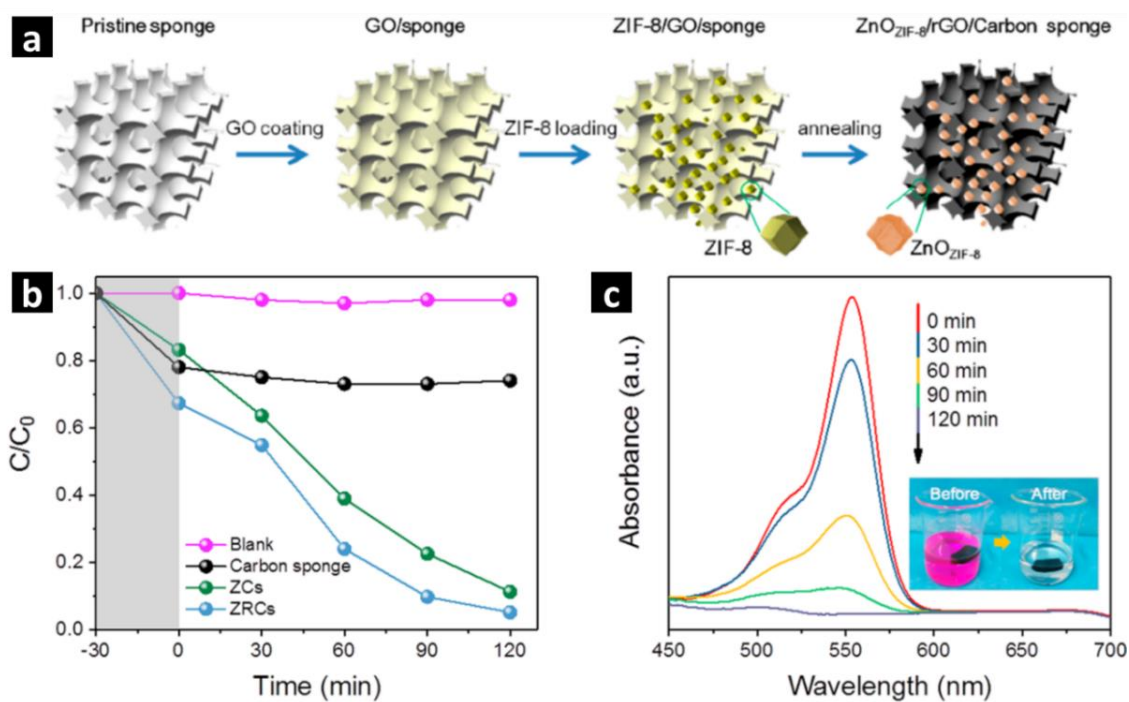


Figure 2.10 (a) Schematic diagram of the formation process of ZnO_{ZIF-8}/rGO/Carbon sponge (b) Photodegradation of RhB under UV-Visible light irradiation (c) Change in intensity of absorption peak of RhB with the progression of time during photocatalysis (inset shows the change in colour of RhB dye before and after complete photodegradation).¹⁶⁹

Table 2.2 Comparison of selected MOF derived nanocomposites for photodegradation of organic pollutants.

MOF precursor	Catalyst	Morphology	Pollutant	Experimental conditions		Degradation efficiency	Ref.
				Amount and concentration of Pollutant	Light source and exposure time		
MIL-53(Fe)	γ -Fe ₂ O ₃ /C	Polyhedral	MG with H ₂ O ₂	5 mL (500 mg L ⁻¹)	Sunlight 3 hr	100 %	160
ZIF-8	ZnO/N-C	Rhombic dodecahedron	MB	100 mL (20 mg L ⁻¹)	> 420 nm 200 W 4 hr	99 %	101
ZIF-8	C-N-ZnO	Rhombic dodecahedron	MB	1000 mL (10 mg L ⁻¹)	Simulated solar light 2,5 hr	100 %	93

ZIF-8/CdS	CdS/MPC	Polyhedron	Antibiotics CPX	100 mL (20 mg L ⁻¹)	> 420 nm 300 W Xe lamp 1.5 hr	90.5 %	158
MOF-5	C@ZnO	Octahedral	RhB	100 mL	> 420 nm 350 W Xe lamp 3.5 hr	~ 90 %	161
HKUST-1-P	P-C/Cu ₂ O	Octahedral	Phenol	10 mL (40 mg L ⁻¹)	> 420 nm 350 W Xe lamp 1.5 hr	99.8 %	159
MOF-5	ZnO@C	Cubic	RhB	24 mg L ⁻¹	UV light 12 hr	98 %	80
Fe ₃ O ₄ @HKU ST-1	Fe ₃ O ₄ @C/Cu	Core/shell	MB with H ₂ O ₂	100 mL (20 mg L ⁻¹)	> 420 nm 500 W Xe lamp 2.5 hr	100 %	108
Zn/Co-ZIF	ZnO@C-N-Co	Core/shell	MO	50 mL (16.5 mg L ⁻¹)	UV light 300 W Xe lamp 2.5 hr	99.5 %	123
ZIF-8/rGO	ZnO/rGO	Core/shell	Orange II	40 mL (10 mg L ⁻¹)	Simulated solar light 5 hr	100 %	125
ZIF-67/GO	Co-G	Nanosheet	AY and PMS	500 mL (100 mg L ⁻¹)	UV light 2 hr	~ 80 %	171
Cd-MOF	CdS/N-C	Nanorod	Antibiotics TC	100 mL (40 mg L ⁻¹)	> 420 nm 300 W Xe lamp 1 hr	83 %	162
MIL-88A	Fe ₂ O ₃ /C	Nanorod	RhB with peroxide and persulfate	500 mL (10 mg L ⁻¹)	UV light 1.5 hr	~90 %	124
MIL-88-Fe	TiO ₂ @C/FeTiO ₃	Nanotube	Phenol	(5 mg L ⁻¹)	Simulated solar light 500 W Xe lamp 3 hr	80 %	163
ZnCo-ZIF	rGO@ZnCo ₂ O ₄	Nanosheet	NO oxidisation	Gas phase 10.8 L continuous flow	Solar light 300 W halogen lamp 1 hr	92.6 %	144

ZIF-8/GO/ Melamine foam	ZnO/rGO/C	3D Sponge	RhB	100 mL (10 mg L ⁻¹)	Simulated solar light 300 W Xe lamp 2 hr	99 %	169
Cu-MOF	N-Cu ₂ O/C	2D Nanoplatelets	MO	50 mL (50 mg L ⁻¹)	> 430 nm 300 W Xe lamp 3 hr	90 %	167

2.6.5 Summary of MOF derived nanocomposites for photodegradation of pollutants

MOF derived nanocomposites with diverse dimensions and a large variety of morphologies with in-situ tunable properties can be derived from MOF precursors via either self-templated or external-templated methods. The morphology of the derived nanocomposites primarily depends upon the morphology of the MOF used as a precursor and/or sacrificial template. These derived composites offer great symbiotic relationships between different structural, textural, physicochemical and semiconducting properties for excellent photocatalytic applications. As summarised in Table 2.2, some transition metals such as Zn, Ti, Fe, Cu, Cd based-MOF derived composites have been reported for the photodegradation of organic dyes, industrial waste chemicals and pharmaceutical contaminants. Nevertheless, more detailed and in-depth investigations need to be carried out to explore new types of MOF derived nanostructures such as multi-layered core/shells, 2D single/multi-layered optimised nanosheets and novel 3D morphologies that are from not only metal oxides but also other metal compounds such as metal sulphides and metal phosphides. Moreover, the formation of MOF derived complex nanostructures needs to be further investigated by controlling the molar/atomic ratios of the (multi)metal compositions and modifying the in-situ formed porous carbons to fully understand and enhance the structural stability as well as their photodegradation efficiencies.

Chapter 3

Experimental methodologies

3.1 Introduction

This chapter presents the experimental methodologies and procedures which were followed in this work for the synthesis of Zn-MOFs and Ti-MOFs, loading of Cu species into the Ti-MOF and the derivation of nanocomposites. The main characterisation techniques and instruments used for the analysis of the prepared materials are discussed. Moreover, the application methods such as photodegradation of organic dye MB and the photocatalytic hydrogen (H₂) evolution from water splitting are also described.

3.2 Synthesis of MOF precursors

All chemicals including Zn(NO₃)₂·6H₂O, Ti(OBu)₄, Cu(NO₃)₂·3H₂O, terephthalic acid, 2-aminoterephthalic acid, 2,5-dihydroxyterephthalic acid, triethylamine, 2-methylimidazole, dimethylformamide, chloroform, ethanol and methanol were purchased from Sigma-Aldrich and used without further purification.

3.2.1 Synthesis of MOF-5

MOF-5 was synthesised at room temperature by following a slightly modified scheme which was first reported by Yaghi *et al.*³³ Typically, 48 mmol of Zn(NO₃)₂·6H₂O and 24 mmol of terephthalic acid (H₂BDC) (molar ratio of 2:1) combined with 19 mL of triethylamine (TEA) was dissolved in 450 mL of dimethylformamide (DMF) in a 500 mL screw jar. The mixed solution was constantly stirred at room temperature for 20 hours. Then the white product was collected by centrifugation and washed twice with DMF to remove the undissolved species. The collected white powder was further washed with chloroform twice and then immersed in chloroform overnight. The obtained product was collected by centrifugation and dried in a vacuum oven at 70 °C overnight.

3.2.2 Synthesis of MOF-74

The MOF-74 was prepared as follows: with a 3:1 molar ratio, 39 mmol of Zn(NO₃)₂·6H₂O and 13 mmol of 2,5-dihydroxyterephthalic acid (H₄DOBDC) were dissolved in 500 mL of DMF and 25 mL of distilled water. The mixed solution was

placed in an oil bath at 110 °C for 20 hours upon constant stirring. The greenish colour product collected by centrifugation and washed with DMF twice to remove the unreacted species, followed by washing with methanol twice, and then immersed in methanol overnight.³³ The final product was collected by centrifugation and dried in a vacuum oven at 70 °C overnight.

3.2.3 Synthesis of ZIF-8

The ZIF-8 was synthesised following a well-established procedure.¹⁷² Typically, 16 mmol of $\text{Zn}(\text{NO}_3)_2 \cdot 6\text{H}_2\text{O}$ and 800 mmol of 2-methylimidazole were dissolved in 400 mL of distilled water. The mixed solution was stirred at room temperature for 20 hours. The white ZIF-8 nanocrystals were collected and washed with water three times. For solvent exchange, the white powder was first washed with methanol twice and then immersed in methanol overnight. The final product was collected by centrifugation and dried in a vacuum oven at 70 °C overnight.

3.2.4 Synthesis of $\text{NH}_2\text{-MIL-125}(\text{Ti})$

The $\text{NH}_2\text{-MIL-125}(\text{Ti})$ was synthesised by the direct mixing method reported in the literature with slight modifications.¹⁷³ In a typical synthesis, 22.45 mmol (4.7 g) of 2-aminoterephthalic acid ($\text{NH}_2\text{-H}_2\text{BDC}$) was dissolved in a solution of 30 mL of DMF and 30 mL of methanol in a 200 mL screw jar. Slowly, 5.5 mmol (1.86 mL) of $\text{Ti}(\text{O}i\text{Bu})_4$ was added and constantly stirred for 15 minutes before sealing and placing it in an oil bath at 130 °C for 40 hours. The yellow-coloured microcrystalline powder was collected by centrifugation followed by washing twice with DMF to remove all unreacted organic ligand species. The same washing procedure was repeated three times with methanol for solvent exchange. The obtained $\text{NH}_2\text{-MIL-125}(\text{Ti})$ was dried in air at 70 °C overnight.

3.2.5 Synthesis of $\text{NH}_2\text{-MIL-125}(\text{Ti}/\text{Cu})$

To load Cu species into the Ti-MOF microcrystals, first, 2 g of activated $\text{NH}_2\text{-MIL-125}(\text{Ti})$ was dispersed in a mixture of DMF and methanol with 1:1 ratio (100 mL each) for 1 hour under ultrasonication. The 0.87 g of $\text{Cu}(\text{NO}_3)_2 \cdot 3\text{H}_2\text{O}$ was dissolved in 20 mL methanol and poured into the MOF dispersion before placing it in an oil bath at 120 °C for 12 hours. Dark green crystals of $\text{NH}_2\text{-MIL-125}(\text{Ti}/\text{Cu})$ were collected upon centrifugation followed by washing twice with methanol for

solvent exchange. The obtained NH₂-MIL-125(Ti/Cu) was dried at 80 °C in air overnight.

3.3 Synthesis of MOF derived nanocomposites

3.3.1 Preparation of MOF derived ZnO/C nanocomposites

The as-prepared MOF-5 was used as a precursor to prepare ZnO, ZnO/C nanocomposites and highly porous carbon. For each sample, 0.20 g of MOF-5 was loaded in an alumina boat and placed in the centre of a flow-through quartz tube sitting in a tube furnace. The furnace was set at a ramp rate of 10 °C min⁻¹ to the target temperature with a dwell time of 1 hour. The flow rate of argon gas was set at 30 mL min⁻¹. The first series of four nanocomposites were obtained at 800 °C in air, argon, argon saturated with water vapour introduced only during 1 hour dwell time (for short time duration; S) and argon with saturated water vapour introduced throughout the entire heat treatment (for longer time duration; L) and the resulting samples were named as ZnO-Air₈₀₀, ZnO/C-Ar₈₀₀, ZnO/C-Ar+W(S)₈₀₀ and ZnO/C-Ar+W(L)₈₀₀ respectively. Following the same protocols, the second series of four composites were prepared at 1000 °C and the resulting samples were labelled as ZnO-Air₁₀₀₀, C-Ar₁₀₀₀, ZnO/C-Ar+W(S)₁₀₀₀ and ZnO/C-Ar+W(L)₁₀₀₀ respectively.

To investigate the structure-property-application relationship in Zn-MOFs derivatives, the ZnO/C nanocomposites were prepared by one-step direct carbonisation of precursors MOF-5, MOF-74 and ZIF-8 at 800 °C under water vapour atmosphere. Typically, 1 g of activated Zn-MOF precursor was loaded in an alumina boat and placed at the centre of a flow-through quartz tube sitting in a tube furnace. The furnace was set at a heating rate of 10 °C min⁻¹ to the target temperature of 800 °C. When the furnace temperature reached 800 °C, water vapour were introduced via argon gas flow through a buffer bottle with water at ambient temperature and maintained the furnace temperature at 800 °C for 1 hour. Then the gas flow was switched to argon only and the furnace cooled down to room temperature. The final black products were collected and were named ZnO/C_{MOF-5}, ZnO/C_{MOF-74} and ZnO/C_{ZIF-8} respectively. To distinguish the role of functionalised porous carbon matrix in photocatalytic activity, these Zn-MOFs precursors were also calcined at 800 °C under air to obtain pure ZnO

nanoparticles (as a reference). The samples were named ZnO_{MOF-5}, ZnO_{MOF-74} and ZnO_{ZIF-8}.

3.3.2 Synthesis of MOF derived TiO₂/C nanocomposites

Similar to the Zn-MOFs derivatives, Ti-MOF derived nanocomposites were also prepared by one-step direct carbonisation of precursor NH₂-MIL-125(Ti). For the in-situ investigation of the thermal decomposition of Ti-MOF, as-synthesised NH₂-MIL-125(Ti) was heat treated via one-step carbonisation under an argon atmosphere at different temperatures from 200 to 900 °C. For each sample, 500 mg of NH₂-MIL-125(Ti) powder was loaded in an alumina boat and placed in the centre of a flow-through quartz tube furnace. Under a constant flow (50 mL min⁻¹) of argon gas, the heating rate of the tube furnace was set at 5 °C min⁻¹ and the dwell time at the target temperature was 2 hours. Inert conditions were established by purging the quartz tube for 30 minutes before the carbonisation process. The samples were prepared at 200, 300, 400, 500, 600, 700, 800 and 900 °C. These derived samples were labelled and discussed with respect to their respective pyrolysis temperature.

3.3.3 Synthesis of MOF derived TiO₂/Cu_xO/C nanocomposites

The nitrogen/carbon co-doped TiO₂/Cu_xO/C nanocomposites were prepared by one-step direct carbonisation of precursor NH₂-MIL-125(Ti/Cu) at 550, 700 and 800 °C under water vapour carried by argon gas, which is formed via argon gas pass through water buffer bottle at room temperature. For each sample, 500 mg of the as-prepared precursor in an alumina boat was placed at the centre of a flow-through quartz tube sitting in a tube furnace. Before starting the heating process, the quartz tube was purged with argon flow for 30 minutes to make sure that no oxygen is present in the tube. The heating was started under argon flow only at a flow rate of 50 mL min⁻¹. When the tube furnace reached the desired temperature, water vapour were introduced along with the argon flow for 2 hours and then it was cooled down to room temperature naturally under argon flow only. The resulting products were designated as TiCuC550, TiCuC700 and TiCuC800 for the sample derived from the pyrolysis of NH₂-MIL-125(Ti/Cu) at the temperature of 550, 700 and 800 °C respectively. For comparison, a sample derived from the pyrolysis of NH₂-MIL-125(Ti) without Cu²⁺ loading was also

synthesised at 700 °C in water vapour for 2 hours and the sample is labelled as TiC700. Figure 3.1 shows the schematics of the experimental setup for the preparation of MOF derivatives.

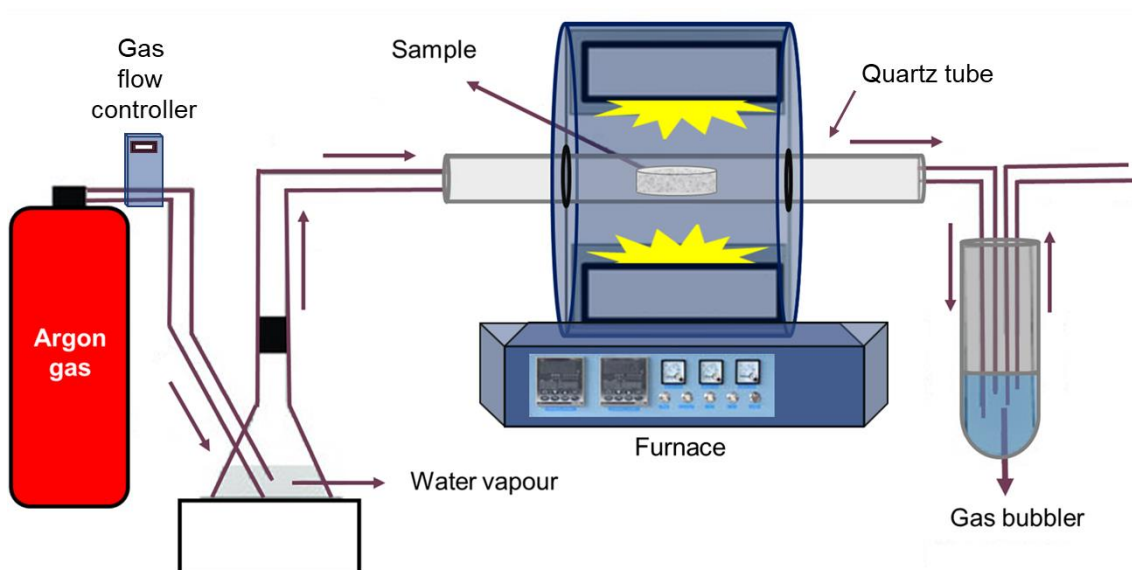


Figure 3.1 Schematics of the experimental setup for the preparation of MOF derived composites.

3.4 Characterisation techniques

3.4.1 Powder X-ray Diffraction (PXRD)

The Powder X-ray Diffraction (PXRD) is a powerful technique to identify the unknown crystalline structures of the materials. The X-rays are generated by a cathode ray tube. The generated X-rays are filtered and collimated to produce concentrated monochromatic radiation. These monochromatic rays interact with a crystalline sample and produce constructive interference when satisfying the conditions of Bragg's law:

$$n\lambda = 2d \sin\theta \quad (1)$$

where n is an integer, λ is the wavelength of incident X-rays, d is the inter-lattice spacing between crystal planes and θ is the incident angle.¹⁷⁴ The incident X-rays produce a diffraction pattern which is interpreted in the form of the angular position 2θ and the intensity of the diffracted X-rays to determine the inter-lattice spacing d . The crystalline sizes can be estimated by the position at 2θ and

breadth (full width half maximum, FWHM) of the XRD peaks using the Scherrer equation:

$$D = \frac{K\lambda}{\beta \cos\theta} \quad (2)$$

where D is the mean size of the crystalline domain (equal to the particle size), K is a crystalline shape factor, λ is the wavelength of the incident X-rays, β is line broadening, FWHM (measured in 2θ radian) of a specific (hkl) plane and θ is the Bragg angle.¹⁷⁵

In this work, the PXRD measurements were performed to confirm the crystalline structures of pristine MOFs precursors and the derived composites using a Bruker D8 instrument with Cu $K\alpha$ radiation (1.54 Å at 40 kV, 40 mA). The samples were prepared by gently pressing the dried powder onto a glass slide to form a thick flat surface. Mostly, the PXRD patterns of MOFs precursors and derived nanocomposites were recorded in the 2θ range from 5° to 90°.

3.4.2 Thermogravimetric Analysis-Mass Spectrometer (TGA-MS)

Thermogravimetric analysis (TGA) along with differential scanning calorimetry (DSC) provides information about the thermal stability, endo/exothermic nature of the reactions and the differences of material properties with the change of temperature over time. The TGA analysis can be carried out under a variety of atmospheres including air, vacuum and inert atmospheres.¹⁷⁶ Mass spectrometry (MS) is a commonly used analytical technique to determine the molecular composition of the chemical compounds by determining their mass to charge ratio. It can be used for the compositional analysis of the gases and chemical compounds produced from the heated samples. In this study, the TGA coupled with a mass spectrometer (TGA-MS) was measured with a Mettler Toledo TGA/DSC 3 in aluminium oxide pans (70 μ L with lid) with sample amounts of 1 to 5 mg. The following thermal program was applied using synthetic air (20 mL min⁻¹, 80% N₂; 20% O₂): At 30 °C isothermal equilibration (15 min), the ramp from 30 °C to 1000 °C with 10 K min⁻¹, at 1000 °C isothermal equilibration (10 min). For measurements under inert conditions, argon atmosphere was established (20 mL min⁻¹, 99.996%) by purging the measurement chamber with argon for

60 min at 30 °C at the beginning of the measurement. Volatiles were analysed using a quadrupole mass spectrometer (MS) gas analysis system “Thermostar” from Pfeiffer Vacuum at base pressures of $\approx 10^{-7}$ mbar in multiple ion detection mode. The device was operated with *Quadera* software package. The following m/z fragments were monitored: 16 (NH₂ / O), 17 (NH₃ / OH), 18 (H₂O), 28 (N₂ / CO) 30 (NO), 44 (CO₂) and 46 (NO₂).

3.4.3 N₂ Physisorption Measurements

The BET method is most often used to determine the (multilayered) physical adsorption of gas molecules on a solid surface of a material to measure the SSA. The standard BET analysis is carried out by physisorption of chemically non-reacting nitrogen (N₂) gas at the boiling point (77 K). The main concept of the BET theory is based on the following assumptions: (1) gas molecules adsorb on the surface of the material in multilayers infinitely; (2) gas molecules only interact with their adjacent layers; (3) the enthalpy of adsorption for the first layer is constant but greater than the second layer and so on; (4) the enthalpy of adsorption for each layer (except the first one) is the same; (5) the adsorption of multilayers of gas is randomly distributed which means that a new layer can start adsorbing before another one is finished.^{177, 178} The BET isotherms represent the number of N₂ gas molecules adsorbed and desorbed on the material surface in a relative pressure range of 0 to 1.

In this work, textural properties such as SSA, micro/mesopore volumes and pore size distribution (PSD) of the MOFs and MOFs derived nanocomposites were measured by N₂ sorption at 77 K on a *Quantachrome* autosorb iQ2 ASiQwin apparatus equipped with a micropore port (1×10^{-5} bar) via the conventional volumetric technique. Before the surface area analysis, the samples were degassed at 180 °C for 6 hours under vacuum. The PSDs was determined using the non-local density functional theory (NLDFT) method.

3.4.4 Fourier-Transform Infrared Spectroscopy (FTIR)

The Fourier-transform infrared (FTIR) spectroscopy is an analytical technique that allows obtaining infrared spectra to identify the chemical substances and functional groups present in materials in solid, liquid or gaseous form. When the infrared (IR) radiation passes through the sample, some part of the incident

radiation absorbs, and some transmit through it. The absorbed/transmitted energies of IR at a certain wavelength are interpreted by the Fourier transform and displayed in the forms of a spectrum. The peaks in a spectrum represent the IR active vibrational modes (fingerprints) such as stretching, bending, twisting or oscillation of the chemical bonds.^{179, 180}

In this work, the FTIR spectra of the MOFs and derived nanocomposites were recorded in the range of 4000-400 cm^{-1} using a Bruker Optics Tensor-27 FTIR spectrometer. The samples for FTIR measurements were prepared by mixing and grinding the dried samples with KBr and pressed in the form of pellets.

3.4.5 Raman Spectroscopy

Raman spectroscopy is a common analytical technique that is used to determine the vibrational modes of molecules for the identification and quantification of chemical structure, crystallinity and polymorphic phases, inelastic stress/strain and molecular interaction.^{181, 182} When a sample is illuminated with monochromatic laser light (in the near-infrared, visible or near-ultraviolet range), it scatters the incident light. The elastic part of the scattered light (Rayleigh scattering) having the same frequency as the incident light is filtered whereas the inelastic part of the scattered light is collected by the detector. This inelastically scattered part of the monochromatic laser light shows a small shift in frequency (Stokes or anti-Stokes Raman scattering) due to the interaction with the vibrational energy levels of the sample. The Raman spectra of the samples are obtained by plotting the intensity of the scattered light versus a frequency shift. In a typical Raman spectrum, the band positions correspond to the vibrational modes of different functional groups of molecules.^{181, 183-185}

To investigate the nature of metal oxide species and the porous carbon in MOFs derived nanocomposites, Raman spectra were recorded by employing Renishaw inVia Reflex Raman System RL532C, Class 3B in the range from 50 to 3000 cm^{-1} with 1 % laser power. The dried powder samples were pressed on the microscope glass slides to form a flat surface and placed under the microscope.

3.4.6 X-Ray Photoelectron Spectroscopy (XPS)

The X-ray photoelectron spectroscopy (XPS) is a very useful surface-sensitive spectroscopic technique that provides quantitative information about the elemental composition, chemical states, overall electronic structure and density of the electronic states of the materials. Normally, a monoenergetic beam of x-rays is irradiated on a sample under ultra-high vacuum condition. The number of ejected photoelectrons and their kinetic energy provide information about the atomic concentrations, chemical states and electronic configuration of the elements in the material. Each element produces a set of characteristic peaks at specific binding energies which correspond to the electronic configuration of electrons in the atoms such as 1s, 2s, 2p, 2s and 3d.^{186, 187} The XPS spectra are obtained by plotting the intensity (no. of detected photoelectrons) versus the binding energy (eV).¹⁸⁸

In this work, the surface chemical analyses of MOFs and derived nanocomposites were obtained by the Kratos Axis Ultra DLD spectrometer with a monochromated Al $K\alpha$ X-ray source operating at 168 W (12 mA \times 14 kV). Data were collected with pass energies of 160 eV for survey spectra, and 20 eV for high-resolution scans with step sizes of 1 eV and 0.1 eV, respectively. The analysis chamber pressure was maintained at 1×10^{-9} bar. The system was operated in the Hybrid mode, using a combination of magnetic immersion and electrostatic lenses and acquired over an area of approximately $300 \times 700 \mu\text{m}^2$. A magnetically confined charge compensation system was used to minimise charging of the sample surface and the take off angle for the photoelectron analyser was 90° . Depth profiling experiments were conducted using a $110 \mu\text{m}$ diameter spot after etching over a $2 \times 2 \text{ mm}$ area using 1×10^{-6} Torr argon at 4 kV. Data were analysed using CasaXPS (v2.3.23) after subtraction of a Shirley background and using modified Wagner sensitivity factors as supplied by the manufacturer.

3.4.7 Scanning Electron Microscopy (SEM)

Scanning electron microscopy (SEM) is one of the very powerful tools to investigate the surface topography of the materials. Briefly, in a standard SEM, an electron beam is thermionically generated from an electron gun, commonly

fitted with a tungsten filament cathode. The generated electron beam (0.2-40 keV) is accelerated between the cathode and the anode by applying the voltage (0.5-30 kV). The electron beam is de-magnified by the condenser lenses and objective lens and then confined and focused on the sample surface to produce a sharper image. The impinging electron beam can cause elastic and inelastic scattering producing backscattered electrons (BSE), secondary electrons (SE), Auger electrons (AE) and X-rays.^{189, 190} The SEs emit from the very top layer (<10 nm) of the sample and can provide morphological information such as shape, size and surface texture of the samples. The detected signals are collected and recorded to generate the image on the computer monitor screen.¹⁸⁹ In this study, SEM images were recorded by using the xT Nova Nanolab 600 FIB. For SEM images, the dried powder samples were spread on conductive carbon tape and sputtered with a gold layer of 5 nm thickness to reduce the effects of charging.

3.4.8 Transmission Electron Microscopy (TEM) and Energy Dispersive X-ray Spectroscopy (EDX)

As suggested by its name, transmission electron microscopy (TEM) creates an image by using the electrons transmitted through the ultra-thin sample. The electron beam for TEM is generated by the field emission of a single crystal or by thermionic emission of a filament. The generated electrons are accelerated and focused through a series of electrostatic and electromagnetic lenses to control the trajectory and shape of the electron beam. Passing through the sample, the incident beam produces transmitted electrons as well as elastically or inelastically scattered electrons. The high-resolution TEM image of the sample is generated by collecting and processing the transmitted electrons. HRTEM can reveal invaluable information about crystallographic structure including grain size, crystal orientation, polymorphic phases and lattice spacing at the atomic scale. In addition, the selected area electron diffraction (SAED) pattern can also be recorded to identify the crystal orientation and measure the lattice parameters of the sample.¹⁹¹ The energy dispersive X-ray analysis (EDX) can be carried out to identify and quantify the elements present in a sample. When the incident high energy electron beam interacts with the sample, it also knocks out some of its innermost electrons generating the X-rays of particular energies, characteristic to the atomic structure of the elements. An energy-dispersive spectrometer coupled

with TEM can produce quantitative information of the elemental composition by recording the number and energy of the X-rays emitted from the selected area of the sample.^{191, 192}

In this work, TEM (JEM 2100 LeB6 200 kV) equipped with EDX was employed to record high-resolution TEM images and EDX elemental mapping. The samples were first dispersed in absolute ethanol under moderate sonication and then pipetted onto a holey carbon Cu grid followed by drying at 70 °C overnight. The in-situ scanning transmission electron microscopy (in-situ STEM) images and EDX elemental mapping of NH₂-MIL-125(Ti) were recorded by using a Jeol 2100 F FEG equipped with a spherical aberration corrector, operating at 200 kV in conventional TEM and the bright field (BF) or high-angle annular dark field (HAADF) scanning transmission electron microscope (STEM) modes with a resolution of 0.11 nm. STEM-EDX mapping was performed using a JEOL Silicon Drift Detector (DrySD60GV: sensor size 60 mm²) with a solid angle of 0.6 sr. In-situ STEM annealing under argon was carried out using a Protochips Atmosphere gas cell used as a TEM holder. The sample was placed between the two SiN membranes of the micro-electrical-mechanical systems (MEMS). The temperature and the gas flow in the cell were finely controlled by the gas delivery manifold. Before the analysis, the sample was dispersed in dichloromethane and drop-casted on the SiN membrane acting as a heater element. The in-situ experiment was done at atmospheric pressure under Ar. The sample was pre-heated from room temperature to 300 °C and then to 800 °C with a ramp rate of 10 °C min⁻¹.

3.4.9 UV-Visible Spectrophotometer

The Ultraviolet-Visible (UV-Vis) spectroscopy represents the absorption or reflectance of incident light by the sample in the ultraviolet and visible region of the electromagnetic spectrum. It is commonly used to determine the EBG between the valence band (highest occupied molecular orbital, HOMO) and conduction band (lowest unoccupied molecular orbital, LUMO) of the materials. When a molecule containing bonding electrons (in σ , π orbitals) and non-bonding electrons (n-electrons) is exposed to UV-Vis light, it can absorb energies at particular wavelengths and the electrons excite to the higher anti-bonding (in σ^* , π^* orbitals) molecular orbitals due to the possible electronic transitions between

π - π^* , n - π^* , σ - σ^* and n - σ^* orbitals. The light absorbed at a particular wavelength corresponds to the difference of energy between HOMO and LUMO, called the EBG. The UV-Vis spectrophotometer measures the intensity of the incident UV-Vis light before passing through the sample (I_0) and after it passes through the sample (I) and compares the difference between them.^{193, 194} The spectra are plotted between the intensity of absorbed light (I) versus the wavelength of the light.

In this work, the UV-Vis absorption spectra of MOFs and the derived composites were acquired by employing a ThermoScientific Evolution 200 spectrophotometer and the EBGs were estimated by the Tauc plots.

3.4.10 Electrochemical Impedance Spectroscopy (EIS)

The electrochemical impedance spectroscopy (EIS) allows measuring the impedance of a system (such as electron transfer resistance in a material) as a function of the frequency of an applied alternating current (AC). To measure the electrochemical impedance, a small AC potential (1-10 mV) is applied to an electrochemical cell and the current through the cell is measured.¹⁹⁵ In this work, the CHI660E electrochemical workstation was employed to measure Electrochemical Impedance Spectra (EIS) at room temperature. In a typical three-electrode electrochemical setup, carbon rod and Ag/AgCl were used as the counter and reference electrodes respectively. A finely polished mirror-like glassy carbon (GC) electrode (2.8 cm²) was used as a working electrode, prepared to test the electrochemical impedance spectra by depositing a 5 μ L solution of the sample (2 mg of photocatalyst dispersed in 1 mL of water-ethanol (4:1 v/v) solution with additional 5 μ L of 5 wt.% Nafion solution by ultrasonic bath for 60 min) followed by drying in air overnight. All EIS measurements were recorded under the same potential in a 0.5 M H₂SO₄ solution used as an electrolyte.

3.5 Photocatalytic applications

3.5.1 Photodegradation of Methylene Blue

Adsorption and photodegradation of organic dye MB from water solution by Zn-MOF derived ZnO/C nanocomposites was evaluated in a dark box. Typically, 10 mg of as-prepared sample was added into 50 mL of 20 ppm aqueous MB solution. For adsorption studies, the suspension was immediately transferred to a dark box

under constant stirring. After different intervals of time, 1 mL aliquots were taken and the concentration of MB in the solution was determined by UV-Vis absorption spectroscopy. Using a similar procedure, the photodegradation of MB by ZnO/C composites were measured under visible light irradiation. The visible light source ($380 \leq \lambda \leq 700$ nm) was provided by 10 lamps of 20 W with a light intensity of 120 mW cm⁻² (PerfectLight). The adsorption/photodegradation of MB (%) was calculated by using the following expression:

$$D (\%) = \frac{C_0 - C}{C_0} \times 100\% \quad (1)$$

Where D is the percentage of degradation, C₀ is the initial concentration and C is the final concentration.¹⁹⁶ To measure the recyclability and stability of the material, the best performing sample was separated from the solution by filtration using a filter paper. Before reusing for the next run, the filtered sample was washed with deionised water several times and dried in an oven at 110 °C overnight. The sample was consecutively used for 5 cycles.

3.5.2 Photocatalytic water splitting for H₂ evolution

Photocatalytic hydrogen evolution reaction (HER) experiments were performed in a methanol/water solution under UV-Vis light using a 500 W Xe/Hg lamp (66983, Newport) with a 285 nm cut-off optical filter. It involved a custom-made Pyrex-glass reactor, a CP 9001 gas chromatograph (GC, Chrompack) for analysis of the headspace and the light source. Light intensity was measured with AvaSpec-3648-2-USB2 (Avantes, the Netherlands). The reactor has a total volume of 42.1 mL including 17.1 mL of headspace. The reactor was equipped with a water jacket to precisely control the temperature. The light emitted by the Xe/Hg lamp passed through a lens assembly (77330, Newport) (focusing the beam with the spot size of 2.27 cm² reaching the reactor window) and an H₂O filter (61945, Newport). A probe of the headspace was analysed every 30 min by the GC. In a typical experiment, 10 mg of the photocatalyst was suspended in 7.5 mL of CH₃OH and 17.5 mL of H₂O. The suspension was then placed in the reactor and was purged by an argon flow of 30 mL min⁻¹ for 30 min to deoxygenate the system. After completely deoxygenating the reactor, the illumination was applied followed by the GC analysis. The suspension was kept under stirring during reaction with a small argon flow through the headspace towards the GC sample

loop. The temperature of the reactor was fixed at 30 °C. The AQY (%) of Ti-MOFs and the derived nanocomposites were calculated at 435 nm by the following equation:^{197, 198}

$$AQY_{\lambda} = \frac{2 \times \text{number of evolved H}_2 \text{ molecules}}{\text{Total number of incident photons}} \times 100 \% \quad (2)$$

Chapter 4

MOF-5 derived porous ZnO/C nanocomposites for efficient dye photodegradation

4.1 Introduction

Due to the high industrialisation, freshwater sources and the oceans are polluted every day. Several industries produce a variety of hazardous contaminants, such as organic chemical wastes, by-products from textile dyes, petrochemicals, pharmaceutical wastes, pesticides and plastics. The treatment of industrial wastewater has become one of the major challenges recently. There have been enormous efforts to utilise metal oxide as photocatalysts to decompose organic wastewater pollutants into environmentally benign species.¹¹⁷ Zinc oxide (ZnO) is an excellent semiconductor material for this purpose because of its abundance and negligible toxicity.^{22, 199} However, the wide EBG of ZnO limits its utilisation in the visible light range of the electromagnetic spectrum since bulk ZnO can only absorb UV light with a wavelength shorter than 380 nm, which consequently restricts the photocatalytic efficiency.²⁰⁰ Furthermore, the low surface area of ZnO and its tendency to agglomerate due to high surface energies are big challenges to effectively utilise ZnO nanoparticles for photocatalysis.^{201, 202}

To overcome these limitations, various approaches were developed to generate ZnO based composites with a narrower EBG to improve their photocatalytic performance.²⁰³ However, the composites synthesised by mechanical and physical methods usually possess low surface area, poor dispersion and heterogeneity. In the last few years, metal-organic frameworks (MOFs) have drawn huge attention as precursors and sacrificial templates due to their tunable properties of the resulting materials.⁴¹ Zinc-based MOFs have been proved to be very promising sacrificial templates to generate homogeneously dispersed crystalline ZnO nanoparticles embedded in porous carbon matrix with high BET surface areas and tunable pore sizes.²⁰⁴ Simultaneously, the carbon atoms (from the organic linkers) can dope into the crystal lattice of ZnO nanoparticles (self-doping) during the high temperature pyrolysis of Zn-MOFs, narrowing their EBG.²⁰⁵ Consequently, it may produce high performing materials for photocatalytic applications under visible light.

In Zn-based MOF-5, the Zn_4O metal cluster is connected to six carboxylates, constructing octahedral-shaped building units linked through rod-like organic BDC²⁻(1,4-benzenedicarboxylate) linkers to form a cubic structure (Figure 4.1) with the composition $Zn_4O(CO_2)_6$.²⁴ However, the direct employment of MOF-5 in photocatalytic wastewater treatment has not been promising due to the structural instability in water.²⁰⁶ To retain the inherent structures, porosity and surface functionalities of MOF-5, one-step pyrolysis of MOF-5 was carried out to derive the ZnO/C nanocomposites.

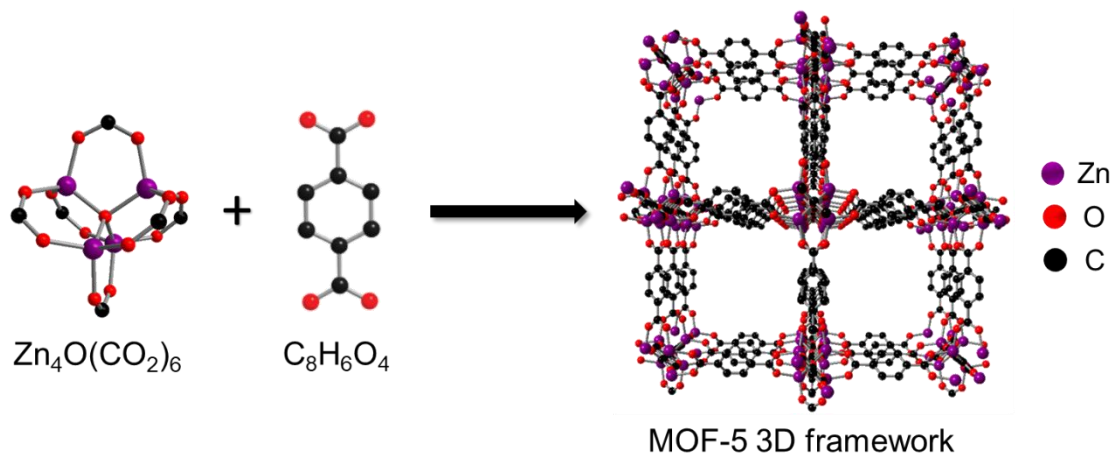


Figure 4.1 Structures of SBU Zn_4O , organic linker and crystalline MOF-5.

A few reports on MOF derived ZnO/C nanocomposites for photocatalytic water treatment have been published.^{80, 101} However, many questions remain unanswered. For instance, the interactions of the nanocomposites with organic dyes and the impact of defects and functional groups on photocatalytic activity have not been thoroughly studied. In this chapter, the effect of temperature and the gaseous atmosphere on the compositions, textural properties and physicochemical properties of the MOF derived ZnO, ZnO/C nanocomposites and the porous C are systematically investigated. For this purpose, as-synthesised MOF-5 was used as a precursor to obtain ZnO, ZnO/C composites and porous C at 800 and 1000 °C under a variety of gaseous atmospheres such as air, argon and water vapour. Water vapour as a gaseous atmosphere is regarded as a weak oxidising agent that can result in slow oxidation rate, therefore it can be anticipated that the mild and finely controllable oxidation process in water vapour atmosphere during the carbonisation of MOFs at high temperatures will not compromise the structures and properties of the target materials. This is especially true when water vapour is used as an oxidation agent

during the generation of porous metal oxide/carbon composites since water vapour can react with and oxidise the formed carbons at high temperatures to introduce hydrophilic functional groups like -COOH on carbon, which may improve their photocatalytic performance.^{101, 207}

4.2 Results and discussion

4.2.1 Characterisations of MOF-5 derived ZnO, ZnO/C and porous carbon

The PXRD patterns (Figure 4.2) show that the pyrolysis of MOF-5 at high temperature in air results in white coloured pure ZnO nanoparticles. The samples ZnO-Air₈₀₀ and ZnO-Air₁₀₀₀ show diffraction peaks at 2θ of 31.7°, 34.4°, 36.2°, 47.5°, 56.5°, 62.8°, 66.3°, 67.9°, 72.5° and 76.9° which confirm the polycrystalline wurtzite structure of ZnO.¹⁰¹ The ZnO-Air₁₀₀₀ shows much stronger diffraction peaks than ZnO-Air₈₀₀, indicating higher crystallinity of the ZnO nanoparticles. However, black products were generated upon heat treatment in argon and water vapour, signifying the carbonisation of the precursor. Heat processing of MOF-5 in argon atmosphere, a significant amount of ZnO appears in the sample ZnO/C-Ar₈₀₀ whereas no ZnO is observed in the PXRD patterns of sample C-Ar₁₀₀₀. This may be because the heat process temperature is above the boiling point of Zn (907 °C), the formed Zn is likely to evaporate. Consequently, no diffraction peaks belonging to Zn or ZnO species are observed in the powder diffraction pattern of sample C-Ar₁₀₀₀. Instead, a broad reflection centred at around $2\theta = 23^\circ$ is due to the (002) lattice plane reflection of amorphous carbon species. The broadening of this diffraction peak indicates the low degree of graphitisation, confirming the amorphous nature of the formed carbon.^{122, 208, 209} It can be observed that the diffraction peaks of ZnO/C are of lower intensity as compared to pure ZnO samples. The closer observation (inset to Figure 4.2a) shows that in sample ZnO/C-Ar+W(S)₈₀₀ the strongest diffraction peak (101) of ZnO shifts slightly from 36.24° to 36.18° 2θ compared to ZnO-Air₈₀₀. Such shifting of peaks can be assigned to the doping induced unit cell deformation. It is further confirmed by DRS, FTIR and Raman spectroscopy that change in ZnO lattice parameters and structural deformation can be attributed to the doping of C atoms, generated defects and narrow EBG.

For the samples obtained at 1000 °C, the nanocomposite ZnO/C-Ar+W(L)₁₀₀₀ shows broad reflections representative for amorphous carbon as well

as the very low intensity peaks of ZnO. However, the ZnO/C-Ar+W(S)₁₀₀₀ showed only the broader diffraction peak of amorphous carbon. The intensities of the ZnO reflections in all samples obtained in argon and water vapour atmosphere at 1000 °C are negligible compared with the samples prepared at 800 °C, most likely due to the relatively low content of ZnO in those samples, as shown in the TGA measurements below. Compared with sample C-Ar₁₀₀₀, the diffraction peaks of amorphous carbon for the water vapour processed samples remained unaffected that indicated the preservation of carbon structure under these conditions, which was also confirmed by Raman spectroscopy and XPS analysis.

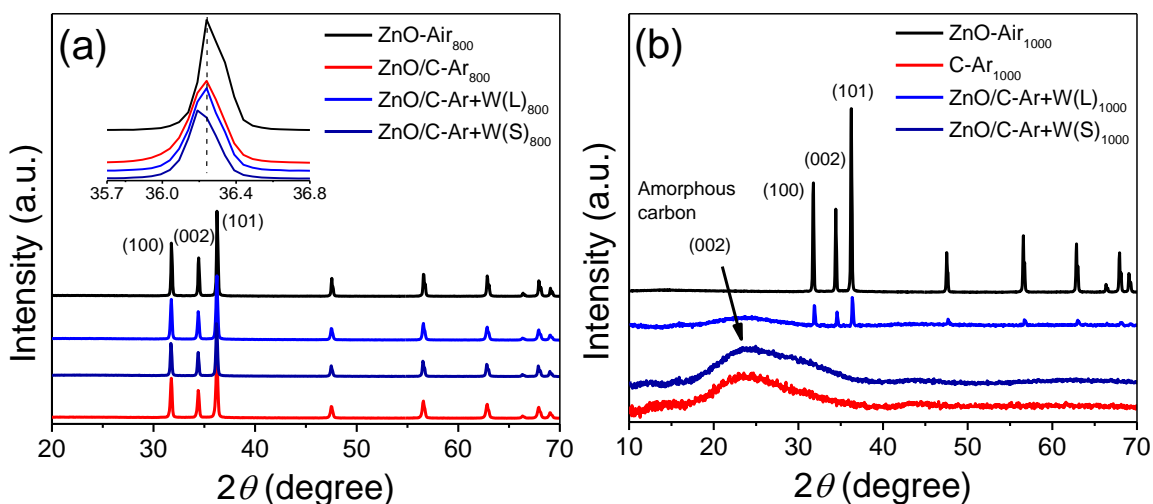


Figure 4.2 PXRD patterns of nanocomposites obtained in different carbonisation atmospheres at (a) 800 °C and (b) 1000 °C. ZnO-Air, ZnO/C-Ar+W(L), ZnO/C-Ar+W(S) and ZnO/C-Ar are represented in black, light blue, dark blue and red, respectively. Numbers in brackets mark the Miller indices of the lattice plane reflections of the wurtzite modification of ZnO. Inset to (a) is the amplified PXRD pattern of peak (101).

The TGA was carried out under air to evaluate the thermal stabilities of nanocomposites as well as to determine the amount of carbon and other species presented in MOF-5 derived nanocomposites. Figure 4.3 represents the TGA profiles of composites obtained at 800 and 1000 °C respectively. Samples ZnO-Air₈₀₀ and ZnO-Air₁₀₀₀ are pure wurtzite polycrystalline ZnO derived from MOF-5 and show no weight loss in the applied temperature range, confirming the absence of carbon in these samples. However, sample C-Ar₁₀₀₀ showed 10% weight loss at 100 °C, implying the removal of adsorbed moisture. A weight loss

of the remaining 90% at 650 °C indicates that only carbon is presented in this sample with no residual ZnO species. This is clearly due to the complete evaporation of Zn species during the carbonisation process that results in the generation of pure porous carbon. However, the composites ZnO/C-Ar₈₀₀, ZnO/C-Ar+W(S)₈₀₀ and ZnO/C-Ar+W(L)₈₀₀ exhibit 11 % to 13 % weight loss at around 550 °C due to the burn-off of carbon. The composites ZnO/C-Ar+W(S)₁₀₀₀ and ZnO/C-Ar+W(L)₁₀₀₀ contain around 96% of carbon. Due to the presence of oxygen species in the water vapour atmosphere, a very small amount of ZnO was still retained in the composites regardless of the high carbonisation temperature. The obtained TGA results show good consistency with the PXRD patterns. It is observed that the water exposure for a shorter time (S) and for a longer time during the entire carbonisation process (L) has less influence on the ZnO content in the composites. However, the longer exposure of water vapour has a considerable impact on the SSAs and functionalisation of composites as confirmed by BET, FTIR and XPS spectroscopies. The composites derived at 1000 °C demonstrated increased thermal stability in comparison to the composites obtained at 800 °C.

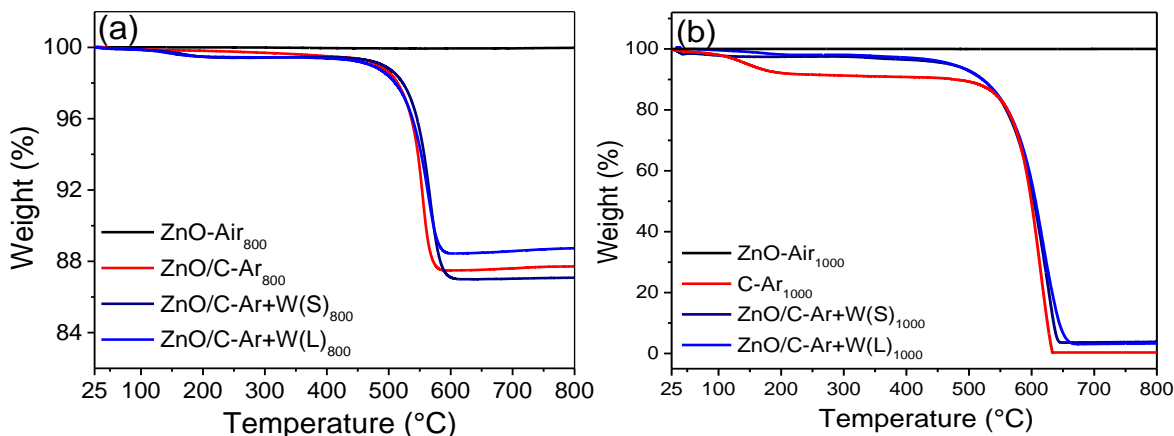


Figure 4.3 TGA profiles of MOF-5 derived composites ZnO-Air (black), ZnO/C-Ar+W(L) (blue), ZnO/C-Ar+W(S) (dark blue) and ZnO/C-Ar (red) obtained under different gaseous atmospheres at (a) 800 °C and (b) 1000 °C.

The morphologies of the MOF-5 precursor and its derived composites were analysed by SEM and TEM. Well-defined cubic crystals of MOF-5, approximately 1 µm in size are observed in the SEM micrographs shown in Figure 4.4a and b. Upon heating to elevated temperatures and carbonisation, the material retained

its cubic morphology which is in agreement with previous reports.²¹⁰ Despite different carbonisation atmospheres, no major morphological differences are observed in samples synthesised at 800 °C (Figure 4.4c). However, at 1000 °C, most of the ZnO reduced to Zn and evaporated, leaving behind highly porous carbon with exceptional BET surface areas confirmed by gas sorption analysis. More hollow and partially broken cubic porous carbon structures can be seen in Figure 4.4d. Srinivas *et al.* argued that this process can be called a self-activation of carbon, which is predominantly influenced by the framework structures, metal centres and initial porosities of the precursor MOFs.²¹⁰

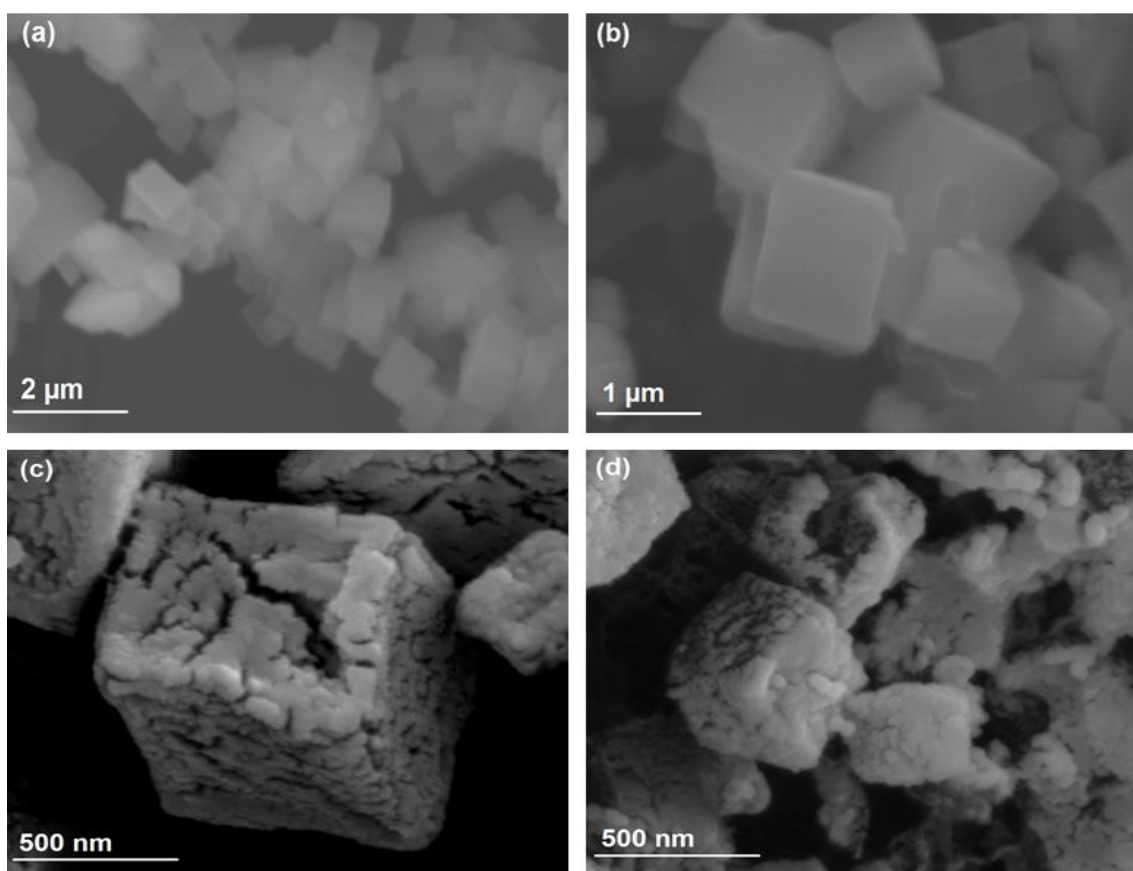


Figure 4.4 Representative SEM micrographs of (a, b) MOF-5, (c) ZnO/C-Ar+W(S)₈₀₀ and (d) ZnO/C-Ar+W(S)₁₀₀₀.

Representative TEM images of selected composites ZnO/C-Ar+W(S)₈₀₀ and ZnO/C-Ar+W(S)₁₀₀₀ are presented in Figure 4.5. The low magnification images (Figure 4.5a and d) confirm the topology of the derived composites. In the High-resolution TEM (HR-TEM) images (Figure 4.5c and f), the small ZnO nanoparticles (estimated sizes of 5-10 nm) embedded in the porous carbon can

be observed. The homogeneous dispersion of ZnO nanoparticles (Figure 4.6 in porous carbon matrices is further confirmed by EDX elemental mapping. The composite ZnO/C-Ar+W(S)₈₀₀ exhibits the homogeneous distribution of Zn, O and C throughout the selected sample area. The elemental mapping of the composite ZnO/C-Ar+W(S)₁₀₀₀ shows the C with a negligible amount of Zn and O, due to the high C content of 96% in this sample. It confirms that homogeneously distributed ZnO nanoparticles in a porous carbon framework can be achieved upon high-temperature carbonisation of MOF-5 sacrificial templates under water vapour atmosphere.¹⁰¹ The nanoparticles with such small sizes usually show broader XRD peaks. However, in these samples, the peaks are of relatively high intensity, which can be due to the fact that during the carbonisation process, the organic linker of MOF-5 transforms into the porous carbon, while the metal cluster transforms into ZnO. Although many of the formed ZnO particles with small size (such as 5-10 nm) are surrounded by the formed amorphous porous carbon, under high temperature pyrolysis conditions, some small ZnO particles inevitably combine to form bigger ZnO particles due to the high surface energy and sintering effect. Therefore, in the PXRD, the strong diffraction peaks from the bigger ZnO particles make it difficult to see the contribution from small particles. In Figure 4.5c and f, the dark spots of isolated ZnO nanoparticles can be seen.

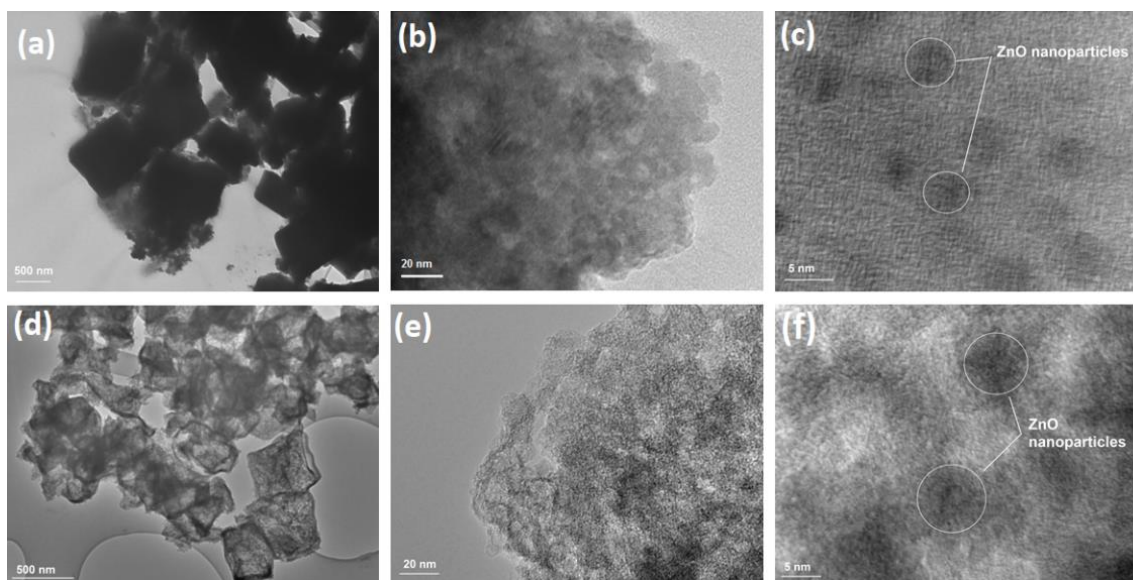


Figure 4.5 TEM and HRTEM images of (a, b, c) ZnO/C-Ar+W(S)₈₀₀ and (d, e, f) ZnO/C-Ar+W(S)₁₀₀₀ at different magnifications.

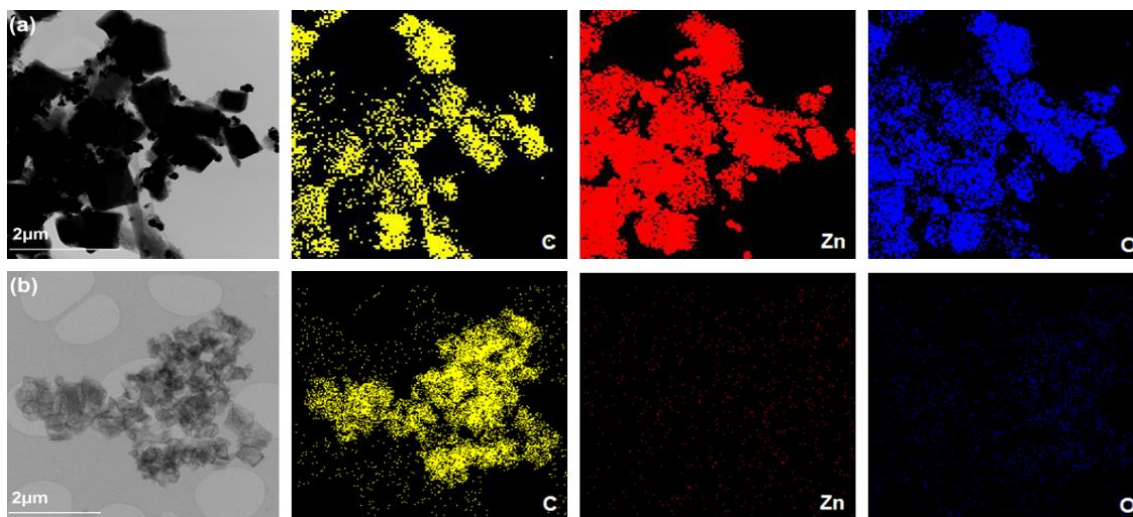


Figure 4.6 The EDX elemental maps of (a) ZnO/C-Ar+W(S)₈₀₀ and (b) ZnO/C-Ar+W(S)₁₀₀₀. The coloured images show the distribution of elements throughout the composite. The C, Zn, and O are represented in yellow, red and blue respectively.

To study the nature of the porous carbon matrix in these nanocomposites and lattice vibrational modes of ZnO, Raman spectra of the MOF-5 derived composites were recorded. As shown in Figure 4.7a and b, samples ZnO-Air₈₀₀ and ZnO-Air₁₀₀₀ show strong signals with main peaks of $E_2(\text{high})$ mode occurring at 438 and 454 cm^{-1} respectively. The other peaks at around 332 and 347 cm^{-1} in these samples correspond to $A_1(\text{TO})$ mode (second-order Raman processes) of ZnO. For bulk ZnO, these peaks commonly appear at around 475 cm^{-1} .²¹¹⁻²¹⁴ The E_2 mode usually occurs at around 436 cm^{-1} for ZnO quantum dots (QDs) with sizes less than 10 nm.³⁷ The observed ZnO peaks indirectly confirm the particle sizes observed by HRTEM. It should be noted that in MOF-5 derived ZnO/C at 800 °C, the $E_2(\text{high})$ and $A_1(\text{TO})$ modes are redshifted to 427 and 321 cm^{-1} respectively, compared to pure ZnO (Inset to Figure 4.7a). The observed redshift can be ascribed to the strain on the ZnO nanoparticles due to the presence of carbon atoms in the crystal lattice. The redshift in Raman spectra can also take place when the incident photons lose energy upon interaction with the vibrational modes of the material (phonons). This energy is absorbed by the material leading to the peak shift toward lower frequencies. It suggests that the doped carbon atoms alter the bond lengths and the lattice parameters of ZnO, generating new crystalline lattice defects and eventually narrowing the EBG.

Two characteristic Raman signals of amorphous carbon are also observed at around 1350 and 1590 cm^{-1} for all samples obtained under argon and water vapour atmosphere at 800 and 1000 $^{\circ}\text{C}$. In the samples ZnO/C-Ar₈₀₀, ZnO/C-Ar+W(S)₈₀₀ and ZnO/C-Ar+W(L)₈₀₀, the G band at around 1588 cm^{-1} is generated by the formation of nanocrystalline carbon and represents the bond stretching of all sp^2 atoms in both hexagonal rings and chains of carbon. The D band at around 1348 cm^{-1} is due to the breathing modes of sp^2 hybridised carbon atoms in hexagonal rings, which signifies the formation of amorphous carbon. This mode is forbidden in perfect graphite crystals and it can only be seen in the presence of disorder in structure. The intensity of the D band and particularly the $I_{\text{D}}/I_{\text{G}}$ ratio is a measure for the content of defects and disorder in the crystalline carbon structures.²¹⁵⁻²¹⁷

As shown in Figure 4.7a and b, the comparison of the $I_{\text{D}}/I_{\text{G}}$ ratios of the composites ZnO/C-Ar₈₀₀ (0.82), ZnO/C-Ar+W(S)₈₀₀ (0.82) and ZnO/C-Ar+W(L)₈₀₀ (0.86) with C-Ar₁₀₀₀ (0.99), ZnO/C-Ar+W(S)₁₀₀₀ (0.89) and ZnO/C-Ar+W(L)₁₀₀₀ (0.84) reveal that increasing the annealing temperature increases the $I_{\text{D}}/I_{\text{G}}$ ratio which indicates that the high temperature and longer exposure to the water vapour during the carbonisation process generate more defects in the carbon matrix, and functionalises the carbon with the hydrophilic carboxylic group eventually enhancing the amorphous nature of the composites.^{217, 218} FTIR spectra were recorded to investigate the presence of carboxylic functional groups on the surface of the nanocomposites.

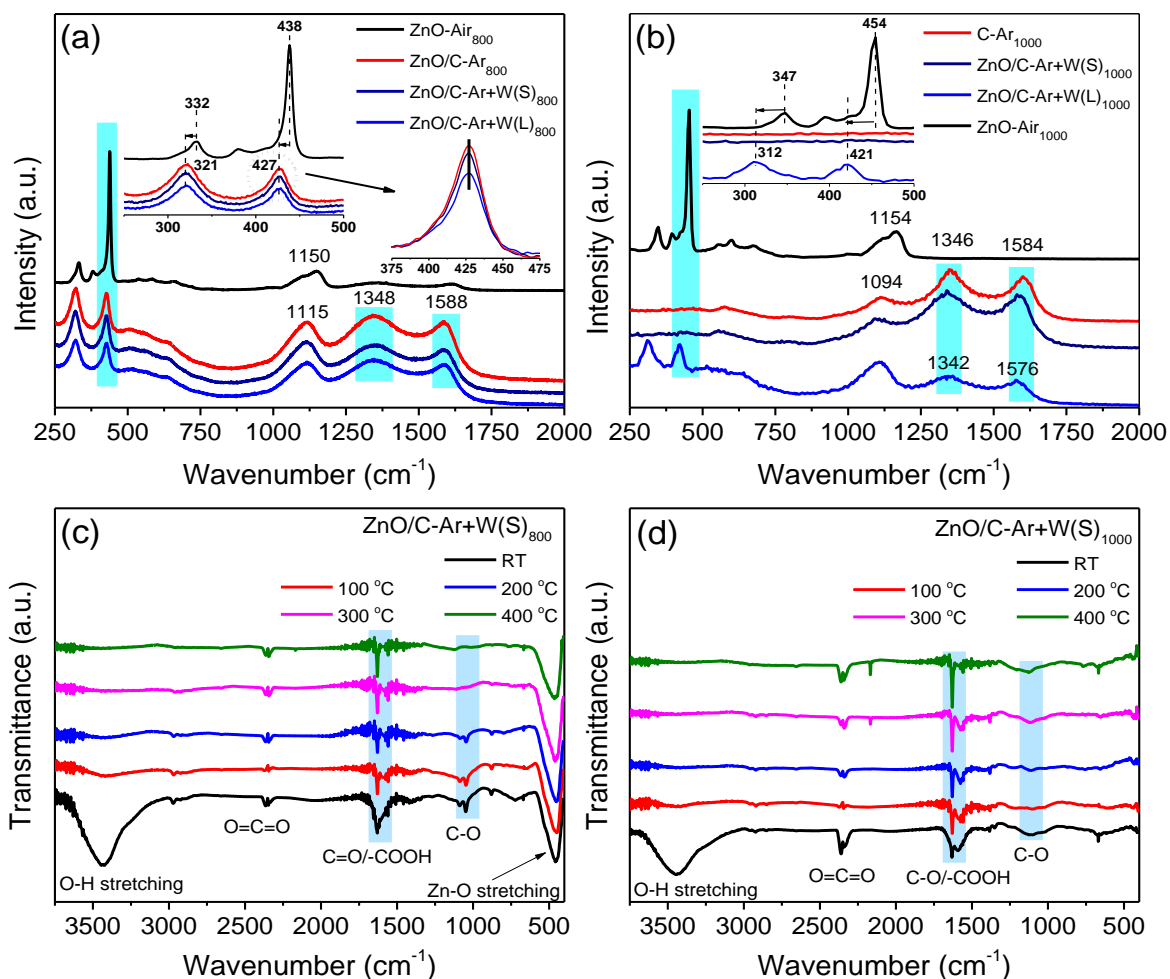


Figure 4.7 Raman Spectra of ZnO-Air (black), ZnO/C-Ar (red), ZnO/C-Ar+W(S) (dark blue) and ZnO/C-Ar+W(L) (light blue) prepared at (a) 800 °C and (b) 1000 °C. FTIR spectra of ZnO/C-Ar+W(S) derived at (c) 800 °C and (d) 1000 °C after heat treatment of the materials at RT (black), 100 °C (red), 200 °C (blue), 300 °C (pink) and 400 °C (green), respectively.

The FTIR spectra of selected samples ZnO/C-Ar+W(s)₈₀₀ and ZnO/C-Ar+W(s)₁₀₀₀ were recorded at room temperature. As shown in Figure 4.7c, ZnO/C-Ar+W(s)₈₀₀ exhibits a strong band at 460 cm⁻¹ which is attributed to the Zn-O stretching from the crystalline wurtzite ZnO. This signal in ZnO/C-Ar+W(s)₁₀₀₀ is negligible (shown in Figure 4.7d), due to the much lower ZnO content in this sample, as demonstrated in XRD, XPS and TGA analysis. A strong signal is observed at around 1630 cm⁻¹ in both samples, which is assigned to the C-OH and C=O bond stretching of -OH and -COOH groups. A comparatively weak band at 2360 cm⁻¹ in these samples is ascribed to O=C=O bond stretching.

A broader signal at 3445 cm^{-1} indicating O-H/Zn-OH bond stretching of adsorbed H_2O , is observed in both samples.¹¹⁷ To confirm the presence of hydrophilic carboxylic (-COOH) groups on the surface of the nanocomposites, the sample was heated in a furnace at 100, 200, 300 and 400 °C for 1 hour followed by the measurement of the FTIR spectra. It was found that the signal at 1630 cm^{-1} became more prominent in both samples during heating, which confirms the presence of -COOH functional groups. This effect is accompanied by the decrease of the broad O-H stretching vibrations at around 3445 cm^{-1} and C-H stretching at 2972 cm^{-1} , indicating the gradual evaporation of the adsorbed H_2O .

To further analyse the elemental compositions of the derived composites, the XPS spectra of selected samples are presented. As shown in Figure 4.8a, the wide elemental spectra confirm the presence of Zn, O and C in all the composites obtained at 800 °C. In the Zn 2p spectrum, the Zn $2p_{3/2}$ and $2p_{1/2}$ doublet (Figure 4.8b) appear at binding energies of 1021.05 and 1044.15 eV, respectively. The binding energy difference between $2p_{3/2}$ and $2p_{1/2}$ (23.1 eV) energy levels implies the presence of Zn^{2+} ions. The Zn peak is stronger in pure ZnO sample whereas the intensity reduces in composites ZnO/C-Ar₈₀₀ and ZnO/C-Ar+W(S)₈₀₀ with a shift in binding energy from 1021.05 to 1021.15 eV, which may be due to the carbon doping into the ZnO lattice.²¹⁹ As shown in Figure 4.8c, the main peak of O 1s in sample ZnO-Air₈₀₀ is observed at 530.13 eV with a small shoulder at 531.59 eV. These peaks are allocated to the Zn-O bond and surface adsorbed oxygen species, respectively.²⁰³ For the sample ZnO/C-Ar₈₀₀, O 1s peaks at 530.35 and 531.74 eV can be ascribed to Zn-O bond, metal carbonate species such as C-O/C=O bonds or surface adsorbed oxygen species respectively. However, for the sample ZnO/C-Ar+W(S)₈₀₀, O 1s peaks can be deconvoluted into three peaks centred at 530.27, 530.99 and 532.19 eV which can be assigned to the Zn-O bond, carbonate species C-O/C=O and carboxylic functional group -COOH, respectively.^{220, 221}

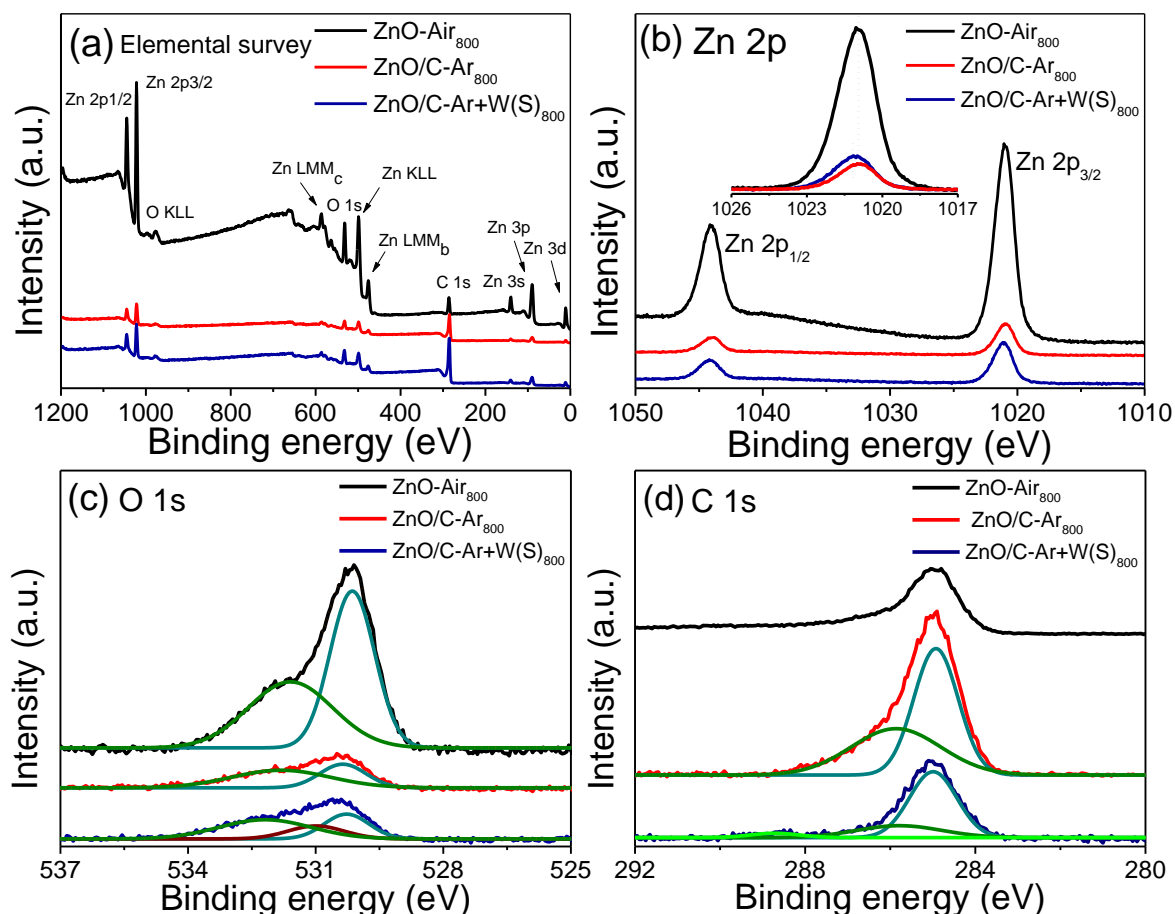


Figure 4.8 XPS spectra of (a) elemental survey (b) Zn 2p (c) O 1s (d) C 1s for ZnO-Air₈₀₀ (black) and ZnO/C-Ar₈₀₀ (red) and ZnO/C-Ar+W(S)₈₀₀(dark blue).

The C 1s spectra (Figure 4.8d) of samples ZnO/C-Ar₈₀₀ and ZnO/C-Ar+W(S)₈₀₀ show the main peak at 284.9 eV. It is in good agreement with the reported C=C bond of sp² hybridised carbon confirmed by Raman spectra.²²² The C 1s peak at around 286 eV in ZnO/C-Ar₈₀₀ and ZnO/C-Ar+W(S)₈₀₀ can be ascribed to carbonate species with different amount of C=O/C-O bonds.¹³¹ A broader peak at 288.9 eV can be observed in sample ZnO/C-Ar+W(S)₈₀₀ which can be assigned to the presence of -COOH functional group as confirmed by O 1s XPS spectra, as well as FTIR spectra (Figure 4.7c).²⁰³ A low intensity peak for carbon in the pure ZnO-Air₈₀₀ is also observed at 285.1 eV, which may due to the background and sample holder.

The SSAs and PSDs of the nanocomposites were determined by N₂ physisorption at 77 K and the isotherms are shown in Figure 4.9. Due to the capillary filling of the micropores, all samples exhibited type IV isotherms. The

composites ZnO/C-Ar₈₀₀, ZnO/C-Ar+W(S)₈₀₀ and ZnO/C-Ar+W(L)₈₀₀ exhibits BET surface areas of 369, 350 and 210 m² g⁻¹ respectively. The BET surface areas of the composites C-Ar₁₀₀₀, ZnO/C-Ar+W(S)₁₀₀₀ and ZnO/C-Ar+W(L)₁₀₀₀ derived at 1000 °C are measured to be 2839, 2390 and 2600 m² g⁻¹ respectively, much higher than those samples derived from 800 °C.²⁰⁶ Upon carbonisation of MOF-5 in argon above the boiling point of Zn, the Zn evaporates leaving behind highly porous amorphous carbon with inherited cubic morphology. The retained high porosity and defects in these derived 3D amorphous cubic carbons show exceptionally high surface areas confirmed by SEM and HRTEM. It is worth noting that the SSAs of the composites obtained in argon atmosphere are higher than the composites obtained in water vapour. It may be due to the water vapour causing some ZnO to stay in the pores reducing the overall surface areas. The TGA measurements confirmed that there are no ZnO nanoparticles in sample C-Ar₁₀₀₀, therefore it has the highest SSA. In contrast, the nanocomposite ZnO/C-Ar+W(L)₈₀₀ showed the lowest surface area among these samples. PSDs of these nanocomposites were analysed based on the N₂ sorption data using the NLDFT model. The porosity of the derived composites primarily depends upon the pyrolysis conditions, in particular, the temperature and gaseous atmosphere. By carefully controlling these conditions, the required pore sizes and shapes can be reproduced. The pore sizes of composites derived at 800 °C and 1000 °C are around 1.2 nm with a significant presence of mesopores exhibiting a broader size distribution. Based on the PSDs, it can be said that MOF-5 derived composites under these pyrolysis conditions are microporous/mesoporous in nature.

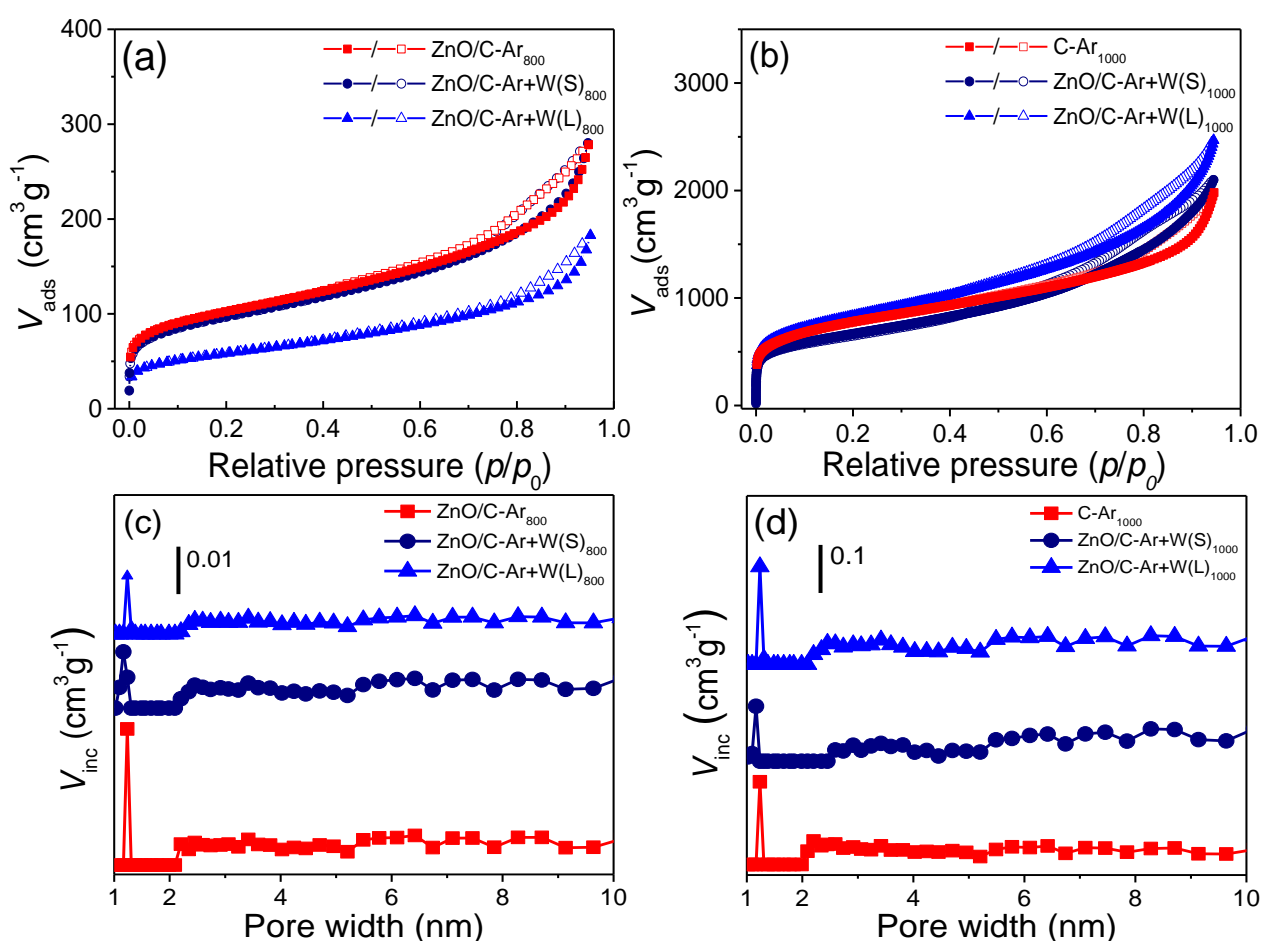


Figure 4.9 N_2 sorption isotherms measured at 77 K for ZnO/C-Ar and C-Ar (red squares), ZnO/C-Ar+W(S) (dark blue circles) and ZnO/C-Ar+W(L) (light blue triangles) derived at (a) 800 °C and (b) 1000 °C respectively. NLDFT PSD of samples derived at (c) 800 °C and (d) 1000 °C respectively. Filled and empty symbols represent adsorption and desorption. The lines are a guide to the eye only.

4.2.2 Optical properties and photodegradation performance

The optical properties of the composites were studied by employing UV-Vis diffuse reflectance spectroscopy (DRS). The reflectance spectra of selected nanocomposites ZnO/C-Ar+W(S)₈₀₀ and ZnO/C-Ar+W(S)₁₀₀₀ (Figure 4.10a) showed redshift to 387 and 395 nm respectively, in comparison to pristine ZnO-Air₁₀₀₀ (inset in Figure 4.10a) which exhibits the reflectance at 380 nm. The EBGs of the composites were calculated by the Tauc plots as shown in Figure 4.10b.

The EBG of MOF-5 derived ZnO-Air₁₀₀₀ (inset in Figure 4.10b) was determined as 3.26 eV which is smaller than the EBG of commercially available ZnO nanoparticles (3.37 eV). However, the EBG of ZnO/C-Ar+W(S)₈₀₀ and ZnO/C-Ar+W(S)₁₀₀₀ were calculated to be 3.0 eV and 3.1 eV respectively. The MOF-5 derived nanocomposites ZnO/C-Ar+W(S)₈₀₀ and ZnO/C-Ar+W(S)₁₀₀₀ showed considerable shifts in EBGs compared to the bulk ZnO.

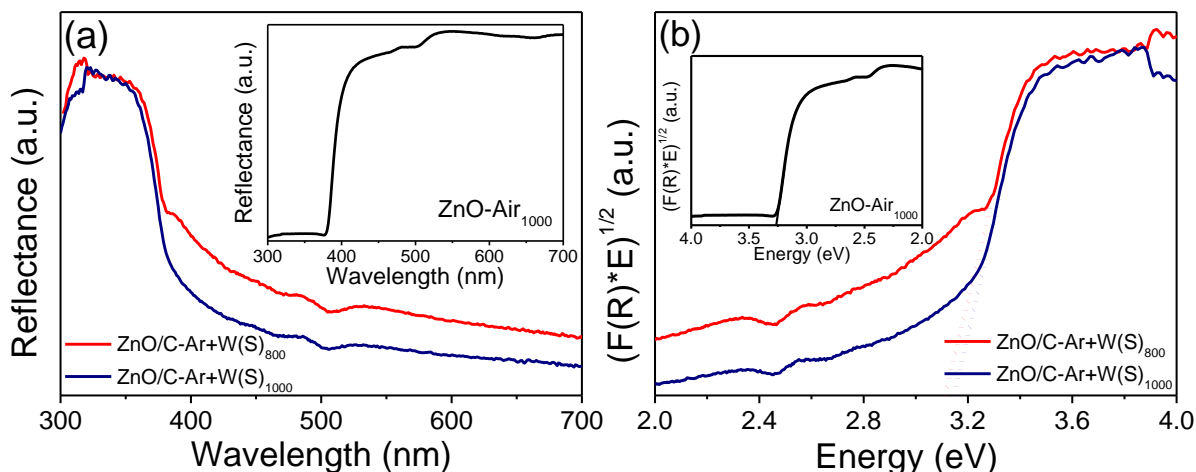


Figure 4.10 (a) Reflectance spectra of selected samples ZnO-Air₁₀₀₀ (black, insets), ZnO/C-Ar+W(S)₈₀₀ (red) and ZnO/C-Ar+W(S)₁₀₀₀ (dark blue) and (b) EBGs of these composites calculated by the Kubelka-Munk function (Tauc plots).

To demonstrate the adsorption and photodegradation capacities of the as-synthesised porous ZnO/C nanocomposites, the degradation of MB was carried out in a dark room and under visible light irradiation respectively. To evaluate the photocatalytic activity of each sample, 10 mg of as-prepared sample was added to 50 ml of 20 ppm MB aqueous solution and the mixture was stirred for 3 hours. As shown in Figure 4.11a, under dark conditions, catalysts ZnO/C-Ar₈₀₀, ZnO/C-Ar+W(S)₈₀₀ and ZnO/C-Ar+W(L)₈₀₀ demonstrated a substantial amount of dye adsorption up to 28, 53 and 34 % respectively. On the contrary, ZnO-Air₈₀₀ exhibits almost no adsorption. The samples C-Ar₁₀₀₀, ZnO/C-Ar+W(S)₁₀₀₀ and ZnO/C-Ar+W(L)₁₀₀₀ (Figure 4.11c) adsorbed 79, 89 and 86 % of MB under darkroom conditions respectively except ZnO-Air₁₀₀₀ which showed no adsorption. Moreover, most of MB was adsorbed by porous composites in the first 30 to 60 minutes before achieving an adsorption/desorption equilibrium. Obviously, the observed high adsorption of MB in darkroom conditions is mainly due to the high BET surface area of the as-synthesised ZnO/C composites, which

is consistent with the published report.¹⁰¹ To measure the photocatalytic performance of the composites, the photodegradation of MB was carried out under visible light irradiation. While sample ZnO-Air₈₀₀ demonstrated 25% of MB photodegradation in 3 hours, samples ZnO/C-Ar₈₀₀, ZnO/C-Ar+W(S)₈₀₀ and ZnO/C-Ar+W(L)₈₀₀ showed adsorption and photodegradation of 82, 99 and 92 %, respectively (Figure 4.11b). Compared with sample ZnO-Air₈₀₀, sample ZnO-Air₁₀₀₀ showed lower photodegradation capacity (7.5 %) under visible light irradiation, may be due to the formation of large ZnO particles at higher heat process temperature. However, Figure 4.11d shows that the composites C-Ar₁₀₀₀, ZnO/C-Ar+W(S)₁₀₀₀ and ZnO/C-Ar+W(L)₁₀₀₀ exhibited 80, 99 and 85 % of adsorption and photocatalytic degeneration of MB respectively. Comparing the photocatalytic activity of best performing composites ZnO/C-Ar+W(S)₈₀₀ and ZnO/C-Ar+W(S)₁₀₀₀ under dark and visible light, it can be observed that the photodegradation of MB is more dominant in ZnO/C-Ar+W(S)₈₀₀ due to high content of ZnO whereas adsorption is more dominant in ZnO/C-Ar+W(S)₁₀₀₀ due to high content of carbon. From UV-Vis absorption spectra, it is difficult to differentiate between simultaneous adsorption and photodegradation. It is evident that under the appropriate conditions the composites ZnO/C-Ar+W(S)₈₀₀ and ZnO/C-Ar+W(S)₁₀₀₀ with homogeneously dispersed and carbon doped ZnO nanoparticles in the functionalised porous carbon matrix show the best adsorption and photodegradation performance. Apparently, a high surface area composite should show the highest adsorption. However, these samples have not demonstrated the best adsorption and dye degradation of MB. Confirmed by various characterisation techniques (i.e., PXRD, HRTEM, Raman spectroscopy, XPS and FTIR) not only surface areas but other parameters such as pore sizes play a crucial role in adsorption and subsequent dye photodegradation. The presence of carboxylic (-COOH) functional groups and oxygen species on the surface of the catalysts provide active sites that improve the hydrophilic behaviour and facilitates the MB molecules to be accommodated inside the pores and subsequently degraded, which consequently result in the higher photocatalytic performance of composites derived in water vapour atmosphere than the ones prepared in an argon atmosphere.

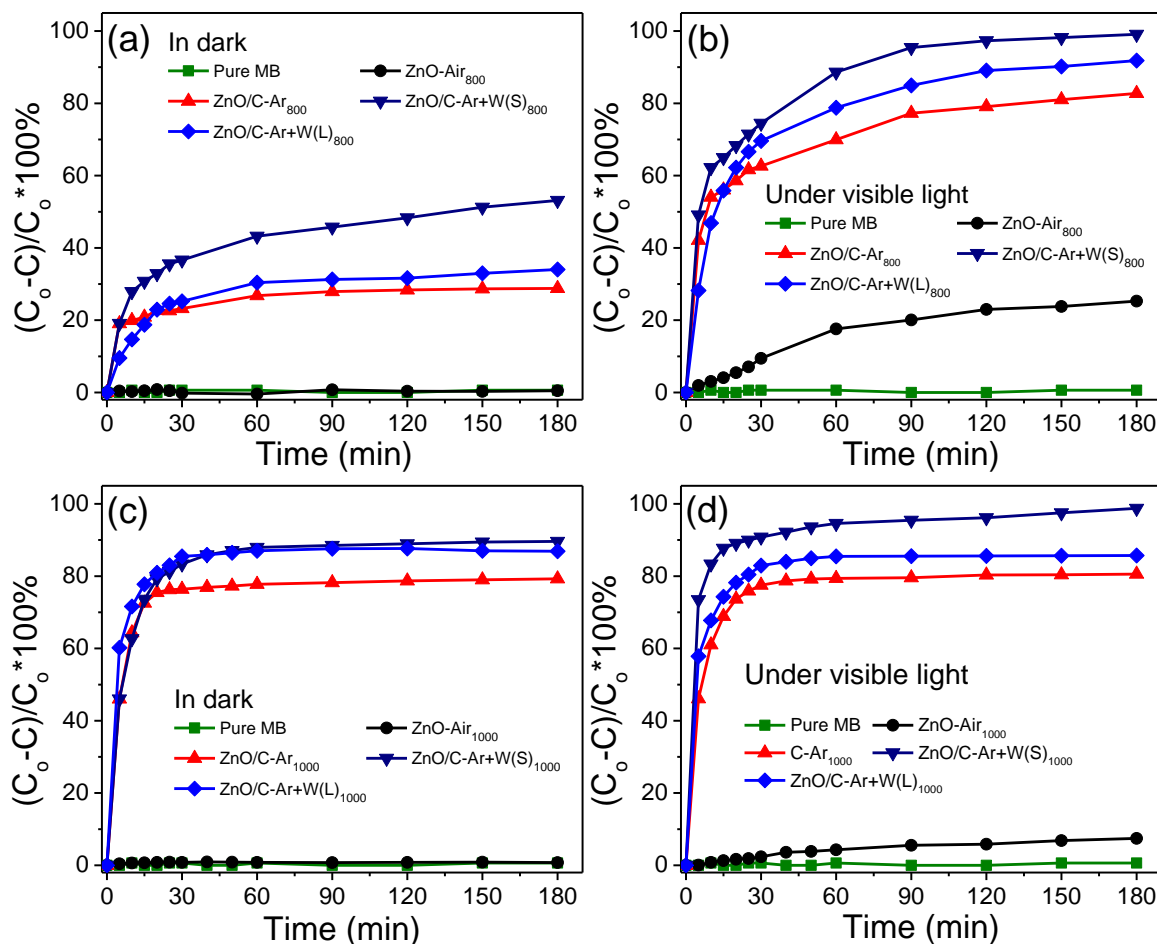


Figure 4.11 The adsorption and photodegradation of MB by ZnO-Air (black circles), ZnO/C-Ar (red triangles), ZnO/C-Ar+W(L) (light blue diamonds) and ZnO/C-Ar+W(S) (dark blue triangles) derived at (a, c) 800 °C and 1000 °C in dark and (b, d) under visible light irradiation respectively. Green squares represent blind test without any catalysts.

It has been reported that the decolourisation of organic dyes could take place due to a self-sensitisation mechanism.¹¹⁷ Organic dyes show light absorption in the visible light region, therefore the charge excitation takes place in the organic dye molecules, resulting in the formation of unstable cation radicals on the surface of the catalyst. These generated active species attack the dye molecules leading to the decolourisation of the dye without mineralisation. The newly produced secondary products could be toxic. This mechanism can prevent the complete mineralisation of the organic dye into neutral species such as CO₂ and H₂O by actual photocatalysis.¹¹⁷ To confirm that the MB was completely neutralised by photocatalytic degradation, 25 mL of pure MB was placed under the visible light for 3 hours and the intensity of the absorption peaks was recorded

by UV-Vis spectrophotometry. There was no change in intensity of the MB for 3 hours which confirmed that the MB did not self-sensitise as shown in Figure 4.11a-d. The proposed mechanism of dye photodegradation by ZnO/C composites is shown in Figure 4.12. Due to the doping of anionic carbon, the valence band of ZnO shifts upwards, resulting in the narrow EBG. It can be expected that with the decrease of EBGs, these homogeneously distributed ZnO nanoparticles in porous carbon can absorb more visible light which will result in improved photocatalytic performance.

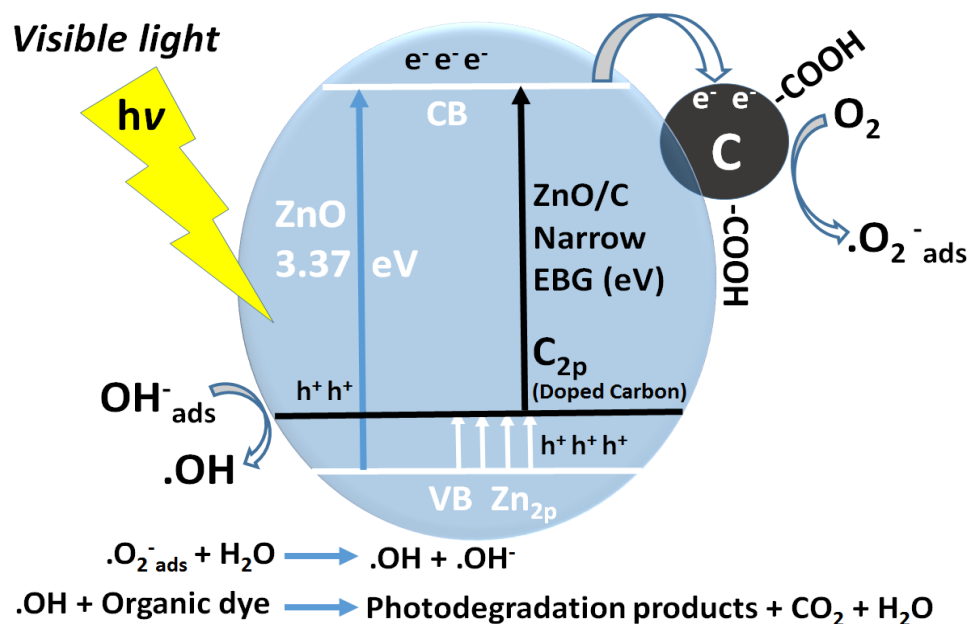


Figure 4.12 Proposed mechanism of dye photodegradation by MOF-5 derived ZnO/C composites under visible light irradiation.

To study the stability and reusability of the composites, selected ZnO/C-Ar+W(S)₁₀₀₀ was tested for 5 consecutive photodegradation cycles. For the reusability test, 30 mg of the catalyst was put into 150 mL of 20 ppm MB solution and stirred for 3 hours. After each cycle, the used catalyst was filtered from the solution, washed several times with deionised water and dried overnight at 110 °C before using for the next run. Figure 4.13a shows that the nanocomposite retains the efficiency over the whole five cycles with only negligible decreases. The 5th cycle showed 95% photodegradation, signifying good stability and reusability of the ZnO/C-Ar+W(S)₁₀₀₀ nanocomposite. Besides, the UV-Vis absorption spectra shown in Figure 4.13b confirmed that the absorption intensity decreases with time during the photocatalytic MB degradation process, no shift

in the absorbance peak position of MB was observed which indicates that no secondary products were formed due to the decolourisation of the dye molecules. Eventually, MB dye molecules are completely mineralised and led to the complete removal of MB from water. Table 4.1 summarises the BET surface areas, EBGs and photocatalytic performance of the MOF-5 derived composites.

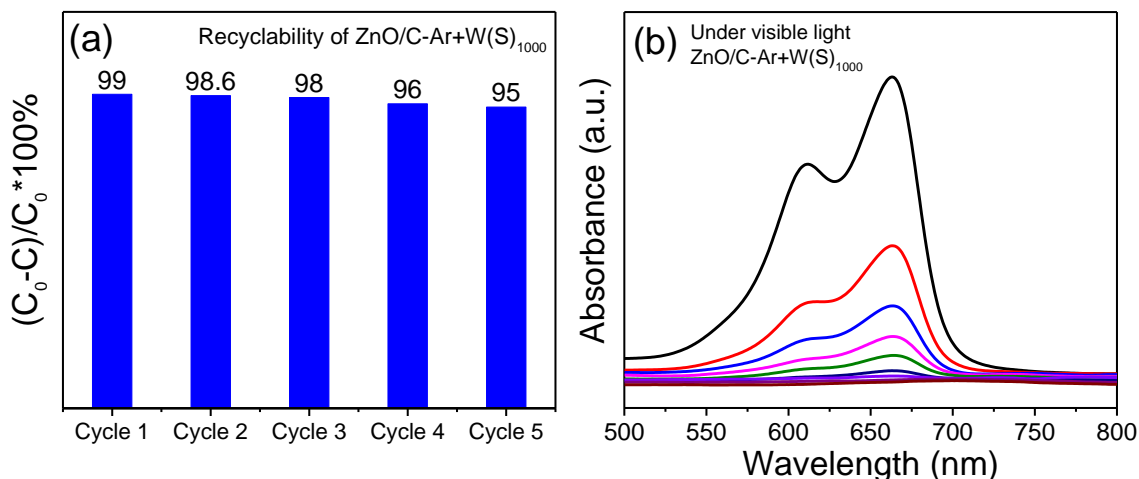


Figure 4.13 (a) Recyclability test of the composite $\text{ZnO/C-Ar+W(S)}_{1000}$ for the adsorption and photodegradation of MB in water under visible-light irradiation for 180 min (b) UV-Vis absorption spectra of adsorption and photodegradation of $\text{ZnO/C-Ar+W(S)}_{1000}$ with time $t = 0$ to 180 min.

Table 4.1 Summary of the BET surface areas, EBGs and photocatalytic performance of the MOF-5 derived composites.

Sample	BET surface area ($\text{m}^2 \text{g}^{-1}$)	EBGs (eV)	Photocatalytic efficiency (%)
ZnO/C-Ar_{800}	369	-	82
$\text{ZnO/C-Ar+W(S)}_{800}$	350	3.0	99
$\text{ZnO/C-Ar+W(L)}_{800}$	210	-	92
C-Ar_{1000}	2839	-	80
$\text{ZnO/C-Ar+W(S)}_{1000}$	2390	3.1	99
$\text{ZnO/C-Ar+W(L)}_{1000}$	2600	-	85

4.3 Summary

The ZnO/C nanocomposites were successfully synthesised by simple one-step pyrolysis of MOF-5 in different carbonisation atmospheres. The ZnO/C composites with different carbon/metal oxide ratios are formed when derived at 800 °C and 1000 °C in air, argon and water vapour atmospheres respectively. After the carbonisation process, the inherent porosity and cubic morphology of precursor MOF-5 retained in the resulting composites. All the composites demonstrated high photocatalytic activity compared to the pure ZnO nanoparticles obtained by heat treatment of MOF-5 in air. The composite derived at 800 °C in argon saturated with water vapour for a short duration (1 h) outperformed all the other composites regarding the photocatalytic MB degradation. Defects in the crystalline structure of carbon doped ZnO and the presence of oxygen-containing hydrophilic -COOH functional groups on the surface of the composite function as traps for dye molecules and facilitate their photodegradation.

Chapter 5

A comparative study of three Zn-MOFs derived ZnO/C nanocomposites for photocatalytic applications

5.1 Introduction

In the past 20 years, metal-organic frameworks (MOFs) have emerged as one of the most exciting advanced materials due to their exceptional textural properties, high thermal stabilities and a wide range of promising applications in energy and environmental applications such as fuel cells, photodegradation of pollutants, photocatalytic H₂ evolution reactions (HER) and O₂ evolution reactions (OER) from water splitting.^{39, 69, 223-225} However, many MOFs are not stable upon interacting with water molecules. Moreover, they exhibit wide EBGs which limit their potential to replace conventional metal oxide nanoparticles based photocatalysts. On the other hand, the conventional metal oxide photocatalysts also face serious limitations due to their low surface areas, agglomerations of particles and inadequate active sites.

To overcome these challenges, researchers made efforts to synthesise metal-oxide/carbon composites, which may be highly efficient in photocatalytic applications due to the synergistic effect of the textural and semiconducting properties.^{107, 226} However, the physical and mechanical mixing approaches do not produce a homogeneous distribution of metal oxides in a carbon matrix. Therefore, poor interfacial contacts between metal-oxide and carbon result in meagre photocatalytic performances of those composites. In the past several years, metal-oxide/carbon composites derived from MOFs emerged as a new class of materials to offer homogeneously distributed metal oxide nanoparticles in a porous carbon matrix. Zn-based MOFs such as MOF-5, MOF-74 and ZIF-8 can generate robust, high surface area ZnO/C composites with cubic, spherical and hexagonal morphologies respectively. Figure 5.1 shows the chemical structures of metal clusters (SBUs), organic linkers and the Zn-MOFs, MOF-5, MOF-74 and ZIF-8.

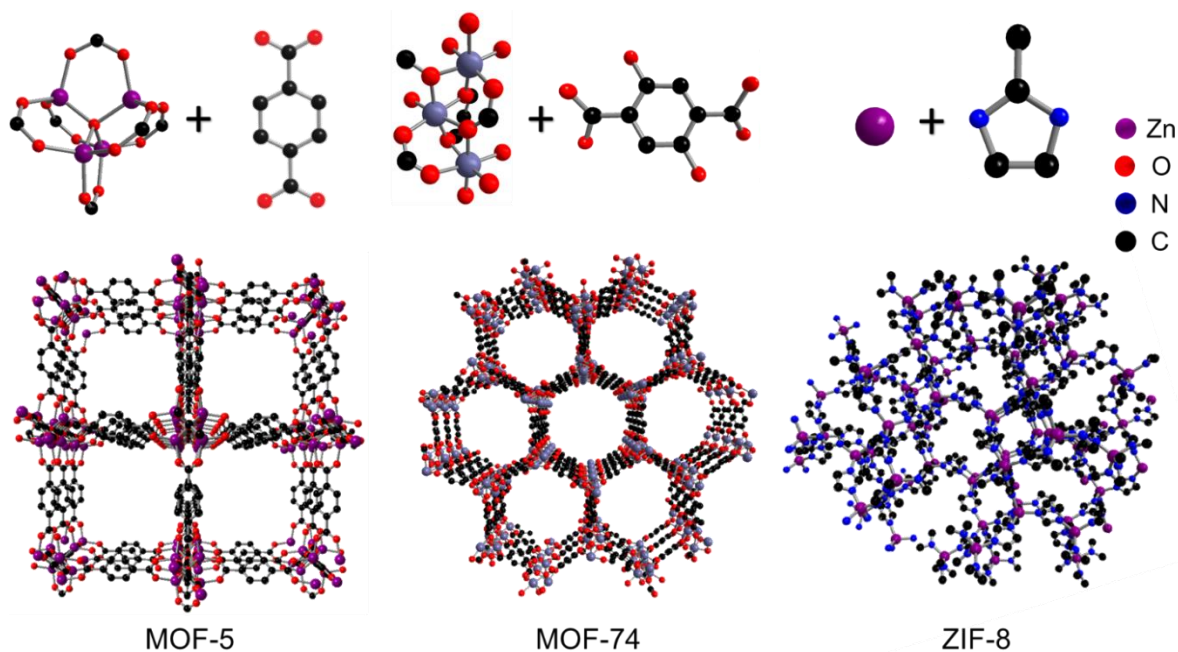


Figure 5.1 Chemical structures of metal clusters ($Zn_4O(CO_2)_6$ for MOF-5 and $Zn_3[O_3(CO_2)_3]$ for MOF-74), organic linkers ($C_8H_6O_4$ for MOF-5, $C_8H_6O_6$ for MOF-74 and $C_4H_6N_2$ for ZIF-8) and the respective MOF-5, MOF-74 and ZIF-8.

Some studies have been reported on the MOFs derived ZnO/C nanocomposites for photocatalytic and photoelectrochemical H_2 evolution.^{55, 101, 131, 227-229} However, there are hardly any studies available that explore the structure-property-application relationship of MOF precursors and their derived ZnO/C composites. It is of utmost importance to understand how the transformation from MOFs to ZnO/C takes place upon high-temperature pyrolysis in a certain gaseous atmosphere. During the carbonisation process, how does the MOF decomposition lead to the formation of metal oxide/carbon structures and what are the relationships between those ZnO/C composites derived from different Zn-MOFs precursors and their photocatalytic performance?

This chapter addresses these questions via systematic investigation of the formation of ZnO/C composites upon carbonisation of MOF-5, MOF-74 and ZIF-8. Built on the understanding of the role of crystal structures and morphologies of the MOF precursors, this comparative study correlates some primary parameters such as morphology, the crystallinity of derived composites, metal oxide and carbon compositions, structural and textural properties, N and/or C doping, functionalities attached on the surface of the porous carbon matrix and their chemical properties, and understand their role in the photocatalytic performance

of these MOFs derived ZnO/C composites. Moreover, the research findings from this work combined with an understanding of the structure-application relationship of the studied materials will help to build up and select appropriate precursors and sacrificial templates to derive modifiable metal oxide/carbon composites with required properties for specific applications.

5.2 Results and discussion

5.2.1 Characterisations of MOFs and derived ZnO/C composites

The PXRD patterns of as-synthesised MOF-5, MOF-74 and ZIF-8 are shown in Figure 5.2a. The main peaks appeared at 2θ of 6.7° , 9.6° and 13.6° for MOF-5, at 6.7° and 11.7° for MOF-74 and 7.9° , 11.9° and 14.9° for ZIF-8, confirm the formation of well crystalline structures.^{131, 227, 228} The MOF-5 and MOF-74 derived composites show main PXRD peaks of crystalline ZnO at 2θ of 31.7° , 34.4° and 36.2° (Figure 5.2b) which correspond to (100), (200) and (101) of wurtzite ZnO. However, no peaks of ZnO are observed in ZIF-8 derived ZnO/C_{ZIF-8}. The absence of ZnO peaks might be due to the poor crystallinity of fine ZnO nanoparticles which are largely embedded in the porous carbon matrix. However, a broad peak observed at around 2θ of 24° and a very low intensity bump at 2θ of 44° which can be indexed to (002) and (101) of amorphous carbon, formed upon the decomposition of the organic linker. These low intensity broad peaks of carbon are suppressed in samples ZnO/C_{MOF-5} and ZnO/C_{MOF-74} due to the relatively high intensity peaks of ZnO nanoparticles. The presence of carbon in all the derived composites is confirmed by TGA, XPS and Raman spectra. The amplified region (inset in Figure 5.2b) shows that the relative intensity and the location of the main XRD peak at 2θ of 36.24° in samples ZnO/C_{MOF-5} and ZnO/C_{MOF-74} are almost identical, indicating the formation of similar crystalline structures of ZnO nanoparticles upon carbonisation of MOF-5 and MOF-74 at 800°C in water vapour saturated argon.

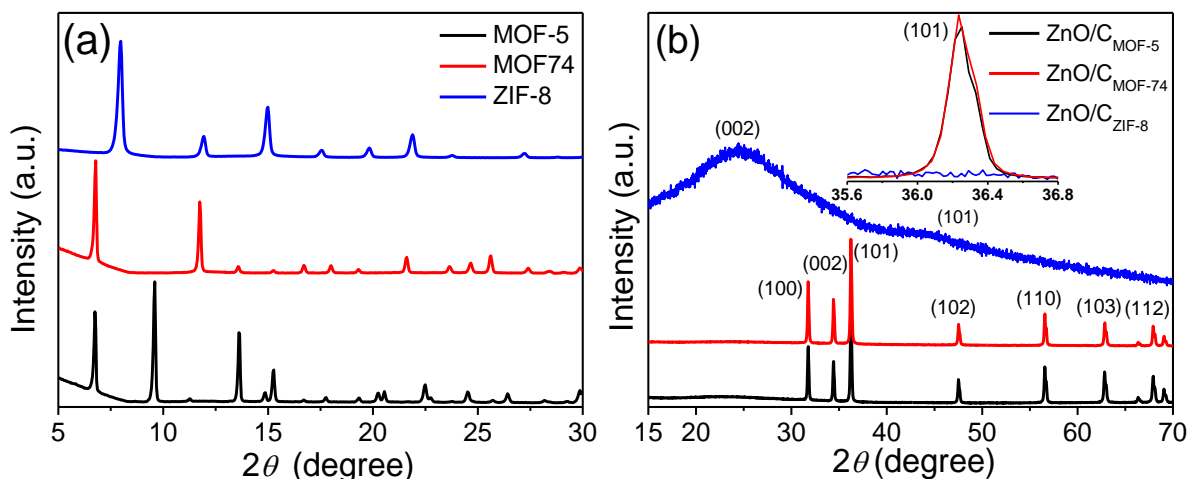


Figure 5.2 PXRD patterns of (a) as-synthesised MOF-5, MOF-74 and ZIF-8 and the (b) derived nanocomposites ZnO/C obtained at 800 °C under water vapour atmosphere. MOF-5 and ZnO/C_{MOF-5} are represented in black, MOF-74 and ZnO/C_{MOF-74} in red while ZIF-8 and ZnO/C_{ZIF-8} in blue respectively. Miller indices of the lattice plane reflections of the wurtzite ZnO are presented in brackets. The inset in (b) is the amplified PXRD pattern of ZnO peak (101).

TGA was carried out under air (Figure 5.3) to determine the thermal stabilities as well as the amount (wt.%) of metal oxide and carbon present in the precursor MOFs and their derived composites. Since the as-synthesised MOF-5, MOF-74 and ZIF-8 were washed with DMF followed by washing with methanol, the first weight loss between 100 and 200 °C for MOFs in Figure 5.3a is due to the removal of the residual solvent. As shown in the inset to Figure 5.3a, after drying at 70 °C overnight, there was 2.5 % chloroform and 4.5 % DMF left in the pores of MOF-5. In MOF-74, almost all the DMF was exchanged with methanol, which evaporated (7 wt.%) below 100 °C. However, ZIF-8 showed only 2 wt.% weight loss around 150 °C due to the removal of the residual methanol in the pores.

The second major weight loss in MOFs precursor is witnessed due to the decomposition of the organic linker molecules and the evaporation of carbon (and nitrogen in ZIF-8) species in the form of CO_x and NO_x. A weight loss of 50.6 % for MOF-5 at 400 °C, 51 % for MOF-74 at 250 °C whereas 62 % for ZIF-8 at 350 °C was observed respectively. The TGA profile indicates that among these MOFs, MOF-5 is thermally more stable with 47.4 wt.% of ZnO content, whereas

MOF-74 is thermally least stable with residual 42 wt.% of ZnO content and ZIF-8 showed relatively moderate thermal stability with 35.8 wt.% ZnO content.^{101, 228,}

230

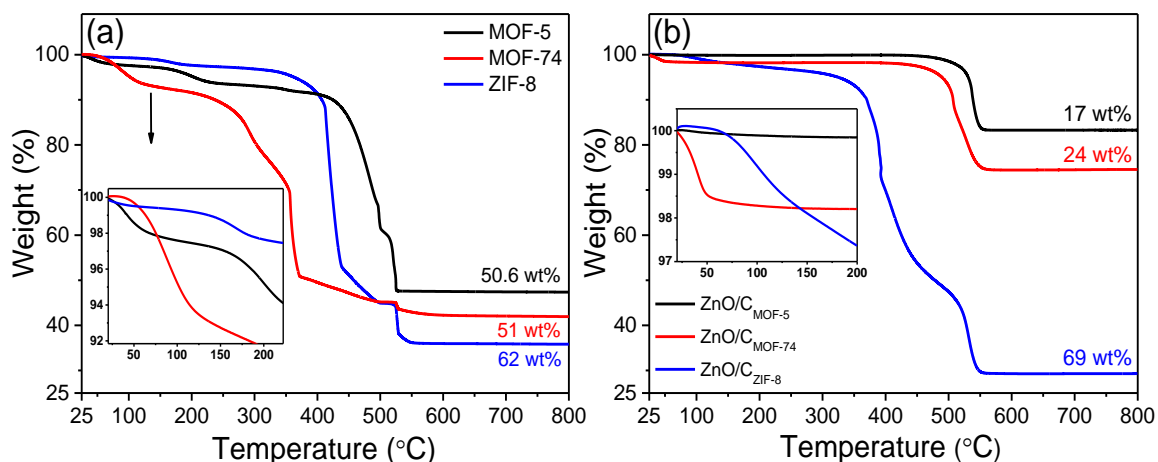


Figure 5.3 TGA profiles of (a) MOFs and (b) derived composites obtained at 800 °C under water vapour atmosphere. MOF-5 and ZnO/C_{MOF-5} are represented in black, MOF-74 and ZnO/C_{MOF-74} in red while ZIF-8 and ZnO/C_{ZIF-8} in blue respectively.

The ZnO/C composites derived from different MOFs demonstrated interesting TGA profiles under air. As shown in Figure 5.3b, all these composites ZnO/C_{MOF-5} , ZnO/C_{MOF-74} and ZnO/C_{ZIF-8} show less than 2 % weight loss at a temperature below 200 °C due to the removal of adsorbed moisture. Moreover, ZnO/C_{MOF-5} showed a steep weight loss of 17 wt.% at 540 °C leaving 83 wt.% of ZnO nanoparticles, while the composite ZnO/C_{MOF-74} exhibited a weight loss of 24 wt.% at 520 °C. The remaining species were ZnO nanoparticles (74.5 wt.%) as confirmed by PXRD. However, the ZnO/C_{ZIF-8} demonstrated the highest weight loss of 69 wt.% in two steps at 380 °C and 540 °C which is due to the higher amount of carbon present in these samples. Moreover, the presence of N species (from the organic linker, 2-methylimidazole) also contributes to the overall weight loss. In ZnO/C_{ZIF-8} , the residual ZnO nanoparticles were 29 wt.%.

As PXRD and TGA confirm that there is different wt.% of ZnO and carbon in these Zn-MOFs, the correlation between MOFs precursor and the derived ZnO/C composites can be understood through the molecular structures of secondary building units (SBUs) which constitute a MOF. As shown in Figure 5.4a, MOF-5 is constituted of SBUs where the Zn_4O tetrahedra make a tetramer

cluster of $Zn_4O(CO_2)_6$ linked through six bidentate linear benzene-1,4-dicarboxylate ($C_8H_6O_4$) linkers arranging in a cubic geometrical order.^{24, 33} Upon carbonisation of MOF-5 at higher temperatures (above 400 °C) under an inert atmosphere, thermal decomposition of MOF-5 takes place due to the breaking of carboxylic bridges between Zn_4O cluster and benzene rings of the organic linkers. As reported by Zhang *et al.*, the collapse of frameworks of MOF-5 could follow three types of the partial breaking of carboxylic bridges: **(1)** Zn-O bond between a carboxylic group and Zn_4O cluster, **(2)** C-O bond of a carboxylic group and **(3)** C-C bond between the benzene ring and carboxylic group.²³⁰ The decomposition of MOF-5 and chemical composition of the derived ZnO/C was further confirmed by FTIR and Raman spectra.

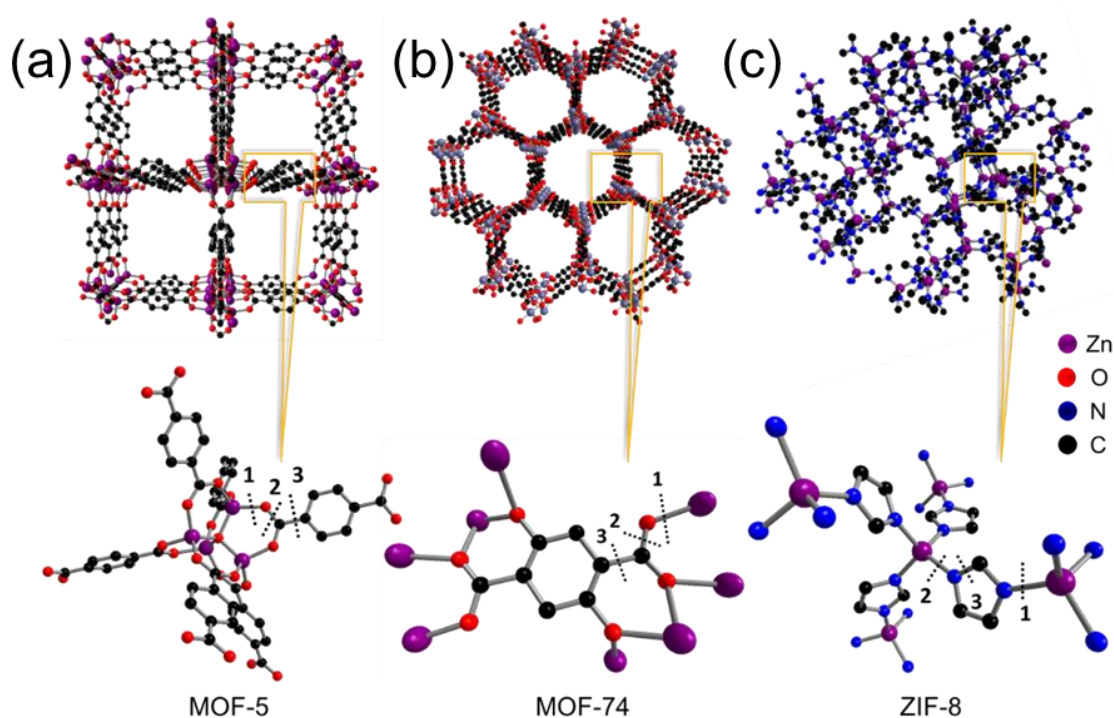


Figure 5.4 The SBUs of Zn ions and organic linkers in crystal structures of (a) MOF-5 (b) MOF-74 and (c) ZIF-8 and the proposed decomposition mechanisms 1, 2 and 3.

The molecular structure of MOF-74 is based on coordinated carboxyl ($-COOH$) and hydroxyl ($-OH$) groups. Helical Zn-O-C rods are fabricated from 6-coordinated Zn(II) centres, where each Zn has three carboxyl groups. Additionally, there are two doubly bridged hydroxy groups bound. As shown in Figure 5.4b, the helical rods (inorganic SBU $Zn_3[O_3(CO_2)_3]_\infty$) are linked together via the benzene rings of 2,5-dihydroxybenzene-1,4-dicarboxylate (DHBDC) to

form a crystalline 3D honeycomb structure of $\text{Zn}_2(\text{C}_8\text{H}_2\text{O}_6)$ with 1D hexagonal pore channels.²³¹ Julien *et al.* reported that the decomposition of MOF-74 takes place (above 200 °C) in the air with 50 % weight loss (wt.%) due to the release of CO_x species, leaving behind pure ZnO nanoparticles, which is in good agreement with the TGA results shown in Figure 5.3a.²²⁷ Based on these experimental results, the proposed decomposition mechanism for MOF-74 can occur via three types of carboxylic and hydroxyl bond breaking: **(1)** Zn-O bond between carboxyl/hydroxyl groups and ZnO_6 octahedral cluster, **(2)** C-O bond of the carboxyl group and **(3)** C-C bond between the benzene ring and carboxyl/hydroxyl group. Similar to MOF-5, the release of CO_2 during exothermal decomposition of MOF-74 suggests that the predominantly bond breaking takes place at positions 1 and 3. As confirmed by TGA and XRD results, a significant amount (74.5 wt.%) of well crystalline ZnO nanoparticles surrounded by carbon was formed at 800 °C under water vapour with preserved overall morphology, which may suggest that the partial breaking of C-O bonds also takes place at position 2 with majority of bonds break at positions 1 and 3.

Figure 5.4c shows the crystal structure of ZIF-8 with sodalite topology. Analogous to zeolites, Zn^{2+} ions in ZIF-8 are coordinated to four nitrogen atoms of imidazole ligands forming the $\text{Zn}(\text{C}_4\text{H}_5\text{N}_2)_2$. James *et al.* reported that carbonisation of ZIF-8 at 300 °C under argon atmosphere leads to the decomposition/disordering of methyl groups and imidazole ring-ring interactions.²³² Xu *et al.* confirmed the decomposition of ZIF-8 under air goes through three steps: a) displacement of methyl groups around 200 °C without collapse of the framework but thermal expansion is the main change to the ZIF-8 lattice; b) further thermal expansion and dislodgement of methyl groups above 300 °C, and finally c) collapse of ZIF-8 framework at temperatures higher than 350 °C and transformation to ZnO at above 400 °C in air.²³³ Based on these observations, three types of bond breakings are possible: **(1)** CH_3 -C detachment, **(2)** Zn-N bond, **(3)** C=N bond of the imidazole ring.²³⁴ These observations are in good agreement with reported experimental results.¹⁰¹ Compared to composites $\text{ZnO}/\text{C}_{\text{MOF-5}}$ and $\text{ZnO}/\text{C}_{\text{MOF-74}}$, composite $\text{ZnO}/\text{C}_{\text{ZIF-8}}$ contains relatively low wt.% (35.8 %) of ZnO, because most of the oxidative interactions occur at methyl substituents of imidazole ligand. Moreover, the lower stoichiometric ZnO nanoparticle formation can be attributed to the deficiency of oxygen and Zn^{2+} ions

in precursor ZIF-8 [$\text{Zn}(\text{C}_4\text{H}_5\text{N}_2)_2$]. The TGA, PXRD and XPS results reported in this chapter are in good agreement with the previously published reports.^{101, 131, 233, 234}

The chemical states and elemental compositions of $\text{ZnO}/\text{C}_{\text{MOF-5}}$, $\text{ZnO}/\text{C}_{\text{MOF-74}}$ and $\text{ZnO}/\text{C}_{\text{ZIF-8}}$ were investigated by XPS. The elemental survey (Figure 5.5a) shows that Zn, O and C in all samples are present. As expected, a strong peak of N (coming from imidazole linkers) is observed in sample $\text{ZnO}/\text{C}_{\text{ZIF-8}}$. Figure 5.5b shows that the intensity of Zn $2p_{3/2}$ peak is lowest in $\text{ZnO}/\text{C}_{\text{ZIF-8}}$, moderate in $\text{ZnO}_{\text{MOF-74}}$ but highest in $\text{ZnO}_{\text{MOF-5}}$. As confirmed by TGA, it may be due to the ZnO content in these samples, $\text{ZnO}/\text{C}_{\text{MOF-5}} > \text{ZnO}/\text{C}_{\text{MOF-74}} > \text{ZnO}/\text{C}_{\text{ZIF-8}}$. The Zn $2p_{3/2}$ peaks appeared at 1022.1, 1021.9 and 1021.4 eV for $\text{ZnO}/\text{C}_{\text{MOF-5}}$, $\text{ZnO}/\text{C}_{\text{MOF-74}}$, and $\text{ZnO}/\text{C}_{\text{ZIF-8}}$ respectively. The slight difference in Zn $2p_{3/2}$ peaks may be due to the different crystallinity, C and/or N doping and oxygen-related defects present in ZnO nanoparticles. In $\text{ZnO}/\text{C}_{\text{MOF-5}}$ and $\text{ZnO}/\text{C}_{\text{MOF-74}}$ composites carbon is doped in Zn-O crystal lattice creating an energy level above the valence band whereas, in $\text{ZnO}/\text{C}_{\text{ZIF-8}}$, C and N can be co-doped into the Zn-O crystal lattice. The presence of Zn-N bond in $\text{ZnO}/\text{C}_{\text{ZIF-8}}$ indicates that the N dopants are incorporated at O sites.¹³¹ In all three composites, the binding energy difference between Zn $2p_{3/2}$ and Zn $2p_{1/2}$ is measured to be 23 eV, confirming the presence of Zn^{2+} ions.

It is evident from the XPS spectra of O 1s (Figure 5.5c) that the relative intensities of O 1s peaks are in very good agreement with Zn $2p_{3/2}$ peaks in $\text{ZnO}/\text{C}_{\text{MOF-5}}$, $\text{ZnO}/\text{C}_{\text{MOF-74}}$, $\text{ZnO}/\text{C}_{\text{ZIF-8}}$. Upon deconvolution O 1s spectra of $\text{ZnO}/\text{C}_{\text{MOF-5}}$, $\text{ZnO}/\text{C}_{\text{MOF-74}}$ and $\text{ZnO}/\text{C}_{\text{ZIF-8}}$, three peaks appear at around 531.2, 531.8 and 533.3 eV which can be assigned to O^{2-} ions of Zn-O bonds, oxygen vacancies (O_{vac}) and/or Zn-O-C bonds due to carbon doping into Zn-O lattice and the surface adsorbed hydroxyl (-OH) and carbonate (C-O/C=O) species respectively. Since the XPS peaks of O_{vac} and C-dopant are heavily overlapped, it is difficult to distinguish them.^{93, 131, 203} The relative intensity of peak at 533.3 eV in $\text{ZnO}/\text{C}_{\text{MOF-5}}$ is higher compared to $\text{ZnO}/\text{C}_{\text{MOF-74}}$ and $\text{ZnO}/\text{C}_{\text{ZIF-8}}$, indicating the higher concentration of carboxyl functional groups (-COOH) attached to the surface of the porous carbon, which is also confirmed by FTIR spectra. Additionally, the lower intensity and broader O 1s combined with the slightly

shifted Zn $2p_{3/2}$ peaks of ZnO/C_{ZIF-8} indicate that N atoms might be co-doped along with the doped C atoms in Zn-O lattice.

The main C 1s peak (Figure 5.5d) in samples ZnO/C_{MOF-5}, ZnO/C_{MOF-74} and ZnO/C_{ZIF-8} appears at around 284.3 eV, which is assigned to C=C pure graphitic sp^2 bonding. The fitted peak at appearing at 285.76 eV in ZnO/C_{MOF-5} and 285.35 eV in ZnO/C_{MOF-74} and ZnO/C_{ZIF-8} samples correspond to Zn-O-C bond. A low intensity broader peak at around 288.83 eV in ZnO/C_{MOF-5} can be attributed to carboxyl functional groups (O-C=O). This peak showed very low intensity in ZnO/C_{MOF-74} which indicates the smaller number of carboxylic functional groups attached to its surface. However, in ZnO/C_{ZIF-8} a fitted broad peak positioned at 287.5 eV is attributed to C-N/C=O bond.^{93, 234} Combined with other characterisations such as TGA and XRD, the XPS analysis results help to find the nature of crystalline structures of MOF derived ZnO/C composites and suggested that the ZnO/C_{MOF-5} and ZnO/C_{MOF-74} are C doped ZnO composites with carboxylic (-COOH) functional groups attached on the surface of the composite. However, the ZnO/C_{ZIF-8} is an N and C co-doped ZnO/C composite with a negligible amount of carboxyl functional groups attached. As shown in Figure 5.5e, a high intensity peak of N 1s at 398.3 eV is attributed to O-Zn-N, indicating that N might be incorporated into ZnO nanoparticles at O sites.¹³¹ Two low intensity shoulder peaks at 400.28 and 401.98 eV can be assigned to metal nitride and NO_x species respectively. No peaks of N 1s were detected in ZnO/C_{MOF-5} and ZnO/C_{MOF-74}.

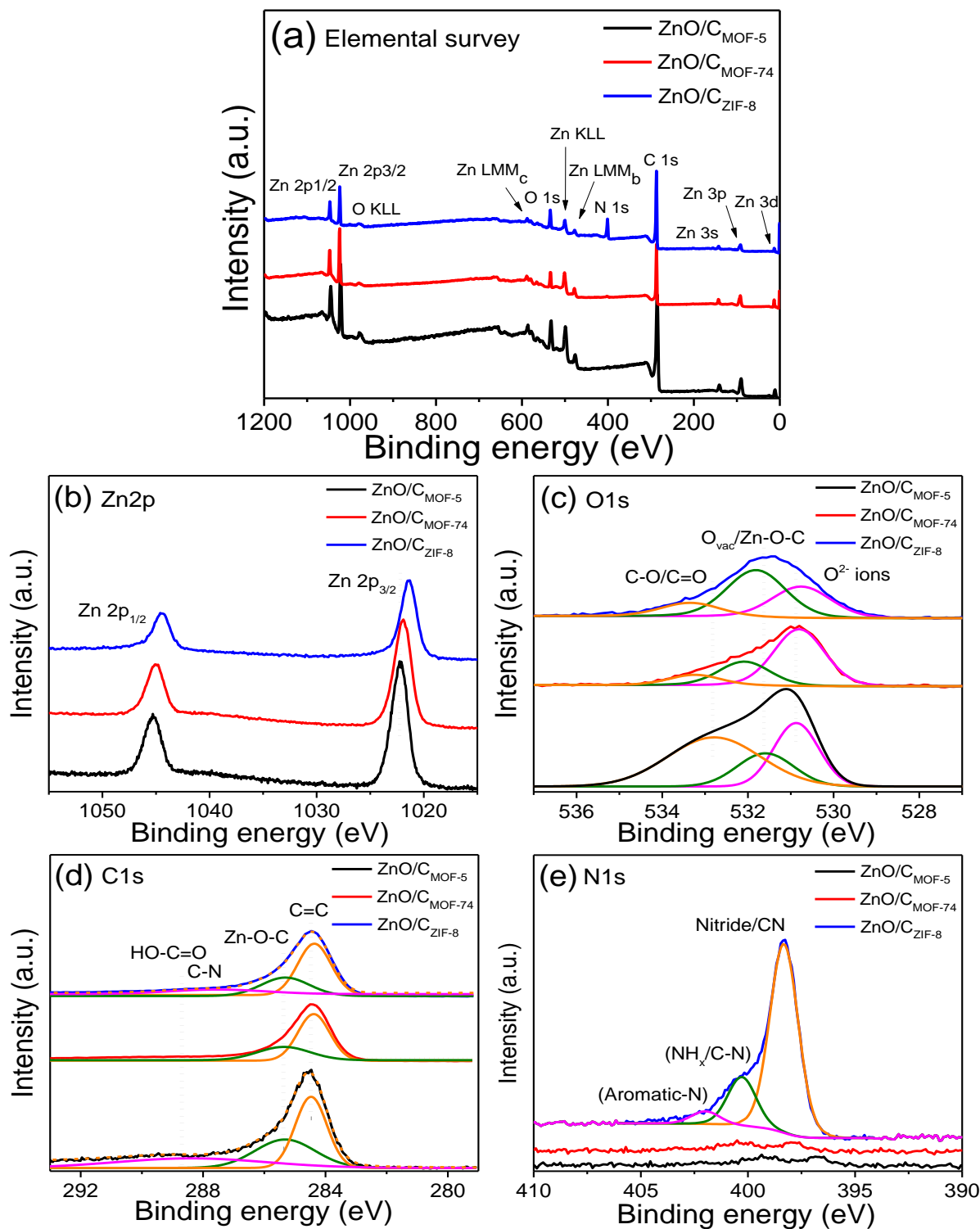


Figure 5.5 XPS spectra of (a) elemental survey (b) Zn 2p (c) O 1s (d) C 1s (e) N 1s for ZnO/C_{MOF-5} (black) and ZnO/C_{MOF-74} (red) and ZnO/C_{ZIF-8} (blue).

The morphologies of the precursor MOFs and derived ZnO/C composites were investigated by SEM. As shown in Figure 5.6, the SEM images confirm that

the morphologies of the MOF-5, MOF-74 and ZIF-8 are preserved in ZnO/C_{MOF-5}, ZnO/C_{MOF-74} and ZnO/C_{ZIF-8} composites derived at 800 °C in water vapour saturated argon. The sizes and shapes of the synthesised precursor MOFs critically depend upon the synthesis parameters. From the SEM images shown in Figure 5.6a-c, the cubic crystals of MOF-5 are in the range of 1 µm whereas the spherical shaped crystals of MOF-74 are around 500 nm. The nanocrystals of ZIF-8 with regular hexagonal shape (confirmed by low magnification TEM) are below 100 nm. As discussed above, carbonisation of MOF-5 at high temperature (above 400 °C) in an inert atmosphere causes the breaking of Zn-O, C-O and C-C bonds leading to decomposition of the MOF crystals forming the relatively shrunk carbon matrix with coarse surfaces (Figure 5.6d). Similarly, MOF-74 and ZIF-8 also preserve their morphologies with relatively coarse surfaces shown in Figure 5.6e and f respectively.

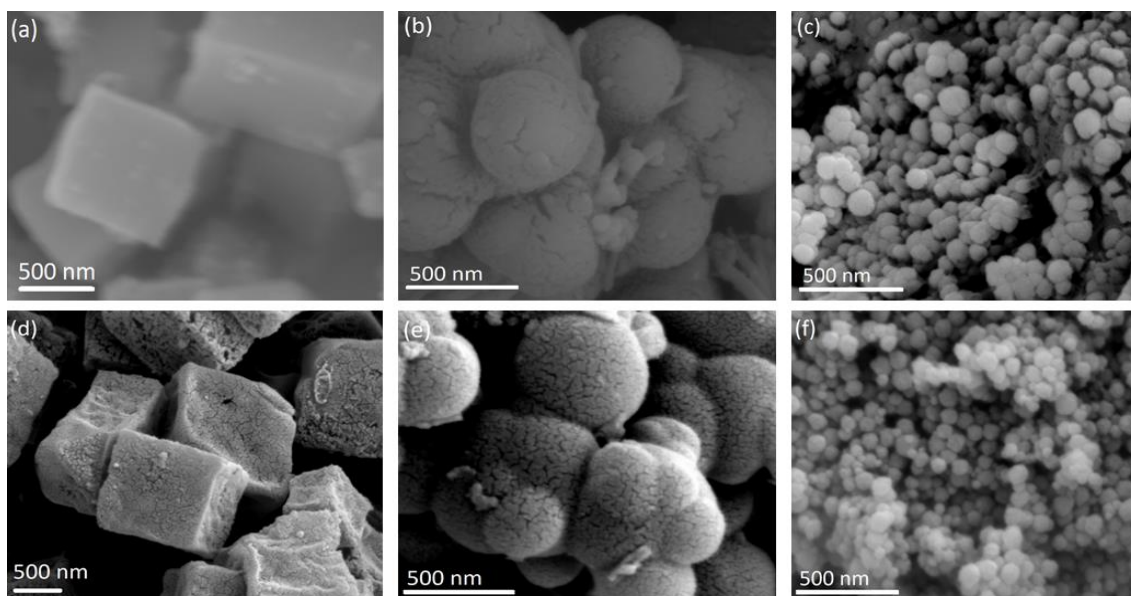


Figure 5.6 SEM micrographs of (a) MOF-5 (b) MOF-74 (c) ZIF-8 (d) ZnO/C_{MOF-5} (e) ZnO/C_{MOF-74} and (f) ZnO/C_{ZIF-8} respectively.

To further investigate the crystal structures and distribution of ZnO in the carbon matrix, TEM and EDX elemental mapping were employed. Figure 5.7 shows the TEM images of ZnO/C_{MOF-5}, ZnO/C_{MOF-74} and ZnO/C_{ZIF-8} composites. From Figure 5.7a, c and e, it is clear that all three MOFs derivatives exhibit homogeneously distributed ZnO nanoparticles with sizes less than 10 nm embedded in a porous carbon matrix without agglomerations. The lattice spacing between lattice fringes of (101) for ZnO is 0.258 nm in C doped ZnO/C_{MOF-5} and

0.259 nm in C doped ZnO/C_{MOF-74} sample, which is larger than that of the (101) for pure ZnO nanoparticles (0.24 nm).^{2, 212} The increase in lattice spacing between the lattice fringes of ZnO/C_{MOF-5} and ZnO/C_{MOF-74} suggests the strain on nanoparticles created by the doped C species in these samples.^{212, 219} The lattice spacing of carbon fringes in ZnO/C_{ZIF-8} is around 0.35 nm, which confirms the amorphous nature of carbon matrix upon carbonisation of MOFs. These findings combined with the results of PXRD and XPS suggest that ZnO nanoparticles in ZnO/C_{MOF-5} and ZnO/C_{MOF-74} are well crystalline while only a small amount of poorly crystalline ZnO nanoparticles is preserved in ZnO/C_{ZIF-8}.

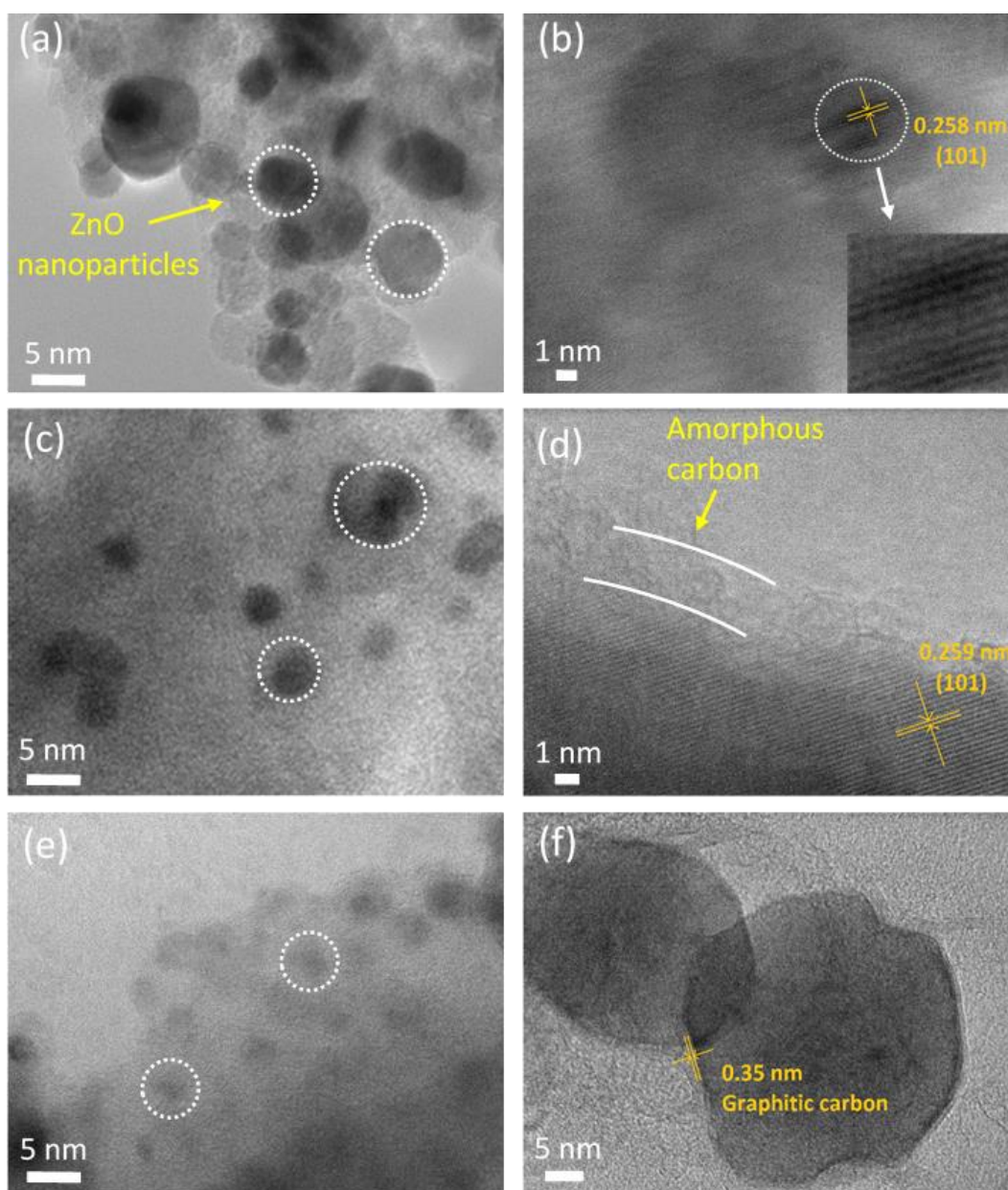


Figure 5.7 HRTEM micrographs of (a, b) ZnO/C_{MOF-5} (c, d) ZnO/C_{MOF-74} and (e, f) ZnO/C_{ZIF-8} respectively.

Figure 5.8 represents the energy-dispersive X-ray spectroscopy (EDX) element mapping of ZnO/C_{MOF-5}, ZnO/C_{MOF-74} and ZnO/C_{ZIF-8} composites respectively. The elemental maps of C, Zn and O for all the 3 composites exhibit similar patterns to their TEM images. Additionally, N is uniformly presented in sample ZnO/C_{ZIF-8}.

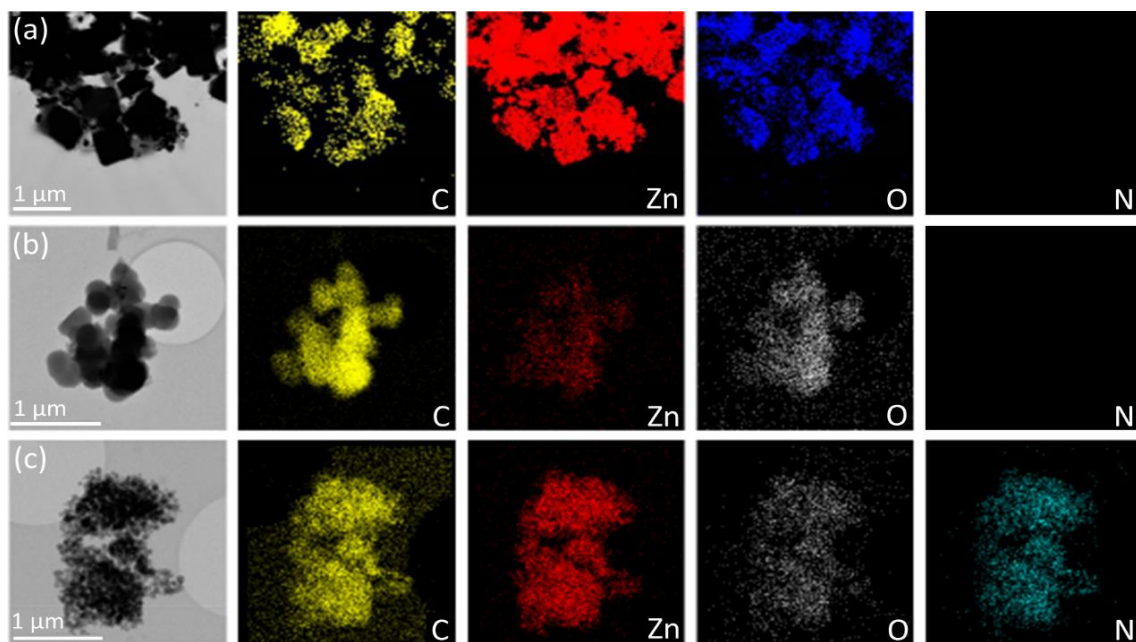


Figure 5.8 Low magnification TEM micrographs and their respective EDX elemental mappings of (a) ZnO/C_{MOF-5} (b) ZnO/C_{MOF-74} and (c) ZnO/C_{ZIF-8}. The coloured images show the distribution of elements throughout the composite. Here, C, Zn, O and N are represented in yellow, red, blue/grey and cyan colours respectively.

To further investigate the ZnO, nature of carbon and carboxyl functional groups attached to the surfaces of the derived ZnO/C_{MOF-5}, ZnO/C_{MOF-74} and ZnO/C_{ZIF-8} composites, Raman and FTIR spectra were recorded. The main Raman peaks of ZnO nanoparticles (Figure 5.9a) appeared at 427.3 and 320.1 cm^{-1} in ZnO/C_{MOF-5} which correspond to $E_2(\text{high})$ and $A_1(\text{TO})$ vibrational modes respectively. The bulk ZnO exhibits $E_2(\text{high})$ mode at 437 cm^{-1} . However, in ZnO/C_{MOF-74} and ZnO/C_{ZIF-8}, $E_2(\text{high})$ mode appears at 428.4 and 431.7 cm^{-1} while $A_1(\text{TO})$ mode appeared at 321.2 cm^{-1} respectively. The low intensity of ZnO peaks in ZnO/C_{ZIF-8} also confirms the relatively poor crystallinity of ZnO nanoparticles observed in PXRD. Moreover, the appearance of $E_2(\text{high})$ vibrational mode at a different frequency in ZnO/C_{ZIF-8} might be due to the

dissimilar doping profile as compared to ZnO/C_{MOF-5} and ZnO/C_{MOF-74}.²¹² The significant redshift indicates the reduced particle sizes compared to the bulk ZnO and the narrowing of EBG due to C and/or N doping in ZnO. The doped C and N atoms may cause a strain that modifies the lattice parameters of ZnO and creates O_{vac} related crystalline defects. Another interesting observation is that sample ZnO/C_{ZIF-8} showed additional peaks at 271 and 574 cm^{-1} , which are not observed in pure ZnO. Numerous reports suggest that these additional peaks come from the activated silent modes $B_1(low)$ and $B_1(high)$ respectively. These modes appear due to the different electronic properties of doped N and the substituted O in ZnO.²³⁵⁻²³⁹ It can be seen (inset in Figure 5.9a) that $B_1(low)$ and $B_1(high)$ modes are also not observed in ZnO/C_{MOF-5} and ZnO/C_{MOF-74}. Furthermore, the $E_2(M)$ multi-phonon vibrational modes appearing at 320.1 cm^{-1} are much stronger in ZnO/C_{MOF-5} and ZnO/C_{MOF-74} compared to ZnO/C_{ZIF-8}. This $E_2(M)$ multi-photon mode in ZnO nanoparticles is commonly attributed to the defects and impurities caused by the C doped species.²¹⁹ In pure ZnO, this mode is negligible. As confirmed by UV-Vis absorption spectra, the doping of N into ZnO creates a new energy level above the valence band. It is evident that C acts as a dopant in MOF-5 and MOF-74 derived ZnO/C composites whereas in ZIF-8 derived ZnO/C composites, N is the primary dopant.^{101, 131} It can be concluded that compared to bulk ZnO, the redshift towards lower frequencies in all these MOF derived ZnO/C composites could be an indirect validation of the narrowed EBGs, which is also confirmed by UV-Vis absorption spectroscopy (Figure 5.10).

The two signature peaks of D and G bands of amorphous carbon at around 1350 and 1580 cm^{-1} are observed in all the composites. The D band at around 1350 cm^{-1} in Raman spectra represents the breathing modes of sp^2 hybridised carbon atoms in hexagonal carbon rings and signifies the (diamond-like sp^3 C-C bonds) amorphous carbon. The G band appearing in the range of 1580-1600 cm^{-1} is due to the in-plane bond stretching of all sp^2 bonded atoms in hexagonal carbon rings and chains. The intensity ratio of D and G bands (I_D/I_G) is analogous to the sp^3/sp^2 ratio which is a measure of amorphisation of carbon.¹³¹ The Raman peaks of D and G bands for samples ZnO/C_{MOF5}, ZnO/C_{MOF-74} and ZnO/C_{ZIF-8} appear at a slightly different position with calculated I_D/I_G ratios of 0.91, 1.17 and 1.06 respectively. It suggests that the decomposition of the organic linker (C₈H₆O₄) in MOF-5 at high temperature leads to a collapse of the framework due

to the breaking of C-O and C-C bonds and give relatively graphitic carbon compared to the MOF-74 and ZIF-8 derived composites. During the carbonisation of ZIF-8 under water vapour gaseous atmosphere, the framework collapses by the breaking of Zn-N and C=N bonds of organic linker 2-methylimidazole ($C_4H_6N_2$). The high content of nitrogen presented on the carbon surface increases the sp^3 hybridised C-C bonds, as confirmed by XPS (Figure 5.5e), which enhances the intensity of the D band. The shift of G band position to 1599 cm^{-1} in ZnO/C_{MOF-74} can presumably be due to the indirect influence of sp^3 content. Ferrari *et al.* suggest that the creation of defects, bond length disorder and sp^3/sp^2 hybridisation play a critical role in the amorphisation of carbon. During the conversion of graphite to nanocrystalline carbon, the G band moves from 1581 cm^{-1} to 1600 cm^{-1} , sp^3 bonding grows and the I_D/I_G ratio increases.²¹⁶ Based on these observations, it can be expected that the decomposition of the organic linker ($C_8H_2O_6$) and breakdown of the spherically arranged framework of MOF-74 leads to relatively more amorphous carbon.

The FTIR spectra of ZnO/C_{MOF-5} , ZnO/C_{MOF-74} and ZnO/C_{ZIF-8} composites derived in water vapour atmosphere (Figure 5.9b) exhibit peaks of Zn-O stretching at 459 cm^{-1} . However, very low intensity of this peak observed in ZnO/C_{ZIF-8} is in good agreement with PXRD (Figure 5.2b) and Raman results (Figure 5.9a). Two strong peaks at 1629 and 1047 cm^{-1} in ZnO/C_{MOF-5} correspond to the bond stretching of carboxyl ($O=C-OH$) and C-O/C-OH functional groups on the surfaces of the composite respectively. These peaks show lower intensity in ZnO/C_{MOF-74} and ZnO/C_{ZIF-8} indicating the relatively lower concentration of C-O bonds.²⁴⁰ However, a pair of prominent peaks at around 2850 and 2911 cm^{-1} appeared in ZnO/C_{MOF-74} and ZnO/C_{ZIF-8} composites which can be assigned to the symmetric and asymmetric stretching modes of sp^3 bonded C-H atoms respectively. As shown in Raman results, the D band is stronger in these samples than in ZnO/C_{MOF-5} , which also endorses the amorphous nature of the carbon. To determine whether the photocatalytic degradation of MB can affect the surface chemistry of the tested composites, FTIR spectra of MB and used samples were recorded. As shown in Figure 5.9c, no peaks of MB were observed in ZnO/C_{MOF-5} , ZnO/C_{MOF-74} and ZnO/C_{ZIF-8} after the photocatalytic dye degradation, suggesting the surface functionalities of the composites remain unaffected.

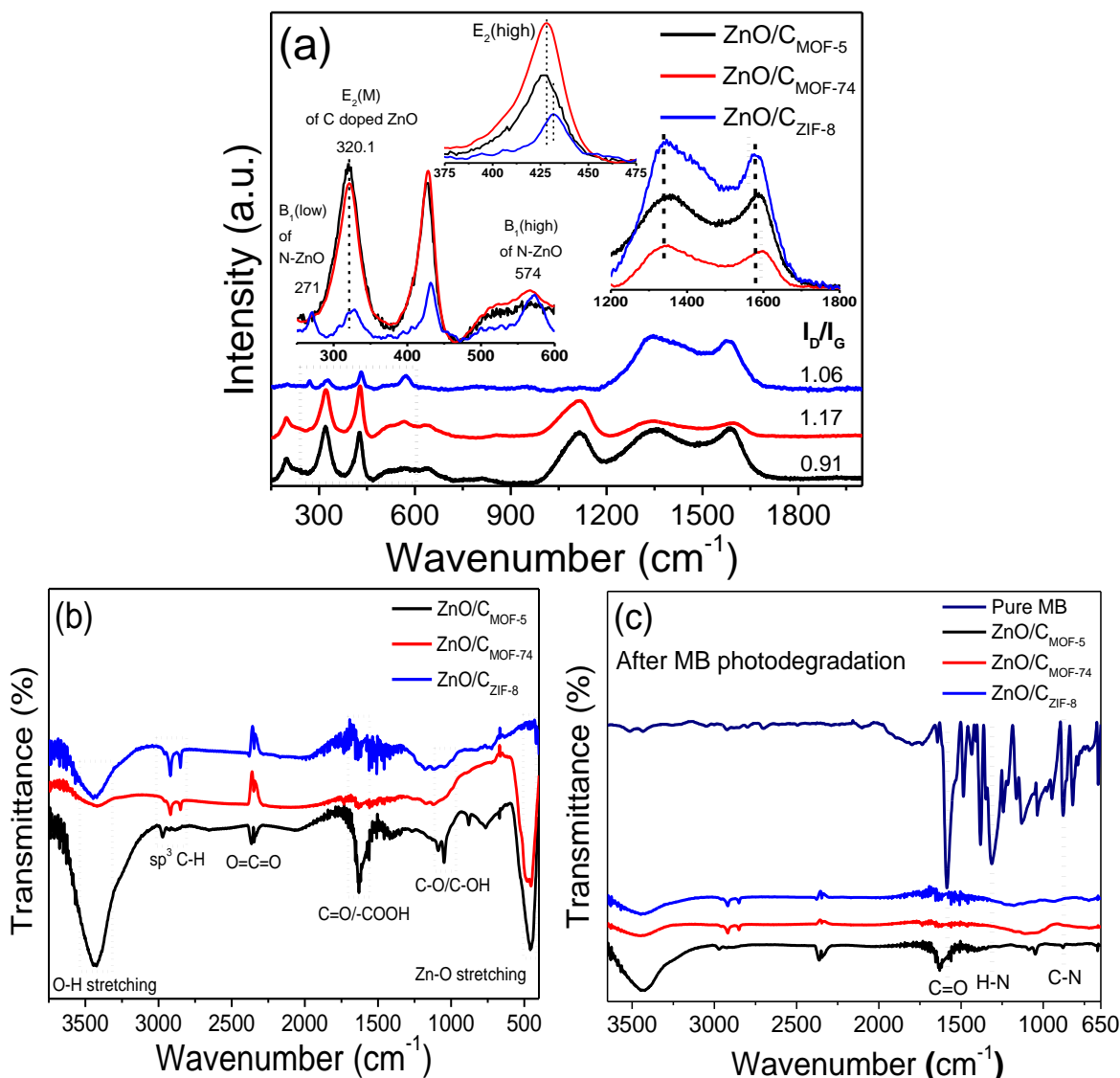


Figure 5.9 (a) Raman spectra of ZnO/C_{MOF-5} (black) ZnO/C_{MOF-74} (red) and ZnO/C_{ZIF-8} (blue). Insets show the highlighted main E₂(high) and E₂(M) modes of ZnO, additional modes (B₁) as well as D and G bands of amorphous carbon (b) FTIR spectra of fresh ZnO/C_{MOF-5} (black), ZnO/C_{MOF-74} (red) and ZnO/C_{ZIF-8} (blue) (c) FTIR spectra of pure MB (navy blue), ZnO/C_{MOF-5} (black), ZnO/C_{MOF-74} (red) and ZnO/C_{ZIF-8} (blue) after dye degradation. These FTIR spectra confirm that all three MOFs derived composites are chemically stable, and no peaks of MB are found after the photocatalytic reactions completed.

The optical properties and EBGs of derived ZnO/C composites were calculated from UV-Vis absorption spectra. In ZnO, the valence band edge comprises O 2p orbitals and conduction band edge of Zn 3d orbitals.²¹² When the dopants are introduced into the crystal lattice, additional electronic states/levels

can be formed below the conduction band or above the valence band. The non-metal dopants such as N and C atoms could form additional interstitial intraband states or substitutional states above the valence band edge by replacing O 2p atoms to form Ti-C or Ti-N bonding states.²¹² As shown in Figure 5.10a, the UV-Vis absorption spectra of ZnO/C_{MOF-5}, ZnO/C_{MOF-74} and ZnO/C_{ZIF-8} appeared at 401, 404 and 431 nm respectively. The overall EBGs of these composites (Figure 5.10b) were estimated (Tauc plots) to be 3.13, 3.11 and 2.97 eV respectively. The redshift in EBGs compared to pure bulk ZnO (3.37 eV) can be assigned to C and/or N doping into the ZnO nanoparticles.²⁰³ The N and C atoms may substitute the O atoms (N→O, C→O) in the ZnO crystal lattice, resulting in the narrowing of the EBG. It is worth noting the EBGs estimated from UV-Vis absorption spectra reflect the overall EBG of the ZnO/C nanocomposite. It is found that regardless of different primary anionic dopants in these composites (C for MOF-5 and MOF-74 derived composites and N for ZIF-8 derived composites), the shift in EBG is in general not very large concerning each other. The relatively larger shift in EBG of ZnO/C_{ZIF-8} could be due to the co-doped N and C atoms into ZnO. Most of the released N during the decomposition of 2-methylimidazole organic linkers at higher temperature is predominately attached to the surface of porous carbon (Raman and XPS spectra). A small amount of N atoms (along with C atoms) is co-doped into the ZnO, which consequently narrow the EBG.^{101, 131} Due to the decrease of EBGs, these homogeneously distributed ZnO nanoparticles in porous carbon matrices absorb more visible light, resulting in improved photocatalytic performance.

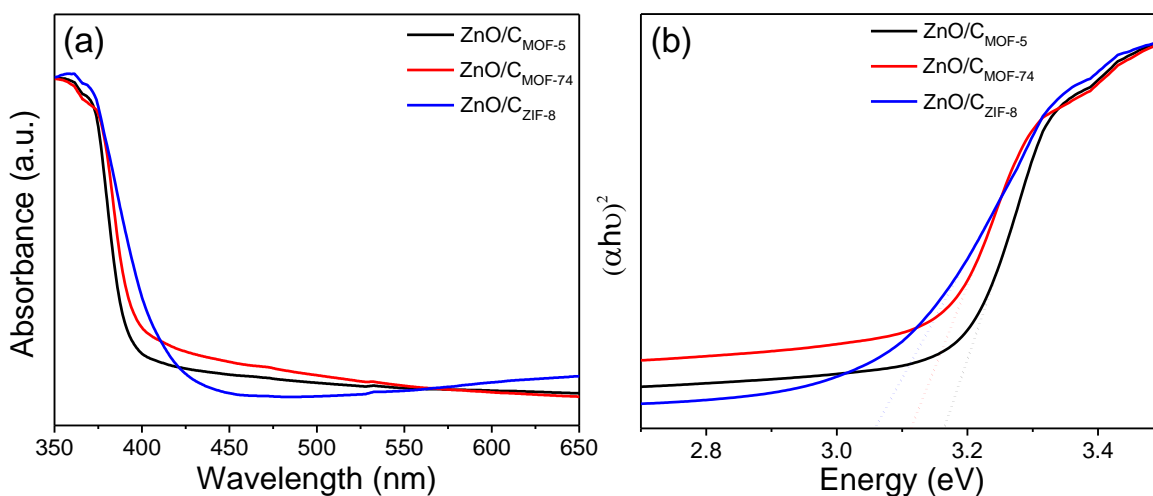


Figure 5.10 (a) The UV-Vis absorption spectra of ZnO/C_{MOF-5} (black), ZnO/C_{MOF-74} (red) and ZnO/C_{ZIF-8} (blue) (b) direct EBGs (Tauc plots) of the composites.

The BET surface areas and PSD of ZnO/C nanocomposites play an important role in adsorption and eventually photodegradation of organic dyes. Figure 5.11a shows the N₂ sorption isotherms at 77K for derived ZnO/C composites. The measured BET surface areas of ZnO/C_{MOF-5}, ZnO/C_{MOF-74} and ZnO/C_{ZIF-8} are 390, 321 and 653 m² g⁻¹, respectively. The qualitative behaviour of isotherms shows that ZnO/C_{MOF-5} displays type IV isotherm with hysteresis above relative pressure (p/p_0) of 0.4, while both ZnO/C_{MOF-74} and ZnO/C_{ZIF-8} exhibit type I isotherms with very small hysteresis at a relative pressure between 0.4 and 0.6, indicating the dominance of micropores with a small volume of mesopores.^{206, 240, 241} The PSD (Figure 5.11b) was calculated by NLDFT method. It can be seen that high N₂ uptake at the lower relative pressure (p/p_0) and linear isotherms (with very small hysteresis loop) demonstrate that micropores are predominated in ZnO/C_{ZIF-8} with pore widths centred at 1.2 and 1.6 nm. However, a small fraction of hierarchical mesopores between 2 and 3.5 nm are also observed. Similarly, ZnO/C_{MOF-74} is dominated with micropores centred at a size of 1.6 nm with a small amount of micropores at 1.2 nm. However, ZnO/C_{MOF-5} exhibited major micropore size at 1.4 nm with a small amount of micropores at 1.7 nm. Additionally, a wide band of hierarchical mesopores between 2.2 and 5 nm are observed due to the evaporation of carbon during pyrolysis, forming a small amount of relatively larger pores.

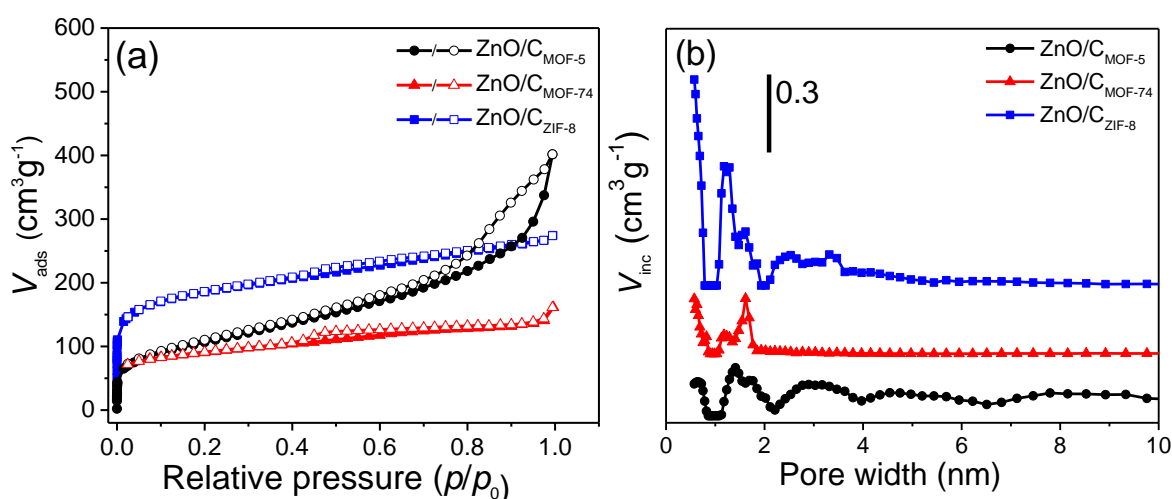


Figure 5.11 (a) N₂ sorption isotherms (at 77 K) and (b) PSD of nanocomposites ZnO/C_{MOF-5} (black circles), ZnO/C_{MOF-74} (red triangles) and ZnO/C_{ZIF-8} (blue squares).

The relationship between pore shapes/sizes of precursor MOF and their derived ZnO/C can be understood by linking the PSD of derived composites with their precursor frameworks. The N₂ sorption isotherms and PSDs of derived ZnO/C composites of MOF-5, MOF-74 and ZIF-8 are in good agreement with pore structures of precursor MOFs. As discussed above and shown in Figure 5.4a, MOF-5, a simple cubic framework consisting of Zn₄O nodes and benzene-dicarboxylate linkers, predominantly possesses an open pore structure, which can allow the small molecules to diffuse into the pores.^{203, 234} The incremental pore volume (Figure 5.11b) shows that after carbonisation at 800 °C under water vapour atmosphere, the organic ligand decomposes and leads to the creation of slightly larger micropores and mesopores. The breakings of Zn-O, C-O and C-C bonds in MOF structure result in partial migration and clustering of Zn atoms from metal centres to the pore cavities. Due to the collapse of the metal cluster-ligand structure, the consequent decomposition of the organic linkers and the migration of Zn species, these pore cavities are randomly blocked, resulting in the decrease in SSAs and the increase in pore sizes of the derivatives relative to their precursors.^{227, 230, 232} Similarly, Zn-N₄ tetrahedra in ZIF-8 are linked through 2-methylimidazole rings forming spherical hexagonal structures with pore size closer to MOF-5. However, ZnN₄-imidazole linked in spherical order (Figure 5.4c) creates more pore openings with a size smaller than that of the cubic shaped MOF-5.^{230, 232} Compared to ZnO/C_{MOF-5} and ZnO/C_{MOF-74}, composite ZnO/C_{ZIF-8} exhibits higher micropore volume and SSA. It is in good agreement with TGA and PXRD results that among these composites discussed here, ZnO/C_{ZIF-8} possesses the least amount of ZnO nanoparticles (35.8 wt.%) upon carbonisation of ZIF-8 at 800 °C in water vapour atmosphere, which results in higher amount (wt.%) of microporous carbon in ZnO/C_{ZIF-8} with increased BET surface area (653 m² g⁻¹).²²⁸

As mentioned above, the pore shapes of MOF-74 are different with respect to the MOF-5 and ZIF-8. Instead of possessing enclosed pores, it consists of long cylindrical channels with 1D hexagonal where metal nodes form the stripes down the channel length as shown in Figure 5.4b.^{210, 242} The narrow pore distribution and the relatively lower BET surface area of the ZnO/C_{MOF-74} (321 m² g⁻¹) as compared to ZnO/C_{MOF-5} and ZnO/C_{ZIF-8}, are related to the lower BET surface area of precursor MOF-74 and its densely packed molecular structure. It can be

assumed that the 1D cylindrical pore structure of MOF-74 does not provide enough path lengths for ZnO nanoparticles to migrate to the cavities upon breaking of C-O, Zn-O bonds and subsequent collapse of the framework, which results in narrow PSD (predominant micropores) and relatively less accessible BET surface area.

5.2.2 Photocatalytic performances of the ZnO/C composites

The composites ZnO/C_{MOF-5}, ZnO/C_{MOF-74} and ZnO/C_{ZIF-8} were tested to study their photocatalytic properties for photodegradation of MB and water splitting for hydrogen (H₂) evolution under visible light. The proposed mechanism of photocatalytic dye degradation and H₂ evolution is shown in Figure 5.12. When the visible light has energy equivalent to or higher than the EBG of ZnO, the energy of visible light is absorbed by the ZnO nanoparticles, the valence band electrons are excited generating electron-hole (e⁻/h⁺) pairs. These photogenerated holes can directly oxidise MB into neutral species. Moreover, these photogenerated holes can also react with water molecules (since the reaction takes place in water) and produce hydroxyl radicals (OH[•]). Simultaneously, photogenerated electrons in the conduction band reduce the oxygen molecules (O₂) to form superoxide ions ([•]O₂⁻). In conventional metal oxide photocatalysts, the recombination of photogenerated e⁻_{CB} and h⁺_{VB} can take place on the surface of the catalyst, which results in a drastic decrease in photocatalytic activity. Also, the metal oxides have high surface energies which tend to agglomerate, therefore providing less access to the photocatalytic active sites. However, in MOF derived composites, metal oxides are uniformly distributed in a porous carbon matrix. Due to their high surface areas and appropriate pore sizes, these composites can adsorb a higher amount of MB molecules. These adsorbed MB molecules have better access to the photocatalytic active sites on metal oxide. As shown in the schematic diagram (Figure 5.12), the photogenerated electrons in the conduction band can also transfer to the carbon matrix which facilitates charge separation by extending the lifetime of photoexcited charge carriers, consequently, the possibilities of charge recombination are minimised. The superoxide radicals ([•]O₂⁻) produced by e⁻_{CB} reduce the adsorbed MB into harmless species. On the valence band, photogenerated h⁺_{VB} and OH[•] radicals oxidise the MB molecules and convert them into neutral species. Some recent

studies used electron spin resonance (ESR) and species trapping experiment results to describe the mechanism of photocatalytic degradation and complete mineralisation of organic dyes by MOF derived C doped ZnO composites.¹⁶¹

For the photocatalytic water splitting for HER under visible light, H₂O/MeOH solution was used. The photoexcited electrons in the conduction band react with H₂O and reduce the H⁺ ions into H₂ gas whereas the MeOH works as a photogenerated holes scavenger. To achieve H₂ evolution through photocatalytic water splitting, the conduction band of the semiconductor should be more negative than the reduction potential of H⁺/H₂O (0 V vs NHE) and the valence band should be more positive than the oxidation potential of H₂O/O₂ (1.23 V vs NHE).²⁴³ Consequently, the minimum energy required to drive the reaction is 1.23 eV. MOF derived ZnO/C composites have EBGs around 3 eV, the incident visible light can therefore easily generate excessive e⁻/h⁺ pairs to carry out the photocatalytic water splitting. In photocatalytic reactions, the electronic structure of the semiconductor guides the charge diffusion and charge transfer to the respective reaction sites, where effective charge diffusion and charge transport usually take place very fast. The interfacial surfaces of ZnO and conductive C in MOF derived composites may facilitate successful charge transport by minimising the possible charge recombination. The photogenerated h⁺_{VB} (as well as OH[•] radicals produced from H₂O) react with MeOH used as a hole/radical scavenger to complete the other half-reaction.²⁴⁴

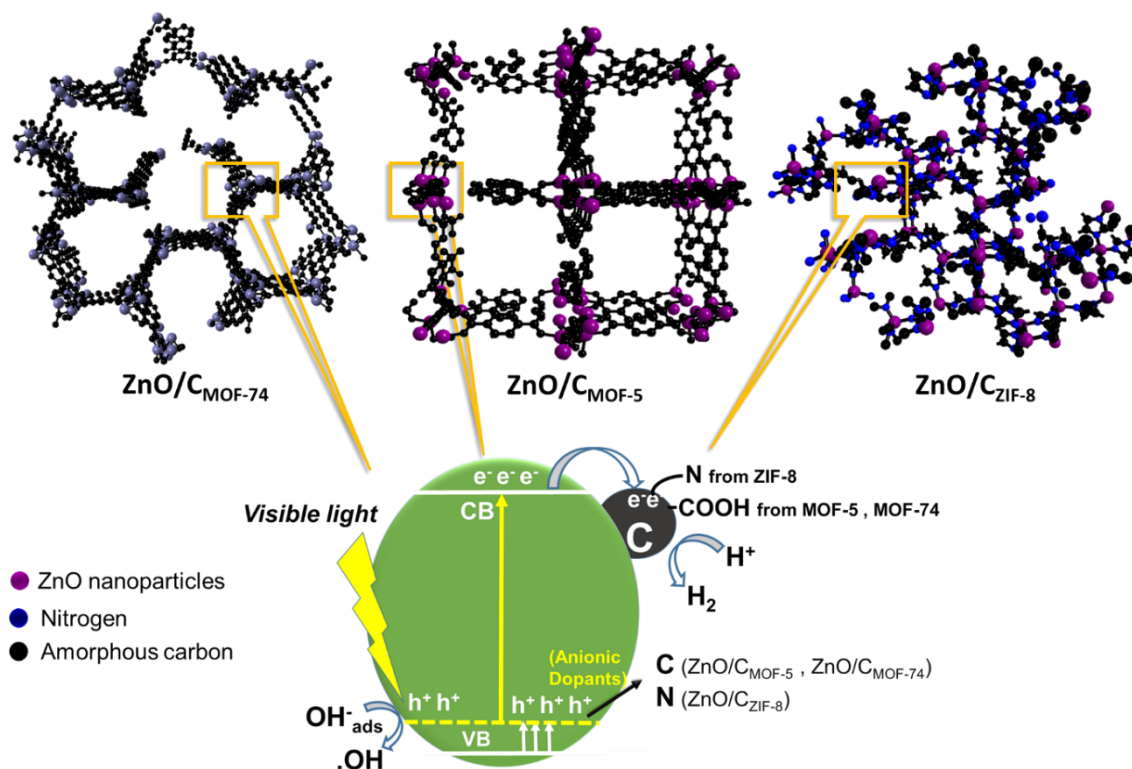


Figure 5.12 Proposed mechanism of photocatalytic HER and the photodegradation of organic pollutant dye MB by ZnO/C_{MOF-5}, ZnO/C_{MOF-74} and ZnO/C_{ZIF-8} under visible light. The photocatalytic oxidation (degradation of MB) reaction takes place through the photogenerated holes (h^+_{VB} and OH^\bullet radicals) in the valence band (half-reaction is shown here) whereas the reduction reaction (H_2 evolution) takes place by photogenerated electrons (e^-_{CB}) in the conduction band (half-reaction is shown here).

5.2.2.1 Photodegradation of methylene blue

In photocatalytic dye degradation, adsorption of organic dye on the catalyst and the subsequent photodegradation take place simultaneously. To distinguish these two simultaneous processes, 10 mg of as-synthesised sample was added into 50 mL of 20 ppm MB solution on constant stirring and the photocatalytic experiment was carried out under dark and visible light. As shown in Figure 5.13a, ZnO/C_{MOF-5}, ZnO/C_{MOF-74} and ZnO/C_{ZIF-8} adsorbed 54, 23 and 40 % of MB respectively in 6 hours. Under visible light (Figure 5.13b) the nanocomposites ZnO/C_{MOF-5}, ZnO/C_{MOF-74} and ZnO/C_{ZIF-8} showed 99 %, 92 % and 94 % dye degradation respectively. To confirm that if any self-sensitisation of MB takes place, pure MB was put under visible light for 6 hours. No self-degradation of MB is observed. The relatively higher adsorption in ZnO/C_{MOF-5} can be due to the

hydrophilic -COOH functional groups attached to the surface of the porous carbon matrix (confirmed by XPS and FTIR). The presence of a relatively higher amount of mesopores in ZnO/C_{MOF-5} and ZnO/C_{ZIF-8} composite (Figure 5.11b) also enables the MB molecules to have better access to penetrate the pores, leading to enhanced adsorption capacity. This observation is in good agreement with previously reported results.^{101, 207} Contrary to that, the poor adsorption of MB on ZnO/C_{MOF-74} after 60 minutes could be due to the narrow 1D pore channels of the carbon matrix which appear less accessible for the MB molecules to penetrate. Therefore, most of the adsorption takes place on the surface of the catalyst.

In the first 60 minutes, ZnO/C_{MOF-5} adsorbed and photodegraded 91 % MB while ZnO/C_{MOF-74} and ZnO/C_{ZIF-8} showed 65 and 70 % adsorption and photodegradation under the visible light respectively. Among these samples, fast adsorption and photodegradation of MB on ZnO/C_{MOF-5} could be due to its relatively larger pore widths and presence of hydrophilic carboxyl functional group as trapping centres (FTIR and XPS) which allow better adsorption of the dye molecules to penetrate and access active sites deep in the porous carbon matrix. The high content of ZnO nanoparticles (83 wt.%) in this sample provides plenty of accessible active sites due to the exposed metal oxide surfaces. It favours the short diffusion lengths for the charge transport, resulting in less charge recombination.

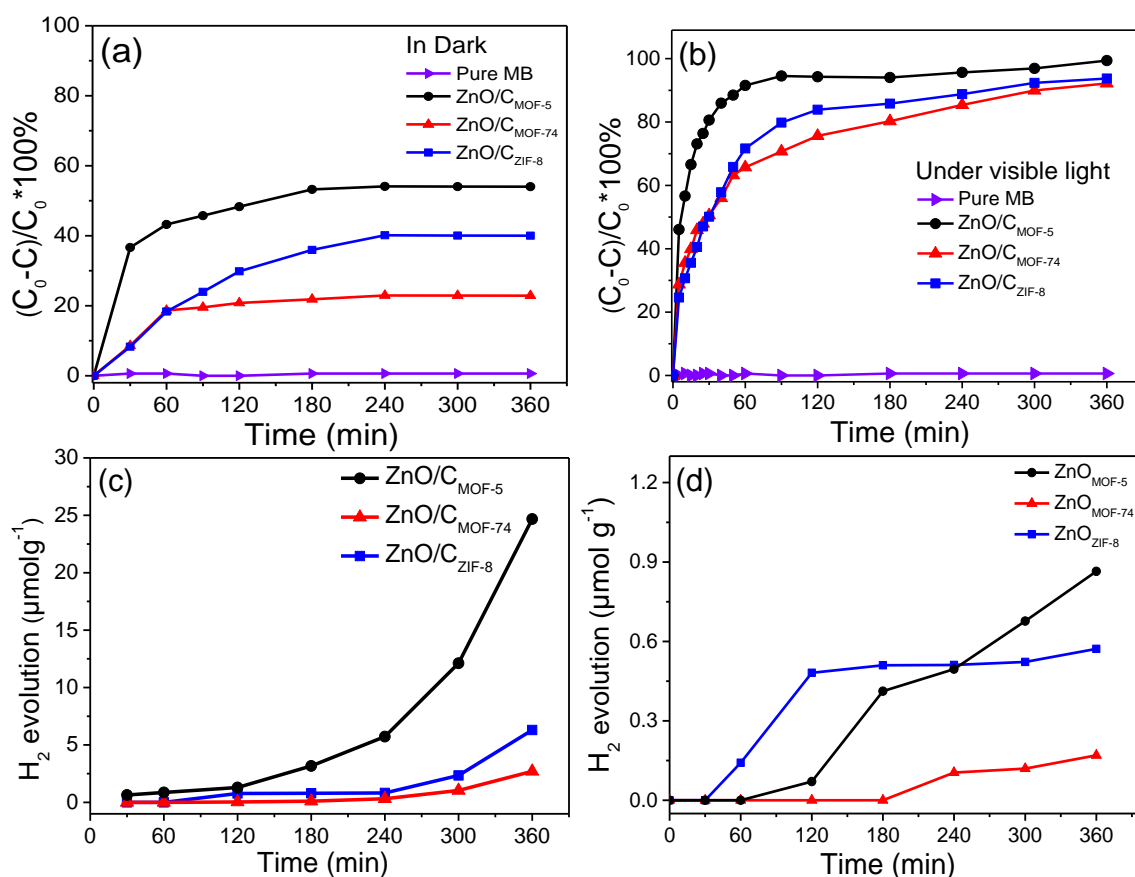


Figure 5.13 (a) The adsorption of MB by ZnO/C_{MOF-5} (black circles), ZnO/C_{MOF-74} (red triangles), ZnO/C_{ZIF-8} (blue squares) respectively in the dark (b) the adsorption and photodegradation of MB by ZnO/C_{MOF-5} (black circles), ZnO/C_{MOF-74} (red triangles) and ZnO/C_{ZIF-8} (blue squares) under visible light irradiation respectively. Olive hexagons represent photodegradation by ZnO_{MOF-5} prepared at 800 °C under air atmosphere. Violet triangles represent the blind test of MB without any catalyst. H₂ evolution by (c) ZnO/C_{MOF-5}, ZnO/C_{MOF-74} and ZnO/C_{ZIF-8} nanocomposites and (d) ZnO_{MOF-5}, ZnO_{MOF-74} and ZnO_{ZIF-8} under visible light irradiation.

Although ZnO/C_{ZIF-8} has the highest BET surface area with nitrogen decorated carbon matrix among these samples, it exhibited moderate adsorption and photodegradation performance in first 60 min, which may be due to the smaller pore openings as well as less amount of ZnO (35.8 wt.%) present in the composite. While the composite ZnO/C_{MOF-74} showed slow adsorption in the first 60 minutes as compared to ZnO/C_{MOF-5}, which might be due to the 1D pore structure and relatively low surface area of ZnO/C_{MOF-74}. However, after 60 min,

it showed the highest degradation performance of MB among all the samples. The overall dye degradation performance in 6 hours is almost the same as ZnO/C_{MOF-5} and ZnO/C_{ZIF-8}. It can be presumed that ZnO/C_{MOF-74} with higher wt.% of ZnO nanoparticles (74.5 %) has more exposed chain-like metal sites that can cause higher photodegradation after 60 min. These observations indicate that photocatalytic dye degradation is a complicated process depending upon many physical parameters including EBGs, ZnO and C ratios in the nanocomposites, SSAs, pore width and pore volume of the composites, crystallinity and functional groups attached on the surface of the catalyst.²⁰⁷ Table 5.1 provides a comparison of photocatalytic MB degradation efficiencies of ZnO and doped ZnO under visible light reported in the literature. The ZnO/C composites derived from MOF precursors are amongst the best performing materials for the photodegradation of MB under visible light irradiation.

The morphology, crystallinity and structural stability of the composites were confirmed by SEM and PXRD of the used samples. To confirm the morphological changes in MOFs derived ZnO/C composites after subject to photocatalytic dye degradation tests, the SEM images of used ZnO/C_{MOF-5}, ZnO/C_{MOF-74} and ZnO/C_{ZIF-8} samples were recorded, shown in 5.14a, b and c respectively. Also, PXRD patterns of ZnO/C_{MOF-5}, ZnO/C_{MOF-74} and ZnO/C_{ZIF-8} composites shown in Figure 5.15a, b and c respectively, after photocatalytic dye degradation tests are identical to the respective fresh samples. It confirms that the morphology, crystallinity and structural stability of these ZnO/C composites remain unaffected after photocatalytic reactions.

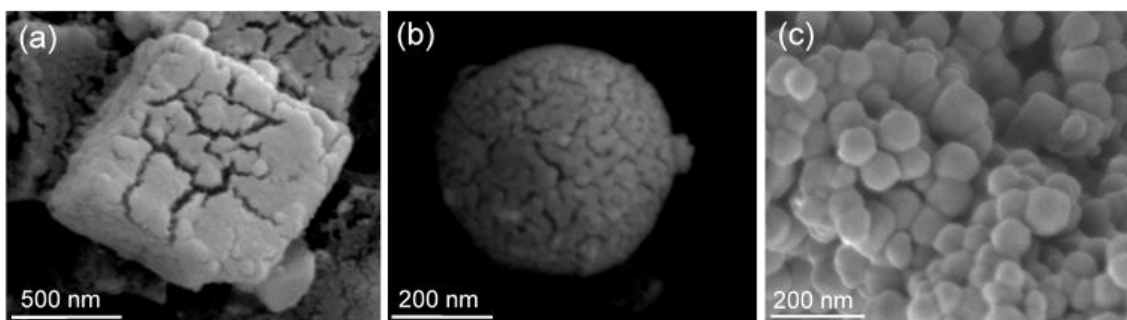


Figure 5.14 SEM micrographs of (a) ZnO/C_{MOF-5} (b) ZnO/C_{MOF-74} and (c) ZnO/C_{ZIF-8} after photodegradation of MB under visible light.

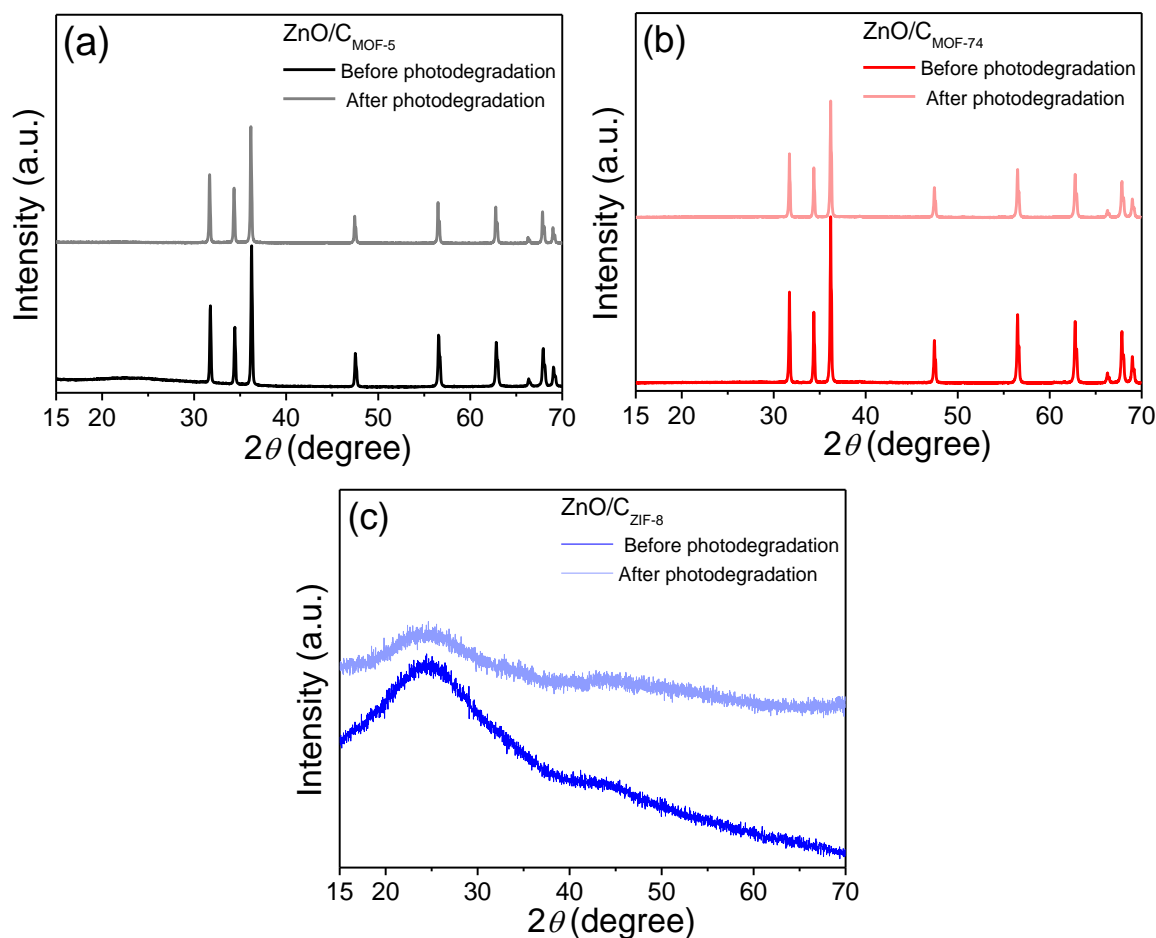


Figure 5.15 PXRD patterns of (a) $\text{ZnO}/\text{C}_{\text{MOF-5}}$ (b) $\text{ZnO}_{\text{MOF-74}}$ and (c) $\text{ZnO}_{\text{ZIF-8}}$ before and after photodegradation of MB under visible light irradiation respectively. The dark colours represent the PXRD patterns of fresh samples whereas the lighter colours show the PXRD patterns of used $\text{ZnO}/\text{C}_{\text{MOF-5}}$ (grey), $\text{ZnO}/\text{C}_{\text{MOF-74}}$ (light red) and $\text{ZnO}/\text{C}_{\text{ZIF-8}}$ (light blue) samples. The crystallinity of the photocatalysts remains unaffected after being used for photocatalytic dye degradation of MB under visible light.

Table 5.1 A comparison of photodegradation of MB by undoped and doped ZnO nanoparticles synthesised by different methods.

Catalyst	Dopant	Light source	Experimental conditions for photodegradation	Efficiency (%)		Ref.
				undoped	doped	
$\text{ZnO}/\text{C}_{\text{MOF-5}}$	C	120 mW cm ⁻²	Catalyst = 200 mg L ⁻¹	32	99.4	This work
		380 ≤ λ ≤ 700 nm	MB _{conc.} = 20 mg L ⁻¹			
$\text{ZnO}/\text{C}_{\text{MOF-74}}$	C	120 mW cm ⁻²	Catalyst = 200 mg L ⁻¹	14	92.2	This work
		380 ≤ λ ≤ 700 nm	MB _{conc.} = 20 mg L ⁻¹			

ZnO/CzIF-8	N, C	120 mW cm ⁻² 380 ≤ λ ≤ 700 nm	Catalyst = 200 mg L ⁻¹ MB _{conc.} = 20 mg L ⁻¹	26	94	This work
ZnO-C nanofibers	N	Solar simulator (Intensity = 80 lux)	Catalyst = 400 mg L ⁻¹ MB _{conc.} = 3.2 mg L ⁻¹	13.9	42.3	245
ZnO	C	14.5 W cm ⁻²	-	8	41	246
ZnO@GO	-	40 W λ = 365 nm	Catalyst = 10 mg L ⁻¹ MB _{conc.} = 3.2 mg L ⁻¹	49	98.5	247
C ₃ N ₄ /ZnO	-	1.2 mW cm ⁻² λ > 400 nm	Catalyst = 500 mg L ⁻¹ MB _{conc.} = 10 mg L ⁻¹	10	72.3	248
ZnO/PMMA	C, N	2 mW cm ⁻² λ = 368 nm	Catalyst = 100 mg L ⁻¹ MB _{conc.} = 0.24 mg L ⁻¹	7	60	249
C,N-ZnO	N	300 W Xe lamp	Catalyst = 250 mg L ⁻¹ MB _{conc.} = 10 mg L ⁻¹	-	100	93
RGO/ZnO@ZI F-8		300 W Xe lamp λ > 420 nm	Catalyst = 1 g L ⁻¹ MB _{conc.} = 10 mg L ⁻¹	46	82	143
Cu-ZnO	Cu	Sunlight	Catalyst = 1 g L ⁻¹ MB _{conc.} = 0.3 mg L ⁻¹	92	90	250
Li-ZnO	Li	1000 W Xe lamp	Catalyst = 1.2 g L ⁻¹ MB _{conc.} = 3.2 mg L ⁻¹	53.1	100	251
Hf-ZnO	Hf	Sunlight (1.263-105 lux)	Catalyst = 250 mg L ⁻¹ MB _{conc.} = 250 mg L ⁻¹	50	85	252

5.2.2.2 Photocatalytic H₂ evolution

Photocatalytic H₂ evolution reaction results of ZnO/C_{MOF-5}, ZnO/C_{MOF-74} and ZnO/C_{ZIF-8} are shown in Figure 5.13c. Interestingly, ZnO/C_{MOF-5} exhibited the highest H₂ evolution capacity of 25 μmol g⁻¹ after 6 hours whereas ZnO/C_{MOF-74} and ZnO/C_{ZIF-8} showed only 3 and 6 μmol g⁻¹ of H₂ evolution respectively under the same condition. To investigate the role of Zn-MOFs derived porous carbon matrix in photocatalytic activity, H₂ evolution activity by pure ZnO nanoparticles derived from the calcination of MOF-5, MOF-74 and ZIF-8 at 800 °C in the air was also measured under the same conditions. As shown in Figure 5.13d, ZnO_{MOF-5}, ZnO_{MOF-74} and ZnO_{ZIF-8} demonstrated only 0.9, 0.2 and 0.6 μmol g⁻¹ H₂ evolution activity under the same experimental conditions respectively. Compared to that, ZnO nanoparticles embedded in the porous carbon matrix, ZnO/C_{MOF-5}, ZnO/C_{MOF-74} and ZnO/C_{ZIF-8} showed 28, 15 and 10 times higher H₂ evolution respectively. It is therefore confirmed that the porous carbon matrix plays a crucial role in photogenerated charge (e⁻/h⁺) transfer as well as preventing the charge recombination. A comparison of photocatalytic H₂ evolution under visible light by selected ZnO based composites is shown in Table 5.2.

As discussed above, the photocatalytic dye degradation and H₂ evolution under visible light critically depend on the EBG of semiconducting metal oxide nanoparticles.^{62, 253} The photogeneration of high numbers of electron-hole (e^-/h^+) pairs upon absorption of incident visible light, the migration of these electrons and holes to the interfaces of the semiconductor nanoparticles and surface chemical reactions between the generated e^-/h^+ and the targeted compounds (MB for photodegradation and H₂O/MeOH for H₂ production) are three mechanistic steps of photocatalysis.²⁵⁴ To improve the photocatalytic performance, narrow EBGs, less charge recombination of e^- and h^+ and a longer lifetime of excited charges are required. Due to the non-metal anionic C and/or N doping, hybridisation of O 2p and C 2p and/or N 2p orbitals takes place, creating a new energy level slightly above the valence band of ZnO nanoparticles. This additional energy level narrows the EBG between the valence and the conduction bands of ZnO nanoparticles and makes them photoactive semiconducting materials under visible light.^{205, 240} Moreover, the improvement in H₂ evolution performance of ZnO/C composites can be understood through the schematic diagram shown in Figure 5.12. The relatively higher H₂ evolution performance (among ZnO/C composites) of ZnO/C_{MOF-5} compared to ZnO/C_{MOF-74} and ZnO/C_{ZIF-8} might be due to the higher amount of uniformly distributed ZnO nanoparticles (83 wt.%, TGA) with better crystallinity (confirmed by XPS and XRD) in catalyst ZnO/C_{MOF-5} and accessible photocatalytic active sites. More electrons are generated on the surface upon interacting with visible light resulting in a higher reduction rate of H⁺ and lesser charge (e^-/h^+) recombination. Consequently, more H₂ is generated. However, in ZnO/C_{ZIF-8}, high content of carbon (TGA profiles) makes it difficult for visible light to penetrate deeper into the porous catalyst to access ZnO nanoparticles. Furthermore, the generated electrons have a longer diffusion path length which causes loss of e^-/h^+ pairs due to charge recombination. Therefore, this catalyst shows relatively poor performance in H₂ evolution.

Table 5.2 A comparison of photocatalytic H₂ evolution under visible light by selected doped ZnO composites with different morphologies.

Catalyst	Morphology	Dopant/ co-catalyst	Light source	H ₂ evolution	Ref.
Black ZnO/C	Nanowires	C	300W Xe lamp	8.6 $\mu\text{mol g}^{-1}$	255
ZnO/C ₃ N ₄ QD	Nanowires	QD decorated	300W Xe lamp (UV-light)	14 $\mu\text{mol cm}^{-2}$	256
ZnO–Au–SnO ₂	Nanorods	Au/Pd	100 mW cm ⁻² white light	1.2 $\mu\text{mol h}^{-1}$	257
ZnO–CdS/RGO	Sheets	Pt	300W Xe lamp (UV-light)	1.5 mmol h ⁻¹	258
ZnO/Cu	Nanoparticles	Cu	500W Xe lamp (Vis-light)	1.2 $\mu\text{mol g}^{-1}$	259
ZnO/C _{MOF-5}	cubic	C	Solar Simulator	25 $\mu\text{mol g}^{-1}$	This work
ZnO/C _{MOF-74}	spherical	C	Solar simulator	3 $\mu\text{mol g}^{-1}$	This work
ZnO/C _{ZIF-8}	regular hexagonal	N, C	Solar simulator	6 $\mu\text{mol g}^{-1}$	This work

Table 5.3 Summary the BET surface areas, pore sizes, EBGs and functionalisation of the MOF-5, MOF-74 and ZIF-8 derived composites.

Sample	BET surface area (m ² g ⁻¹)	Pore width (nm)	EBGs (eV)	Surface functionalisation
ZnO/C _{MOF-5}	390	1.4, 2 - 4	3.13	-OH / -COOH
ZnO/C _{MOF-74}	321	1.2, 1.6	3.11	-OH / -COOH
ZnO/C _{ZIF-8}	653	1.2, 2 - 4	2.97	-N, -OH / -COOH

5.3 Summary

Three different ZnO/C composites, derived from different Zn-MOFs at 800 °C in water vapour saturated argon atmosphere, were systematically investigated and correlated for structure-property-application relationship. The as-synthesised nanocomposites were further evaluated as photocatalysts for dye degradation and H₂ evolution under visible light. It was found that thermal decomposition of

MOF-5 and MOF-74 under water vapour generate highly crystalline ZnO nanoparticles with high ZnO content whereas ZIF-8 produces poorly crystalline ZnO nanoparticles with a lower weight percentage of ZnO in the composites. The ZnO/C_{MOF-5} show the highest thermal stability, ZnO/C_{MOF-74} with moderate stability while ZnO/C_{ZIF-8} are found to be thermally less resistant at high temperature. XPS and Raman analysis of derived composites confirm that C is the only dopant in ZnO/C_{MOF-5} and ZnO/C_{MOF-74}, while N plays the role of primary dopant in ZnO/C_{ZIF-8}. Moreover, the thermal decomposition of 2-methylimidazole linker in ZIF-8 gives more disordered carbon in the resulting composite ZnO/C_{ZIF-8} (more C-C sp³ bonds). FTIR spectra demonstrate that carboxyl (-COOH) functional groups are better attached on the surface of ZnO/C_{MOF-5} due to the availability of more active sites on organic linker (terephthalic acid) as compared to ZnO/C_{MOF-74} where the organic linker is 2,5-dihydroxyterephthalic acid. The high level of N present on the carbon surface in ZnO/C_{ZIF-8} results in less oxygen-containing functionalities to attach to the surface of the catalyst under these experimental conditions. SEM, TEM and EDX elemental mapping demonstrate that all three composites retain the morphologies of their precursors and display well-dispersed ZnO nanoparticles homogeneously distributed in the porous carbon matrix. Due to the N and/or C doping, all three derived composites show redshift in UV-Vis absorption spectra indicating the narrow EBGs (around 3 eV) as compared to the bulk ZnO (3.37 eV). High BET surface area and appropriate pore sizes of nanocomposites facilitate the adsorption and penetration of the organic dye into the micro/mesopores of the catalyst. Among these selected Zn-MOFs, the MOF-5 derived ZnO/C composite proved to be the best photocatalyst with the highest performance for MB dye degradation and H₂ evolution under visible light.

Chapter 6

An in-situ investigation of the thermal decomposition of metal-organic framework NH₂-MIL-125(Ti)

6.1 Introduction

As discussed in the previous chapters, metal-organic frameworks (MOFs) are exceptionally porous coordination polymers fabricated by the formation of coordination bonds between organic ligands and inorganic metal clusters (called secondary building units, SBUs) producing highly crystalline reticular networks.^{23, 24} Despite the high crystallinity, relatively moderate strength of coordination bonds between constituent organic linkers and metal ions/clusters and poor semiconducting properties restrict them to be directly used for photocatalytic applications at commercial scale.^{34, 39, 41, 42, 130} However, their unique properties such as rationally designed structures, a large choice of morphologies, diverse dimensions (0D, 1D, 2D and 3D) together with high surface areas and modifiable porosities, make them excellent sacrificial templates and precursors to derive highly efficient nanocomposites with adjustable semiconducting properties.^{41, 42, 55, 64, 260, 261} Actually, all MOFs can be carbonised under appropriate pyrolysis conditions to obtain the respective metal oxides, carbides, sulphides, nitrides and phosphides embedded in a porous carbon matrix.^{41, 260, 262, 263} Similar to their parental precursors, tunable MOF derived composites present great opportunity and challenge at the same time. The enormous multivariate parameters of MOF design and synthesis multiplies with the post-synthetic process parameters during pyrolysis. Therefore, it is desirable to understand the parameters individually in this complex transformation process at the atomic scale.

In chapter 5, three Zn-MOFs derived ZnO/C composites were investigated to understand their structural, morphological and physicochemical properties for photocatalytic applications. Similarly, it is very important to understand the thermal decomposition mechanism of Ti-MOFs before selecting them as precursors and sacrificial templates to derive rationally designed nanocomposites for photocatalytic applications. Various studies have demonstrated that the intrinsic nature of metal-ions is the key determinant of the phase of derived metal (compounds) nanoparticles and the organic linkers, as well as the synthetic conditions of the parent MOFs, are the factors to affect the possible morphology,

composition, degree of graphitisation and porosity of the derived carbons.^{89, 260, 262, 264} Although a few studies attempted to carry out in-depth in-situ investigations of the decomposition processes of MOFs, the change of crystallinity, morphology, textural and physicochemical properties of MOF during pyrolysis is still a fundamental issue to be addressed.^{89, 230, 265} Therefore, it is of utmost importance to further understand the transformation mechanisms of the MOF reticular structures, the evolution of porosity and simultaneous recrystallisation of the metal species in the derived composites, so that to optimise the pyrolysis condition for high performing nanomaterials.

This chapter presents an in-situ investigation of the thermal decomposition of $\text{NH}_2\text{-MIL-125(Ti)}$ under an inert atmosphere. $\text{NH}_2\text{-MIL-125(Ti)}$ is one of the most common and stable MOFs which comprises $\text{Ti}_8\text{O}_8(\text{OH})_4$ octamers SBUs interconnected with each six 2-amino-terephthalic acid $[(\text{O}_2\text{C}-\text{C}_6\text{H}_4(\text{NH}_2)-\text{CO}_2)]$ organic linkers through coordination bonds.²⁸ Figure 6.1 shows the chemical structures of Ti oxo-cluster, organic linker and $\text{NH}_2\text{-MIL-125(Ti)}$. The carbonisation of $\text{NH}_2\text{-MIL-125(Ti)}$ under suitable conditions can afford derived TiO_x nanoparticles or TiO_x/C nanocomposite with modifiable crystalline phases, adjustable EBGs, functionalised porous carbon with high surface area and tunable porosities.^{46, 47, 52, 64, 80}

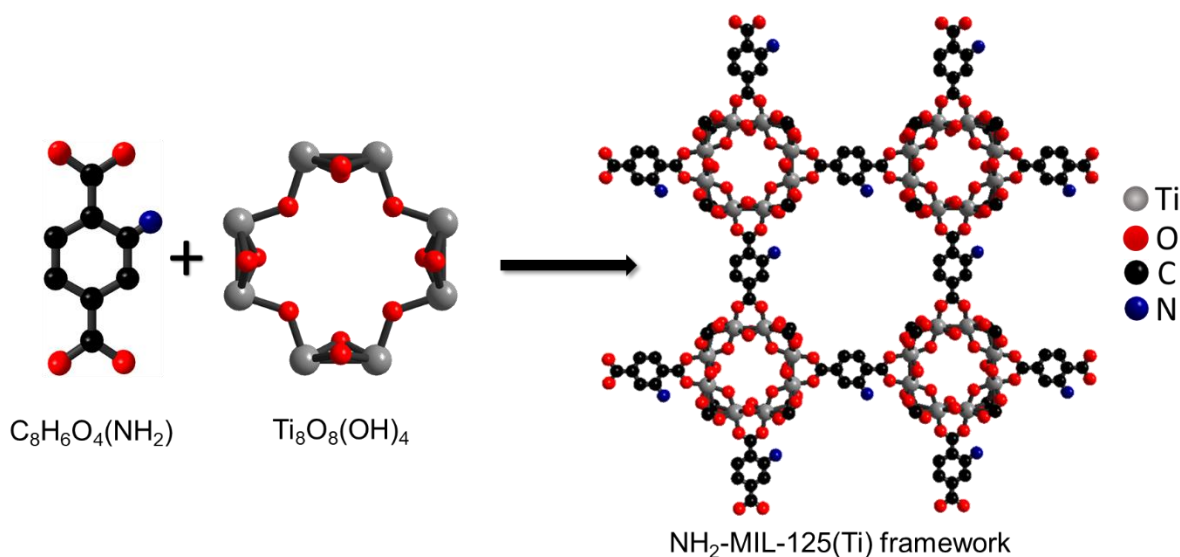


Figure 6.1 Chemical structures of metal clusters, organic linkers and the crystalline $\text{NH}_2\text{-MIL-125(Ti)}$.

6.2 Results and discussion

6.2.1 Composition and structural properties

TGA-MS was performed under oxidative (synthetic air) atmosphere as well as in inert atmosphere to study the thermal properties of NH₂-MIL-125(Ti). Though the thermal decomposition in synthetic air proceeds faster than in the inert argon atmosphere, suggesting the complete transformations of MOF precursor in the air during the exothermic processes, both TGA curves (Figure 6.2a and b) show a similar four-step (1-4) decomposition pattern of NH₂-MIL-125(Ti). Under oxidative conditions (synthetic air), in stage (1), NH₂-MIL-125(Ti) experiences around 15 % weight loss at temperatures below 200 °C due to the removal of the residual free solvent molecules of MeOH from the pores and the surface absorbed moisture, which is confirmed by the observed MS signals (Figure 6.2c) with mass fragments of $m/z = 18$ (water), 30 (NO) and 44 (CO₂) from partially oxidised DMF. In stage (2) at temperatures below 280 °C, removal of the residual DMF together with the partially or fully oxidised DMF products including CO₂ and some free amino groups like carbamates or amides contribute to around 13 % of weight loss. In step (3) at above 350 °C up to 470 °C, a major weight loss event which can be assigned to the decomposition and oxidation of organic framework constituents, accompanied with the formation of metal oxide particles and non-volatile macromolecular carbonaceous species, as confirmed in Figure 6.2c by the emission of CO₂, NO₂, NO and H₂O. In step (4), those formed small amount of non-volatile macromolecular carbonaceous species are further oxidised and only metal oxide is left as a residue.

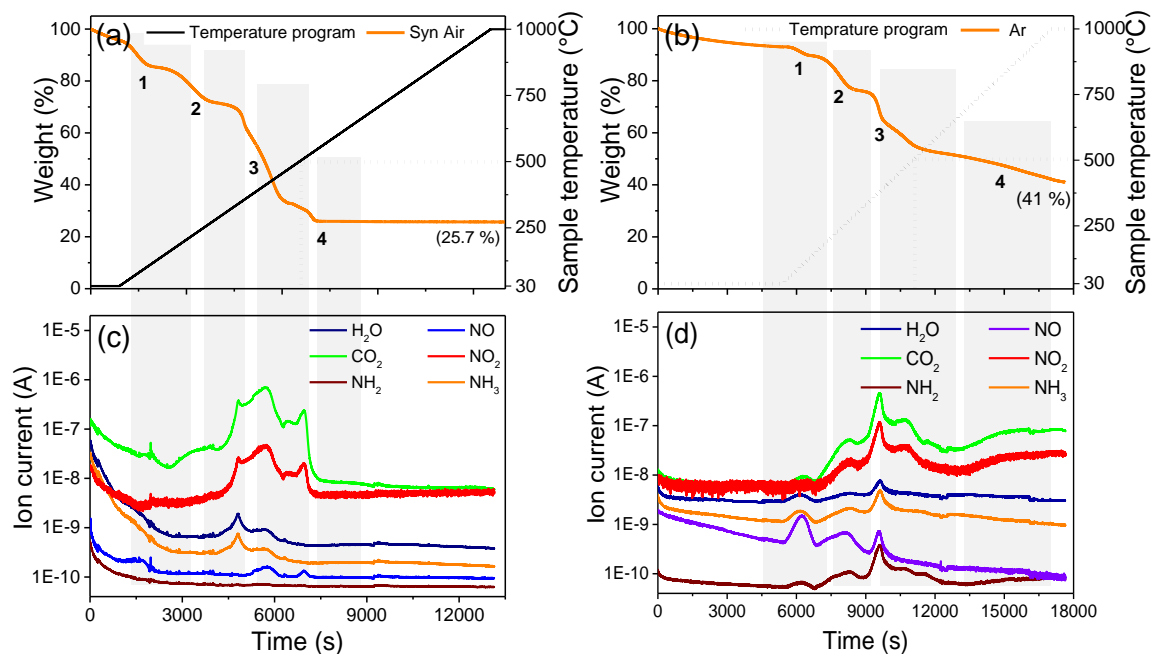


Figure 6.2 TGA of NH₂-MIL-125(Ti) (a) under synthetic air and (b) under argon atmosphere. The MS of NH₂-MIL-125(Ti) (c) under synthetic air and (d) under argon atmosphere.

Similar weight loss events are also observed for NH₂-MIL-125(Ti) thermolysis in an argon atmosphere, but the TGA curve exhibits much less weight loss at each step and occurs at a higher temperature, clearly suggesting the impact of the temperature and gas atmosphere on the thermal behaviour of NH₂-MIL-125(Ti). In an inert argon atmosphere, as presented in Figure 6.2d, step (3) is different from that in synthetic air and shows only a small weight loss which may attribute to the decomposition and thermolysis of organic constituents of the framework via decarbonylation, decarboxylation, dehydrogenation and even oxidation, indicating the pronounced formation of non-volatile carbonaceous phases together with TiO₂ (confirmed by XRD). These intermediate non-volatile carbonaceous species slowly decompose in step (4) with increasing temperature up to 1000 °C, allowing cluster migration towards TiO₂ nanoparticle crystallisation and transformation of amorphous carbon.

The main difference of TGA-MS of NH₂-MIL-125(Ti) in synthetic air and argon originates from nitrogen-containing species. Upon heat processing the precursor sample NH₂-MIL-125(Ti) in air, the NH₂ functional group in the MOF is oxidised

to NO_x with $m/z = 30$ and 46 in step **(3)**; While under inert conditions in argon atmosphere, $\text{NH}_2\text{-MIL-125(Ti)}$ precursor does not completely change the oxidation state of the amino groups with radical NH_2 species ($m/z = 16$) being observed at around 580°C . However, the NH_2 group is also eliminated as NH_3 ($m/z = 17$), as shown in Figure 6.2d. It is worth noting that in argon atmosphere, the $m/z = 30$ is attributed to NO , which may be derived from the NH_2 -containing organic component is partially oxidised by the presence of oxygen-containing -COOH groups in the organic linker. Based on the TGA-MS, the potential thermal decomposition mechanisms of $\text{NH}_2\text{-MIL-125(Ti)}$ and a putative reaction equation under both atmospheres are provided in Figure 6.3.

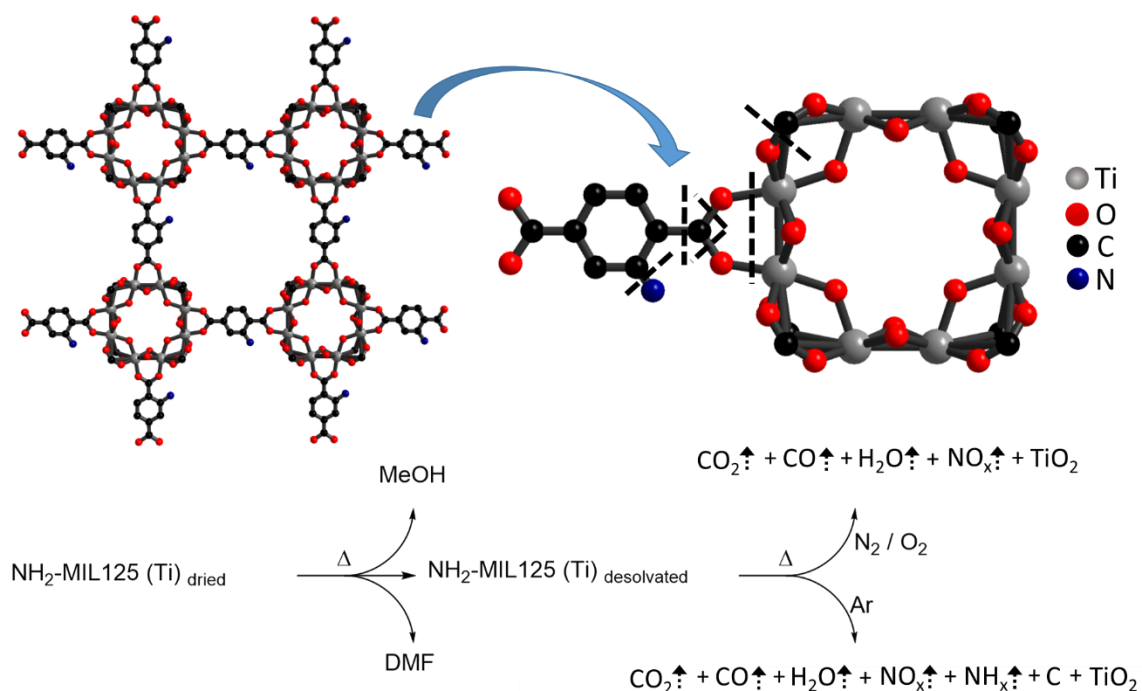


Figure 6.3 A proposed scheme of thermal decomposition and putative reaction products of $\text{NH}_2\text{-MIL-125(Ti)}$ under synthetic air and argon atmosphere based on TGA-MS results.

The PXRD patterns (Figure 6.4a) confirm the phase purity of highly crystalline $\text{NH}_2\text{-MIL-125(Ti)}$ as the precursor compound. The main peaks appearing at 2θ of 6.7° , 9.7° and 11.6° correspond to the simulated XRD pattern of MIL-125(Ti) .²⁸ In this structure, six $\text{NH}_2\text{-BDC}$ organic linkers interconnect the chains of $\mu\text{-OH}$ corner-sharing $\text{Ti}_8\text{O}_8(\text{OH})_4$ metal cluster, forming the disc-like tetragonal 3-dimensional reticular structures shown in Figure 6.3.^{44, 173} Upon high-temperature pyrolysis under an argon atmosphere, the precursor MOF

structure decomposes at above 350 °C forming the amorphous TiO₂ from Ti oxo-cluster and porous carbon matrix from organic linkers. The PXRD patterns of the heat treated samples from 200 to 900 °C (Figure 6.4a) show that the NH₂-MIL-125(Ti) molecular structure stays stable up to 300 °C. The decrease in peak intensity at 300 °C might be related to the reorganisation of the MOF structure due to the removing of hydroxo groups and partial breaking of -NH₂ bonds (confirmed by TGA-MS). The XRD peaks at 400 and 500 °C show no trivial peaks of NH₂-MIL-125(Ti) and formed TiO₂ nanoparticles confirming the collapse of MOF structure and the formation of the intermediate amorphous phase of TiO₂ and carbon. Here, only a small hump at around 2θ of 26° represents the amorphous carbon. However, at 600 °C, a broad peak of poorly crystalline anatase TiO₂ emerges at 2θ of 25.2°. From 700 to 800 °C, well crystalline anatase and rutile peaks are observed at 2θ of 25.3° and 27.4° respectively. However, at 800 °C, the rutile phase becomes relatively more prominent compared to the anatase phase and finally, the highly crystalline rutile phase dominates at 900 °C with complete disappearance of the anatase phase of TiO₂. Moreover, a small shift in the rutile peak of TiO₂ (Figure 6.4b) toward higher 2θ (from 700 to 900 °C) can be observed in these MOF derived well crystalline TiO₂ nanoparticles. This shift in rutile peak positions can be attributed to the modification in the crystalline structure and nitrogen and/or carbon self-doping (N from NH₂-BDC linker) in TiO₂ lattice.^{44, 266}

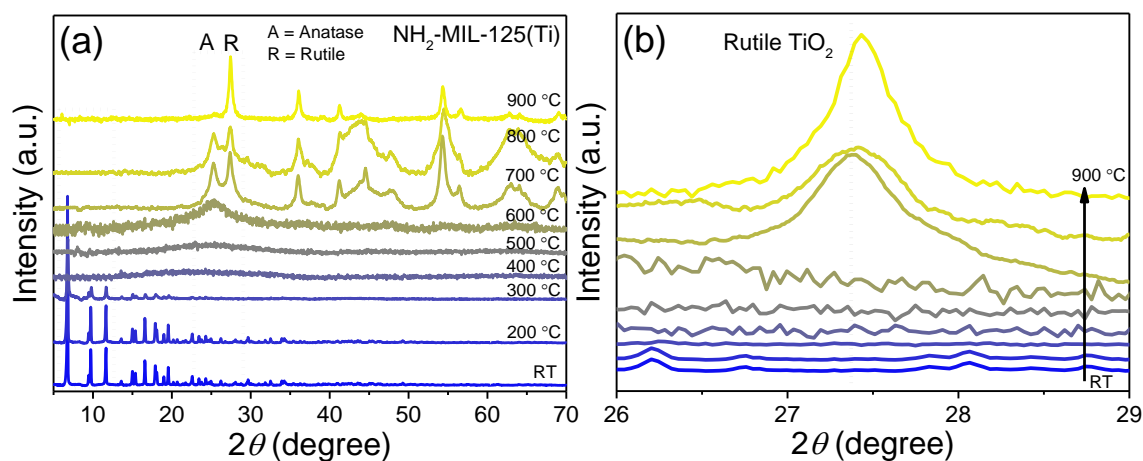


Figure 6.4 (a) PXRD patterns of NH₂-MIL-125(Ti) heat treated from RT to 900 °C. The NH₂-MIL-125(Ti) structure is stable up to 300 °C. The MOF structure disintegrates at above 350 °C followed by the recrystallisation of TiO₂ nanoparticles at above 550 °C. (b) Highlighted rutile TiO₂ peaks show the shift in peak positions due to modified crystalline structure.

The FTIR spectra (Figure 6.5a) show the shift in intensity and peak positions of the organic linker (NH₂-BDC) and the Ti-O (metal cluster) upon thermal processing of NH₂-MIL-125(Ti) from RT to 900 °C. In as-prepared NH₂-MIL-125(Ti), a large stretching band observed at around 3400 cm⁻¹ corresponds to the presence of NH₂ functional groups of the organic linker and the -OH stretching of residual solvents (DMF + MeOH + H₂O). As the temperature increases, the intensity of this band gradually drops due to the breaking of NH₂ functional groups and evaporation of the residual solvents, but a minor peak retains in samples obtained at heat treatment temperature higher than 600 °C due to the surface adsorbed moisture. A shoulder peak around 1710 cm⁻¹ in pristine NH₂-MIL-125(Ti) can be ascribed to the stretching modes of -COOH groups coordinated with Ti oxo-cluster.²⁶⁷ The characteristic vibrational bands of carboxylate linker appear at 1534 and 1426 cm⁻¹.²⁶⁸ These vibrational bands remain unchanged up to 300 °C, confirming that no structural change occurs in NH₂-MIL-125(Ti). However, the intensities of these peaks gradually decrease upon heating and almost disappear above 400 °C, due to the breaking of the carboxylate bridges and coordination bonds between NH₂-BDC linkers and the Ti (octahedra) metal cluster. Although -COOH and -NH₂ groups may break and evaporate, the aromatic rings in the organic linkers transform to carbonaceous materials and still have the benzene ring groups in the carbon materials. Above 400 °C, a strong band at around 1615 and 1385 cm⁻¹ can be ascribed to the stretching vibrational modes of C=C in the aromatic ring and bending vibrational modes of C-O-H respectively. A peak at around 1255 cm⁻¹ can be attributed to the C-N stretching modes of the aromatic amine group.²⁶⁸ The vibrational bands between 800-400 cm⁻¹ correspond to the O-Ti-O bonds in Ti oxo-cluster.²⁶⁷ Similar to the carboxylate modes, these vibrations show no trivial variation up to 300 °C confirming the stability of the MOF structure. However, at 400 °C, these sharp peaks disappear leaving a broad shoulder band which can be attributed to the formation of amorphous TiO₂. However, a broader peak of crystalline TiO₂ can be observed at 630 cm⁻¹ in samples obtained above 500 °C.²⁶⁹ In accordance with the XRD, this slight shift in the peak position (at around 630 cm⁻¹) of TiO₂ in samples obtained at temperatures 500 to 900 °C could be attributed to the transformation of crystalline phase from anatase to rutile and changes in the local chemical environment of TiO₂ nanoparticles.^{44, 269} The thermal decomposition

and the changes in the chemical states of TiO₂ and carbon were further investigated by XPS.

In Figure 6.5b, the Raman spectra of selected heat treated samples (500 and 800 °C) show the $E_g(1)$ vibrational modes of TiO₂ at around 154 cm⁻¹ and E_g vibration modes between 350-700 cm⁻¹ respectively.^{182, 270} The peaks appearing at 1258 and 1424 cm⁻¹ in NH₂-MIL-125(Ti) (dried at 200 °C) can be assigned to the symmetric stretching and bending modes of Ti-O-Ti-O octamer rings in the metal cluster while the peaks appeared at around 1492 and 1630 cm⁻¹ correspond to the C-C and N-H vibration modes of the organic linker (NH₂-BDC).^{44, 271} However, pyrolysing at high temperature, these peaks disappear and two signature peaks of D and G bands of carbon are observed in both samples obtained at 500 °C and 800 °C. The D band (breathing modes of sp² hybridised carbon atoms in hexagonal rings) signifies the amorphous carbon whereas the G band (bond stretching of all sp² atoms in hexagonal rings and chains) represents the graphitic carbon which appears due to the formation of nanocrystalline carbon.^{215, 216} The D band appeared at 1368 cm⁻¹ in the sample obtained at 500 °C which shifted to 1354 cm⁻¹ in the sample obtained at 800 °C. Likewise, the G band was observed at 1595 cm⁻¹ in sample 500 °C whereas it appeared at 1617 cm⁻¹ for the sample 800 °C respectively. The blueshift in G band can be ascribed to the electronegative N functionalisation, the formation of surface defects, oxygen-related defects and the diamond-like (C-C) sp³ bonding in amorphous carbon.²¹⁶ The intensities of D and G bands suggest that carbon obtained from pyrolysis of NH₂-MIL-125(Ti) up to 800 °C remains amorphous with little graphitisation.^{272, 273} These observations were further confirmed by XPS spectra.

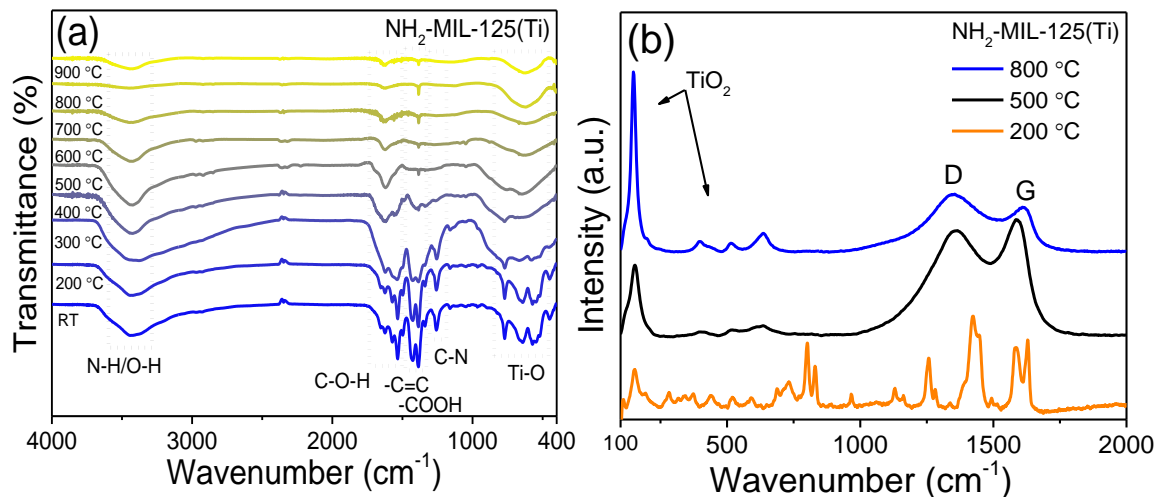


Figure 6.5 (a) FTIR spectra of heat treated $\text{NH}_2\text{-MIL-125(Ti)}$ from RT to 900 °C (b) Raman spectra of selected samples at 200 °C (orange) 500 °C (black) and 800 °C (blue).

The modifications in electronic and chemical states of the constituent elements such as Ti, O, C and N during carbonisation of the $\text{NH}_2\text{-MIL-125(Ti)}$ were investigated by the XPS of selected samples. The Ti $2p_{3/2}$ and Ti $2p_{1/2}$ peaks appeared at 458.8 and 464.7 eV respectively in $\text{NH}_2\text{-MIL-125(Ti)}$ heated at 200 °C (Figure 6.6a). The difference in binding energies ($\Delta E_{\text{B.E}}$) of Ti $2p_{3/2}$ and Ti $2p_{1/2}$ was calculated to be 5.9 eV confirming the presence of Ti(IV) chemical state in Ti oxo-cluster.²⁷⁴ However, Ti $2p_{3/2}$ and Ti $2p_{1/2}$ peaks appeared at around 458.6 and 464.6 eV respectively in samples obtained at 500 and 800 °C. The small shift in Ti $2p_{3/2}$ (0.2 eV) toward lower binding energy and the change in $\Delta E_{\text{B.E}}$ upon thermal decomposition can be attributed to the formation of TiO_2 nanoparticles.²⁷⁵ This shift in the binding energy of Ti $2p_{3/2}$ might be due to the incorporation of N and/or C atoms in TiO_2 crystal lattice substituting the O^{2-} as well as the formation of Ti^{3+} chemical states.^{9, 19, 168} The O 1s spectra (Figure 6.6b) of $\text{NH}_2\text{-MIL-125(Ti)}$ heated at 200 °C can be deconvoluted into two peaks appeared at 531.9 and 531.6 eV which refer to the characteristic peaks of oxygen atoms in Ti oxo-cluster and C=O bonds respectively.²⁷⁴ However, in samples obtained at 500 °C, the O 1s peaks appeared at 531.3 and 530.2 eV can be attributed to the OH groups on the carbon surface and the signature peak of Ti-O in TiO_2 lattice respectively.^{276, 277} These peaks shifted to 531.2 and 530.1 eV in the sample at 800 °C with a small broadening which confirmed the growth of oxygen-related defects in TiO_2 lattice.^{19, 278}

The deconvoluted peaks of C 1s (Figure 6.6c) in NH₂-MIL-125(Ti) heated at 200 °C appeared at 284.8, 286.2 and 288.4 eV which correspond to sp² hybridised C=C, C-O-C bonds and the O-C=O of organic linker respectively.^{271, 274, 279} At 500 °C the NH₂-MIL-125(Ti) collapsed and the organic linker transformed into the amorphous carbon. The C 1s peaks of this sample (500 °C) appeared at 284.8, 285.8 and 288.2 eV attributed to C=C, C-O and O-C=O bonds respectively.^{207, 276} However, further heating the sample to 800 °C, the C 1s peaks were shifted to 284.2, 285.1 and 287.7 eV which indicate the modification in the chemical state of carbon species. It is interesting to observe that the sample at 800 °C showed a significant decrease in the intensity of the sp² hybridised C=C bond with a simultaneous increase in the intensity of the C-C bond (inset in Figure 6.6c) compared to the sample obtained at 500 °C.^{19, 168, 261} It confirmed the growth of defects in carbon matrix and the formation of oxygen vacancies as well as a decrease in O 1s intensities with pyrolysis temperature. This observation is in very good agreement with Raman spectra (Figure 6.5b).

The N 1s peaks in NH₂-MIL-125(Ti) heated at 200 °C (Figure 6.6d) appeared at 399.9 and 402 eV and can be attributed to the N of the amine functional group (-NH₂) attached to the organic linker of MOF.^{280, 281} Above 380 °C, it cleaves off from the linker (NH₂-BDC) by breaking of C-N covalent bond under inert atmosphere (TGA-MS) freeing the N atoms which can potentially be doped into TiO₂ lattice as well as functionalise the surface of the porous carbon. The intensity of N 1s peaks drops at high temperature indicating that most of the N evaporates in the form of NO₂ under an oxidative environment and NH₂/NH₃ under an inert atmosphere (TGA-MS). The deconvoluted N 1s peaks in the sample obtained at 500 °C appeared at 400.4 and 398.3 eV which can be assigned to the pyrrolic N species and the pyridine-like N atoms present in the porous carbon matrix respectively.^{260, 282, 283} However, heating the sample to 800 °C under an argon atmosphere, along with these two pyrrolic and pyridine peaks, a new peak emerged at 396.1 eV (highlighted inset in Figure 6.6d) due to the substitution of N into the TiO₂ lattice. Valentin *et al.* reported that XPS N 1s core levels appear between 396-397 eV due to the substitutional N-dopants in TiO₂ representative of the Ti-N bonds.⁸ This substituted N atoms replace oxygen in TiO₂ crystal lattices with N 1s core levels signifying the Ti-N bond formation. These intraband states lie just above the valence band of TiO₂ narrowing down

its EBG.⁹ Based on these observations, it can be assumed that during the intermediate amorphous phase of thermal decomposition of NH₂-MIL-125(Ti), it is difficult to introduce the dopants such as N atoms into TiO₂ at lower temperatures. For that, high temperature pyrolysis of MOF is required under appropriate conditions to modify the EBGs and the chemical properties of the MOF derived composites. For a clear overview, the XPS results are summarised in Table 6.2.

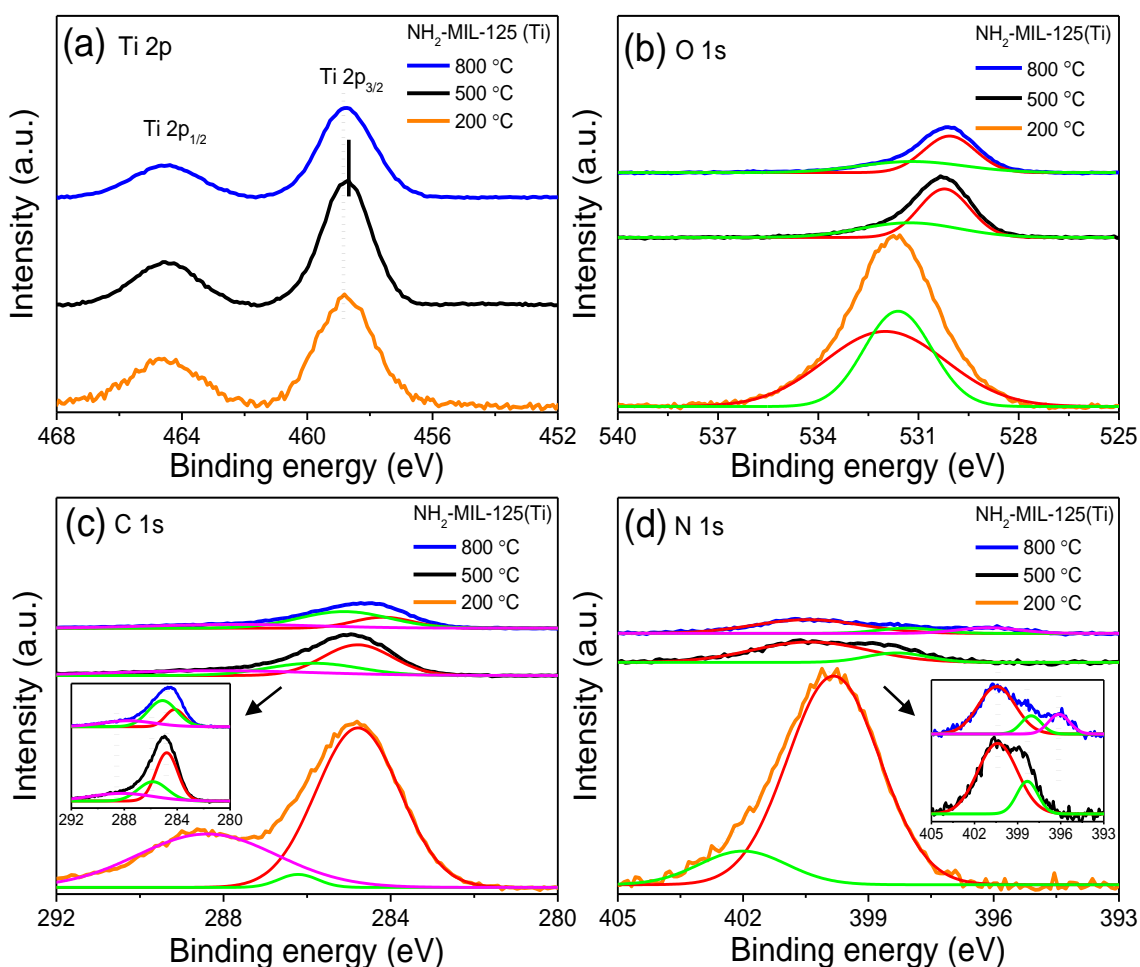


Figure 6.6 XPS spectra of (a) Ti 2p (b) O 1s (c) C 1s and (d) N 1s of selected heat treated NH₂-MIL-125(Ti) at 200 °C (orange) 500 °C (black) and 800 °C (blue).

6.2.2 Textural properties

The N₂ sorption isotherms of selected samples such as as-prepared NH₂-MIL-125(Ti) and heat treated at 200 °C (no structural change), 500 °C (intermediate amorphous phase) and 800 °C (recrystallised phase) were measured at 77 K to access surface areas and PSD. The NH₂-MIL-125(Ti) exhibited type I isotherm

(Figure 6.7a) with high adsorption below the relative pressure (p/p_0) of 0.1 due to the capillary filling of micropores. The adsorption and desorption isotherms are reversible with no hysteresis, signifying the presence of predominantly uniform micropores. The BET surface area of activated NH₂-MIL-125(Ti) is estimated to be 1465 m² g⁻¹ ($SA_{\text{micropore}}/SA_{\text{external}} = 1336/129 \text{ m}^2 \text{ g}^{-1}$) with a pore volume of 0.6 cm³ g⁻¹ and pore diameter of 0.7 nm (Figure 6.7b).^{28, 173} The sample heat treated at 200 °C showed a small hysteresis above relative pressure (p/p_0) of 0.4 with no significant loss of BET surface area calculated to be 1435 m² g⁻¹ ($SA_{\text{micropore}}/SA_{\text{external}} = 784/651 \text{ m}^2 \text{ g}^{-1}$). The emergence of minor mesopores and relatively higher pore volume might be due to the removal of residual solvents (DMF/MeOH) and unreacted organic linkers sitting in the pores (confirmed by TGA-MS).

Defect creation by harsh thermal activation is a known phenomenon in MOFs.²⁸⁴ Interestingly, the BET surface area of the sample obtained at 500 °C dramatically dropped to 157 m² g⁻¹ ($SA_{\text{micropore}}/SA_{\text{external}} = 72/85 \text{ m}^2 \text{ g}^{-1}$) due to the disintegration of the crystalline framework. It can be assumed that the pore windows are blocked by the organic residue which prevents entry of N₂ to the pores during the BET measurement. In this sample, the pore volume is reduced to 0.11 cm³ g⁻¹ and the average pore diameter is increased to 1.0 nm. However, with a further increase in temperature, TiO₂ nanoparticles fully recrystallise and a fraction of pore-blocking carbonaceous species evaporate subsequently regenerating the access to the porosity. The micropore diameter systematically increases with the formation of relatively larger pores at higher temperatures. The BET surface area of the sample at 800 °C was calculated to be 315 m² g⁻¹ ($SA_{\text{micropore}}/SA_{\text{external}} = 46.5/267.5 \text{ m}^2 \text{ g}^{-1}$) with a pore volume of 0.32 cm³ g⁻¹ and pore diameter of 1.4 nm respectively. As confirmed by TGA, BET and HRTEM, TiO₂ nanoparticles tend to diffuse out due to the shrinkage of the framework at higher temperature creating a more hollow carbon matrix and mesopores with a higher surface area. The BET and PSD results are summarised in Table 6.1. The surface area, pore volume and pore sizes of the derived composites can be finely tuned by optimising the pyrolysis conditions.

Table 6.1 Summary of the textural properties of as-prepared and selected heat treated NH₂-MIL-125(Ti).

NH ₂ -MIL-125(Ti)	BET surface area (m ² g ⁻¹)			Pore volume (cm ³ g ⁻¹)	Pore diameter (nm)
	Total SA	Micropore SA	External SA		
RT	1465	1336	129	0.60	0.7
200 °C	1435	784	651	0.76	0.7
500 °C	157	72	85	0.11	1.0
800 °C	315	46.5	267.5	0.32	1.4

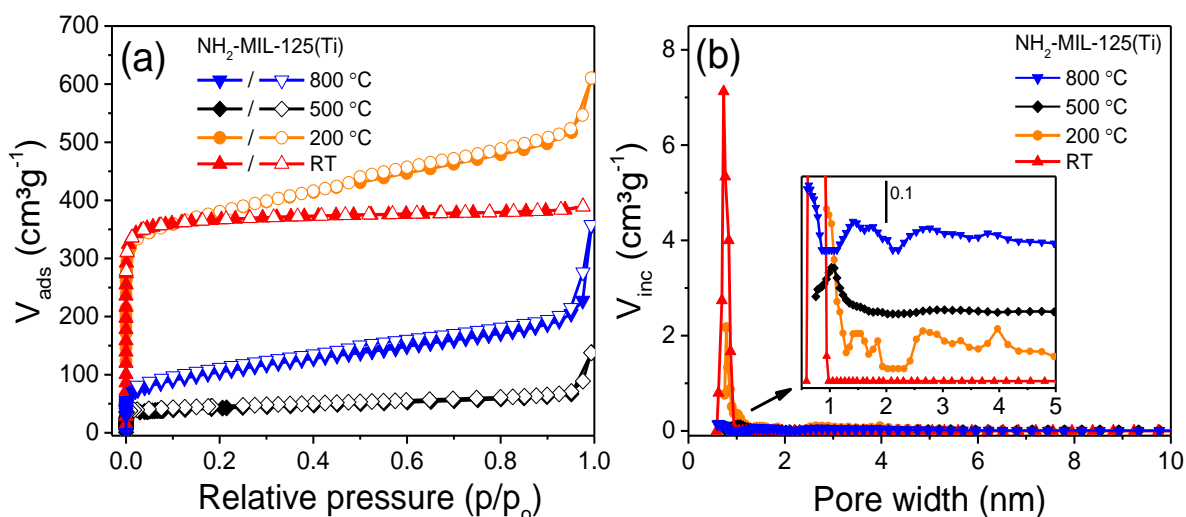


Figure 6.7 (a) BET and (b) PSD of as-prepared NH₂-MIL-125(Ti) (red) and heat treated at 200 °C (orange) 500 °C (black) and 800 °C (blue).

6.2.3 Morphology

The in-situ STEM images (Figure 6.8) show that heating NH₂-MIL-125(Ti) in an argon atmosphere up to 300 °C exhibits no apparent structural change and the size of the selected crystallites remain almost unchanged (width = 0.90 μm, apparent thickness = 0.34 μm). However, as the temperature is increased beyond 350 °C, the MOF reticular structure loses the periodicity/crystallinity (as suggested by XRD and TGA results) initiating the reduction of carbon from organic linker (NH₂-BDC) at around 450 °C causing shrinkage of the MOF grains

(width = 0.74 μm , apparent thickness = 0.29 μm) along with the disintegration of the metal cluster $\text{Ti}_8\text{O}_8(\text{OH})_4$ and organic linker $[\text{O}_2\text{C}-\text{C}_6\text{H}_3(\text{NH}_2)-\text{CO}_2]_6$. Further increase in temperature above 550 $^\circ\text{C}$ and the concurrently progressive carbon removal allows more migration within the lattice. Thus, with the recrystallisation of the metal species, the anatase phase of TiO_2 appears (confirmed by PXRD, Figure 6.4a). As shown in Figure 6.2b and d (TGA-MS), during the carbonisation of $\text{NH}_2\text{-MIL-125(Ti)}$ under an inert atmosphere, the residual species evaporate in the form of CO_2 , HCOOH and H_2O leaving TiO_2 nanoparticles and amorphous carbon. At 550 $^\circ\text{C}$, along with the recrystallisation of TiO_2 , accessible porosity is recovered inside the decomposed grains (width = 0.68 μm , apparent thickness = 0.27 μm). With further increase in temperature, the grain size continues to shrink (width = 0.64 μm , apparent thickness = 0.24 μm at 700 $^\circ\text{C}$) along with the enlargement of the micropores as well as the gradual growth of mesopores. At 800 $^\circ\text{C}$, approximately 35 % volume shrinkage takes place in grain size (width = 0.58 μm , apparent thickness = 0.23 μm) (Figure 6.8) compared to the pristine $\text{NH}_2\text{-MIL-125(Ti)}$. Further confirmed by SEM images (Figure 6.9), the overall tetragonal 3D disc-like morphology of $\text{NH}_2\text{-MIL-125(Ti)}$ remains preserved in the derived N and/or C doped TiO_2/C composites. Simultaneously, well crystalline anatase and rutile TiO_2 nanoparticles are immobilised uniformly in the porous carbon matrix which is further confirmed by in-situ HRTEM and EDX elemental mapping.

The in-situ HRTEM images of selected samples at three different stages of pyrolysis such as as-prepared $\text{NH}_2\text{-MIL-125(Ti)}$ at room temperature, the intermediate amorphous phase at 500 $^\circ\text{C}$ and the fully carbonised well crystalline phase at 800 $^\circ\text{C}$ are shown in Figure 6.10. No individual Ti or TiO_2 nanoparticles are visible in as-prepared $\text{NH}_2\text{-MIL-125(Ti)}$ (Figure 6.10a and b) whereas amorphous or poorly crystalline anatase TiO_2 nanoparticles can be observed (Figure 6.10c and d). However, at 800 $^\circ\text{C}$, well crystalline anatase and rutile TiO_2 nanoparticles (Figure 6.10e and f) can be seen homogeneously distributed on the surface and inside the porous carbon matrix. At 800 $^\circ\text{C}$, the average TiO_2 particle sizes are estimated around 20 nm and lattice spacing is calculated to be 0.33 nm.¹⁶⁸ From these observations, it is evident that above 600 $^\circ\text{C}$, TiO_2 nanoparticles are recrystallised in the anatase phase, finally transforming into the rutile phase at 900 $^\circ\text{C}$. Conventionally, metal oxides tend to form larger particles

and agglomerates due to the sintering effect when heated above Tamman temperature (approximately half of the melting point of metal species).⁴¹ However, the thermal decomposition of MOFs starts mostly at temperatures typically lower than the Tamman temperature of their constituent metal species (such as Ti). Therefore, once the MOF decomposes, the metal cluster transforms into respective metal oxide nanoparticles. As the pyrolysis temperature increases, larger particles are formed at the expense of the smaller nanoparticles. It is interesting to directly observe that in MOF derived composites, the carbon matrix restricts the mobility of the metal species preventing them to sinter and agglomerate which ensures a homogeneous distribution of the formed metal oxide nanoparticles embedded in high surface area porous carbon matrix.

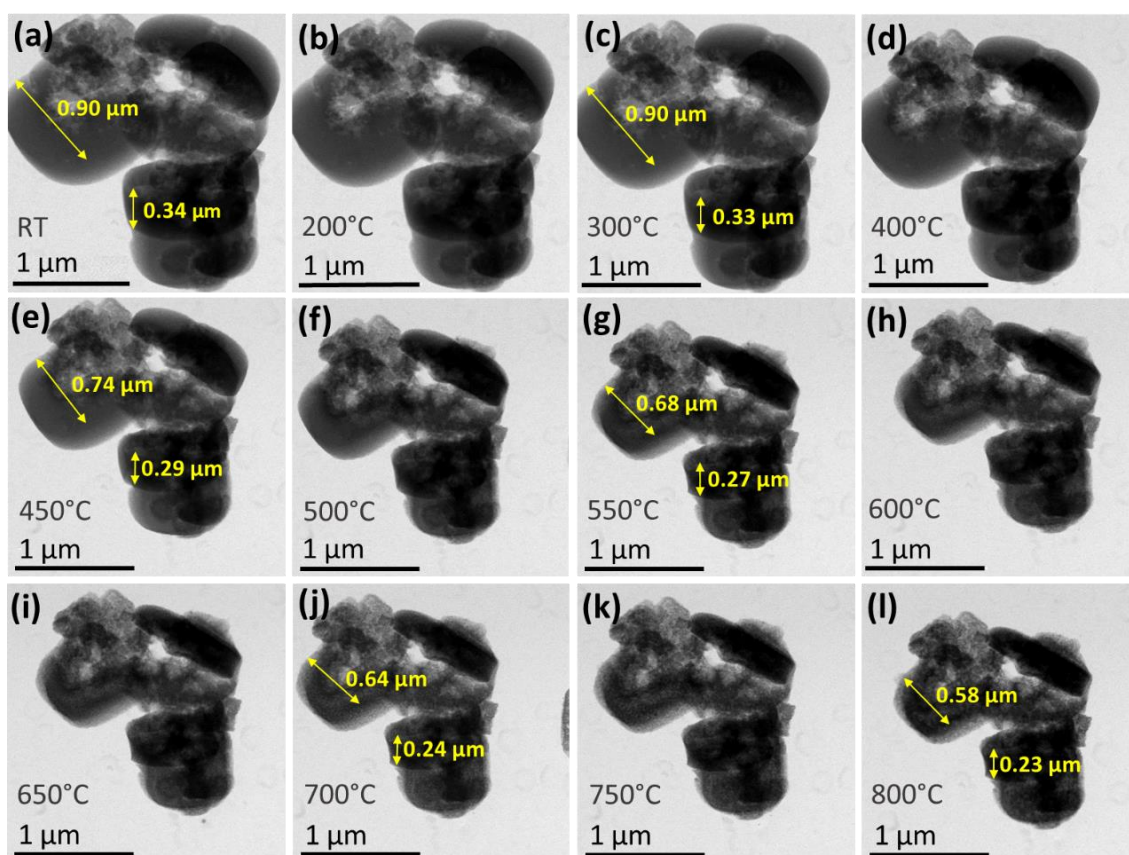


Figure 6.8 (a-l) In-situ STEM images recorded during the heat treatment of $\text{NH}_2\text{-MIL-125(Ti)}$ under argon atmosphere displaying the porosity formation and shrinkage of the crystals at higher temperature with the preservation of the general morphology.

The in-situ EDX elemental mapping of as-prepared NH₂-MIL-125(Ti) and heated up to 800 °C (Figure 6.11) confirm that the Ti, O and C species remain homogeneously distributed throughout the porous carbon matrix.

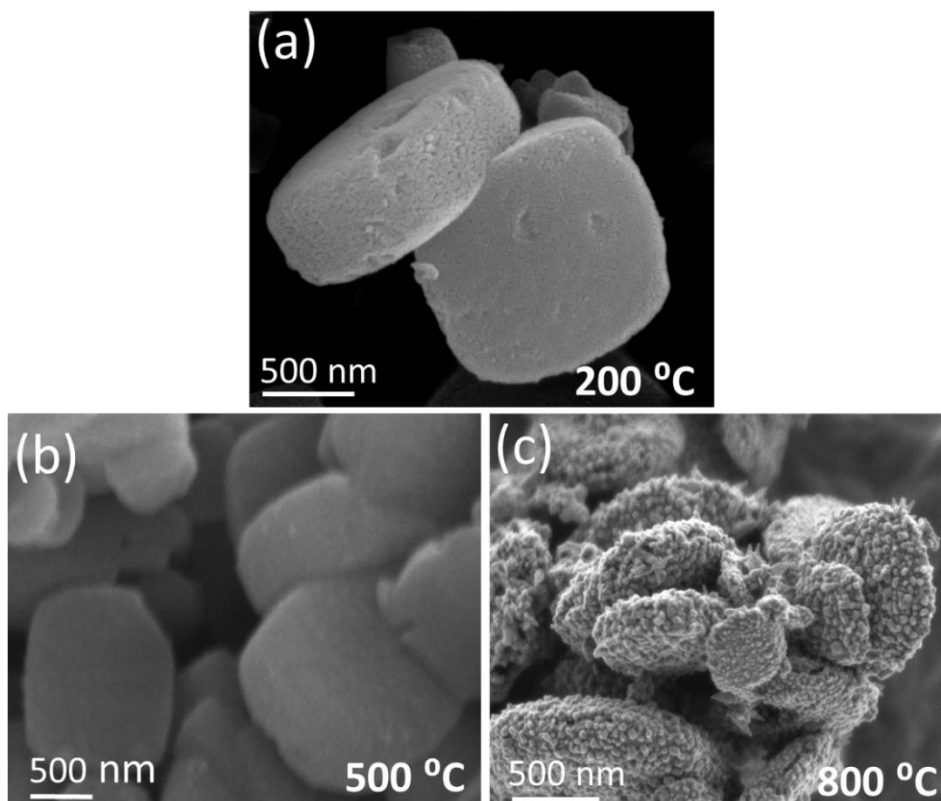


Figure 6.9 SEM images of selected samples obtained by heat treatment of NH₂-MIL-125(Ti) at (a) 200 °C (b) 500 °C and (c) 800 °C.

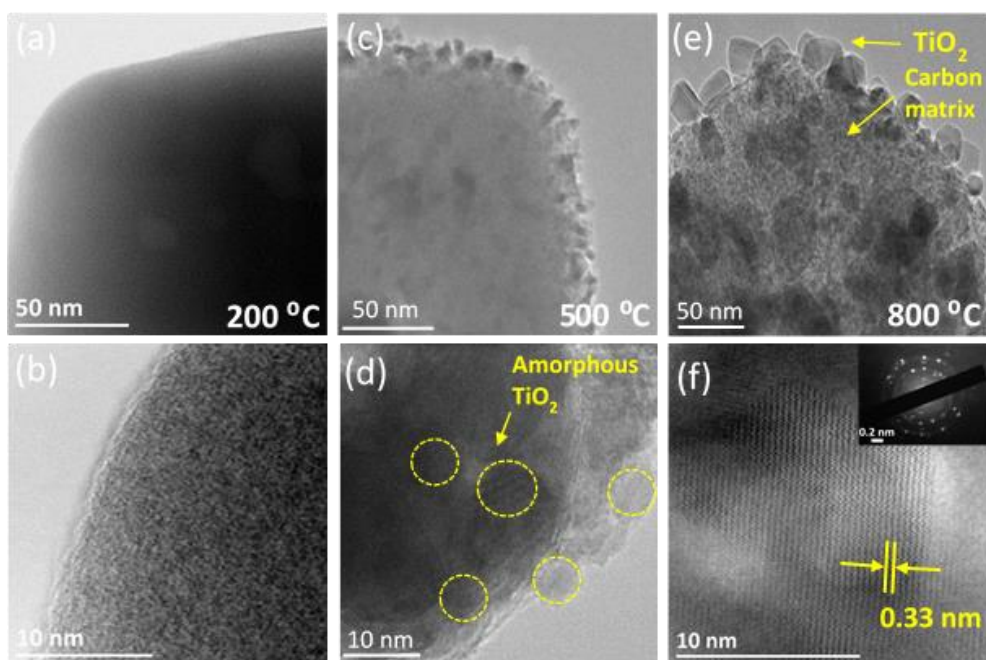


Figure 6.10 HRTEM images of selected samples obtained by heat treatment of NH₂-MIL-125(Ti) at (a, b) 200 °C (c, d) 500 °C and (e, f) 800 °C.

Table 6.2 Summary of XPS data of samples treated at 200, 500 and 800 °C respectively.

200 °C		500 °C		800 °C	
B.E. (eV)	Assignment	B.E. (eV)	Assignment	B.E. (eV)	Assignment
Carbon					
284.8	C=C (sp ²)	284.8	C=C	284.2	C=C
286.2	C-O-C	285.8	C-O	285.1	C-O
288.4	O-C=O	288.2	O-C=O	287.7	O-C=O
Nitrogen					
399.9	-NH ₂ (organic linker)	398.3	Pyridine-like N atoms	396.1	Substituted N in TiO ₂ lattice
402	-NH ₂	400.4	Pyrrolic N	398.3	Pyridine-like N atoms
-	-	-	-	400.4	Pyrrolic N
Oxygen					
531.9	Ti oxo-cluster	531.3	-OH group	531.2	-OH group
531.6	C=O	530.2	Ti-O	530.1	Ti-O
Titanium					
458.8	Ti 2p _{3/2}	458.6	Ti 2p _{3/2}	458.6	Ti 2p _{3/2}
464.7	Ti 2p _{1/2}	464.6	Ti 2p _{1/2}	464.6	Ti 2p _{1/2}

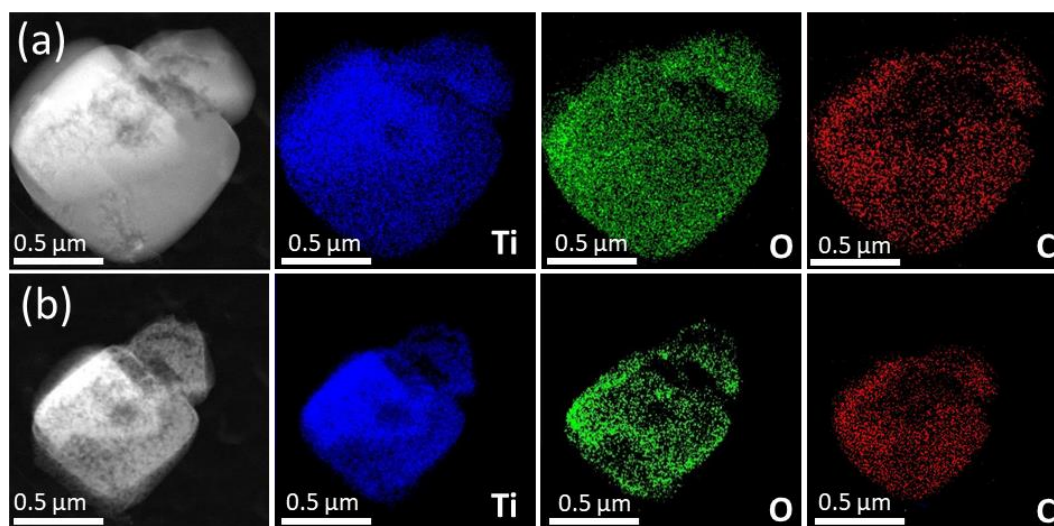


Figure 6.11 In-situ EDX elemental maps of samples (a) NH₂-MIL-125(Ti) and heat treated at (b) 800 °C.

6.3 Summary

In summary, thermal annealing (TGA-MS) and in-situ STEM analysis in combination with EDX elemental mapping under inert atmosphere and several other characterisation techniques were employed to investigate the structural, physicochemical, textural and morphological properties of as-synthesised NH₂-MIL-125(Ti) and the derived nanocomposites. Based on the experimental observations, the carbonisation of the MOF and subsequent formation of the metal oxide/carbon nanocomposites can be defined as a 3 stage process in the following order: Phase-pure, highly porous and crystalline MOF → Intermediate amorphous phase without accessible porosity → Recrystallised porous phase. The thermal annealing revealed that the NH₂-MIL-125(Ti) framework disintegrates above 350 °C through dissociation of both coordination and covalent bonds of the organic linker [O₂C-C₆H₃(NH₂)-CO₂]₆ and the Ti oxo-cluster Ti₈O₈(OH)₄. As monitored by TGA-MS, the organic fragments gradually evaporate in the form of H₂O, CO, CO₂, NO_x and NH₂/NH₃. Moreover, N released from the cleavage of covalent bonds of –NH₂ functional groups from the organic linker dope into the TiO₂ nanoparticles as well as functionalises the porous carbon. During the carbonisation of NH₂-MIL-125(Ti), the elemental distribution (Ti, O, C and N) remains homogeneous in the porous carbon matrix. Between 350 and 550 °C, an intermediate amorphous phase is formed without accessible porosity. However, above 550 °C, the metal species recrystallise forming the anatase TiO₂ nanoparticles followed by the formation of well crystalline rutile TiO₂ phase at around 650 °C. Simultaneously, the carbonaceous matrix originating from the organic linker undergoes subsequent decomposition and evaporation above 450 °C causing the particle shrinkage and reopening of the pore windows regenerating accessible porosity as N₂ physisorption analysis reveals. Besides, the removal of organic linkers triggers fusion of the formerly well-defined MOF pores into larger and less defined (meso)pores. With increasing temperature, the grain sizes continue to shrink and show approximately 35 % shrinkage at 800 °C compared to the pristine MOF. The general morphology of the MOF remains preserved in derived N and/or C doped TiO₂/C composites.

Chapter 7

Bimetal-organic framework (bi-MOFs) derived TiO₂/Cu_xO/C multi-heterostructured nanocomposites for highly efficient photocatalytic H₂ evolution

7.1 Introduction

Hydrogen (H₂) gas evolution from water splitting by using the sunlight is regarded as one of the most cost-effective and cleanest energy sources.^{1, 12, 13, 126, 285} Commercially, H₂ is largely produced by methane steam reforming which is an energy-consuming and environmentally unsustainable process. H₂ evolution from water splitting under sunlight mimics natural photosynthesis and it is generally accepted that if achieved at an economically affordable scale, photocatalytically generated H₂ can be commercially used as a clean fuel in automobiles, fuel cells and domestic heating.^{35, 38, 286-289} The mechanism of photocatalytic H₂ evolution from water splitting has been discussed in chapter 2. TiO₂ is proved to be the most promising semiconducting material due to its appropriate conduction band position (more negative than 0 eV vs NHE at pH = 0) and valence band position (more positive than 1.23 eV vs NHE at pH = 0). However, due to the large EBGs, these photocatalysts can only be activated under UV light. To overcome the challenges of the wide EBG, several methods have been reported such as the doping of anionic (such as N, C, S, P) and cationic (like metals atoms) species into semiconducting metal oxides to create new energy levels above the valence and below the conduction band edges to narrow down the EBGs respectively.²⁹⁰ Although doping of such species in pure TiO₂ results in enhanced visible light absorption, a serious challenge of the low performance for such single metal oxide based photocatalyst is the recombination of photogenerated electrons and holes.^{7, 17, 19, 291, 292} Therefore, it is important to improve the charge separation and charge migration in the photocatalyst particles for enhanced quantum yield.

Many strategies have been developed to increase charge separation and charge migration efficiencies of photocatalytic systems, such as constructing phase junction between the different phases of the same metal oxide (e.g. anatase and rutile phase TiO₂) or heterojunction at the interfaces of different metal and/or non-metal compounds (e.g. TiO₂/CuO_x, Cu₂O/g-C₃N₄) to spatially separate the photogenerated electrons and holes.^{1, 12, 293-295} Moreover, the

number of active sites for photocatalytic water reduction reaction are increased with the help of noble metal (e. g. Pt, Au and Pd) cocatalysts.^{1, 20, 292, 296-298} Although many of these strategies can enhance the photocatalytic H₂ evolution performance compared to the commercially available pure TiO₂ nanoparticles, the synthesis methods are generally complicated, expensive and not commercially affordable. A promising solution to solve these problems is to synthesise metal compound/carbon composite materials as photocatalysts.^{295, 299} However, the conventional approaches such as physical mixing of high surface area graphene or carbon materials and metal oxides hardly form homogeneous distribution of metal oxide in carbon materials with convincing interfacial contacts for better charge transfer and quenching of surface charge recombination.^{300, 301}

In recent years, MOFs have been proven to be excellent precursors and sacrificial templates to derive (multi)metal oxide/carbon nanocomposites. The photoactive transition metal-based MOFs can be used as sacrificial templates to derive heteroatom doped single/multi-metal oxide nanoparticles embedded in functionalised porous carbon structures with inherited morphologies, high BET surface areas, modifiable textural properties and tunable heterostructures for photocatalytic applications.^{36, 41, 52, 62, 90, 114, 148, 302} Based on the understanding of thermal decomposition of NH₂-MIL-125(Ti) and the subsequent formation of TiO₂/C composites (discussed in chapter 6), Ti-MOFs can be employed to form nanocomposites with appropriate semiconducting properties by optimising the synthesis parameters.

This chapter presents a Cu²⁺ coordinated bimetal-organic framework (bi-MOF), NH₂-MIL-125(Ti/Cu), which can be employed as a suitable sacrificial template to simply derive TiO₂/Cu_xO/C multi-heterojunction for enhanced photocatalytic H₂ evolution. This study demonstrates the successful formation of bi-MOF derived nanocomposite multi-heterostructures with simultaneous phase junctions between anatase/rutile TiO₂ and Cu₂O/CuO as well as p-n heterojunction between TiO₂ and Cu_xO, which exhibited remarkable photocatalytic H₂ evolution performance.

7.2 Results and discussion

7.2.1 Characterisations of NH₂-MIL-125(Ti/Cu) and derived TiO₂/Cu_xO/C

The PXRD patterns (Figure 7.1a) of activated MOF, NH₂-MIL-125(Ti) and bi-MOF, NH₂-MIL-125(Ti/Cu) confirm the successful formation and incorporation of Cu²⁺ in the NH₂-MIL-125(Ti/Cu) with no formation of additional phases. The PXRD peaks that appeared at 2θ of 6.8° and 9.8° are in good agreement with the simulated XRD pattern of NH₂-MIL-125(Ti). To confirm the Cu²⁺ ions are coordinated to the amino (-NH₂) group, the XPS spectra of N 1s of NH₂-MIL-125(Ti/Cu) was recorded. As shown in Figure 7.1b, the deconvoluted peaks appeared at 399.3 and 400.1 eV, which can be assigned to the positively charged amino group (-NH₂⁺) due to the charge transfer to the coordinated Cu²⁺ species represented in the schematics diagram (Figure 7.1c). The emergence of the shoulder peak can be attributed to the donation of non-bonded lone pair electrons of -NH₂ group to the Cu²⁺ ions resulting in the formation of quaternary valence -NH₂⁺.³⁰³

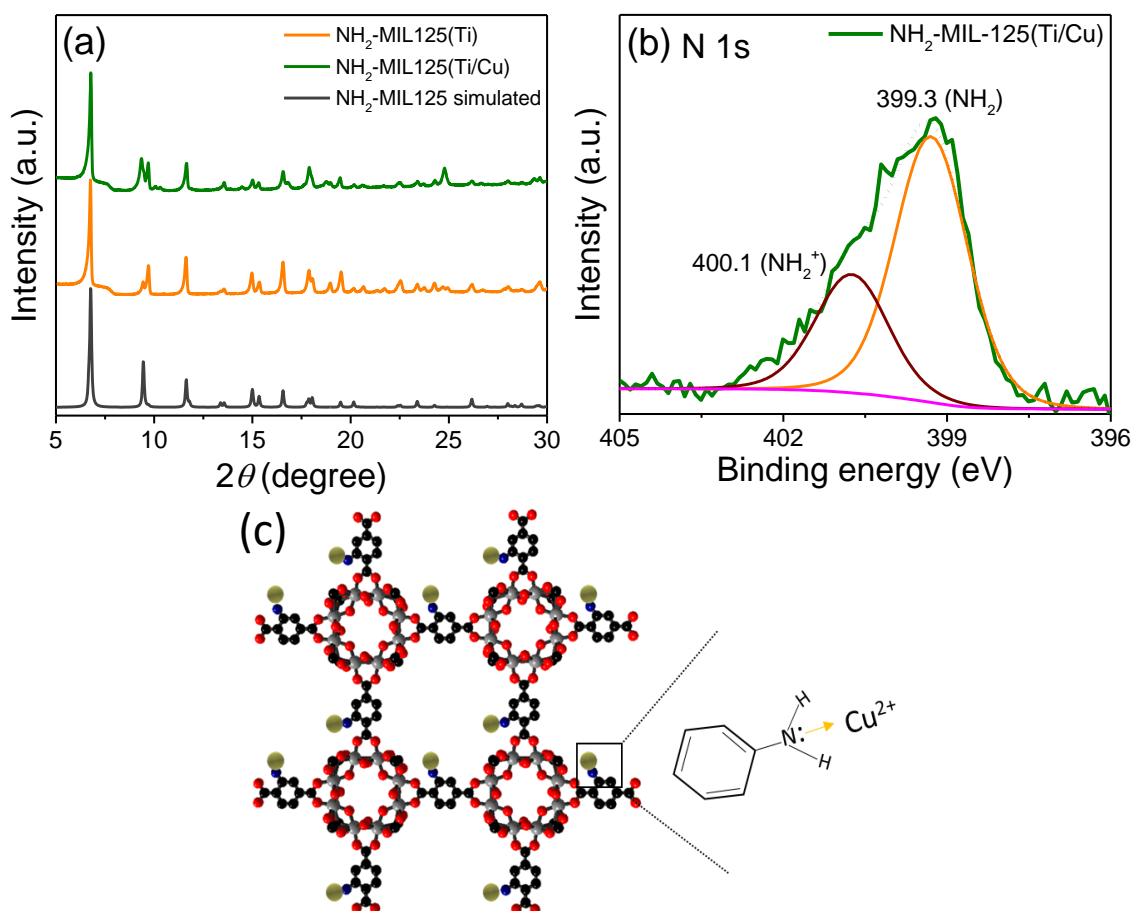


Figure 7.1 (a) PXRD patterns of simulated (dark grey), as-synthesised NH₂-MIL-125(Ti) (orange) and NH₂-MIL-125(Ti/Cu) (olive) (b) Deconvoluted N 1s XPS

spectra of as-prepared NH₂-MIL-125(Ti/Cu) (c) schematics diagram of the charge transfer to coordinated Cu²⁺.

Pyrolysis of the bi-MOF NH₂-MIL-125(Ti/Cu) at 550, 700 and 800 °C in water vapour resulted in the decomposition of NH₂-MIL-125(Ti/Cu) into TiO₂, Cu_xO and Cu species embedded in a porous carbon matrix. The PXRD patterns (Figure 7.2a) show the main peaks of anatase (101) and rutile (110) appearing at 2θ of 25.2° and 36.4° respectively with varying intensity. Depending upon the pyrolysis temperatures, the ratios of anatase to rutile phase of TiO₂ polymorphs were calculated to be 91/9, 45/55 and 10/90 for samples derived at pyrolysis temperature of 550, 700 and 800 °C under water vapour respectively. Moreover, with the increase of pyrolysis temperatures, relatively larger TiO₂ nanoparticles were formed which may be due to the sintering effect.⁴¹ Using the Scherrer equation, the average particle sizes of anatase and rutile phases of TiO₂ were calculated to be 2.6/4.8, 10.3/18.8 and 11.4/23.4 nm for the sample obtained at 550, 700 and 800 °C respectively. In addition, along with the formation of optimised TiO₂ polymorphs, TiO₂/Cu_xO heterojunction formed during the pyrolysis of the Cu-loaded bi-MOF NH₂-MIL-125(Ti/Cu). Das *et al.* reported that the metals with a reduction potential above -0.27 V such as Cu²⁺ usually form pure metal nanoparticles (Cu⁰) upon pyrolysis of the MOFs in an inert atmosphere.¹⁰³ However, pyrolysis under controlled water vapour (PXRD Figure 7.2a) results in the transformation of Cu²⁺ into Cu₂O at 550 °C as a dominant phase with a trace amount of CuO phase, whereas pyrolysis at 700 °C, Cu₂O and CuO phases co-exist with some residual Cu⁰ nanoparticles. However, at the pyrolysis temperature of 800 °C, CuO becomes the dominant phase with a small amount of Cu₂O and Cu⁰ nanoparticles in the resulting composite. The highlighted PXRD peaks of Cu_xO (inset in Figure 7.2a) suggest that the pyrolysis temperatures also affect the 2θ values of the crystallites therefore the particle sizes of the formed Cu_xO phases. These observations are further confirmed by XPS of Cu 2p as well as Raman spectra.

TGA profiles of NH₂-MIL-125(Ti/Cu) and the derived composites were recorded under synthetic air to quantify the amount of TiO₂, Cu_xO and C species. As shown in Figure 7.2b, NH₂-MIL-125(Ti) and NH₂-MIL-125(Ti/Cu) exhibited around 9 % weight loss up to 300 °C due to the release of adsorbed moisture and

the residual organic linker. The NH₂-MIL-125(Ti) framework starts to decompose above 300 °C in the air releasing primarily CO₂ and NO_x due to the oxidation of organic linker and leaving behind 34 wt.% TiO₂ nanoparticles.⁴⁴ However, the TGA profile of bi-MOF, NH₂-MIL-125(Ti/Cu) shows the decomposition of the framework starting at around 250 °C due to the breaking of Cu-N bonds resulting in the formation of CuO nanoparticles under synthetic air. The weight percentage of Cu species is estimated to be 10.5 wt.% which is in good agreement with EDX elemental mapping results. Similarly, the TGA profiles of NH₂-MIL-125(Ti/Cu) derived nanocomposites presented in Figure 7.2c indicate that the amount of carbon for samples obtained at pyrolysis temperature of 550, 700 and 800 °C is 27, 15 and 5 wt.% respectively, which is burned off in the temperature range of 300-400 °C in air. The decreased amount of carbon for TiCuC800 is maybe because part of the formed carbons can readily react with water vapour at high pyrolysis temperature and release as CO/CO₂.

It is important to distinguish that the TGA profiles shown in Figure 7.2b represent the profiles of as-prepared NH₂-MIL-125(Ti) and NH₂-MIL-125(Ti/Cu) precursors heated in air. However, the relative weight loss (TGA) in Figure 7.2c represents the amount of amorphous carbon and nitrogen species present in bi-MOF derived TiO₂/Cu_xO/C composites, which are obtained by heat treatment of NH₂-MIL-125(Ti/Cu) precursor under water vapour at high temperatures 550, 700 and 800 °C. During the heat process, the coordination bonds between Ti oxo-cluster and Cu²⁺ coordinated NH₂-BDC (organic linker) in NH₂-MIL-125(Ti/Cu) start breaking off at above 300 °C. The metal cluster and coordinated Cu species are transformed into TiO₂ and Cu_xO nanoparticles whereas the organic linker is transformed into a functionalised porous carbon matrix, accompanied by the release of CO₂ and NO₂. Since these TiO₂/Cu_xO/C composites were generated under the water vapour at a higher temperature, they largely contain C=O, -OH, C-N even N-O functional groups, as confirmed by FTIR. These functional groups are readily decomposed and transformed to CO₂, H₂O and NO₂ when heated in air. The multiple MS signals of H₂O indicate the release of surface absorbed moisture and the burning off surface-functionalised groups including -NH_x, -OH and -COOH.

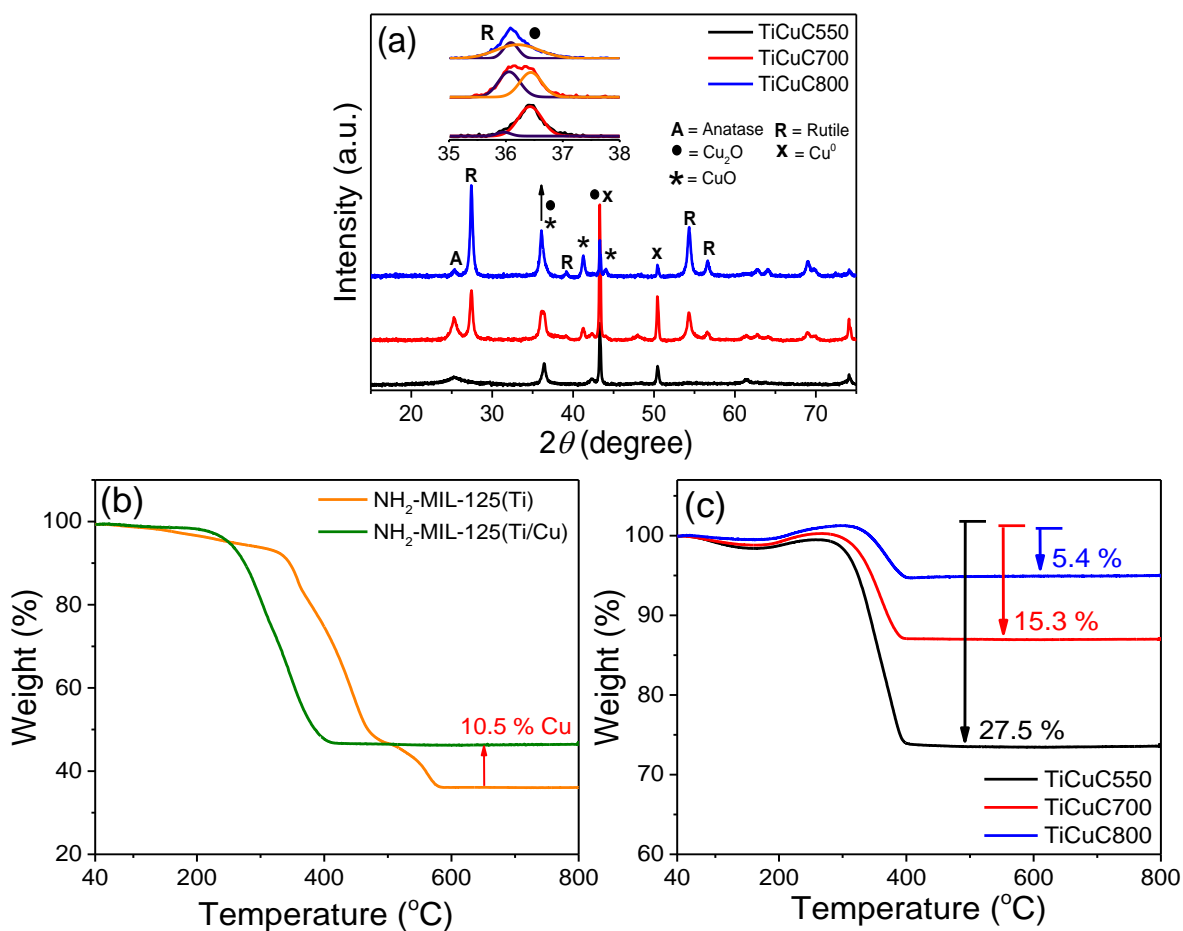


Figure 7.2 (a) PXRD (b) TGA profiles of as-prepared $\text{NH}_2\text{-MIL-125(Ti)}$ and $\text{NH}_2\text{-MIL-125(Ti/Cu)}$ in air and (c) TGA profiles of derived composites in air. Inset in (a) shows deconvoluted peaks separating rutile TiO_2 and Cu_2O .

The representative SEM images suggest that with the increase of pyrolysis temperature from 550 $^\circ\text{C}$ to 800 $^\circ\text{C}$, the thermal decomposition of bi-MOF $\text{NH}_2\text{-MIL-125(Ti/Cu)}$ in water vapour results in the formation of carbon, TiO_2 and Cu_xO nanocomposites with disc-like morphologies similar to their precursor $\text{NH}_2\text{-MIL-125(Ti/Cu)}$ with a particle size up to 1.5 μm (Figure 7.3a). However, the particle surface of the nanocomposites turns rougher compared to their precursor. At pyrolysis temperature of 550 $^\circ\text{C}$ in water vapour, the TiO_2 and Cu_xO nanoparticles are buried inside the carbon matrix of sample TiCuC550 with a rougher surface compared to $\text{NH}_2\text{-MIL-125(Ti/Cu)}$. For sample TiCuC700 obtained at 700 $^\circ\text{C}$, more TiO_2 and Cu_xO species are exposed but still embedded homogeneously in a porous carbon matrix. In the case of sample TiCuC800 at pyrolysis temperature of 800 $^\circ\text{C}$ in water vapour, more formed carbon is turned into CO_2 , which results

in the TiO_2 and Cu_xO nanoparticles fully exposed. Based on the results from TGA and the representative SEM images, a schematic diagram of $\text{NH}_2\text{-MIL-125(Ti/Cu)}$ derived nanocomposites (Figure 7.3b) is presented. This observation is also in good agreement with the TEM images of the samples derived at 550, 700 and 800 °C (Figure 7.3c, d and e) which show a relative recession in carbon matrix as well as enlargement of TiO_2 nanoparticles with the increase of pyrolysis temperature.

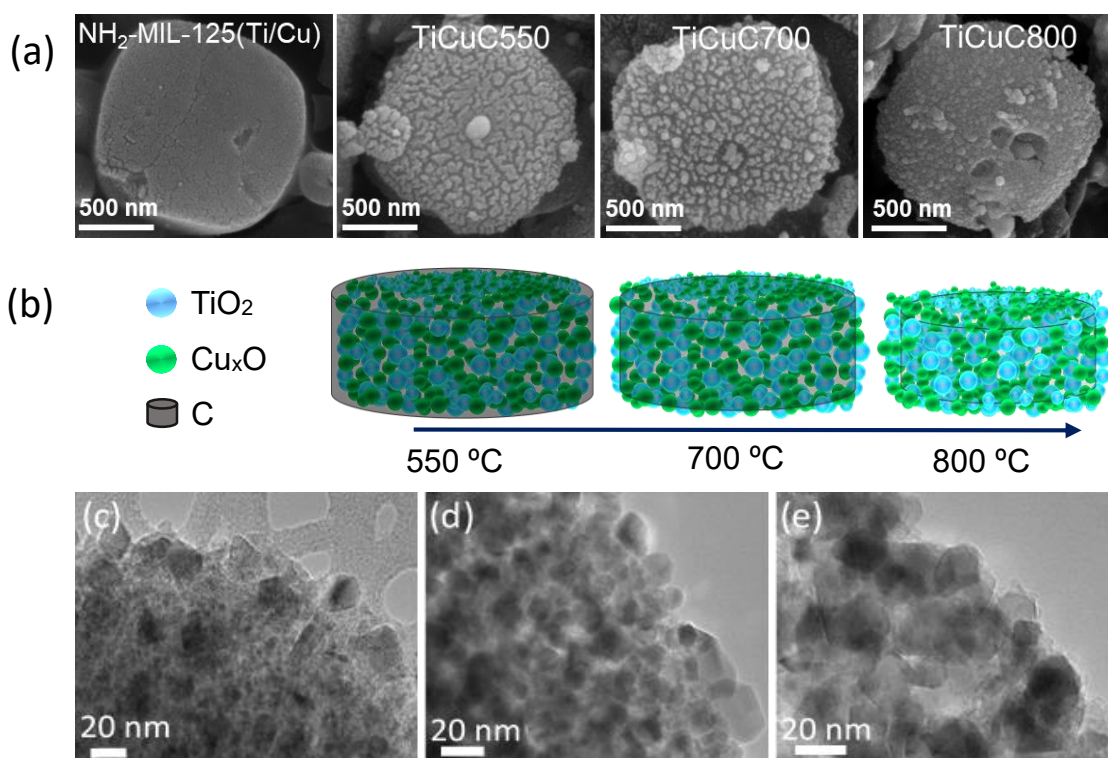


Figure 7.3 (a) SEM images and (b) representative schematic diagrams of bi-MOF $\text{NH}_2\text{-MIL-125(Ti/Cu)}$ derived nanocomposites named TiCuC550 , TiCuC700 and TiCuC800 obtained at temperatures 550, 700 and 800 °C respectively. TEM images of (c) TiCuC550 (d) TiCuC700 and (e) TiCuC800 .

The textural properties of the bi-MOF precursor together with its derived nanocomposites were evaluated via gas sorption analysis. The N_2 sorption isotherms for the precursor $\text{NH}_2\text{-MIL-125(Ti)}$ and $\text{NH}_2\text{-MIL-125(Ti/Cu)}$ (Figure 7.4a) are typical microporous materials with narrow PSD (inset in Figure 7.4a). Their BET surface areas and pore volumes are summarised in Table 7.1, which are in good agreement with literature reports.³⁰³ N_2 sorption isotherms for the MOF derived nanocomposites largely exhibited reversible adsorption and

desorption branches (Figure 7.4b) and their textural properties are summarised in Table 7.1. In general, a higher pyrolysis temperature increases the BET surface area of the resulting samples. Despite the higher weight percentage of carbon, the relatively lower BET surface area in sample TiCuC550 might be due to the presence of residual species from the decomposed organic linkers blocking the pores, whereas the relatively lower BET surface area in the sample TiCuC800 compared to the TiCuC700 can be due to the evaporation of most of the carbon (lower wt.%) in the form of CO₂. In addition, sample TiCuC700 with the highest BET surface area is dominated by relatively narrow micropores, however, mesopores turn to be dominant in sample TiCuC800 (inset in Figure 7.4b).

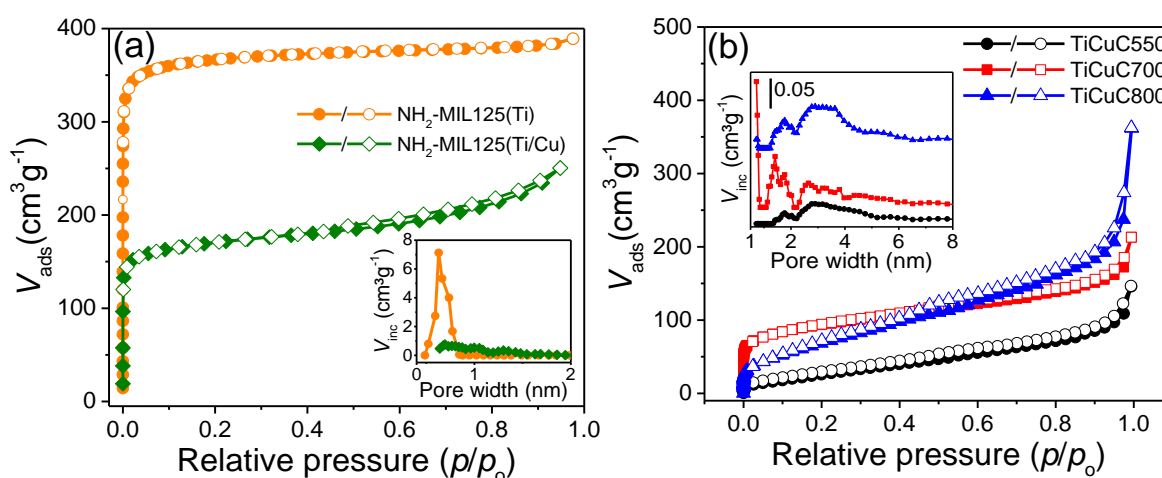


Figure 7.4 N₂ sorption isotherms of (a) NH₂-MIL-125(Ti) and NH₂-MIL-125(Ti/Cu) and (b) derived nanocomposites. Insets in (a) and (b) correspond to their respective PSD.

Raman spectra were recorded to investigate the vibrational modes of TiO₂ and Cu_xO as well as the nature of carbon presented in these samples. In pure TiO₂ the prominent vibrational mode $E_g(1)$ of anatase TiO₂ appear at 144 cm⁻¹.²⁷⁰ However, in samples TiCuC550 and TiCuC700 this mode is observed at 146 and 154 cm⁻¹ respectively, whereas it is negligibly small in sample TiCuC800. This shift of $E_g(1)$ mode in TiCuC700 may be ascribed to the dominance of rutile phase along with the phase changing of anatase, the lattice vibrations as well as the formation of localised defects due to in-situ anionic N and C doping into TiO₂ nanoparticles, which will be further confirmed by UV-Vis absorption spectra and XPS. As exhibited in PXRD results, at 550 °C poorly crystalline anatase phase of TiO₂ is dominant while at 700 °C both highly crystalline anatase and rutile phases

are formed with a phase ratio of 45/55. At 800 °C, the anatase phase almost disappears with the dominant emergence of the rutile phase. This is also in very good agreement with Raman spectra results. At 700 °C, a slightly broader but intense peak of $E_g(1)$ vibrational mode is observed. The inset in Figure 7.5a shows the deconvoluted peaks of Ti-O symmetric bending mode (B_{1g}) of anatase phase at 412 cm^{-1} and the vibrational modes E_g of rutile phase at 430 and 442 cm^{-1} in TiCuC700 and TiCuC800 respectively. Moreover, the rutile phase also shows a similar shift in E_g vibrational modes, which suggests that the presence of N and C atoms may cause a dopant induced strain on the TiO_2 crystal lattices that result in a shift in frequencies of E_g modes.¹⁸² It is worth noting that for $\text{NH}_2\text{-MIL-125(Ti)}$ derived TiC700 nanocomposite obtained under identical pyrolysis conditions (in water vapour at 700 °C for 2 hours) in the absence of Cu species, the E_g vibrational modes of rutile phase appear at 441 cm^{-1} . This indicates that the presence of Cu_2O and/or Cu nanoparticles at the interfacial contact with TiO_2 nanoparticles may modify the band positions and therefore result in a shift in the frequencies of vibrational modes. The deconvoluted vibrational bands of Cu_2O (inset in Figure 7.5a) can be observed at around 285 , 266 , 246 and 630 cm^{-1} for sample TiCuC700, which are also all observed in samples TiCuC550 and TiCuC800 with slightly shifted frequencies and varying intensities. While the peaks at around 246 , 285 and around 585 cm^{-1} can be ascribed to the second-order Raman allowed vibrational modes of Cu_2O crystals, the peak at around 630 cm^{-1} may correspond to the B_g allowed stretching modes of $\text{Cu}_2\text{O}/\text{CuO}$ nanoparticles.^{304, 305}

As discussed above, the precursor $\text{NH}_2\text{-MIL-125(Ti/Cu)}$ thermally decomposes under water vapour and the organic linker in the precursor transforms into N and O-containing functional porous carbon. Figure 7.5a also shows the signature peaks of D and G bands in the first-order Raman spectra of MOF derived carbon, appearing at around 1352 and 1593 cm^{-1} respectively in samples TiCuC550 and TiCuC700. However, these D and G bands are slightly shifted to 1342 and 1598 cm^{-1} in sample TiCuC800. The D band is due to the breathing modes of sp^2 hybridised carbon atoms in hexagonal rings and represents the number of defects and disorders in carbon. The increase in the intensity, as well as the redshift of D band (Figure 7.5a) of carbon presented in TiCuC700 and TiCuC800, correspond to the formation of a higher amount of

surface defects in these samples. The G band in Raman spectra of carbon arises from the bond stretching of all sp^2 atoms in hexagonal rings and chains of carbon. This band appears due to the formation of nanocrystalline carbon.^{215, 216} The shift in G bands of derived carbon samples TiCuC550, TiCuC700 and TiCuC800 can be attributed to the oxidation of the organic linker NH_2 -BDC under water vapour to form N-containing and hydroxyl/carboxyl group functionalities.³⁰⁶ The I_D/I_G ratios in TiCuC550, TiCuC700 and TiCuC800 are calculated to be 0.63, 0.92 and 0.91 respectively which indicate the higher pyrolysis temperature results in a higher amount of defects in the formed carbon matrix.²⁰⁷

Pyrolysis of MOFs under water vapour also functionalises the porous carbon matrix with hydrophilic carboxylic groups.^{101, 207, 261} The presence of surface functional groups in the NH_2 -MIL-125(Ti/Cu) derived nanocomposites is confirmed by FTIR spectra. As shown in Figure 7.5b, a strong band that appeared at 1630 cm^{-1} can be assigned to the carboxyl ($-COOH$) functional groups introduced via water vapour during the pyrolysis process at high temperature.²⁰⁷ While the strong peak at 1385 cm^{-1} can be ascribed to $C=O$ bond stretching, the $C-N$ bond vibration at around 1240 cm^{-1} arises from the N species decorated on the carbon matrix.^{261, 303} In the organic species, the peaks of CH_x bond stretching usually appear around 2900 and 1400 cm^{-1} .³⁰⁷ Obviously, the CH_x bonds at around 2900 cm^{-1} in these composites are negligible and $C-O$, $N-O$, $O=C-OH$ and $C-N$ bonds are clearly presented between 1700 - 1200 cm^{-1} as surface functional groups in these as-prepared $TiO_2/Cu_xO/C$ composites. The negligible CH_x bonds at around 2900 cm^{-1} in these samples might be due to the $C-H$ lattice vibrations of aromatic rings in the formed carbon matrix. Of course, one cannot rule out the small FTIR peaks around 2900 cm^{-1} in these $TiO_2/Cu_xO/C$ composites due to the surface contamination, where the measurements were carried out in ambient and the apparatus (glass slides, spatula) were normally cleaned with organic solvents. The bond stretching modes for pure Cu_2O and TiO_2 usually appear at 630 and 628 cm^{-1} respectively.^{6, 308, 309} However, in NH_2 -MIL-125(Ti/Cu) derived nanocomposites, the $Ti-O$ and $Cu-O$ peaks appeared at 633 , 628 and 608 cm^{-1} in samples TiCuC550, TiCuC700 and TiCuC800 respectively. This frequency shift of $Ti-O$ and $Cu(I)-O$ bond stretching modes may be due to the change of particle sizes at a higher temperature and the doping of N and C atoms into the TiO_2 and Cu_2O nanoparticles, as well as the localised surface defects formed

during the thermal decomposition of the bi-MOF precursor into the metal oxide species.⁶

The UV-Vis absorption spectra of NH₂-MIL-125(Ti) and NH₂-MIL-125(Ti/Cu) are shown in Figure 7.5c. The Cu²⁺ ions coordinated to the -NH₂ functional group improves the visible light absorption for NH₂-MIL-125(Ti/Cu), which results in a redshift from 470 to 484 nm due to the d-d transitions. The change of colour (inset in Figure 7.5c) for NH₂-MIL-125(Ti) from yellow to greenish for NH₂-MIL-125(Ti/Cu) is consistent with the redshift towards the higher wavelength of the visible region.^{303, 310} The EBGs of NH₂-MIL-125(Ti/Cu) derived nanocomposites were estimated from the UV-Vis absorption spectra (inset in Figure 7.5d). The Tauc plots (Figure 7.5d) show that the EBGs of in-situ N/C co-doped TiCuC550, TiCuC700 and TiCuC800 are estimated to be 2.54, 2.47 and 2.56 eV respectively. These samples are predominantly black due to the presence of a significant amount of porous carbons.

The XPS spectra at lower binding energy were recorded to determine the valence band positions of N/C co-doped TiO₂ and Cu₂O nanoparticles. As shown in Figure 7.5e, the valence band spectra exhibit two shoulder-like bends attributed to the valence band edges of TiO₂ and Cu₂O nanoparticles with respect to the Fermi level. The valence band positions of TiO₂ nanoparticles were estimated to be 1.49, 1.36 and 1.48 eV for TiCuC550, TiCuC700 and TiCuC800 respectively. For Cu₂O, the valence band positions were estimated to be 0.23, 0.11 and 0.12 eV for samples TiCuC550, TiCuC700 and TiCuC800 respectively. As confirmed by PXRD, the anatase to rutile phase ratio in sample TiCuC700 is 0.8:1; therefore, a big shift in valence band position of TiO₂ in TiCuC700 may be due to the band bending at the interfaces of anatase and rutile phases. Based on the values of EBGs obtained from the Tauc plots and the valence band positions from XPS, the energy band alignments of TiO₂ and Cu_xO with respect to the core levels of Ti 2p and Cu 2p respectively, the formation of the p-n heterojunction can be anticipated between n-type TiO₂ and p-type Cu₂O.^{3, 311, 312} Due to the formation of p-n heterojunction between N/C co-doped TiO₂ and Cu₂O nanoparticles and the presence of homogeneously dispersed Cu⁰ atoms without agglomerations in porous carbon, these black nanocomposites are expected to provide not only better visible light absorption, but also improved separation and migration of

photogenerated electrons and holes that can result in the enhanced photocatalytic H₂ evolution.

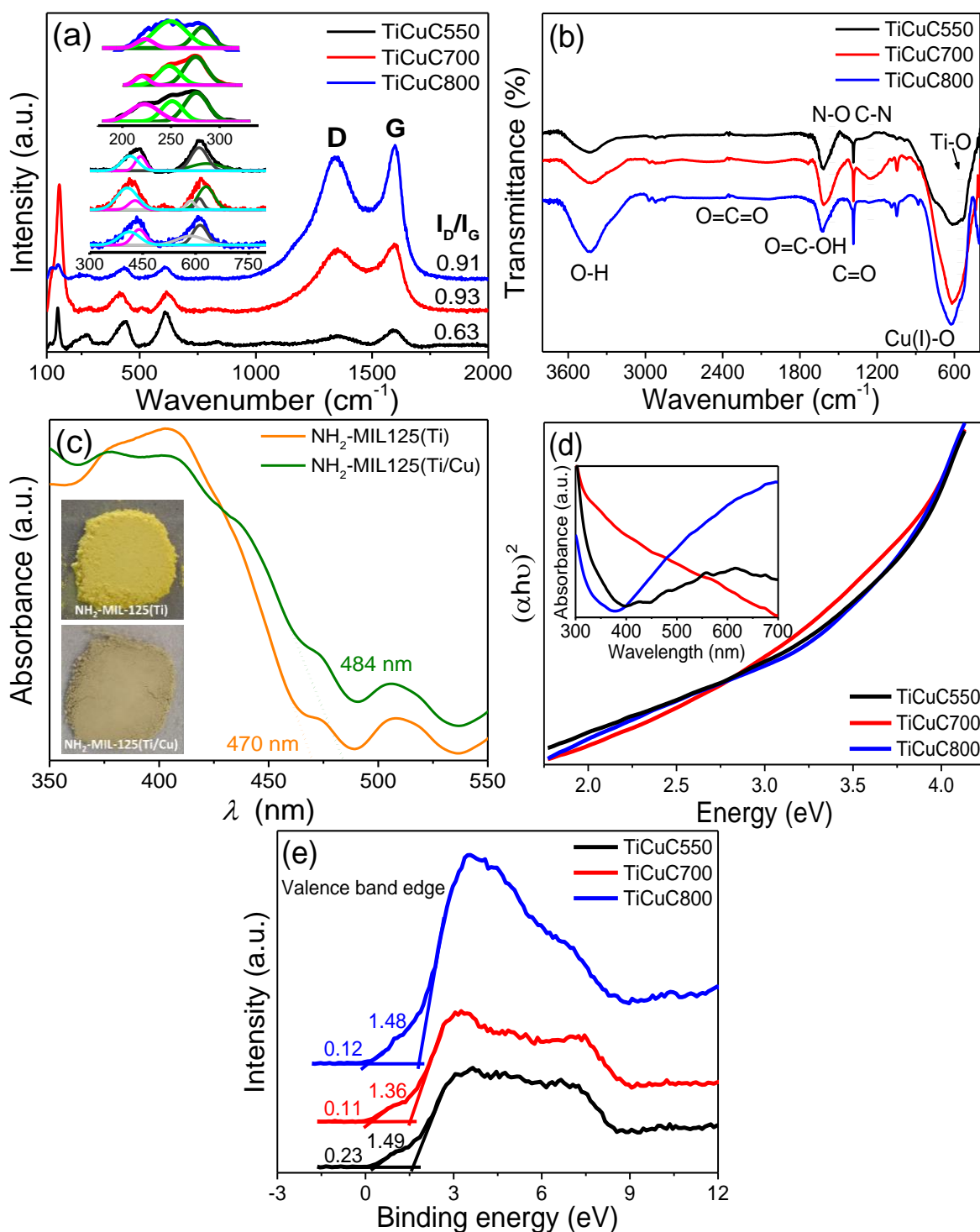


Figure 7.5 (a) Raman spectra and (b) FTIR spectra of TiCuC550 (black), TiCuC700 (red) and TiCuC800 (blue). (c) UV-Vis absorption spectra of NH₂-MIL-125(Ti) and NH₂-MIL-125(Ti/Cu). (d) Tauc plots (UV-Vis absorption spectra in inset) and (e) XPS valence band positions of TiCuC550, TiCuC700 and TiCuC800.

The high-resolution HRTEM images of TiCuC550, TiCuC700 and TiCuC800 (Figure 7.6) confirm that the TiO₂, Cu₂O and Cu⁰ interfaces are physically in contact forming the heterojunctions. Figure 7.6a and d show predominant anatase phase of TiO₂ with an interplanar spacing of 0.32 nm and Cu₂O present in TiCuC550 as confirmed by PXRD. However, for sample TiCuC700, well crystalline anatase (101) and rutile (110) TiO₂ polymorphs with an interplanar spacing of 0.32 and 0.31 nm respectively can be seen in Figure 7.6b and e along with the Cu₂O and Cu⁰ nanoparticles. The crystalline sizes observed in HRTEM images are in good agreement with the particle sizes calculated from the PXRD patterns using the Scherrer equation, which are around 10 nm and 20 nm for rutile and anatase phases of TiCuC700 respectively. The reported lattice spacing of pure TiO₂ usually is around 0.35 and 0.32 nm for anatase and rutile phases respectively.³¹³ The shift in the interplanar spacing of the NH₂-MIL-125(Ti/Cu) derived nanocomposites indicates that the doping of N and C atoms into TiO₂ creates the localised energy states above the valence band which may result in the narrowing of the lattice spacing.^{15, 17} For sample TiCuC800 (Figure 7.6c and f) the predominant rutile phase of TiO₂ forms a heterojunction with Cu_xO nanoparticles. The interplanar spacing of rutile TiO₂ estimated from SAED (inset in Figure 7.6c) is 0.31 nm which is consistent with the value calculated from PXRD patterns.

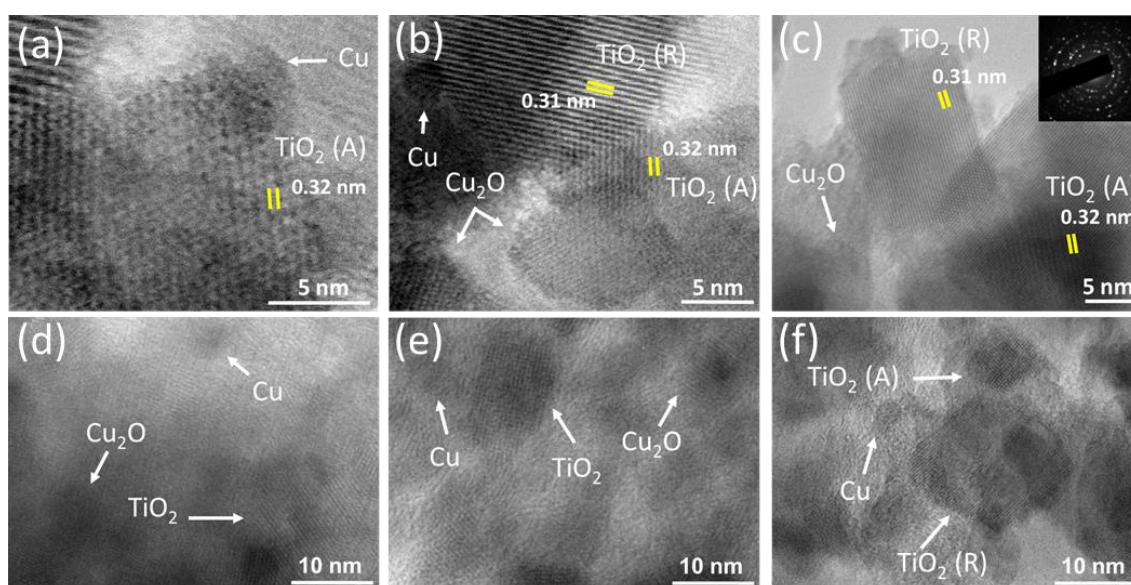


Figure 7.6 Representative HRTEM images of (a, d) TiCuC550 (b, e) TiCuC700 and (c, f) TiCuC800 (SAED in inset).

As sacrificial templates, pyrolysis of MOFs transforms them into metal oxide nanoparticles uniformly distributed in porous carbon matrix without significant change of the morphologies. Energy Dispersive X-ray (EDX) elemental mapping was performed to investigate the distribution of elements Ti, O, Cu, C and N in the NH₂-MIL-125(Ti/Cu) derived nanocomposites. It is evident from the EDX elemental mappings that all the elemental species are uniformly distributed throughout the nanocomposite. The EDX elemental maps of NH₂-MIL-125(Ti/Cu) and the derived TiCuC550, TiCuC700 and TiCuC800 (Figure 7.7) confirm all the elements are homogeneously presented in these samples.

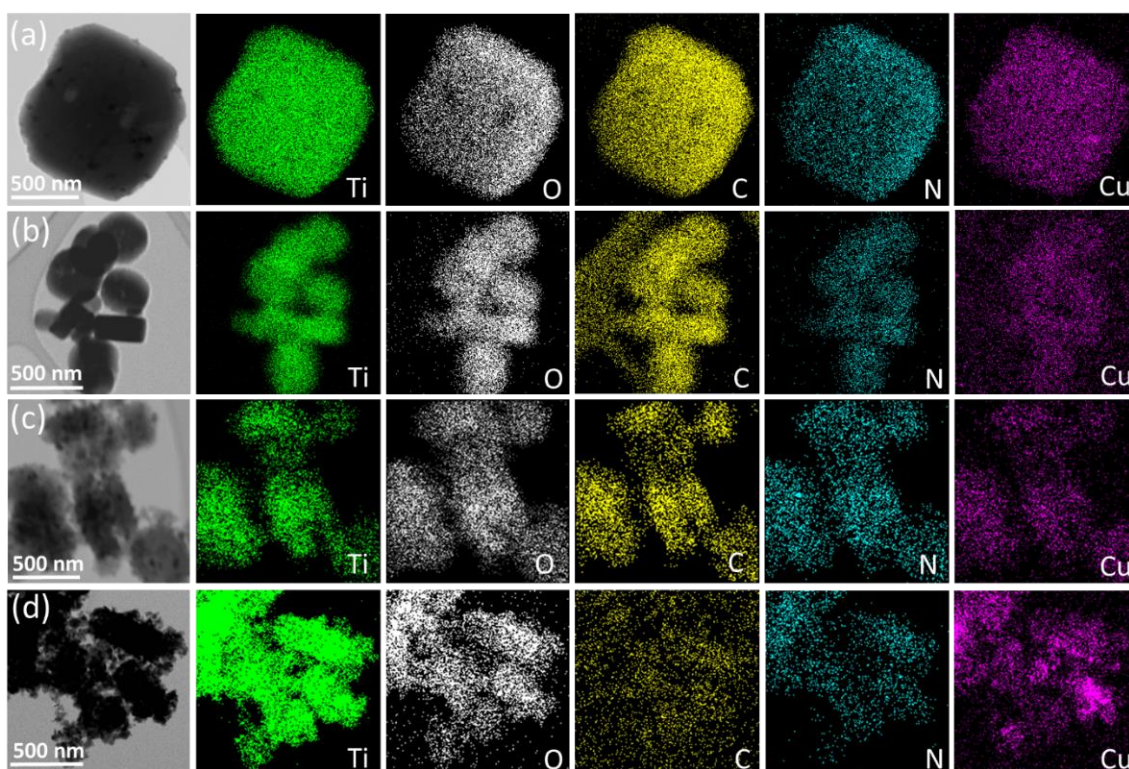


Figure 7.7 EDX elemental mappings of Ti, O, C, N and Cu for sample (a) NH₂-MIL-125(Ti/Cu) (b) TiCuC550 (c) TiCuC700 and (d) TiCuC800.

The elemental composition, the chemical and electronic states of each element in the NH₂-MIL-125(Ti/Cu) derived nanocomposites were investigated by XPS. The element survey spectrum (Figure 7.8a) confirms the presence of Ti, Cu, O, C and N species in all three composites, which is also in agreement with the EDX elemental analysis. As shown in Figure 7.8b, the Ti 2p_{3/2} peak for samples TiCuC550, TiCuC700 and TiCuC800 appear at 458.3, 458.5 and 458.2 eV respectively, which confirm the Ti⁴⁺ oxidation state of O-Ti-O in TiO₂

nanoparticles. In pure TiO₂ nanoparticles, this peak appears at around 459.3 eV.³¹⁴ The shift of Ti 2p_{3/2} peak towards lower binding energy compared to the pure TiO₂ is caused by the doping of N and C species into TiO₂ crystals as well as the formation of oxygen-related defects due to the substituted N atoms.^{8, 315} Moreover, the formation of heterojunction at the interfaces of Cu_xO nanoparticles and TiO₂ nanoparticles may also influence the local chemical environment around Ti atoms which can also result in the shift in the binding energy.³¹⁶ In sample TiCuC700, the presence of anatase and rutile phases with a ratio of 0.8:1 (based on PXRD pattern) may cause a relatively smaller shift in binding energies compared to the single-phase TiO₂.

The XPS signals of O 1s (Figure 7.8c) can be deconvoluted in three peaks, appeared at 533.6, 531.5 and 529.8 eV for sample TiCuC550. The strongest peak at around 529.8 eV is attributed to the O lattice in Ti-O and Cu-O bonds in the TiO₂ and Cu_xO nanoparticles, whereas the second peak observed at around 531.5 eV can be assigned to the hydroxyl (-OH) groups present on the surface of the TiCuC nanocomposites.²⁹⁴ The third peak with low intensity at around 533.6 eV can be ascribed to the surface functionalised carboxyl groups (O=C-OH) attached to the carbon matrix.²⁷⁶ These peaks are slightly shifted for sample TiCuC700 where these peaks are observed at 533.7, 531.8 and 529.9 eV respectively. For sample TiCuC800, these peaks are shifted to 533.7, 531.3 and 529.6 eV respectively which confirms the effect of temperature on the localised chemical environment and atomic distribution of the O 1s species.

The XPS spectra of Cu 2p_{3/2} (Figure 7.8d) for sample TiCuC550 are deconvoluted into two main peaks at around 933.9 and 932.2 eV that can be attributed to the Cu(II) and Cu(I)/Cu(0) chemical states respectively.^{312, 317} Two satellite peaks are observed at 939.9 and 943.3 eV. For sample TiCuC700, the main peaks of Cu(II) and Cu(I)/Cu(0) appear at 933.5 and 932.4 eV respectively. However, for sample TiCuC800, these two peaks of Cu(II) and Cu(I)/Cu(0) are observed at 933.4 and 932.2 eV respectively. Obviously, the binding energies of Cu(II) peaks are shifted for sample TiCuC550 at 933.9 eV to at 933.4 eV for composite TiCuC800. The shift in binding energies can be attributed to the transformation of crystalline phases of Cu(II) and Cu(I). It is worth noting that the change in relative intensities of Cu(I) and Cu(II) peaks confirm the formation of dominant Cu₂O nanoparticles with a minor amount of CuO nanoparticles present

in samples obtained at lower pyrolysis temperatures (550 °C and/or 700 °C), whereas CuO is the dominant phase with a minor amount of Cu₂O and Cu⁰ nanoparticles in TiCuC800. These observations are consistent with the PXRD (Figure 7.2a) and Raman spectra (Figure 7.5a). The relative atomic concentration of Cu(II) in sample TiCuC800 is much higher compared to that of in samples TiCuC550 and TiCuC700, due to the presence of a higher amount of CuO nanoparticles at the outer surface of MOF derived TiCuC800 nanocomposite as the XPS is a surface-sensitive spectroscopic technique. As confirmed by TGA and EDX elemental mapping, pyrolysis of NH₂-MIL-125(Ti/Cu) in water vapour atmosphere at 800 °C results in part of the carbon species in the MOF turning into CO₂, leaving more TiO₂ and CuO/Cu₂O species exposed to the outer surface of the nanocomposite (schematic diagram Figure 7.3b). Moreover, high pyrolysis temperature is helpful to the fast diffusion of Cu species and results in a high concentration of CuO migrate to the outer surface of the nanocomposite. This observation is in very good agreement with the SEM, BET and XPS results.

The XPS results of C 1s for all three samples (Figure 7.8e) exhibited the main peak at 284.6 eV which is attributed to the sp² (C=C) bond in hybridised porous carbon, while a low-intensity peak appeared at 285.4 eV can be assigned to the surface functionalised C-N bond.^{318, 319} A broader peak observed at 285.7 eV is attributed to the C-O bond whereas a small peak at 288.8 eV represents the carboxyl (O=C-OH) functional groups attached to the porous carbon matrix due to the pyrolysis of NH₂-MIL-125(Ti/Cu) in water vapour atmosphere.^{261, 276} The peak intensity of C 1s for sample TiCuC800 is, in general, lower than that for sample TiCuC700 and TiCuC550, which is in agreement with the decreased amount of carbon in the sample TiCuC800, as observed by TGA (Figure 7.2c). The N 1s XPS spectrum of sample TiCuC550 (Figure 7.8f) can be deconvoluted into two peaks at 398.5 and 400.3 eV with the atomic concentration of 1.92 and 1.85%, which corresponds to the pyridinic and highly coordinated quaternary pyrrolic N species respectively.²⁶⁰ However, these pyridinic and pyrrolic N peaks for sample TiCuC700 and TiCuC800 are slightly shifted to 398.3 and 400.6 eV respectively. The change in relative intensities of the pyridinic and pyrrolic N peaks further confirms the formation of defects in the porous carbon matrix at higher pyrolysis temperature in sample TiCuC800, these peaks appeared at around 399.5 and 400.1 eV respectively. It is worth noting that the intensities of

these N 1s peaks are reduced from sample TiCuC550 to TiCuC800 because the increased pyrolysis temperature results in the easy breaking of C-N bonds to form NO_x and consequently fewer N species remaining in the formed composites. During the pyrolysis of $\text{NH}_2\text{-MIL-125(Ti)}$ under water vapour at 700 °C, the N atoms from the $\text{NH}_2\text{-BDC}$ organic linker not only functionalise the porous carbon matrix but also cause in-situ doping of interstitial N atoms into the TiO_2 . Due to the oxygen-rich gaseous atmosphere (water vapour), the formation of oxygen-rich N like interstitial/intraband states above the valence band can be anticipated.^{8, 269} The N 1s XPS peaks of such interstitial N sites usually appear above 400 eV.⁸ A low-intensity peak at around 402.4 eV in samples TiCuC700 and TiCuC800 can be assigned to the doped oxygen-rich N species forming an interstitial/intraband states above the valence band of TiO_2 .^{8, 320}

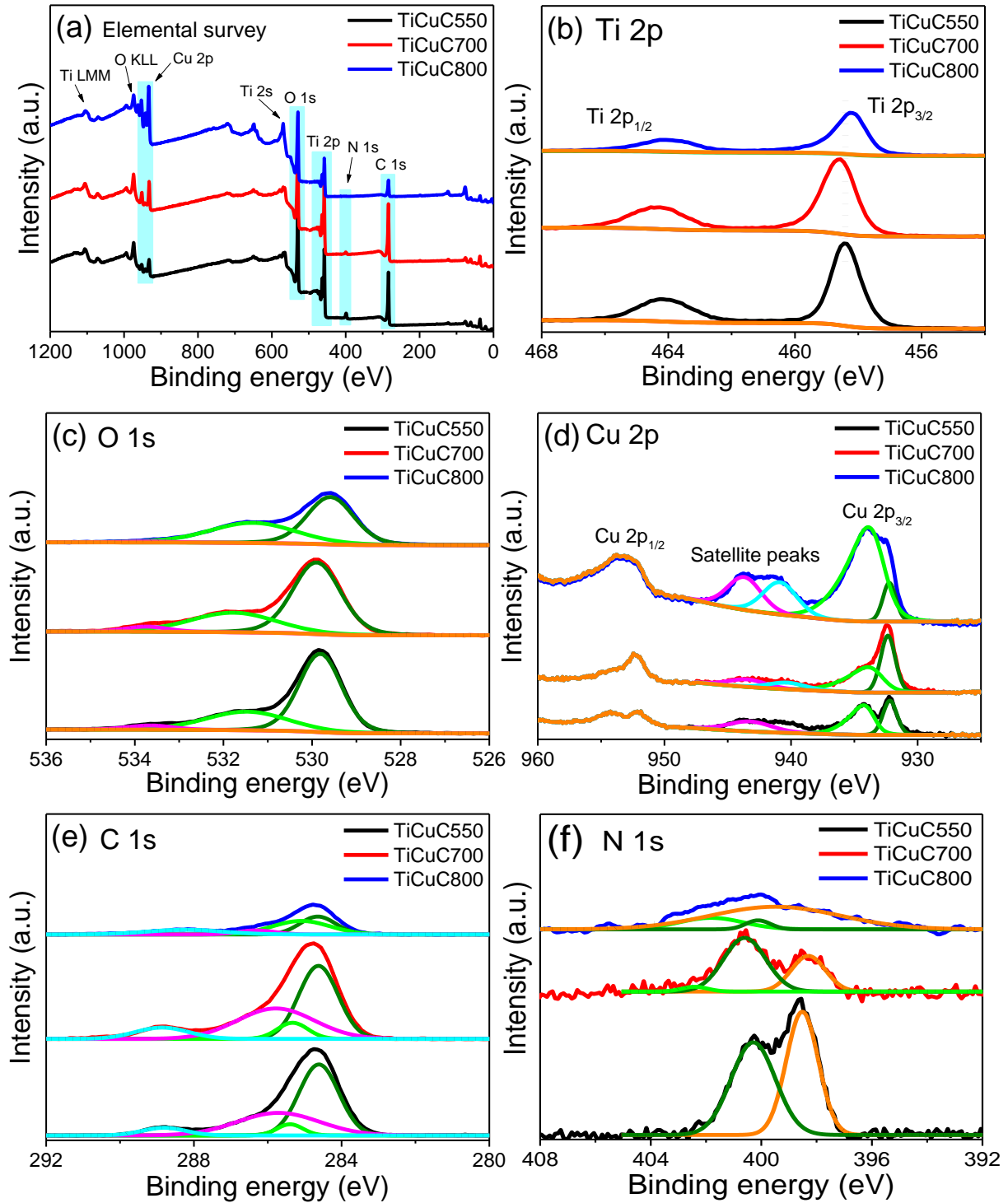


Figure 7.8 XPS spectra for (a) Elemental survey (b) Ti 2p (c) O 1s (d) Cu 2p (e) C 1s (f) N 1s of samples TiCuC550 (black), TiCuC700 (red) and TiCuC800 (blue).

The XPS is a surface analysis technique whereas EDX is semi-quantitative. The sample surfaces exposed to the ambient can be contaminated with adventitious carbon. The inductively coupled plasma (ICP) measurements could

provide additional confirmation of the metal concentrations of the catalysts. However, complete digestion of all the components of these MOF derived $\text{TiO}_2/\text{Cu}_x\text{O}/\text{C}$ composites in strong acids was not successful, which inevitably leads to the incorrect estimation of the relative concentrations of the species in the $\text{TiO}_2/\text{Cu}_x\text{O}/\text{C}$ composites. Therefore, alternative methods were adopted to determine the metal concentration in the as-prepared $\text{TiO}_2/\text{Cu}_x\text{O}/\text{C}$ composites. The XPS depth profiling can be helpful to identify the atomic distribution of the elemental species. The depth profiles of selected sample TiCuC700 (Figure 7.9) (etched depth up to 160 nm) confirm the atomic concentrations of Ti 2p, O 1s, C 1s, N 1s and Cu 2p averaged to be 16, 33, 44.8, 2.5 and 3.7 % respectively, distributed uniformly throughout the matrix. However, the relatively higher amount of C at the surface of the sample (up to 30 nm) is due to the contamination of adventitious carbon.

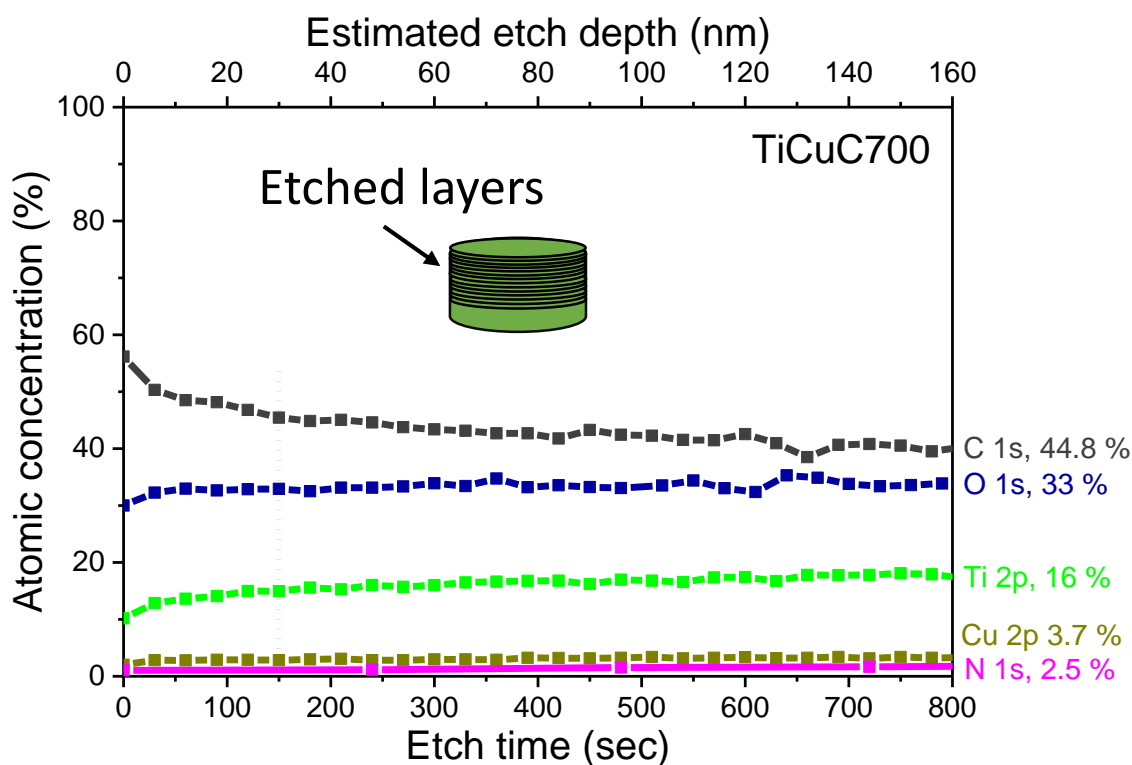


Figure 7.9 The XPS depth profiles of the selected sample TiCuC700.

7.2.2 Photocatalytic H₂ evolution

The photocatalytic HER of the NH₂-MIL-125(Ti/Cu) derived nanocomposites were evaluated under UV-Vis light filtered by a 285 nm cut-off optical filter in a methanol/water solution without using noble metals such as Pt, Au or Pd as an electron mediator. The photocatalytic HER reactor setup is shown in Figure 7.10. Under the UV-Vis light, the HER activities of the NH₂-MIL-125(Ti/Cu) derived nanocomposites change with reaction time (Figure 7.11a) which demonstrate that the pyrolysis temperature of the samples plays a very important role in determining their photocatalytic HER performance. After 6 hours of UV-Vis light exposure, the H₂ evolution activities are 556, 18455 and 6880 $\mu\text{mol g}_{\text{cat}}^{-1}$ for samples TiCuC550, TiCuC700 and TiCuC800 respectively, which are much higher than that of the commercial TiO₂ (P-25) measured to be 493 $\mu\text{mol g}_{\text{cat}}^{-1}$ under the identical experimental condition. It is obvious that the nanocomposite TiCuC700 derived from NH₂-MIL-125 (Ti/Cu) under water vapour at 700 °C exhibits much higher H₂ evolution activity than other studied nanocomposites under UV-Vis light. As presented in Table 7.1, without the loading of noble metals as co-catalyst, sample TiCuC700 shows one of the highest photocatalytic H₂ evolution performance amongst the relevant materials reported in the literature.

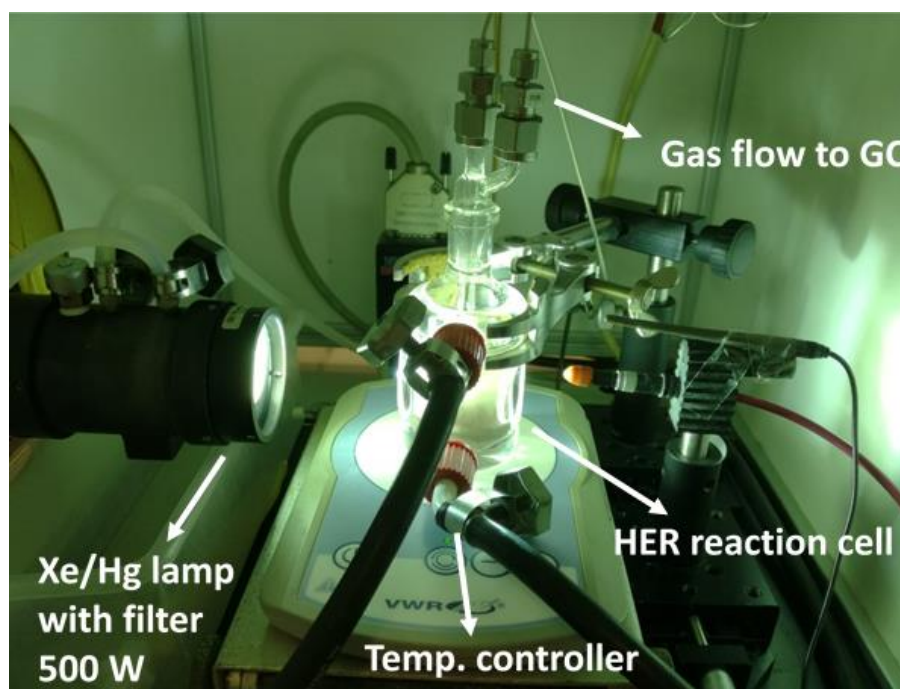


Figure 7.10 Photocatalytic setup with HER reaction cell with temperature controller and magnetic stirrer. The HER reaction cell is connected to GC. On the left side, there is a 500 W Xe/Hg lamp with a 285 nm cut-off filter.

The high photocatalytic H₂ evolution activities of NH₂-MIL-125(Ti/Cu) derived nanocomposites, particularly nanocomposite TiCuC700 without loading an expensive cocatalyst like Pt or Au, may be due to the formation of N/C co-doped TiO₂ polymorph nanoparticles as well as producing a p-n heterojunction between the TiO₂ and Cu_xO nanoparticles. These nanoparticles are homogeneously distributed in N and carboxyl groups (-COOH) functionalised high surface area porous carbon matrix without agglomerations, which result in increased absorption of incident light and more accessible active sites for photocatalytic reactions consequently lead to the significantly enhanced photocatalytic H₂ evolution performance.

As presented in Figure 7.11b, these nanocomposites TiCuC550, TiCuC700 and TiCuC800 demonstrated H₂ evolution activities of 198, 3298 and 1360 μmol g_{cat}⁻¹ h⁻¹ respectively. To elucidate the effect of Cu_xO/Cu⁰ species on the H₂ evolution performance of the nanocomposites, a sample TiC700 derived from NH₂-MIL-125(Ti) without Cu²⁺ loading was synthesised under identical experimental conditions for comparison. This sample shows H₂ evolution activity of 426 μmol g_{cat}⁻¹ h⁻¹ under the identical experimental condition. Obviously, the presence of Cu species in the TiCuC700 benefits the formation of TiO₂/Cu_xO p-n heterojunction that helps to enhance the H₂ evolution activity remarkably up to 7.7 folds compared to the sample TiC700. The AQY (%) of derived nanocomposites were calculated at 435 nm. The detailed calculation of AQY % for a selected sample TiCuC700 is given below:

$$AQY_{\lambda} = \frac{2 \times \text{number of evolved H}_2 \text{ molecules}}{\text{Total number of incident photons}} \times 100 \%$$

$$\text{Energy of photons (435 nm)} = E = \frac{h \times c}{\lambda} = 4.56 \times 10^{-19} \text{ J/photon}$$

where E is the energy of the photon, h is Planck's constant (6.63×10^{-34} J.sec⁻¹) and c is the speed of light (3×10^8 m/sec). The light source is a 500 W Xe/Hg lamp (66983, Newport). The light beam is focused with the spot size of 2.23 cm² reaching the reactor window) and an H₂O filter (61945, Newport). The calculation is provided for the wavelength $\lambda = 435$ nm (closer to the EBG of the photocatalyst).

The absolute irradiance at each wavelength can be obtained from the spectrum recorded with help of a photon counter.

$$\text{Absolute Irradiance} = \frac{P}{\lambda} = 28994.1 \mu\text{Wcm}^{-2}\text{nm}^{-1}$$

where P is radiant flux (power) and λ is the wavelength of the light.

$$\text{Total no. of photons}_{(435 \text{ nm})} = \frac{\text{Absolute Irradiance}}{\text{Energy of photons}} = \frac{28994.1 \mu\text{Jsec}^{-1}\text{cm}^2\text{nm}^{-1}}{4.56 \times 10^{-19}\text{J}}$$

$$\text{Total no. of photons}_{(435 \text{ nm})} = 6.35 \times 10^{22} \mu\text{s}^{-1}\text{cm}^2\text{nm}^{-1}$$

$$\text{Total no. of photons in moles} = \frac{\text{No. of photons} (\mu\text{s}^{-1}\text{cm}^2\text{nm}^{-1}) \times (100 \times 10^2)}{(N_A)}$$

where N_A is Avogadro's number = $6.02 \times 10^{23} \text{ mol}^{-1}$

$$\text{No. of photons in moles} = 1055 \mu\text{mols}^{-1}\text{m}^2\text{nm}^{-1}$$

$$\text{Photon count within the irradiated area} (2.23 \text{ cm}^2) = 1055 \mu\text{mols}^{-1}\text{m}^2 \times 0.000223 \text{ m}^2$$

$$\text{Total number of incident photons in irradiated area} = 0.235 \mu\text{mols}^{-1}$$

$$\text{The total amount of evolved H}_2 \text{ molecules for sample TiCuC700} = 3298 \mu\text{molg}^{-1}\text{h}^{-1}$$

$$\text{Number of evolved H}_2 \text{ molecules by the catalyst used (10 mg)} = 32.98 \mu\text{molh}^{-1} = 0.0092 \mu\text{mols}^{-1}$$

$$\text{AQY}_{(435 \text{ nm})} = \frac{2 \times 0.0092 \mu\text{mols}^{-1}}{0.235 \mu\text{mols}^{-1}} \times 100 \%$$

$$\text{AQY}_{(435 \text{ nm})} = 7.79 \%$$

The same calculation was followed to determine the AQY (%) of other samples at 435 nm. The results are summarised in Table 7.1. The AQY % value for sample TiCuC700 is the highest amongst the studied nanocomposites and it is 17 and 2.5 times of that for samples TiCuC550 and TiCuC800 respectively. The AQY % values for these composites are, in general, consistent with their H₂ evolution activities.

Table 7.1 Textural properties, estimated EBGs from Tauc plots, H₂ evolution activities and the calculated AQY (%) at 435 nm of the bi-MOF derived composites.

Sample	BET surface area (m ² g ⁻¹)	Total pore volume (cm ³ g ⁻¹)	EBG (eV)	H ₂ evolution (μmol g _{cat} ⁻¹ h ⁻¹)	AQY at 435 nm (%)
NH ₂ -MIL-125(Ti)	1462	0.60	-	-	-
NH ₂ -MIL-125(Ti/Cu)	654	0.38	-	-	-
TiCuC550	122	0.17	2.54	198	0.45
TiCuC700	337	0.26	2.47	3298	7.79
TiCuC800	277	0.37	2.56	1360	3.12
TiC700	378	0.33	2.95	426	-
Comm. TiO ₂	41	0.21	3.16	82	-

The stability of the best performed sample TiCuC700 was also evaluated. For this test, the UV-Vis light was turned on after 30 min of loading the photocatalyst in MeOH/H₂O solution. Then after every 5 hours reaction, the UV-Vis light was turned off and the system was purged with argon for half an hour before turning on the UV-Vis light again. As presented in Figure 7.11c, sample TiCuC700 shows generally good stability towards the photocatalytic H₂ evolution performance in MeOH/H₂O solution under UV-Vis light. After 5 consecutive cycles, this nanocomposite exhibited a less than 15% decrease in photocatalytic H₂ evolution activities. The decrease in photocatalytic performance may be due to the photocorrosion of the catalysts.

Since the photogenerated charge (e⁻/h⁺) density and charge transfer of photocatalysts are widely considered as important issues that can affect the photocatalytic HER activity of the nanomaterials, the electric charge transfer resistances (R_{ct}) of the nanocomposites were measured by EIS.³⁰³ The diameter of the arc or semi-circle in the high-frequency region of the Nyquist diagram represents the interfacial resistance between the electrode and the electrolyte.^{260, 321} The Nyquist Impedance spectra (Figure 7.11d) show that the R_{ct} values of samples TiCuC550, TiCuC700 and TiCuC800 are 277, 64 and 187 Ω respectively. The relatively smaller R_{ct} value of TiCuC700 suggests that the

formation of multi-heterojunctions including the phase junctions between anatase/rutile TiO_2 and $\text{Cu}_2\text{O}/\text{CuO}$ and heterojunction between TiO_2 and Cu_xO , which provide multiple pathways for electrons that enhance the electrical conductivity and charge transfer efficiency of the materials.³²² These results are in very good agreement with their photocatalytic HER results.

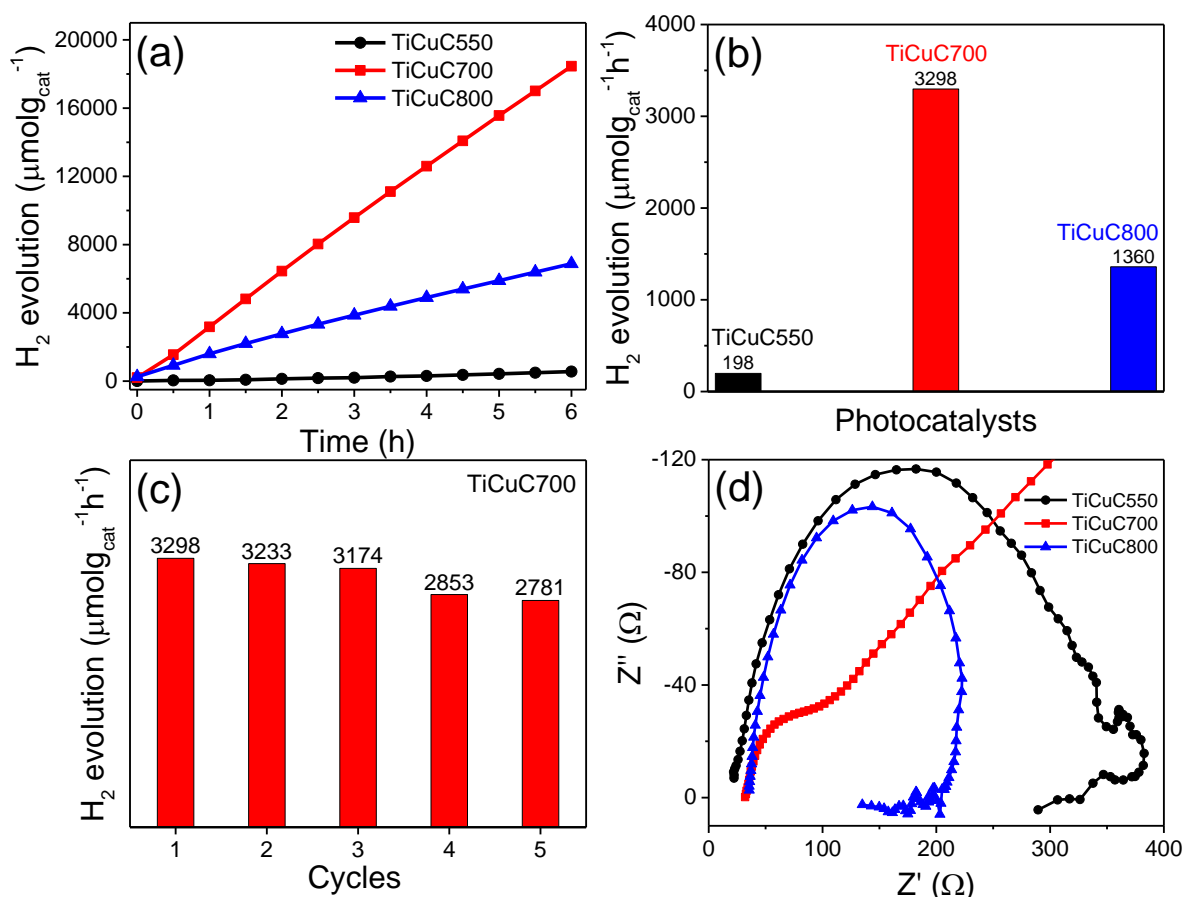


Figure 7.11 (a) Photocatalytic H_2 evolution performance of samples with reaction time (b) comparison of the photocatalytic H_2 evolution in $\mu\text{mol g}_{\text{cat}}^{-1} \text{h}^{-1}$ of TiCuC550 (black), TiCuC700 (red) and TiCuC800 (blue) (c) the recyclability test of the selected TiCuC700 nanocomposite and (d) EIS Nyquist plots of TiCuC550, TiCuC700, TiCuC800 under the same potential in 0.5 M H_2SO_4 .

Based on the characterisations and photocatalytic HER application results of the $\text{NH}_2\text{-MIL-125}(\text{Ti}/\text{Cu})$ derived nanocomposites, a schematic diagram of the photocatalytic mechanism for the best performed sample TiCuC700, which is obtained at pyrolysis temperature of 700 $^\circ\text{C}$ in water vapour, is proposed in Figure 7.12. In sample TiCuC700, the anatase to rutile TiO_2 phase percentage is 45% to 55% (based on PXRD) which is close to the optimum ratio of 1:1. Since the

anatase and rutile phases of pure TiO₂ polymorphs formed type II staggered bands where the valence band of the rutile phase is 0.55 eV above that of the anatase phase. Meanwhile, the conduction band of the rutile phase is also positioned 0.35 eV above that of the anatase phase, which results in the formation of a phase junction.³¹¹ In such a type II phase junction with staggered band alignment, the anatase phase possesses higher electron affinity and the photogenerated electrons tend to migrate from the conduction band of the rutile phase to that of the anatase phase. For NH₂-MIL-125(Ti/Cu) derived nanocomposites such as TiCuC700, the valence bands of anatase and rutile phases are further elevated with respect to the Ti 2p core levels due to the doping of N/C atoms into the crystal lattices of TiO₂, which is confirmed by the UV-Vis absorption spectra and the XPS valence band position of Ti_{2p}. This further narrows the overall EBGs (2.47 eV) of the TiCuC700 nanocomposite compared to the pure TiO₂ nanoparticles (3.16 eV), which substantially favours the improved absorption of visible light in an expanded wavelength range. The second important factor that can enhance the photocatalytic activity of the nanocomposite is the formation of the Cu₂O/CuO heterojunction. As estimated from the deconvoluted XPS Cu 2p peaks, the valence band edges of Cu₂O and CuO with respect to the Cu 2p core level lie at 932.3 and 933.5 eV respectively and heterojunction can be formed between Cu₂O and CuO nanoparticles.³²³ Moreover, the valence band edge of Cu₂O/CuO lies at 0.11 eV below the Fermi level which is close to the conduction bands of TiO₂. These energy band alignments of the nanoparticles with respect to the Fermi level enable the TiO₂ and Cu_xO nanoparticles to form a p-n heterojunction between them. In addition, the presence of Cu⁰ nanoparticles may also facilitate the faster electron transfer from the conduction bands, suppresses the charge recombination as well as prolongs the lifetime of the photogenerated electrons, which result in better interaction between these photogenerated electrons and the water molecules.²⁹⁴ As a result, multi-heterojunctions formed in the nanocomposite sample TiCuC700 enable multiple pathways to transfer photogenerated electrons to reduce water molecules with significantly improved absorption of visible light due to the remarkable decrease of the overall EBG of the nanocomposite, which results in the highest photocatalytic HER performance of the nanocomposite TiCuC700. Table 7.2 presents a comparison of photocatalytic H₂ evolution activities by similar catalysts reported in the literature.

Table 7.2 Photocatalytic HER performances of the selected similar materials reported in the literature.

Photocatalyst	Morphology	Sacrificial electron donor	Light source	H ₂ evolution ($\mu\text{mol g}_{\text{cat}}^{-1} \text{h}^{-1}$)	Ref.
Cu/TiO ₂	Octahedral shell	methanol	300 W Xe lamp (UV light)	62.16	324
Mixed phase TiO ₂	Disc-like	methanol	300 W Xe lamp (UV-Vis light)	1394	293
CuO@MTs (MT = Mesoporous TiO ₂)	Mesoporous tablets	methanol	1000 W cm ⁻² (Xe lamp)	4760	325
Cu-(Ti-MOF)	Disc-like	TEOA	Sunlight (88500 lux)	1583.5	303
Ternary TiO ₂ /CuO/Cu	Mesoporous nanofibers	methanol	Xenon lamp	851.3	294
Cu ₂ O/TiO ₂ composite	Microcubes	methanol	300 W Xenon lamp	500.4	295
NH ₂ -MIL-125(Ti)	Disc-like	CH ₃ CN/TEA	500 W Xe/Hg lamp (UV-Vis light)	49.3	310
TiO ₂ -Ag-Cu ₂ O	Nanotubes	methanol	350 W Xe arc lamp (UV-Vis light)	874.7	299
Graphene/TiO ₂	Nanosheets	methanol	350 W Xe arc lamp	736	16
TiO ₂ /Cu ₂ O/C multi-heterojunction	Disc-like	methanol	500 W Xe/Hg lamp (UV-Vis light)	3298	This work

In the proposed mechanism, the electron-rich anatase phase of TiO₂ and the CuO act as photocatalytic active sites to reduce the water molecules into H₂ species, whereas the oxidation of hole scavenger methanol takes place at the valence bands of the rutile phase of TiO₂ and Cu₂O. Moreover, the photogenerated electrons can migrate from Cu₂O to anatase TiO₂. Also, the high surface area porous carbon matrix that is decorated with N species and hydrophilic hydroxyl/carboxyl functional groups enhance the accessibility to the

photocatalytic active sites.³²⁶ Consequently, water molecules can have significantly improved interaction with the active sites and the photocatalytic H₂ evolution activity for sample TiCuC700 enhances up to 40 folds compared to the commercial TiO₂ (P-25). On the other hand, the relatively lower HER performance for samples TiCuC550 and TiCuC800 obtained at pyrolysis temperature of 550 and 800 °C respectively is due to the formation of only a single heterojunction between TiO₂ and Cu_xO nanoparticles with a relatively wider band gap. Only the anatase phase with poorly crystalline TiO₂ and Cu₂O phase predominantly exist in sample TiCuC550 whereas only the rutile phase of TiO₂ and CuO is present in nanocomposite TiCuC800. This current work demonstrates that making use of the binary metal-organic framework as a sacrificial template, nanocomposites with multi-heterojunction and tunable polymorph components of N/C co-doped TiO₂ and Cu_xO as well as high BET surface area porous carbon matrix with hydrophilic functional groups can be readily produced via a simple one-step method. The resulting nanocomposites are excellent photocatalytic materials that can dramatically enhance H₂ evolution activities at room temperature. The photocatalytic performance of this bi-MOF derived TiO₂/Cu_xO/C nanocomposites could be further improved by adjusting the amount of Cu loading on NH₂-MIL-125(Ti), deciphering the individual role of TiO₂, Cu_xO and C species and the optimisation of the formation of multi-heterojunction in the nanocomposites.

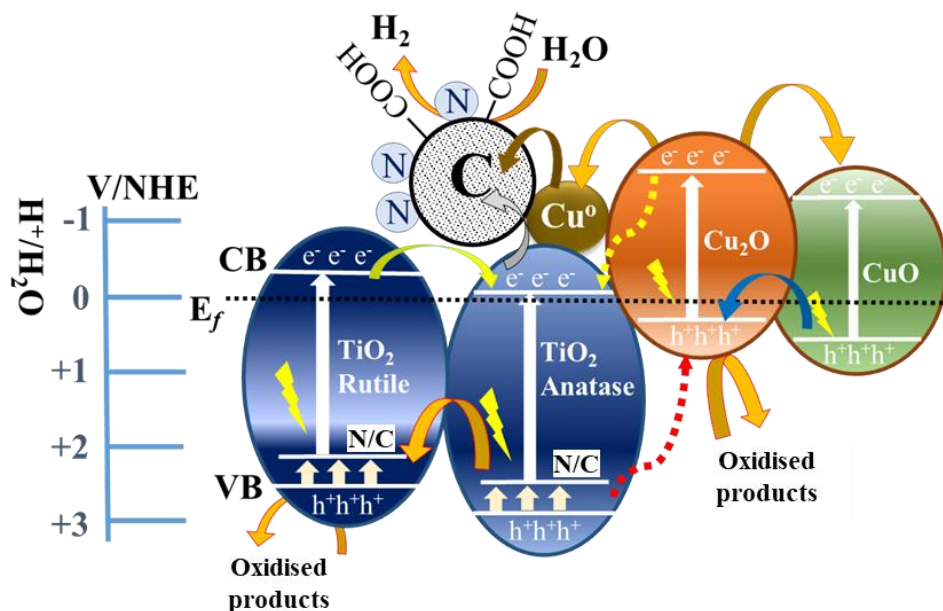


Figure 7.12 The schematic illustration of the proposed mechanism of photocatalytic H₂ evolution over NH₂-MIL-125(Ti/Cu) derived multi-heterojunction TiCuC700 under UV-Vis light.

7.3 Summary

The formation of p-n heterojunction between TiO_2 and Cu_xO nanoparticles is achieved via controlled pyrolysis of a bi-MOF, $\text{NH}_2\text{-MIL-125(Ti/Cu)}$ under water vapour atmosphere. It is found that pyrolysis of bi-MOF at $550\text{ }^\circ\text{C}$ only results in poorly crystalline anatase TiO_2 and Cu_2O , while at pyrolysis temperature of $800\text{ }^\circ\text{C}$ only rutile TiO_2 with predominant CuO nanoparticles forms the heterojunction. However, pyrolysis of bi-MOF at $700\text{ }^\circ\text{C}$ under water vapour atmosphere leads to the in-situ formation of optimal well-crystalline anatase and rutile phases of TiO_2 with type-II staggered phase junction as well as the formation of heterostructure between Cu_2O and CuO . Most importantly, these TiO_2 and Cu_xO form the p-n heterojunction due to the appropriate alignment of EBGs. These multi-heterostructured nanocomposites with narrowed EBGs embedded in high surface area porous carbon matrix retain the disc-like morphology inherited from the $\text{NH}_2\text{-MIL-125(Ti/Cu)}$ precursor. The symbiotic structural, textural and semiconducting properties provide easy access to the multiple active sites, which result in higher charge generation for photocatalytic redox reactions. Moreover, these multi-heterojunctions offer multiple pathways to photoinduced electrons and holes for improved charge migration that reduce the bulk charge recombination. In addition, the anionic doping of N and C atoms into the TiO_2 lattices narrows the EBG which enhances the absorption of visible light. Consequently, $\text{NH}_2\text{-MIL-125(Ti/Cu)}$ derived nanocomposite TiCuC700 without loading any noble metals exhibits photocatalytic H_2 evolution activity of $3298\text{ }\mu\text{mol g}_{\text{cat}}^{-1}\text{ h}^{-1}$ under UV-Vis light, which is 40 folds higher than that of the commercial TiO_2 (P-25). The one-step formation of the optimised $\text{TiO}_2/\text{Cu}_x\text{O}$ multi-heterojunctions embedded in -N/-COOH functionalised porous carbon matrix with the inherited textural properties of MOF precursor makes these bi-MOF derived nanocomposites excellent materials for photocatalytic H_2 evolution. It can be concluded that the formation of multi-heterostructures between N/C co-doped optimal TiO_2 and Cu_xO , functionalisation of porous carbon matrix and tuned textural properties are the key parameters that determine the photocatalytic activities of these nanocomposites. Further efforts to develop experimental approaches that can individually tune the above-mentioned properties of materials may result in even higher photocatalytic H_2 evolution performance.

Chapter 8

Conclusions and further work

8.1 Conclusions

This PhD thesis aimed to synthesise Zn-MOFs and Ti-MOFs derived nanocomposites to investigate the structure-property-application relationship. This work contributes towards an in-depth understanding of the role of structure, crystallinity, composition, morphology, textural properties, surface functionalities, physicochemical and semiconducting properties of MOFs derived nanocomposites for photocatalytic applications. For this purpose, first ZnO/C nanocomposites were synthesised by a simple one-step high temperature pyrolysis of MOF-5 in different carbonisation atmospheres. As discussed in chapter 4, pure ZnO, ZnO/C nanocomposites with different wt.% of metal oxide and carbon or highly porous carbon are formed by heating MOF-5 at 800 °C and 1000 °C in air, argon and water vapour atmospheres. It was found that the cubic morphology of precursor MOF-5 remains preserved in the resulting composites. The BET surface area and pore volume of derived materials dramatically change depending upon pyrolysis temperature and gaseous atmosphere. All the ZnO/C composites demonstrate high photocatalytic activity compared to the pure ZnO nanoparticles. The composite derived at 1000 °C in water vapour saturated argon atmosphere (water vapour exposure for a short duration of 1 hour at target temperature) outperforms all the other composites regarding the MB adsorption and photodegradation. The presence of oxygen-containing hydrophilic -COOH functional groups on the surface of the porous carbon functioned as traps for dye molecules to facilitate the maximum adsorption and their subsequent photodegradation by C doped ZnO nanoparticles under visible light.

To further investigate the correlation between the structure and morphology of the precursors and derived composites, three ZnO/C composites were derived from morphologically different Zn-MOFs at high temperature in water vapour saturated argon atmosphere and evaluated as photocatalysts for dye degradation and H₂ evolution under visible light. Chapter 5 presents these results concluding that thermal decomposition of Zn-MOF-5 and Zn-MOF-74 generate highly crystalline ZnO nanoparticles with high ZnO content whereas ZIF-8 produces poorly crystalline ZnO nanoparticles with the relatively lower

Wt.% of ZnO in the composites. The ZnO/C_{MOF-5} shows the highest thermal stability, ZnO/C_{MOF-74} with moderate stability while ZnO/C_{ZIF-8} are found to be thermally less resistant at high temperature. In ZnO/C_{MOF-5} and ZnO/C_{MOF-74}, C atoms are doped into the ZnO while N atoms are primary dopant in ZnO/C_{ZIF-8}. Regarding the functionality of the porous carbon, it was found that there are more carboxyl (-COOH) functional groups attached on the surface of ZnO/C_{MOF-5} due to the availability of more active sites on organic linker (terephthalic acid) as compared to ZnO/C_{MOF-74} where the organic linker is 2,5-dihydroxyterephthalic acid. The high level of N present on the carbon surface in ZnO/C_{ZIF-8} results in less oxygen-containing functionalities to attach to the surface of the catalyst under these experimental conditions. However, all three composites retain the morphologies of precursors and well-dispersed ZnO nanoparticles homogeneously distributed in the porous carbon matrix. Due to the N and/or C doping, all three derived composites exhibit narrow EBGs (around 3 eV) as compared to the bulk ZnO (3.37 eV). High BET surface areas and appropriate pore sizes of nanocomposites facilitate the adsorption of organic dye onto the surface of the catalyst. Among these selected Zn-MOFs, the MOF-5 derived ZnO/C composite proved to be the best photocatalyst with the highest performance for MB dye photodegradation and photocatalytic H₂ evolution under visible light.

To understand the thermal decomposition mechanism and transformation of a MOF into metal oxide/carbon composite, thermal annealing and in-situ STEM/EDX under inert atmosphere and several other characterisation techniques were employed to investigate the structural, physicochemical, textural and morphological properties of as-synthesised NH₂-MIL-125(Ti) and the derived nanocomposites. Chapter 6 discusses these experimental observations that the carbonisation of the Ti-MOF and subsequent formation of the metal oxide/carbon nanocomposites can be defined as a 3 stage process in the following order: well crystalline porous MOF → an intermediate amorphous phase without accessible porosity → recrystallised porous phase. As monitored by TGA-MS, the organic linkers gradually evaporate in the form of H₂O, CO₂, NO_x and -NH_x. Moreover, N released from the cleavage of covalent bonds of -NH₂ functional groups from the organic linker dope into the TiO₂ nanoparticles as well as functionalises the porous carbon. Like Zn-MOFs, the elemental distribution (Ti, O, C and N) in NH₂-

MIL-125(Ti) derived composites also remains homogeneous. During pyrolysis, an intermediate amorphous phase is formed between 350 and 550 °C without accessible porosity. However, above 550 °C, the metal species recrystallise forming the anatase TiO₂ nanoparticles followed by the formation of well crystalline rutile TiO₂ phase at around 650 °C. Simultaneously, the carbonaceous matrix originating from the organic linker undergoes subsequent decomposition and evaporation above 450 °C causing the particle shrinkage and reopening of the pore windows regenerating accessible micropores along with the formation of larger and less defined (meso)pores. The morphology of the precursor Ti-MOF remains preserved in derived N and/or C doped TiO₂/C composites.

Built on the in-depth understanding of thermal decomposition of Ti-MOF, rationally designed bi-MOFs were synthesised by loading Cu into Ti-MOF via a post-synthetic treatment method and bimetal oxide/carbon nanocomposites were derived for photocatalytic H₂ evolution. It was found that the in-situ formation of heterostructures between metal oxides can be tuned by optimising the pyrolysis conditions such as temperature and gaseous atmosphere. In chapter 7, the formation of p-n heterojunction between TiO₂ and Cu_xO nanoparticles was achieved via controlled pyrolysis of bi-MOF, NH₂-MIL-125(Ti/Cu) under water vapour. It is concluded that pyrolysis of bi-MOF at 700 °C in water vapour leads to optimal well-crystalline anatase and rutile phases of TiO₂ with type-II staggered phase junction as well as Cu₂O and CuO heterostructures and the formation of p-n heterojunction between TiO₂ and Cu_xO. These multi-heterostructures embedded in high surface area functionalised porous carbon matrix with disc-like morphology possess multiple active sites for higher charge generation for photocatalytic redox reactions and provide multiple pathways for electron/hole migration to minimise charge recombination, therefore prolonging the lifetime of the photogenerated charges. Besides, the anionic doping of N and C atoms into TiO₂ nanoparticles causes the further narrowing of the EBG which result in enhanced absorption of visible light and better accessibility to the active sites. Consequently, NH₂-MIL-125(Ti/Cu) derived nanocomposite at 700 °C in water vapour without loading any noble metals exhibit high photocatalytic H₂ evolution activity of 3298 μmol g_{cat}⁻¹ h⁻¹ under UV-Vis light, which is 40 folds higher than the commercial TiO₂ (P-25).

8.2 Further work

Based on 4 years of experimental work on this topic and the obtained experimental results, the following suggestions for further work can be proposed:

- Zn-MOF derived ZnO/C nanocomposites show better photocatalytic degradation of organic pollutants compared to the pure metal compounds due to the presence of functionalised conductive carbon matrix which offers enhanced adsorption capacities, well-exposed active sites and improved charge separation/migration pathways. These MOF derived composites should be tested for adsorption and degradation of other pollutants such as volatile organic compounds (VOCs), pharmaceutical contaminants, micro/nanoplastics and per- and polyfluoroalkyl substances (PFAs).
- Because of the complexity of these symbiotic systems, it is still a challenge to customise and in-situ tune the physical and chemical properties of these nanocomposites at atomic scale for application-specific purposes. Therefore, it is very important to develop new experimental and analytical methods which can individually study and modify the structural, textural and physicochemical properties for maximum performance.
- In this work, attempts were made to investigate the mechanism of thermal decomposition of Zn-MOFs and Ti-MOFs and the formation of ZnO/C and TiO₂/C composites. These composites show excellent semiconducting properties due to highly crystalline and heteroatom doped ZnO and TiO₂ nanoparticles dispersed in conductive porous carbon. However, in-depth investigations of the interfacial contacts between metal oxides and porous carbons need to be carried out through synchrotron/beamline experiments to better understand the mechanisms of photogenerated charge generation and migration/transfer from metal oxide to the carbon matrix.
- Bi-MOF(Ti/Cu) derived TiO₂/Cu_xO/C composites at 700 °C in controlled water vapour atmosphere showed excellent photocatalytic H₂ evolution. However, the amount of Cu loading on NH₂-MIL-125(Ti) still needs to be optimised to find out the ideal molar ratios of Ti and Cu species for maximum H₂ evolution performance. Moreover, new combinations of multimetallic guest species (in particular transition metals) encapsulated in Ti-MOF precursors are required to be rationally designed to derive

complex, multi-level hierarchical nanostructures that can improve structural stabilities and generate synergistic effects to further enhance the photocatalytic performance without expensive cocatalysts.

- As discussed in chapter 2, MOFs derived nanocomposites for photocatalytic CO₂ reduction and conversion into hydrocarbons is a less explored research area, therefore more effort needs to be devoted to this highly interesting and important field. The bi-MOF(Ti/Cu) derived TiO₂/Cu_xO/C compounds can be advantageous to simultaneously capture and reduce CO₂ into different value-added products such as CO, CH₄, CH₃OH and C₂H₅OH. These MOFs derived nanocomposites should be tested for photocatalytic CO₂ reduction.

In general, systematic operando/in-situ investigations by advanced spectroscopic techniques are required to further understand the transformation of the MOF precursors and sacrificial templates into nanocomposites. In-depth studies may reveal interesting new features to advance our understanding of the structure-property-application relationships, which will enable us to rationally design and develop high-performance novel photocatalysts without relying on expensive noble metals. Along with the experimental work, theoretical and simulation studies are also essential to understand the role of each parameter (metallic species, heterojunctions, dopants, defects, functionalities, pore shape/size, carbon matrix, energy band structures and active sites) and other relevant properties in solar-light-driven photocatalytic applications under visible light.

References

1. J. Low, J. Yu, M. Jaroniec, S. Wageh and A. A. Al-Ghamdi, *Adv. Mater.*, 2017, **29**, 1601694.
2. S. Rehman, R. Ullah, A. M. Butt and N. D. Gohar, *J. Hazard Mater.*, 2009, **170**, 560-569.
3. A. Meng, L. Zhang, B. Cheng and J. Yu, *Adv. Mater.*, 2019, **31**, 1807660.
4. A. L. Linsebigler, G. Lu and J. T. Yates, *Chem. Rev.*, 1995, **95**, 735-758.
5. R. Quesada-Cabrera, C. Sotelo-Vazquez, J. A. Darr and I. P. Parkin, *Appl. Catal. B*, 2014, **160-161**, 582-588.
6. B. Qiu, Y. Zhou, Y. Ma, X. Yang, W. Sheng, M. Xing and J. Zhang, *Sci. Rep.*, 2015, **5**, 8591.
7. C. Moslah, M. Kandyla, G. A. Mousdis, G. Petropoulou and M. Ksibi, *Phys. Status Solidi (A)*, 2018, **215**, 1800023.
8. C. Di Valentin, E. Finazzi, G. Pacchioni, A. Selloni, S. Livraghi, M. C. Paganini and E. Giamello, *Chem. Phys.*, 2007, **339**, 44-56.
9. R. Asahi, T. Morikawa, T. Ohwaki, K. Aoki and Y. Taga, *Science*, 2001, **293**, 269-271.
10. Q. L. Xu, L. Y. Zhang, J. G. Yu, S. Wageh, A. A. Al-Ghamdi and M. Jaroniec, *Mater. Today*, 2018, **21**, 1042-1063.
11. K. Vijayarangamuthu, J.-S. Youn, C.-M. Park and K.-J. Jeon, *Catal. Today*, 2018, **347**, 18-22.
12. J. Fu, J. Yu, C. Jiang and B. Cheng, *Adv. Energy Mater.*, 2017, **8**, 1701503.
13. S. Cao, L. Piao and X. Chen, *Trends Chem.*, 2020, **2**, 57-70.
14. Y. Yang, P. Gao, Y. Wang, L. Sha, X. Ren, J. Zhang, Y. Chen, T. Wu, P. Yang and X. Li, *Nano Energy*, 2017, **33**, 29-36.
15. P. Ribao, M. J. Rivero and I. Ortiz, *Environ. Sci. Pollut. Res.*, 2017, **24**, 12628-12637.
16. Q. Xiang, J. Yu and M. Jaroniec, *Nanoscale*, 2011, **3**, 3670-3678.
17. G. Yang, Z. Jiang, H. Shi, T. Xiao and Z. Yan, *J. Mater. Chem.*, 2010, **20**, 5301-5309.
18. Y. Xu, Y. Mo, J. Tian, P. Wang, H. Yu and J. Yu, *Appl. Catal. B*, 2016, **181**, 810-817.

19. D. H. Wang, L. Jia, X. L. Wu, L. Q. Lu and A. W. Xu, *Nanoscale*, 2012, **4**, 576-584.
20. C. Han, Y. Wang, Y. Lei, B. Wang, N. Wu, Q. Shi and Q. Li, *Nano Res.*, 2014, **8**, 1199-1209.
21. T. Kawahara, Y. Konishi, H. Tada, N. Tohge, J. Nishii and S. Ito, *Angew. Chem. Int. Ed.*, 2002, **41**, 2811-2813.
22. A. Kubacka, M. Fernández-García and G. Colón, *Chem. Rev.*, 2012, **112**, 1555-1614.
23. O. M. Yaghi, M. O'Keeffe, N. W. Ockwig, H. K. Chae, M. Eddaoudi and J. Kim, *Nature*, 2003, **423**, 705-714.
24. H. Li, M. Eddaoudi, M. O'Keeffe and O. M. Yaghi, *Nature*, 1999, **402**, 276-279.
25. O. M. Yaghi, G. Li and H. Li, *Nature*, 1995, **378**, 703-706.
26. H. Furukawa, K. E. Cordova, M. O'Keeffe and O. M. Yaghi, *Science*, 2013, **341**, 1230444.
27. S. Wang, Q. Wang, X. Feng, B. Wang and L. Yang, *Adv. Mater.*, 2017, **29**, 1701898.
28. M. Dan-Hardi, C. Serre, T. Frot, L. Rozes, G. Maurin, C. Sanchez and G. Férey, *J. Am. Chem. Soc.*, 2009, **131**, 10857-10859.
29. S. Kitagawa and K. Uemura, *Chem. Soc. Rev.*, 2005, **34**, 109-119.
30. J. J. Perry Iv, J. A. Perman and M. J. Zaworotko, *Chem. Soc. Rev.*, 2009, **38**, 1400-1417.
31. K. Maeda and K. Domen, *J. Phys. Chem. C*, 2007, **111**, 7851-7861.
32. R. Robson, *Dalton Trans.*, 2008, 5113-5131.
33. D. J. Tranchemontagne, J. R. Hunt and O. M. Yaghi, *Tetrahedron*, 2008, **64**, 8553-8557.
34. C. H. Hendon, A. J. Rieth, M. D. Korzynski and M. Dinca, *ACS Cent. Sci.*, 2017, **3**, 554-563.
35. J. Zhu, P.-Z. Li, W. Guo, Y. Zhao and R. Zou, *Coordin. Chem. Rev.*, 2018, **359**, 80-101.
36. H. Luo, Z. Zeng, G. Zeng, C. Zhang, R. Xiao, D. Huang, C. Lai, M. Cheng, W. Wang, W. Xiong, Y. Yang, L. Qin, C. Zhou, H. Wang, Y. Zhou and S. Tian, *Chem. Eng. J.*, 2020, **383**, 123196.
37. A. Dhakshinamoorthy, A. M. Asiri and H. García, *Angew. Chem. Int. Ed.*, 2016, **55**, 5414-5445.

38. H. Wang, Q.-L. Zhu, R. Zou and Q. Xu, *Chem*, 2017, **2**, 52-80.
39. M. A. Nasalevich, M. van der Veen, F. Kapteijn and J. Gascon, *CrystEngComm*, 2014, **16**, 4919-4926.
40. W. Xia, A. Mahmood, R. Zou and Q. Xu, *Energy Environ. Sci.*, 2015, **8**, 1837-1866.
41. L. Oar-Arteta, T. Wezendonk, X. Sun, F. Kapteijn and J. Gascon, *Mater. Chem. Front.*, 2017, **1**, 1709-1745.
42. S. Dang, Q.-L. Zhu and Q. Xu, *Nat. Rev. Mater.*, 2017, **3**, 17075.
43. D. Li, H.-Q. Xu, L. Jiao and H.-L. Jiang, *EnergyChem*, 2019, **1**, 100005.
44. S. Hu, M. Liu, K. Li, Y. Zuo, A. Zhang, C. Song, G. Zhang and X. Guo, *CrystEngComm*, 2014, **16**, 9645-9650.
45. Y. Han, M. Liu, K. Li, Y. Zuo, Y. Wei, S. Xu, G. Zhang, C. Song, Z. Zhang and X. Guo, *CrystEngComm*, 2015, **17**, 6434-6440.
46. Z. Xie, W. Xu, X. Cui and Y. Wang, *ChemSusChem*, 2017, **10**, 1645-1663.
47. F. Marpaung, M. Kim, J. H. Khan, K. Konstantinov, Y. Yamauchi, M. S. A. Hossain, J. Na and J. Kim, *Chem. Asian J.*, 2019, **14**, 1331-1343.
48. W. Chaikittisilp, K. Ariga and Y. Yamauchi, *J. Mater. Chem. A*, 2013, **1**, 14-19.
49. L. Lu, B. Wu, W. Shi and P. Cheng, *Inorg. Chem. Front.*, 2019, **6**, 3456-3467.
50. X. Zhang, A. Chen, M. Zhong, Z. Zhang, X. Zhang, Z. Zhou and X.-H. Bu, *Electrochem. Energy Rev.*, 2019, **2**, 29-104.
51. W. Zhan, L. Sun and X. Han, *NanoMicro Lett.*, 2019, **11**, 1.
52. Y.-Z. Chen, R. Zhang, L. Jiao and H.-L. Jiang, *Coordin. Chem. Rev.*, 2018, **362**, 1-23.
53. L. Feng, K.-Y. Wang, J. Powell and H.-C. Zhou, *Matter*, 2019, **1**, 801-824.
54. N. Stock and S. Biswas, *Chem. Rev.*, 2012, **112**, 933-969.
55. Y. Song, X. Li, L. Sun and L. Wang, *RSC Adv.*, 2015, **5**, 7267-7279.
56. J. Chen and Y. Li, *Chem. Rec.*, 2016, **16**, 1456-1476.
57. L. Wang, Y. Han, X. Feng, J. Zhou, P. Qi and B. Wang, *Coordin. Chem. Rev.*, 2016, **307**, 361-381.
58. X. Huang, M.-G. Willinger, H. Fan, Z.-I. Xie, L. Wang, A. Klein-Hoffmann, F. Girgsdies, C.-S. Lee and X.-M. Meng, *Nanoscale*, 2014, **6**, 8787-8795.
59. S.-N. Zhao, G. Wang, D. Poelman and P. Van Der Voort, *Molecules*, 2018, **23**, 2947.

60. X. Zhang, J. Wang, X.-X. Dong and Y.-K. Lv, *Chemosphere*, 2020, **242**, 125144.
61. Q. Wang, Q. Gao, A. M. Al-Enizi, A. Nafady and S. Ma, *Inorg. Chem. Front.*, 2020, **7**, 300-339.
62. F. Song, W. Li and Y. Sun, *Inorganics*, 2017, **5**, 40.
63. I. A. Khan, Y. Qian, A. Badshah, M. A. Nadeem and D. Zhao, *ACS Appl. Mater. Interfaces*, 2016, **8**, 17268-17275.
64. X. Cao, C. Tan, M. Sindoro and H. Zhang, *Chem. Soc. Rev.*, 2017, **46**, 2660-2677.
65. A. Kidanemariam, J. Lee and J. Park, *Polymers*, 2019, **11**, 2090.
66. L. Zeng, X. Guo, C. He and C. Duan, *ACS Catal.*, 2016, **6**, 7935-7947.
67. L. Li, J. He, Y. Wang, X. Lv, X. Gu, P. Dai, D. Liu and X. Zhao, *J. Mater. Chem. A*, 2019, **7**, 1964-1988.
68. C.-C. Wang, Y.-Q. Zhang, J. Li and P. Wang, *J. Mol. Struct.*, 2015, **1083**, 127-136.
69. C.-C. Wang, J.-R. Li, X.-L. Lv, Y.-Q. Zhang and G. Guo, *Energy & Environ. Science*, 2014, **7**, 2831-2867.
70. A. Dhakshinamoorthy, Z. Li and H. Garcia, *Chem. Soc. Rev.*, 2018, **47**, 8134-8172.
71. I. Ahmed and S. H. Jung, *Mater. Today*, 2014, **17**, 136-146.
72. J.-D. Xiao and H.-L. Jiang, *Acc. Chem. Res.*, 2019, **52**, 356-366.
73. W. Chen, J. Fang, Y. Zhang, G. Chen, S. Zhao, C. Zhang, R. Xu, J. Bao, Y. Zhou and X. Xiang, *Nanoscale*, 2018, **10**, 4463-4474.
74. Z. Wu, X. Yuan, J. Zhang, H. Wang, L. Jiang and G. Zeng, *ChemCatChem*, 2017, **9**, 41-64.
75. B. Li, H.-M. Wen, Y. Cui, W. Zhou, G. Qian and B. Chen, *Adv. Mater.*, 2016, **28**, 8819-8860.
76. L.-H. Xie, M.-M. Xu, X.-M. Liu, M.-J. Zhao and J.-R. Li, *Adv. Sci.*, 2020, **7**, 1901758.
77. W. Liu, R. Yin, X. Xu, L. Zhang, W. Shi and X. Cao, *Adv. Sci.*, 2019, **6**, 1802373.
78. K. Shen, X. Chen, J. Chen and Y. Li, *ACS Catal.*, 2016, **6**, 5887-5903.
79. Y. V. Kaneti, J. Tang, R. R. Salunkhe, X. Jiang, A. Yu, K. C. W. Wu and Y. Yamauchi, *Adv. Mater.*, 2017, **29**, 1604898.

80. S. J. Yang, J. H. Im, T. Kim, K. Lee and C. R. Park, *J. Hazard. Mater.*, 2011, **186**, 376-382.
81. S. Hermes, M.-K. Schröter, R. Schmid, L. Khodeir, M. Muhler, A. Tissler, R. W. Fischer and R. A. Fischer, *Angew. Chem. Int. Ed.*, 2005, **44**, 6237-6241.
82. K. Khaletskaya, A. Pougin, R. Medishetty, C. Rösler, C. Wiktor, J. Strunk and R. A. Fischer, *Chem. Mater.*, 2015, **27**, 7248-7257.
83. Z. N. Yu, L. Tetard, L. Zhai and J. Thomas, *Energy Environ. Sci.*, 2015, **8**, 702-730.
84. B. Liu, H. Shioyama, T. Akita and Q. Xu, *J. Am. Chem. Soc.*, 2008, **130**, 5390-5391.
85. Y.-J. Li, J.-M. Fan, M.-S. Zheng and Q.-F. Dong, *Energy Environ. Sci.*, 2016, **9**, 1998-2004.
86. S. Wang and X. Wang, *Small*, 2015, **11**, 3097-3112.
87. C. Wang, Y. V. Kaneti, Y. Bando, J. Lin, C. Liu, J. Li and Y. Yamauchi, *Mater. Horiz.*, 2018, **5**, 394-407.
88. R. Li, *Chinese J. Catal.*, 2017, **38**, 5-12.
89. K. J. Lee, J. H. Lee, S. Jeoung and H. R. Moon, *Acc. Chem. Res.*, 2017, **50**, 2684-2692.
90. W. Wang, X. Xu, W. Zhou and Z. Shao, *Adv. Sci. (Weinh)*, 2017, **4**, 1600371.
91. C. Hu, T. Lu, F. Chen and R. Zhang, *J. Chinese Adv. Mater. Soc.*, 2013, **1**, 21-39.
92. P. Singh, P. Shandilya, P. Raizada, A. Sudhaik, A. Rahmani-Sani and A. Hosseini-Bandegharai, *Arab. J. Chem.*, 2020, **13**, 3498-3520.
93. P. Liang, C. Zhang, H. Sun, S. Liu, M. Tadé and S. Wang, *RSC Adv.*, 2016, **6**, 95903-95909.
94. J. Xu, Y. Qi, C. Wang and L. Wang, *Appl. Catal. B*, 2019, **241**, 178-186.
95. X. Yang, L. Qiu and X. Luo, *RSC Adv.*, 2018, **8**, 4890-4894.
96. B. Yan, L. Zhang, Z. Tang, M. Al-Mamun, H. Zhao and X. Su, *Appl. Catal. B*, 2017, **218**, 743-750.
97. J. Li, X. Xu, X. Liu, W. Qin and L. Pan, *Ceram. Int.*, 2017, **43**, 835-840.
98. I. Majeed, M. A. Nadeem, A. Badshah, F. K. Kanodarwala, H. Ali, M. A. Khan, J. A. Stride and M. A. Nadeem, *Catal. Sci. Technol.*, 2017, **7**, 677-686.

99. X. Zhao, Y. Tan, F. Wu, H. Niu, Z. Tang, Y. Cai and J. P. Giesy, *Sci. Total Environ.*, 2016, **571**, 380-387.
100. J.-Y. Xu, X.-P. Zhai, L.-F. Gao, P. Chen, M. Zhao, H.-B. Yang, D.-F. Cao, Q. Wang and H.-L. Zhang, *RSC Adv.*, 2016, **6**, 2011-2018.
101. B. Chen, G. Ma, D. Kong, Y. Zhu and Y. Xia, *Carbon*, 2015, **95**, 113-124.
102. B. N. Bhadra, A. Vinu, C. Serre and S. H. Jung, *Mater. Today*, 2019, **25**, 88-111.
103. R. Das, P. Pachfule, R. Banerjee and P. Poddar, *Nanoscale*, 2012, **4**, 591-599.
104. S. N. Habisreutinger, L. Schmidt-Mende and J. K. Stolarczyk, *Angew. Chem. Int. Ed.*, 2013, **52**, 7372-7408.
105. C. Burda, Y. Lou, X. Chen, A. C. S. Samia, J. Stout and J. L. Gole, *Nano Lett.*, 2003, **3**, 1049-1051.
106. J. Low, B. Cheng and J. Yu, *Appl. Surf. Sci.*, 2017, **392**, 658-686.
107. K. M. Lee, C. W. Lai, K. S. Ngai and J. C. Juan, *Water Res.*, 2016, **88**, 428-448.
108. Y.-F. Zhang, L.-G. Qiu, Y.-P. Yuan, Y.-J. Zhu, X. Jiang and J.-D. Xiao, *Appl. Catal. B*, 2014, **144**, 863-869.
109. H. Zhang, T. Wang, J. Wang, H. Liu, T. D. Dao, M. Li, G. Liu, X. Meng, K. Chang, L. Shi, T. Nagao and J. Ye, *Adv. Mater.*, 2016, **28**, 3703-3710.
110. L. Yu, G. Li, X. Zhang, X. Ba, G. Shi, Y. Li, P. K. Wong, J. C. Yu and Y. Yu, *ACS Catal.*, 2016, **6**, 6444-6454.
111. K. Takanabe, *ACS Catal.*, 2017, **7**, 8006-8022.
112. T. Hisatomi, K. Takanabe and K. Domen, *Catal. Lett.*, 2015, **145**, 95-108.
113. A. T. Garcia-Esparza and K. Takanabe, *J. Mater. Chem. A*, 2016, **4**, 2894-2908.
114. H. Chen, Z.-G. Gu, S. Mirza, S.-H. Zhang and J. Zhang, *J. Mater. Chem. A*, 2018, **6**, 7175-7181.
115. J. Xu, J. Gao, Y. Qi, C. Wang and L. Wang, *ChemCatChem*, 2018, **10**, 3327-3335.
116. Y.-H. Chiu, M. T.-F. Chang, C.-Y. Chen, M. Sone and Y.-J. Hsu, *Catalysts*, 2019, **9**, 2073-4344.
117. M. Rochkind, S. Pasternak and Y. Paz, *Molecules*, 2015, **20**, 88-110.
118. L. Yuan, C. Han, M.-Q. Yang and Y.-J. Xu, *Int. Rev. Phys. Chem.*, 2016, **35**, 1-36.

119. V. P. Indrakanti, J. D. Kubicki and H. H. Schobert, *Energy Environ. Sci.*, 2009, **2**, 745-758.
120. C.-Y. Hu, J. Zhou, C.-Y. Sun, M.-m. Chen, X.-L. Wang and Z.-M. Su, *Chem. Eur. J.*, 2019, **25**, 379-385.
121. K. Zhao, S. Zhao, C. Gao, J. Qi, H. Yin, D. Wei, M. F. Mideksa, X. Wang, Y. Gao, Z. Tang and R. Yu, *Small*, 2018, **14**, 1800762.
122. N. L. Torad, M. Hu, S. Ishihara, H. Sukegawa, A. A. Belik, M. Imura, K. Ariga, Y. Sakka and Y. Yamauchi, *Small*, 2014, **10**, 2096-2107.
123. H. Chen, K. Shen, J. Chen, X. Chen and Y. Li, *J. Mater. Chem. A*, 2017, **5**, 9937-9945.
124. K.-Y. Andrew Lin and F.-K. Hsu, *RSC Adv.*, 2015, **5**, 50790-50800.
125. B. Tatykayev, F. Donat, H. Alem, L. Balan, G. Medjahdi, B. Uralbekov and R. Schneider, *ACS Omega*, 2017, **2**, 4946-4954.
126. A. Fujishima and K. Honda, *Nature*, 1972, **238**, 37-38.
127. X. Chen and S. S. Mao, *Chem. Rev.*, 2007, **107**, 2891-2959.
128. X. Chen and C. Burda, *J. Am. Chem. Soc.*, 2008, **130**, 5018-5019.
129. X. Chen, L. Liu and F. Huang, *Chem. Soc. Rev.*, 2015, **44**, 1861-1885.
130. L.-M. Gao, J.-H. Zhao, T. Li, R. Li, H.-Q. Xie, P.-L. Zhu, X.-Y. Niu and K. Li, *CrystEngComm*, 2019, **21**, 3686-3693.
131. P. Liang, C. Zhang, H. Sun, S. Liu, M. Tade and S. Wang, *Energy Fuels*, 2017, **31**, 2138-2143.
132. Q. Xiang, B. Cheng and J. Yu, *Angew. Chem. Int. Ed.*, 2015, **54**, 11350-11366.
133. K. Jayaramulu, T. Toyao, V. Ranc, C. Rösler, M. Petr, R. Zboril, Y. Horiuchi, M. Matsuoka and R. A. Fischer, *J. Mater. Chem. A*, 2016, **4**, 18037-18042.
134. X. Cao, B. Zheng, W. Shi, J. Yang, Z. Fan, Z. Luo, X. Rui, B. Chen, Q. Yan and H. Zhang, *Adv. Mater.*, 2015, **27**, 4695-4701.
135. W.-H. Li, K. Ding, H.-R. Tian, M.-S. Yao, B. Nath, W.-H. Deng, Y. Wang and G. Xu, *Adv. Funct. Mater.*, 2017, **27**, 1702067.
136. B. Hu, J.-Y. Yuan, J.-Y. Tian, M. Wang, X. Wang, L. He, Z. Zhang, Z.-W. Wang and C.-S. Liu, *J. Colloid Interface Sci.*, 2018, **531**, 148-159.
137. Y. Jin, C. Zhao, Z. Sun, Y. Lin, L. Chen, D. Wang and C. Shen, *RSC Adv.*, 2016, **6**, 30763-30768.

138. M. Zhang, J. Luo, X. Liang, B. Yan, M. I. Baikenov, X. Su, L. Chi and C. Yang, *Mater. Lett.*, 2018, **210**, 73-76.
139. T. He, B. Ni, S. Zhang, Y. Gong, H. Wang, L. Gu, J. Zhuang, W. Hu and X. Wang, *Small*, 2018, **14**, 1703929.
140. T. Rodenas, I. Luz, G. Prieto, B. Seoane, H. Miro, A. Corma, F. Kapteijn, F. X. Llabrés i Xamena and J. Gascon, *Nat. Mater.*, 2015, **14**, 48-55.
141. R. Makiura, S. Motoyama, Y. Umemura, H. Yamanaka, O. Sakata and H. Kitagawa, *Nat. Mater.*, 2010, **9**, 565-571.
142. Z. Zhang, Y. Chen, S. He, J. Zhang, X. Xu, Y. Yang, F. Nosheen, F. Saleem, W. He and X. Wang, *Angew. Chem. Int. Ed.*, 2014, **53**, 12517-12521.
143. G. Zhu, X. Li, H. Wang and L. Zhang, *Catal. Commun.*, 2017, **88**, 5-8.
144. S. Xiao, D. Pan, R. Liang, W. Dai, Q. Zhang, G. Zhang, C. Su, H. Li and W. Chen, *Appl. Catal. B*, 2018, **236**, 304-313.
145. J. Jia, Y. Wang, M. Xu, M.-I. Qi, Y. Wu and G. Zhao, *J. Sol-Gel Sci. Tech.*, 2020, **93**, 123-130.
146. M.-L. Xu, J.-D. Cui, J.-H. Zhao, F.-T. Liu and K. Li, *CrystEngComm*, 2018, **20**, 5490-5495.
147. K. Li, Y. Zhang, Y.-Z. Lin, K. Wang and F.-T. Liu, *ACS Appl. Mater. Interfaces*, 2019, **11**, 28918-28927.
148. J. Liu, X. Zhao, P. Jing, W. Shi and P. Cheng, *Chem. Eur. J.*, 2019, **25**, 2330-2336.
149. M. Li, S. Song, C. Su, L. Li, Z. Yan and X. Cao, *Catal. Sci. Technol.*, 2019, **9**, 3828-3835.
150. J.-H. Zhao, L.-W. Liu, K. Li, T. Li and F.-T. Liu, *CrystEngComm*, 2019, **21**, 2416-2421.
151. S. H. Ahn and A. Manthiram, *J. Mater. Chem. A*, 2017, **5**, 2496-2503.
152. M. Wan, S. Cui, W. Wei, S. Cui, K. Chen, W. Chen and L. Mi, *RSC Adv.*, 2019, **9**, 2441-2450.
153. M. Aleksandrak, D. Baranowska, T. Kedzierski, K. Sielicki, S. Zhang, M. Biegun and E. Mijowska, *Appl. Catal. B*, 2019, **257**, 117906.
154. M. J. Valero-Romero, J. G. Santaclara, L. Oar-Arteta, L. van Koppen, D. Y. Osadchii, J. Gascon and F. Kapteijn, *Chem. Eng. J.*, 2019, **360**, 75-88.

155. T. Wang, L. Gao, J. Hou, S. J. A. Herou, J. T. Griffiths, W. Li, J. Dong, S. Gao, M.-M. Titirici, R. V. Kumar, A. K. Cheetham, X. Bao, Q. Fu and S. K. Smoukov, *Nat. Commun.*, 2019, **10**, 1340.
156. C. Avci, J. Ariñez-Soriano, A. Carné-Sánchez, V. Guillerme, C. Carbonell, I. Imaz and D. MasPOCH, *Angew. Chem. Int. Ed.*, 2015, **54**, 14417-14421.
157. M. Zhang, Y.-L. Huang, J.-W. Wang and T.-B. Lu, *J. Mater. Chem. A*, 2016, **4**, 1819-1827.
158. C. Yang, J. Cheng, Y. Chen and Y. Hu, *Appl. Surf. Sci.*, 2017, **420**, 252-259.
159. A. A. Dubale, I. N. Ahmed, X.-H. Chen, C. Ding, G.-H. Hou, R.-F. Guan, X. Meng, X.-L. Yang and M.-H. Xie, *J. Mater. Chem. A*, 2019, **7**, 6062-6079.
160. C. Zhang, F. Ye, S. Shen, Y. Xiong, L. Su and S. Zhao, *RSC Adv.*, 2015, **5**, 8228-8235.
161. Y. Zhang, J. Zhou, X. Chen, Q. Feng and W. Cai, *J. Alloys Compd.*, 2019, **777**, 109-118.
162. H.-L. Cao, F.-Y. Cai, K. Yu, Y.-Q. Zhang, J. Lü and R. Cao, *ACS Sustain. Chem. Engin.*, 2019, **7**, 10847-10854.
163. J. Wang, C. Xue, W. Yao, J. Liu, X. Gao, R. Zong, Z. Yang, W. Jin and D. Tao, *Appl. Catal. B*, 2019, **250**, 369-381.
164. S. Rai, A. Ikram, S. Sahai, S. Dass, R. Shrivastav and V. R. Satsangi, *Renew. Energy*, 2015, **83**, 447-454.
165. G. K. Pradhan, D. K. Padhi and K. M. Parida, *ACS Appl. Mater. Interfaces*, 2013, **5**, 9101-9110.
166. Y. Pang, Z. Li, X. Jiao, D. Chen and C. Li, *ChemistrySelect*, 2020, **5**, 1047-1053.
167. Y. Lin, H. Wan, F. Chen, X. Liu, R. Ma and T. Sasaki, *Dalton Trans.*, 2018, **47**, 7694-7700.
168. Z. Guo, J. K. Cheng, Z. Hu, M. Zhang, Q. Xu, Z. Kang and D. Zhao, *RSC Adv.*, 2014, **4**, 34221-34225.
169. Y. Su, S. Li, D. He, D. Yu, F. Liu, N. Shao and Z. Zhang, *ACS Sustain. Chem. Engin.*, 2018, **6**, 11989-11998.
170. X. Cao, B. Zheng, X. Rui, W. Shi, Q. Yan and H. Zhang, *Angew. Chem. Int. Ed.*, 2013, **53**, 1404-1409.

171. K.-Y. Andrew Lin, F.-K. Hsu and W.-D. Lee, *J. Mater. Chem. A*, 2015, **3**, 9480-9490.
172. J. Cravillon, S. Münzer, S.-J. Lohmeier, A. Feldhoff, K. Huber and M. Wiebcke, *Chem. Mater.*, 2009, **21**, 1410-1412.
173. M. Sohail, Y.-N. Yun, E. Lee, S. K. Kim, K. Cho, J.-N. Kim, T. W. Kim, J.-H. Moon and H. Kim, *Cryst. Growth Des.*, 2017, **17**, 1208-1213.
174. B. D. Cullity, *Elements of x-ray diffraction*, Addison-Wesley Publishing Company, Inc., Reading, MA, 1978.
175. A. L. Patterson, *Phys. Rev.*, 1939, **56**, 978-982.
176. A. W. Coats and J. P. Redfern, *Analyst*, 1963, **88**, 906-924.
177. K. S. W. Sing, *Adv. Colloid Interface Sci.*, 1998, **76-77**, 3-11.
178. J. Rouquerol, P. Llewellyn and F. Rouquerol, in *Studies in Surface Science and Catalysis*, eds. P. L. Llewellyn, F. Rodriguez-Reinoso, J. Rouquerol and N. Seaton, Elsevier, 2007, vol. 160, pp. 49-56.
179. M. J. Baker, C. S. Hughes and K. A. Hollywood, in *Biophotonics: Vibrational Spectroscopic Diagnostics*, Morgan & Claypool Publishers, 2016, DOI: 10.1088/978-1-6817-4071-3, ch. 2, pp. 2-14.
180. P. R. Griffiths and J. A. d. Haseth, in *Fourier Transform Infrared Spectrometry*, 2007, DOI: 10.1002/9780470106310, ch. 18, pp. 375-393.
181. C. V. Raman and K. S. Krishnan, *Nature*, 1928, **122**, 12-13.
182. W. F. Zhang, Y. L. He, M. S. Zhang, Z. Yin and Q. Chen, *J. Phys. D Appl. Phys.*, 2000, **33**, 912.
183. A. Smekal, *Naturwissenschaften*, 1923, **11**, 873-875.
184. D. A. Long, in *The Raman Effect*, ed. D. A. Long, 2002, DOI: 10.1002/0470845767, ch. 5, pp. 85-152.
185. A. B. S. Elliott, R. Horvath and K. C. Gordon, *Chem. Soc. Rev.*, 2012, **41**, 1929-1946.
186. J. W. John F. Watts, in *An Introduction to Surface Analysis by XPS and AES*, Wiley Online Books, 2020, DOI: 10.1002/9781119417651, ch. 1, pp. 1-18.
187. J. G. Jenkin, R. C. G. Leckey and J. Liesegang, *J. Electron Spectros. Relat. Phenomena*, 1977, **12**, 1-35.
188. S. Hüfner, *Springer-Verlag Berlin Heidelberg*, 2003, DOI: 10.1007 / 978-3-662-09280-4.

189. A. Yoshida, Y. Kaburagi and Y. Hishiyama, in *Materials Science and Engineering of Carbon*, eds. M. Inagaki and F. Kang, Butterworth-Heinemann, 2016, DOI: 10.1016/B978-0-12-805256-3.00005-2, ch. 5, pp. 71-93.
190. N. Erdman, D. C. Bell and R. Reichelt, in *Springer Handbook of Microscopy*, eds. P. W. Hawkes and J. C. H. Spence, Springer International Publishing, Cham, 2019, DOI: 10.1007/978-3-030-00069-1_5, pp. 229-318.
191. D. B. Williams and C. B. Carter, in *Transmission Electron Microscopy: A Textbook for Materials Science*, eds. D. B. Williams and C. B. Carter, Springer US, Boston, MA, 2009, DOI: 10.1007/978-0-387-76501-3_1, ch. 1, pp. 3-22.
192. J. Mast, E. Verleysen, V.-D. Hodoroaba and R. Kaegi, in *Characterization of Nanoparticles*, eds. V.-D. Hodoroaba, W. E. S. Unger and A. G. Shard, Elsevier, 2020, DOI: 10.1016/B978-0-12-814182-3.00004-3, ch. 2.1.2, pp. 29-48.
193. B. P. Kafle, in *Chemical Analysis and Material Characterization by Spectrophotometry*, ed. B. P. Kafle, Elsevier, 2020, DOI: 10.1016/B978-0-12-814866-2.00002-6, ch. 2, pp. 17-38.
194. B. P. Kafle, in *Chemical Analysis and Material Characterization by Spectrophotometry*, ed. B. P. Kafle, Elsevier, 2020, DOI: 10.1016/B978-0-12-814866-2.00005-1, ch. 5, pp. 79-145.
195. M. E. O. B. Tribollet, in *Electrochemical Impedance Spectroscopy*, Wiley Online Books, 2008, ch. 23, pp. 447-459.
196. L. Huang, H. Wang, J. Chen, Z. Wang, J. Sun, D. Zhao and Y. Yan, *Microporous Mesoporous Mater.*, 2003, **58**, 105-114.
197. R. Li and C. Li, in *Advances in Catalysis*, ed. C. Song, Academic Press, 2017, vol. 60, pp. 1-57.
198. N. Serpone, *J. Photochem. Photobiol. A*, 1997, **104**, 1-12.
199. R. E. Galian and J. Pérez-Prieto, *Energy Environ. Sci.*, 2010, **3**, 1488-1498.
200. J. Wang, Z. Wang, B. Huang, Y. Ma, Y. Liu, X. Qin, X. Zhang and Y. Dai, *ACS Appl. Mater. Interfaces*, 2012, **4**, 4024-4030.
201. S. Liu, C. Li, J. Yu and Q. Xiang, *CrystEngComm*, 2011, **13**, 2533-2541.

202. S. Cho, J.-W. Jang, J. S. Lee and K.-H. Lee, *CrystEngComm*, 2010, **12**, 3929-3935.
203. A. S. Alshammari, L. Chi, X. Chen, A. Bagabas, D. Kramer, A. Alromaeh and Z. Jiang, *RSC Adv.*, 2015, **5**, 27690-27698.
204. S. J. Yang, S. Nam, T. Kim, J. H. Im, H. Jung, J. H. Kang, S. Wi, B. Park and C. R. Park, *J. Am. Chem. Soc.*, 2013, **135**, 7394-7397.
205. L. Pan, T. Muhammad, L. Ma, Z.-F. Huang, S. Wang, L. Wang, J.-J. Zou and X. Zhang, *Appl. Catal. B*, 2016, **189**, 181-191.
206. S. S. Kaye, A. Dailly, O. M. Yaghi and J. R. Long, *J. Am. Chem. Soc.*, 2007, **129**, 14176-14177.
207. M. Z. Hussain, A. Schneemann, R. A. Fischer, Y. Zhu and Y. Xia, *ACS Appl. Energy Mater.*, 2018, **1**, 4695-4707.
208. Z. Abbasi, E. Shamsaei, S. K. Leong, B. Ladewig, X. Zhang and H. Wang, *Microporous Mesoporous Mater.*, 2016, **236**, 28-37.
209. J. Hafizovic, M. Bjørgen, U. Olsbye, P. D. C. Dietzel, S. Bordiga, C. Prestipino, C. Lamberti and K. P. Lillerud, *J. Am. Chem. Soc.*, 2007, **129**, 3612-3620.
210. G. Srinivas, V. Krungleviciute, Z.-X. Guo and T. Yildirim, *Energy Environ. Sci.*, 2014, **7**, 335-342.
211. M. Han, X. Yin, S. Ren, W. Duan, L. Zhang and L. Cheng, *RSC Adv.*, 2016, **6**, 6467-6474.
212. Ü. Özgür, Y. I. Alivov, C. Liu, A. Teke, M. A. Reshchikov, S. Doğan, V. Avrutin, S. J. Cho and H. Morkoç, *J. Appl. Phys.*, 2005, **98**, 041301.
213. D. I. Son, B. W. Kwon, D. H. Park, W.-S. Seo, Y. Yi, B. Angadi, C.-L. Lee and W. K. Choi, *Nat. Nanotechnol.*, 2012, **7**, 465-471.
214. R. Cuscó, E. Alarcón-Lladó, J. Ibáñez, L. Artús, J. Jiménez, B. Wang and M. J. Callahan, *Phys. Rev. B*, 2007, **75**, 165202.
215. P. K. Chu and L. Li, *Mater. Chem. Phys.*, 2006, **96**, 253-277.
216. A. C. Ferrari and J. Robertson, *Phys. Rev. B*, 2000, **61**, 14095-14107.
217. R. O. Dillon, J. A. Woollam and V. Katkanant, *Phys. Rev. B*, 1984, **29**, 3482-3489.
218. F. C. Tai, S. C. Lee, C. H. Wei and S. L. Tyan, *Mater. Trans.*, 2006, **47**, 1847-1852.

219. D. K. Mishra, J. Mohapatra, M. K. Sharma, R. Chattarjee, S. K. Singh, S. Varma, S. N. Behera, S. K. Nayak and P. Entel, *J. Magn. Magn. Mater.*, 2013, **329**, 146-152.
220. S. Yang, L. Zhi, K. Tang, X. Feng, J. Maier and K. Müllen, *Adv. Funct. Mater.*, 2012, **22**, 3634-3640.
221. J. Wang, H.-x. Zhong, Y.-l. Qin and X.-b. Zhang, *Angew. Chem. Int. Ed.*, 2013, **52**, 5248-5253.
222. A. C. Ferrari, *Solid State Commun.*, 2007, **143**, 47-57.
223. H.-P. Jing, C.-C. Wang, Y.-W. Zhang, P. Wang and R. Li, *RSC Adv.*, 2014, **4**, 54454-54462.
224. T. Toyao, M. Saito, Y. Horiuchi, K. Mochizuki, M. Iwata, H. Higashimura and M. Matsuoka, *Catal. Sci. Technol.*, 2013, **3**, 2092-2097.
225. Q. Yu, H. Dong, X. Zhang, Y.-X. Zhu, J.-H. Wang, F.-M. Zhang and X.-J. Sun, *CrystEngComm*, 2018, **20**, 3228-3233.
226. C. B. Ong, L. Y. Ng and A. W. Mohammad, *Renew. Sustain. Energy Rev.*, 2018, **81**, 536-551.
227. P. A. Julien, K. Užarević, A. D. Katsenis, S. A. J. Kimber, T. Wang, O. K. Farha, Y. Zhang, J. Casaban, L. S. Germann, M. Etter, R. E. Dinnebier, S. L. James, I. Halasz and T. Friščić, *J. Am. Chem. Soc.*, 2016, **138**, 2929-2932.
228. S. Gadipelli and Z. Guo, *Chem. Mater.*, 2014, **26**, 6333-6338.
229. R. R. Salunkhe, Y. V. Kaneti and Y. Yamauchi, *ACS Nano*, 2017, **11**, 5293-5308.
230. L. Zhang and Y. H. Hu, *J. Phys. Chem. C*, 2010, **114**, 2566-2572.
231. N. L. Rosi, J. Kim, M. Eddaoudi, B. Chen, M. O'Keeffe and O. M. Yaghi, *J. Am. Chem. Soc.*, 2005, **127**, 1504-1518.
232. J. B. James and Y. S. Lin, *J. Phys. Chem. C*, 2016, **120**, 14015-14026.
233. B. Xu, Y. Mei, Z. Xiao, Z. Kang, R. Wang and D. Sun, *Phys. Chem. Chem. Phys.*, 2017, **19**, 27178-27183.
234. S. Gadipelli and Z. X. Guo, *ChemSusChem*, 2015, **8**, 2123-2132.
235. M. Wang, F. Ren, J. Zhou, G. Cai, L. Cai, Y. Hu, D. Wang, Y. Liu, L. Guo and S. Shen, *Sci. Rep.*, 2015, **5**, 12925.
236. H. Sudrajat and S. Babel, *Environ. Sci. Pollut. Res.*, 2016, **23**, 10177-10188.

237. F. J. Manjón, B. Marí, J. Serrano and A. H. Romero, *J. Appl. Phys.*, 2005, **97**, 053516.
238. A. Kaschner, U. Haboeck, M. Strassburg, M. Strassburg, G. Kaczmarczyk, A. Hoffmann, C. Thomsen, A. Zeuner, H. R. Alves, D. M. Hofmann and B. K. Meyer, *Appl. Phys. Lett.*, 2002, **80**, 1909-1911.
239. S. Sun, X. Chang, X. Li and Z. Li, *Ceram. Int.*, 2013, **39**, 5197-5203.
240. H.-x. Zhong, J. Wang, Y.-w. Zhang, W.-l. Xu, W. Xing, D. Xu, Y.-f. Zhang and X.-b. Zhang, *Angew. Chem. Int. Ed.*, 2014, **53**, 14235-14239.
241. J. M. Simmons, H. Wu, W. Zhou and T. Yildirim, *Energy Environ. Sci.*, 2011, **4**, 2177-2185.
242. H. Wu, W. Zhou and T. Yildirim, *J. Am. Chem. Soc.*, 2009, **131**, 4995-5000.
243. T. Hisatomi, J. Kubota and K. Domen, *Chem. Soc. Rev.*, 2014, **43**, 7520-7535.
244. E. Antolini, *Appl. Catal. B*, 2018, **237**, 491-503.
245. M. Samadi, H. A. Shivaee, A. Pourjavadi and A. Z. Moshfegh, *Appl. Catal. A: Gen.*, 2013, **466**, 153-160.
246. B. M. Rajbongshi, A. Ramchiary and S. K. Samdarshi, *Mater. Lett.*, 2014, **134**, 111-114.
247. R. Atchudan, T. N. J. I. Edison, S. Perumal, D. Karthikeyan and Y. R. Lee, *J. Photochem. Photobiol. B*, 2016, **162**, 500-510.
248. Y. Wang, R. Shi, J. Lin and Y. Zhu, *Energy Environ. Sci.*, 2011, **4**, 2922-2929.
249. A. Di Mauro, M. Cantarella, G. Nicotra, G. Pellegrino, A. Gulino, M. V. Brundo, V. Privitera and G. Impellizzeri, *Sci. Rep.*, 2017, **7**, 40895.
250. S. Kuriakose, B. Satpati and S. Mohapatra, *Phys. Chem. Chem. Phys.*, 2015, **17**, 25172-25181.
251. I. Ganesh, P. S. C. Sekhar, G. Padmanabham and G. Sundararajan, *Appl. Surf. Sci.*, 2012, **259**, 524-537.
252. M. Ahmad, E. Ahmed, Z. L. Hong, Z. Iqbal, N. R. Khalid, T. Abbas, I. Ahmad, A. M. Elhissi and W. Ahmed, *Ceram. Int.*, 2013, **39**, 8693-8700.
253. H. Ahmad, S. K. Kamarudin, L. J. Minggu and M. Kassim, *Renew. Sust. Energ. Rev.*, 2015, **43**, 599-610.
254. K. Maeda, *ACS Catal.*, 2013, **3**, 1486-1503.

255. Z. Nan, S. Chong-Xin, T. Hua-Qiao, Z. Qi, W. Shuang-Peng, S. Zai-Cheng, X. Yong-de and S. De-Zhen, *Nanotechnology*, 2016, **27**, 22LT01.
256. H. Yang, Z. Jin, H. Hu, G. Lu and Y. Bi, *Catalysts*, 2017, **7**, 99.
257. J.-M. Li, H.-Y. Cheng, Y.-H. Chiu and Y.-J. Hsu, *Nanoscale*, 2016, **8**, 15720-15729.
258. X. Wang, L. Yin and G. Liu, *ChemComm.*, 2014, **50**, 3460-3463.
259. P. Gomathisankar, K. Hachisuka, H. Katsumata, T. Suzuki, K. Funasaka and S. Kaneco, *Int. J. Hydrog. Energy*, 2013, **38**, 11840-11846.
260. Z. Huang, Z. Yang, M. Z. Hussain, B. Chen, Q. Jia, Y. Zhu and Y. Xia, *Electrochim. Acta*, 2020, **330**, 135335.
261. M. Z. Hussain, G. S. Pawar, Z. Huang, A. A. Tahir, R. A. Fischer, Y. Zhu and Y. Xia, *Carbon*, 2019, **146**, 348-363.
262. X. Hou, S. L. Stanley, M. Zhao, J. Zhang, H. Zhou, Y. Cai, F. Huang and Q. Wei, *J. Alloys Compd.*, 2019, **777**, 982-990.
263. Y. Liu, X. Xu, Z. Shao and S. P. Jiang, *Energy Storage Mater.*, 2020, **26**, 1-22.
264. W. Sun, X. Tang and Y. Wang, *Electrochem. Energy Rev.*, 2020, **3**, 127-154.
265. K. He, Z. Cao, R. Liu, Y. Miao, H. Ma and Y. Ding, *Nano Res.*, 2016, **9**, 1856-1865.
266. Z. Luo, A. S. Poyraz, C.-H. Kuo, R. Miao, Y. Meng, S.-Y. Chen, T. Jiang, C. Wenos and S. L. Suib, *Chem. Mater.*, 2014, **27**, 6-17.
267. A. Gómez-Avilés, M. Peñas-Garzón, J. Bedia, D. D. Dionysiou, J. J. Rodríguez and C. Belver, *Appl. Catal. B*, 2019, **253**, 253-262.
268. M. Oveisi, M. A. Asli and N. M. Mahmoodi, *J. Hazard. Mater.*, 2018, **347**, 123-140.
269. M. Z. Hussain, Z. Yang, B. v. d. Linden, Z. Huang, Q. Jia, E. Cerrato, R. A. Fischer, F. Kapteijn, Y. Zhu and Y. Xia, *J. Energy Chem.*, 2021, **57**, 485-495.
270. O. Frank, M. Zúkalová, B. Lasková, J. Kürti, J. Koltai and L. Kavan, *Phys. Chem. Chem. Phys.*, 2012, **14**, 14567-14572.
271. P. Karthik, R. Vinoth, P. Zhang, W. Choi, E. Balaraman and B. Neppolian, *ACS Appl. Energy Mater.*, 2018, **1**, 1913-1923.
272. Y. Gong, Y. Tang, Z. Mao, X. Wu, Q. Liu, S. Hu, S. Xiong and X. Wang, *J. Mater. Chem. A*, 2018, **6**, 13696-13704.

273. H. Karimi, M. A. Heidari, H. B. M. Emrooz and M. Shokouhimehr, *Diam. Relat. Mater.*, 2020, **108**, 107999.
274. Q. Wang, G. Wang, X. Liang, X. Dong and X. Zhang, *Appl. Surf. Sci.*, 2019, **467-468**, 320-327.
275. N. C. Saha and H. G. Tompkins, *J. Appl. Phys.*, 1992, **72**, 3072-3079.
276. P. Iamprasertkun, A. Krittayavathananon and M. Sawangphruk, *Carbon*, 2016, **102**, 455-461.
277. X. Song, W. Li, D. He, H. Wu, Z. Ke, C. Jiang, G. Wang and X. Xiao, *Adv. Energy Mater.*, 2018, **8**, 1800165.
278. T. C. Jagadale, S. P. Takale, R. S. Sonawane, H. M. Joshi, S. I. Patil, B. B. Kale and S. B. Ogale, *J. Phys. Chem. C*, 2008, **112**, 14595-14602.
279. H. Liu, Y. Ma, J. Chen, M. Wen, G. Li and T. An, *Appl. Catal. B*, 2019, **250**, 337-346.
280. D. Ao, J. Zhang and H. Liu, *J. Photochem. Photobiol. A*, 2018, **364**, 524-533.
281. J. Qiu, L. Yang, M. Li and J. Yao, *Mater. Res. Bull.*, 2019, **112**, 297-306.
282. F. Kapteijn, J. A. Moulijn, S. Matzner and H. P. Boehm, *Carbon*, 1999, **37**, 1143-1150.
283. J. R. Pels, F. Kapteijn, J. A. Moulijn, Q. Zhu and K. M. Thomas, *Carbon*, 1995, **33**, 1641-1653.
284. S. Dissegna, K. Epp, W. R. Heinz, G. Kieslich and R. A. Fischer, *Adv. Mater.*, 2018, **30**, 1704501.
285. G. U. Fayomi, S. E. Mini, O. S. I. Fayomi, O. Oyeleke, D. O. Omole and I. I. Akinwumi, *IOP Conf. Ser.: Mater. Sci. Eng.*, 2019, **640**, 012097.
286. Y. Qi, S. Chen, M. Li, Q. Ding, Z. Li, J. Cui, B. Dong, F. Zhang and C. Li, *Chem. Sci.*, 2017, **8**, 437-443.
287. J. Qiu, X. Zhang, Y. Feng, X. Zhang, H. Wang and J. Yao, *Appl. Catal. B*, 2018, **231**, 317-342.
288. Z. Tong, D. Yang, Y. Sun, Y. Nan and Z. Jiang, *Small*, 2016, **12**, 4093-4101.
289. H. Zou, B. He, P. Kuang, J. Yu and K. Fan, *Adv. Funct. Mater.*, 2018, **28**, 1706917.
290. D. E. Scaife, *Sol. Energy*, 1980, **25**, 41-54.
291. G. Yan, M. Zhang, J. Hou and J. Yang, *Mater. Chem. Phys.*, 2011, **129**, 553-557.

292. Q. Wang, T. Hisatomi, S. S. K. Ma, Y. Li and K. Domen, *Chem. Mater.*, 2014, **26**, 4144-4150.
293. S. Kampouri, C. P. Ireland, B. Valizadeh, E. Oveisi, P. A. Schouwink, M. Mensi and K. C. Stylianou, *ACS Appl. Energy Mater.*, 2018, **1**, 6541-6548.
294. H. Hou, M. Shang, F. Gao, L. Wang, Q. Liu, J. Zheng, Z. Yang and W. Yang, *ACS Appl. Mater. Interfaces*, 2016, **8**, 20128-20137.
295. Y.-H. Zhang, Y.-L. Li, B.-B. Jiu, F.-L. Gong, J.-L. Chen, S.-M. Fang and H.-L. Zhang, *Nanotechnology*, 2019, **30**, 145401.
296. F. Xu, W. Xiao, B. Cheng and J. Yu, *Int. J. Hydrog. Energy*, 2014, **39**, 15394-15402.
297. M. E. Aguirre, R. Zhou, A. J. Eugene, M. I. Guzman and M. A. Grela, *Appl. Catal. B*, 2017, **217**, 485-493.
298. Y. Liao, P. Deng, X. Wang, D. Zhang, F. Li, Q. Yang, H. Zhang and Z. Zhong, *Nanoscale Res. Lett.*, 2018, **13**, 221.
299. J. Fu, S. Cao and J. Yu, *J. Materiomics*, 2015, **1**, 124-133.
300. H. Hou, F. Gao, L. Wang, M. Shang, Z. Yang, J. Zheng and W. Yang, *J. Mater. Chem. A*, 2016, **4**, 6276-6281.
301. K. Qi, B. Cheng, J. Yu and W. Ho, *Chinese J. Catal.*, 2017, **38**, 1936-1955.
302. M. H. Yap, K. L. Fow and G. Z. Chen, *Green Energy Environ.*, 2017, **2**, 218-245.
303. P. Karthik, A. R. M. Shaheer, A. Vinu and B. Neppolian, *Small*, 2020, **16**, 1902990.
304. S. Chaurasiya, J. Udaya Bhanu and P. Thangadurai, *Trans. Indian Inst. Met.*, 2018, **71**, 1185-1191.
305. N. G. Elfadill, M. R. Hashim, K. M. Chahrour, M. A. Qaeed and M. Bououdina, *Superlattices Microstruct.*, 2015, **85**, 908-917.
306. L. Bokobza, J.-L. Bruneel and M. Couzi, *C—J. Carbon Res.*, 2015, **1**, 77-94.
307. J. Y. Choi, C. K. Lim, B. Park, M. Kim, A. Jamal and H. Song, *J. Mater. Chem. A*, 2019, **7**, 15068-15072.
308. W. Ho, Q. Tay, H. Qi, Z. Huang, J. Li and Z. Chen, *Molecules*, 2017, **22**, 677.
309. A. Sahai, N. Goswami, S. D. Kaushik and S. Tripathi, *Appl. Surf. Sci.*, 2016, **390**, 974-983.

310. M. A. Nasalevich, C. H. Hendon, J. G. Santaclara, K. Svane, B. van der Linden, S. L. Veber, M. V. Fedin, A. J. Houtepen, M. A. van der Veen, F. Kapteijn, A. Walsh and J. Gascon, *Sci. Rep.*, 2016, **6**, 23676.
311. D. O. Scanlon, C. W. Dunnill, J. Buckeridge, S. A. Shevlin, A. J. Logsdail, S. M. Woodley, C. R. Catlow, M. J. Powell, R. G. Palgrave, I. P. Parkin, G. W. Watson, T. W. Keal, P. Sherwood, A. Walsh and A. A. Sokol, *Nat. Mater.*, 2013, **12**, 798-801.
312. W. Zhen, W. Jiao, Y. Wu, H. Jing and G. Lu, *Catal. Sci. Technol.*, 2017, **7**, 5028-5037.
313. M. Rehan, X. Lai and G. M. Kale, *CrystEngComm*, 2011, **13**, 3725-3732.
314. U. Diebold and T. E. Madey, *Surf. Sci. Spectra*, 1996, **4**, 227-231.
315. R. Asahi, T. Morikawa, H. Irie and T. Ohwaki, *Chem. Rev.*, 2014, **114**, 9824-9852.
316. J. Xing, Z. P. Chen, F. Y. Xiao, X. Y. Ma, C. Z. Wen, Z. Li and H. G. Yang, *Chem. Asian J.*, 2013, **8**, 1265-1270.
317. X. Qiu, M. Miyauchi, K. Sunada, M. Minoshima, M. Liu, Y. Lu, D. Li, Y. Shimodaira, Y. Hosogi, Y. Kuroda and K. Hashimoto, *ACS Nano*, 2012, **6**, 1609-1618.
318. J. Ederer, P. Janoš, P. Ecorchard, J. Tolasz, V. Štengl, H. Beneš, M. Perchacz and O. Pop-Georgievski, *RSC Adv.*, 2017, **7**, 12464-12473.
319. H. Wang, X. Yuan, Y. Wu, G. Zeng, X. Chen, L. Leng, Z. Wu, L. Jiang and H. Li, *J. Hazard. Mater.*, 2015, **286**, 187-194.
320. Y. Yuan, K. Sheng, S. Zeng, X. Han, L. Sun, I. Lončarić, W. Zhan and D. Sun, *Inorg. Chem.*, 2020, **59**, 5456-5462.
321. J. Ângelo, P. Magalhães, L. Andrade and A. Mendes, *Appl. Surf. Sci.*, 2016, **387**, 183-189.
322. D. Barreca, G. Carraro, A. Gasparotto, C. Maccato, M. Cruz-Yusta, J. L. Gómez-Camer, J. Morales, C. Sada and L. Sánchez, *ACS Appl. Mater. Interfaces*, 2012, **4**, 3610-3619.
323. H. Li, Z. Su, S. Hu and Y. Yan, *Appl. Catal. B*, 2017, **207**, 134-142.
324. R. Li, S. Wu, X. Wan, H. Xu and Y. Xiong, *Inorg. Chem. Front.*, 2016, **3**, 104-110.
325. Y.-T. Liao, Y.-Y. Huang, H. M. Chen, K. Komaguchi, C.-H. Hou, J. Henzie, Y. Yamauchi, Y. Ide and K. C. W. Wu, *ACS Appl. Mater. Interfaces*, 2017, **9**, 42425-42429.

326. Q. Xu, L. Zhang, J. Yu, S. Wageh, A. A. Al-Ghamdi and M. Jaroniec, *Mater. Today*, 2018, **21**, 1042-1063.